

# **AEROSPACE RESEARCH IN BULGARIA**

Volume 26, Sofia, 2014  
Space Research and Technology Institute  
Bulgarian Academy of Sciences

## **Editorial Board**

Prof. Garo Mardirossian (*Editor-in-Chief*)  
Chief Assistant Lyudmila Todorieva (*English Language Editor*)  
Tsveta Srebrova, MS (*Technical Editor*)

Acad. Valeri Bondour – Russia

Prof. Gerassimos Papadopoulos – Greece

Prof. Stefano Tinti – Italy

Prof. Rupert Gertzer – Germany

Corr. Member Petar Getsov

Corr. Member Filip Filipov

Corr. Member Petar Velinov

Prof. Petko Nenovski

Prof. Eugenia Roumenina

Prof. Dimitar Teodossiev

Assoc. Prof. Tania Ivanova

Assoc. Prof. Lachezar Filipov

Assoc. Prof. Stefan Chapkunov

## **Address**

AEROSPACE RESEARCH IN BULGARIA  
Space Research and Technology Institute  
bl. 1, *Acad. G. Bonchev* St., Sofia 1113, Bulgaria

e-mail: journal@space.bas.bg

*Pre-Publication Processing*

Tsveta Srebrova

© Space Research and Technology Institute – Bulgarian Academy of Sciences

ISSN 1313 – 0927

**This issue of *Aerospace Research in Bulgaria* is published with financial support from the Bulgarian National Science Fund – Contract No ДНП 04/85**

# **Aerospace Research in Bulgaria**

**26**

**Sofia, 2014**

## **C o n t e n t s**

1. *Dimitar Dimitrov*  
ANALYTICAL COMPUTATION OF TWO INTEGRALS, APPEARING IN THE THEORY OF ELLIPTICAL ACCRETION DISCS. III. SOLVING OF THE FULL SET OF AUXILIARY INTEGRALS, CONTAINING LOGARITHMIC FUNCTIONS INTO THEIR INTEGRANDS. . . . . 5
  
2. *Dimitar Dimitrov*  
ANALYTICAL COMPUTATION OF TWO INTEGRALS, APPEARING IN THE THEORY OF ELLIPTICAL ACCRETION DISCS. IV. SOLVING OF THE INTEGRALS, ENSURING THE EVALUATION OF THE DERIVATIVES, ENTERING INTO THE WRONSKI DETERMINANT. . 21
  
3. *Tsvetan Dachev, Jordanka Semkova, Borislav Tomov, Yury Matviichuk, Plamen Dimitrov, Nikolay Bankov, Rositsa Koleva, Stefan Malchev*  
DESCRIPTION OF THE LIULIN TYPE INSTRUMENTS AND MAIN SCIENTIFIC RESULTS.. . . . 46
  
4. *Tsvetan Georgiev*  
ROBUST SMOOTHING OF TIME SERIES BY SIMPLE FAST ALGORITHM. TRACING OF TREND IN STELLAR FLICKERING AND CONTINUUM OF STELLAR SPECTRUM . . . . . 100
  
5. *Filip Filipov*  
FRACTAL APPROACH TO SPACE STRUCTURES, OBJECTS AND DYNAMIC PHENOMENA. . . . . 117
  
6. *Velko Velkov*  
HYPOTHESIS OF A COSMOLOGICAL MODEL OF THE UNIVERSE WITHOUT GRAVITATION. . . . . 136

7.	<b><i>Veneta Guineva, Irina Despirak, Boris Kozelov</i></b> VARIATIONS OF SUBSTORMS CONNECTED WITH DIFFERENT SOLAR WIND CONDITIONS. ....	145
8.	<b><i>Vassil Vassilev, Eugenia Roumenina</i></b> CROP MONITORING USING SPOT-VGT NDVIs S10 TIME-SERIES PRODUCT FOR NORTHEAST BULGARIA. ....	155
9.	<b><i>Vassil Vassilev</i></b> CROP AREA ESTIMATES BASED ON PER-PIXEL SUPERVISED CLASSIFICATION ON EO-1 ALI IMAGE FOR A TEST SITE IN NORTHEAST BULGARIA. ....	179
10.	<b><i>Lachezar Filchev</i></b> SATELLITE HYPERSPECTRAL EARTH OBSERVATION MISSIONS – A REVIEW. ....	191
11.	<b><i>Svetoslav Zabunov, Peter Getsov, Garo Mardirossian</i></b> DEVELOPMENT OF THE EXPERIMENTAL MULTIROTOR UNMANNED AERIAL VEHICLE HELICOPTER MODELS OF THE XZ-SERIES. ....	207
12.	<b><i>Ivan Nikolov, Stefka Kasarova, Nina Sultanova</i></b> SOME AEROSPACE APPLICATIONS OF OPTICAL POLYMERS. ....	220
13.	<b><i>Vasil Kavardzhikov, Dessislava Pashkouleva, Ivan Nikolov</i></b> MICRO- AND NANO-FOCUSING OPTICS INTENDED FOR REMOTE IMAGING SYSTEMS. ....	243
14.	<b><i>Konstantin Metodiev</i></b> SATURATED HYDRAULIC CONDUCTIVITY COEFFICIENT MEASUREMENTS OF BALKANINE™ AND TURFACE® SUBSTRATA THROUGH THE CONSTANT HEAD METHOD. ....	257
15.	<b><i>Peter Velinov</i></b> NEW ANALYTICAL APPROACH FOR COSMIC RAY IONIZATION MODELING IN PLANETARY ENVIRONMENTS BY USING THE IONIZATION YIELD FUNCTIONS . ....	266
	<b><i>New books</i></b>	
	<b><i>Garo Mardirossian</i></b> INTERESTING BOOK OF THE DAY. ....	291

# С Ъ Д Ъ Р Ж А Н И Е

1. **Димитър Димитров**  
АНАЛИТИЧНО ПРЕСМЯТАНЕ НА ДВА ИНТЕГРАЛА, ВЪЗНИКВАЩИ  
В ТЕОРИЯТА НА ЕЛИПТИЧНИТЕ АКРЕЦИОННИ ДИСКОВЕ.  
III. РЕШАВАНЕ НА ПЪЛНАТА СИСТЕМА ОТ СПОМАГАТЕЛНИ  
ИНТЕГРАЛИ, СЪДЪРЖАЩИ ЛОГАРИТМИЧНИ ФУНКЦИИ В ТЕХНИТЕ  
ИНТЕГРАНДИ. . . . . 5
2. **Димитър Димитров**  
АНАЛИТИЧНО ПРЕСМЯТАНЕ НА ДВА ИНТЕГРАЛА, ВЪЗНИКВАЩИ  
В ТЕОРИЯТА НА ЕЛИПТИЧНИТЕ АКРЕЦИОННИ ДИСКОВЕ.  
IV. РЕШАВАНЕ НА ЕДИН ИНТЕГРАЛ, ОБЕЗПЕЧАВАЩ ОЦЕНЯВАНЕТО  
НА ПРОИЗВОДНИТЕ, ВЛИЗАЩИ В ДЕТЕРМИНАНТАТА НА ВРОНСКИ. . . 21
3. **Цветан Дачев, Йорданка Семкова, Борислав Томов,  
Юрий Матвийчук, Пламен Димитров, Николай Банков,  
Росица Колева, Стефан Малчев**  
ОПИСАНИЕ НА ПРИБОРИТЕ ОТ ТИПА „ЛЮЛИН“ И ГЛАВНИ НАУЧНИ  
РЕЗУЛТАТИ. . . . . 46
4. **Цветан Георгиев**  
РОБАСТО ИЗГЛАЖДАНЕ НА РЕДОВЕ ОТ ДАННИ ЧРЕЗ ПРОСТ БЪРЗ  
АЛГОРИТЪМ. ПРЕКАРВАНЕ НА ТРЕНДА ПРИ ЗВЕЗДЕН ФЛИКЕРИНГ  
И КОНТИНУУМ ПРИ ЗВЕЗДЕН СПЕКТЪР. . . . . 100
5. **Филип Филипов**  
ФРАКТАЛЕН ПОДХОД КЪМ КОСМИЧЕСКИ СТРУКТУРИ,  
ОБЕКТИ И ДИНАМИЧНИ ЯВЛЕНИЯ. . . . . 117
6. **Велко Велков**  
ХИПОТЕЗА ЗА КОСМОЛОГИЧЕН МОДЕЛ НА ВСЕМИРА  
БЕЗ ГРАВИТАЦИЯ. . . . . 136
7. **Венета Гинева, Ирина Деспирак, Борис Козелов**  
ИЗМЕНЕНИЯ ПРИ СУББУРИ, СВЪРЗАНИ С РАЗЛИЧНИ УСЛОВИЯ  
В СЛЪНЧЕВИЯ ВЯТЪР. . . . . 145

8. <b>Васил Василев, Евгения Руменина</b> МОНИТОРИНГ НА ЗЕМЕДЕЛСКИТЕ КУЛТУРИ ЧРЕЗ ВРЕМЕВИ СЕРИИ ОТ SPOT-VGT NDVIs S10 ПРОДУКТ ЗА СЕВЕРОИЗТОЧНА БЪЛГАРИЯ. ....	155
9. <b>Васил Василев</b> ОЦЕНКА НА ЗЕМЕДЕЛСКИТЕ ПЛОЩИ ЧРЕЗ ПИКСЕЛНО- ОРИЕНТИРАНА КОНТРОЛИРАНА КЛАСИФИКАЦИЯ ВЪРХУ ИЗОБРАЖЕНИЕ НА EO-1 ALI ЗА ТЕСТОВИ УЧАСТЪК ЖИТЕН, РАЗПОЛОЖЕН В СЕВЕРОИЗТОЧНА БЪЛГАРИЯ. ....	179
10. <b>Лъчезар Филчев</b> РАЗВИТИЕ НА СПЪТНИКОВИТЕ СПЕКТРОМЕТРИЧНИ ДИСТАНЦИОННИ ИЗСЛЕДВАНИЯ – ОБЗОР. ....	191
11. <b>Светослав Забунов, Петър Гецов, Гаро Мардиросян</b> ЕКСПЕРИМЕНТАЛНИ МОДЕЛИ МУЛТИРОТОРНИ БЕЗПИЛОТНИ ХЕЛИКОПТЕРИ ОТ СЕРИЯТА XZ. ....	207
12. <b>Иван Николов, Стефка Касърова, Нина Султанова</b> НЯКОИ АЕРОКОСМИЧЕСКИ ПРИЛОЖЕНИЯ НА ОПТИЧНИТЕ ПОЛИМЕРИ. ....	220
13. <b>Васил Кавърджиков, Десислава Паикулева, Иван Николов</b> МИКРО- И НАНО-ФОКУСИРАЩА ОПТИКА, ПРЕДНАЗНАЧЕНА ЗА ДИСТАНЦИОННИ ИЗОБРАЗЯВАЩИ СИСТЕМИ. ....	243
14. <b>Константин Методиев</b> ИЗМЕРВАНЕ НА КОЕФИЦИЕНТА НА НАСИТЕНА ХИДРАВЛИЧНА ПРОВОДИМОСТ ЗА СУБСТРАТИ БАЛКАНИН И ТУРФЕЙС ПО МЕТОДА НА ПОСТОЯННИЯ ВОДЕН НАПОР. ....	257
15. <b>Петър Велинов</b> НОВ АНАЛИТИЧЕН ПОДХОД ЗА МОДЕЛИРАНЕ НА ЙОНИЗАЦИЯТА НА КОСМИЧЕСКИТЕ ЛЪЧИ В ОКОЛОПЛАНЕТНИТЕ ПРОСТРАНСТВА ПОСРЕСТВОМ ИЗПОЛЗВАНЕТО НА ПОРАЖДАЩИ ЙОНИЗАЦИЯТА ФУНКЦИИ. ....	266
 <b>Нови книги</b>	
<b>Гаро Мардиросян</b> ИНТЕРЕСНА И АКТУАЛНА КНИГА. ....	291

## ANALYTICAL COMPUTATION OF TWO INTEGRALS, APPEARING IN THE THEORY OF ELLIPTICAL ACCRETION DISCS. III. SOLVING OF THE FULL SET OF AUXILIARY INTEGRALS, CONTAINING LOGARITHMIC FUNCTIONS INTO THEIR INTEGRANDS

*Dimitar Dimitrov*

*Space Research and Technology Institute - Bulgarian Academy of Sciences  
 e-mail: dim@mail.space.bas.bg*

### **Abstract**

*The present investigation encloses the started in the earlier papers [3] and [4] analytical evaluations of some kinds definite integrals. These solutions are necessary steps towards the revealing the mathematical structure of the dynamical equation, governing the properties of the stationary elliptical accretion discs, which apse lines of all orbits are in line with each other[5]. Though the considered here task, at first glance, may seem as a purely mathematical one, there are some restrictions of physical nature on the variables, entering as arguments into the integrals. In this paper we resolve analytically the following two definite integrals, including into their nominators (as a factor) the logarithmic function  $\ln(1 + e\cos\varphi)$ . Concretely, we find in an explicit form the solutions of the integrals  $L_i(\mathbf{e}, \dot{\mathbf{e}}) \equiv$*

$$\equiv \int_0^{2\pi} [\ln(1 + e\cos\varphi)] (1 + e\cos\varphi)^{-1} [1 + (e - \dot{e})\cos\varphi]^{-i} d\varphi, \quad (i = 0, \dots, 3),$$

$$\text{and } K_j(\mathbf{e}, \dot{\mathbf{e}}) \equiv \int_0^{2\pi} [\ln(1 + e\cos\varphi)] [1 + (e - \dot{e})\cos\varphi]^{-j} d\varphi, \quad (j = 1, \dots, 5).$$

*Here we have used the following notations:  $\varphi$  is the azimuthal angle. The integration over  $\varphi$  from 0 to  $2\pi$  means an averaging over the whole trajectory for each disc particle. Each such particle spirals inward to the center of the disc, moving on (quasi-) elliptical orbits with focal parameters  $\mathbf{p}$ . These parameters  $\mathbf{p}$  are allowed to vary for different elliptical orbits. In the our approach of computations, we treat  $\mathbf{e}(\mathbf{u})$  and  $\dot{\mathbf{e}}(\mathbf{u})$  as independent variables. The physically imposed restrictions (which, to some extend, lead to simplifications of the problems) are  $|\mathbf{e}(\mathbf{u})| < 1, |\dot{\mathbf{e}}(\mathbf{u})| < 1$  and  $|\mathbf{e}(\mathbf{u}) - \dot{\mathbf{e}}(\mathbf{u})| < 1$  for all admitted values of  $\mathbf{u}$ . That is to say, between the innermost and outermost orbits of the disc. Consequently, the established in this paper analytical solutions for the integrals  $L_i(\mathbf{e}, \dot{\mathbf{e}})$ ,*

( $i = 0, \dots, 3$ ) and  $\mathbf{K}_j(\mathbf{e}, \dot{\mathbf{e}})$ , ( $j = 1, \dots, 5$ ), are, probably, not the most general ones, even in the domain of the real analysis. But nevertheless, they are sufficient for our aim to simplify the dynamical equation.

## 1. Introduction

Recent investigations ([1] – [4] and the references therein) have shown that it is possible to simplify to some extent the dynamical equation of the *stationary* elliptical accretion discs, having apse lines of the particle orbits in line with each other. This class of models, and, correspondingly, the accompanying their description dynamical equation, was developed by Lyubarskij et al. [5]. The simplifications, adopted for such models, allow to write the later equation as a second order ordinary differential equation. According to the theory of the ordinary differential equations, its solution exists and is unique. Of course, under given physically motivated suitable initial and boundary conditions. We underline that our up to now, and also forthcoming investigations are dealing only with the subclass of the *stationary* accretion flows. That is to say, for simplicity restrictions, we select only this part of the models, considered by Lyubarskij et al. [5], which does not concern the evolution of discs with the time. We shall not discuss here how the knowledge of the solutions for the *stationary* discs may hint the finding of the solutions of the dynamical equation in the *non-stationary* case. The property, that the *space* structure of the elliptical accretion disc (*having, as we just stressed above, characteristics which do not evolve with the time*) is described mathematically by an ordinary differential equation, stimulates our intention to try to solve it analytically. Or simplify it, by means of analytical transformations, to a form, which reveals in a more clear way its physical and mathematical interpretation. This situation is, evidently, much more easy for an analytical treatment, than the case when the particle orbits of the elliptical discs do not share a common longitude of periastron. Then the dynamical equation, governing the structure of the accretion flow, is, generally speaking, a *partial* differential equation [6]. It is known that the partial differential equations, in contrast to the ordinary such, do not possess guarantees that their solutions are unique, if the later exist at all!

During the process of finding of linear relations between the terms, entering into the dynamical equation of the disc, we strike with the necessity to compute the following two kinds of integrals:

$$(1) \quad \mathbf{L}_i(e, \dot{e}) \equiv \int_0^{2\pi} [\ln(1 + e \cos \varphi)] (1 + e \cos \varphi)^{-1} [1 + (e - \dot{e}) \cos \varphi]^{-i} d\varphi ; \quad \mathbf{i} = 0, \dots, 3 ,$$

$$(2) \quad \mathbf{K}_j(e, \dot{e}) \equiv \int_0^{2\pi} [\ln(1 + e \cos \varphi)] [1 + (e - \dot{e}) \cos \varphi]^{-j} d\varphi ; \quad \mathbf{j} = 1, \dots, 5 .$$

In an earlier paper [4], we have already evaluated analytically the “initial” integrals  $\mathbf{L}_0(e)$ ,  $\mathbf{K}_0(e)$  and  $\mathbf{K}_1(e, \dot{e})$ , considered as starting points into the recurrence relations, which enable us to solve the integrals with  $\mathbf{i} = 1, 2, 3$  and  $\mathbf{j} = 2, \dots, 5$ . We rewrite here these solutions:

$$(3) \quad \mathbf{L}_0(e) = -2\pi(1 - e^2)^{-1/2} \ln\{[1 + (1 - e^2)^{1/2}][2(1 - e^2)]^{-1}\}; \quad ([4], \text{equality (53)}),$$

$$(4) \quad \mathbf{K}_0(e) = 2\pi \ln\{[1 + (1 - e^2)^{1/2}]/2\}; \quad ([4], \text{equality (54)}),$$

$$(5) \quad \mathbf{K}_1(e, \dot{e}) = 2\pi[1 - (e - \dot{e})^2]^{-1/2} \ln\{2 - 3e^2 + e^4 + 3e\dot{e} - 2e^3\dot{e} - \dot{e}^2 + e^2\dot{e}^2 + (-2 + 2e^2 - 3e\dot{e} + \dot{e}^2)(1 - e^2)^{1/2} + (-2 + 2e^2 - e\dot{e})[1 - (e - \dot{e})^2]^{1/2} + (2 - e^2 + e\dot{e})(1 - e^2)^{1/2}[1 - (e - \dot{e})^2]^{1/2}\}(e - \dot{e})^{-2}[1 - (1 - e^2)^{1/2}]^{-1}\}; \quad ([4],$$

equality (116)).

For further use, it is helpful also to adduce the definitions of the following three integrals  $\mathbf{A}_i(e, \dot{e})$ , ( $\mathbf{i} = 1, \dots, 5$ ),  $\mathbf{J}_j(e, \dot{e})$ , ( $\mathbf{j} = 1, \dots, 4$ ) and  $\mathbf{H}_j(e, \dot{e})$ , ( $\mathbf{j} = 1, \dots, 4$ ):

$$(6) \quad \mathbf{A}_i(e, \dot{e}) \equiv \int_0^{2\pi} [1 + (e - \dot{e}) \cos \varphi]^{-i} d\varphi ; \quad (\mathbf{i} = 1, \dots, 5),$$

$$(7) \quad \mathbf{J}_j(e, \dot{e}) \equiv \int_0^{2\pi} (1 + e \cos \varphi)^{-1} [1 + (e - \dot{e}) \cos \varphi]^{-j} d\varphi ; \quad (\mathbf{j} = 1, \dots, 4),$$

$$(8) \quad \mathbf{H}_j(e, \dot{e}) \equiv \int_0^{2\pi} (1 + e \cos \varphi)^{-j} [1 + (e - \dot{e}) \cos \varphi]^{-1} d\varphi ; \quad (\mathbf{j} = 1, \dots, 4).$$

The analytical evaluations of the later three integrals (6) – (8) were derived and discussed in paper [3]. It is worth to note, that the integration over the azimuthal angle  $\varphi$  in the above written integrals (1) – (8) is a consequence of the angle averaging over the each particle orbit in the interval  $\varphi \in [0, 2\pi]$ . We have also to stress, that the applied in the next chapters approaches for analytical evaluations of the integrals  $\mathbf{L}_i(e, \dot{e})$  and  $\mathbf{K}_j(e, \dot{e})$  are useful for higher integer values of the powers of the denominator  $[1 + (e - \dot{e}) \cos \varphi]$ . That is to say, for  $\mathbf{i} > 3$ , or  $\mathbf{j} > 4$ . But we shall restrict us only to those generality levels, which are enough to solve the considered by us particular problem of analyzing the dynamical equation of the *stationary* elliptical accretion discs. We do not set ourselves as an object to solve the complete mathematical task for all  $\mathbf{i}$  and  $\mathbf{j}$ .



## 2. Analytical computation of the integral $\mathbf{K}_2(e, \dot{e}) \equiv \int_0^{2\pi} [\ln(1 + e \cos \varphi)][1 + (e - \dot{e}) \cos \varphi]^{-2} d\varphi$

It is appropriate to begin the evaluation of the integrals  $\mathbf{K}_j(e, \dot{e})$ , ( $j = 2, \dots, 5$ ) (using correlation relations), from the integral  $\mathbf{K}_2(e, \dot{e})$ , not from the integral  $\mathbf{K}_5(e, \dot{e})$ . Hence, according to the definitions (2):

$$\begin{aligned}
 (9) \quad \mathbf{K}_2(e, \dot{e}) &\equiv \int_0^{2\pi} [\ln(1 + e \cos \varphi)][1 + (e - \dot{e}) \cos \varphi]^{-2} d\varphi = \\
 &= -(e - \dot{e})^{-2} \int_0^{2\pi} [1 - (e - \dot{e})^2 \cos^2 \varphi][\ln(1 + e \cos \varphi)][1 + (e - \dot{e}) \cos \varphi]^{-2} d\varphi + \\
 &+ (e - \dot{e})^{-2} \int_0^{2\pi} [\ln(1 + e \cos \varphi)][1 + (e - \dot{e}) \cos \varphi]^{-2} d\varphi - \\
 &- (e - \dot{e})^{-1} \int_0^{2\pi} (\sin \varphi)[\ln(1 + e \cos \varphi)][1 + (e - \dot{e}) \cos \varphi]^{-2} d[1 + (e - \dot{e}) \cos \varphi] = \\
 &= -(e - \dot{e})^{-2} \mathbf{K}_1(e, \dot{e}) + (e - \dot{e})^{-2} \int_0^{2\pi} \ln(1 + e \cos \varphi) d\varphi - (e - \dot{e})^{-2} \mathbf{K}_1(e, \dot{e}) + (e - \dot{e})^{-2} \mathbf{K}_2(e, \dot{e}) - \\
 &- (e - \dot{e})^{-2} \int_0^{2\pi} \{[1 + (e - \dot{e}) \cos \varphi] - 1\} [1 + (e - \dot{e}) \cos \varphi]^{-1} [\ln(1 + e \cos \varphi)] d\varphi + \\
 &+ [e/(e - \dot{e})] \int_0^{2\pi} (1 - \cos^2 \varphi)(1 + e \cos \varphi)^{-1} [1 + (e - \dot{e}) \cos \varphi]^{-1} d\varphi = \\
 &= (e - \dot{e})^{-2} [\mathbf{K}_2(e, \dot{e}) - \mathbf{K}_1(e, \dot{e})] + \{(e^2 - 1)/[e(e - \dot{e})]\} \mathbf{J}_1(e, \dot{e}) + [e/(e - \dot{e})] \mathbf{A}_1(e, \dot{e}) - \\
 &- (e - \dot{e})^{-2} \int_0^{2\pi} \{[1 + (e - \dot{e}) \cos \varphi] - 1\} [1 + (e - \dot{e}) \cos \varphi]^{-1} d\varphi = (e - \dot{e})^{-2} [\mathbf{K}_2(e, \dot{e}) - \mathbf{K}_1(e, \dot{e})] + \\
 &+ \{(e^2 - 1)/[e(e - \dot{e})]\} \mathbf{J}_1(e, \dot{e}) + [e(e - \dot{e})]^{-1} \mathbf{A}_1(e, \dot{e}) - 2\pi(e - \dot{e})^{-2} + (e - \dot{e})^{-2} \mathbf{A}_1(e, \dot{e}).
 \end{aligned}$$

This relation gives the final expression for the integral  $\mathbf{K}_2(e, \dot{e})$ . Using the already computed expressions for  $\mathbf{K}_1(e, \dot{e})$  (see equality (5)),  $\mathbf{J}_1(e, \dot{e})$  (see equality (27) from paper [3]) and  $\mathbf{A}_1(e, \dot{e})$  (see equality (7) from paper [3]), we are in a position to write the explicit **analytical** solution for  $\mathbf{K}_2(e, \dot{e})$ . Finally, we obtain that:

$$\begin{aligned}
 (10) \quad \mathbf{K}_2(e, \dot{e}) &= 2\pi[1 - (e - \dot{e})^2]^{-3/2} \ln\{[2 - 3e^2 + e^4 + 3e\dot{e} - 2e^3\dot{e} - \dot{e}^2 + e^2\dot{e}^2 + \\
 &+ (-2 + 2e^2 - 3e\dot{e} + \dot{e}^2)(1 - e^2)^{1/2} + (-2 + 2e^2 - e\dot{e})[1 - (e - \dot{e})^2]^{1/2} + \\
 &+ (2 - e^2 + e\dot{e})(1 - e^2)^{1/2}[1 - (e - \dot{e})^2]^{1/2}\}(e - \dot{e})^{-2}[1 - (1 - e^2)^{1/2}]^{-1} - 2\pi e\dot{e}^{-1}[1 - (e - \dot{e})^2]^{-1/2} + \\
 &+ 2\pi(e - e^3 - \dot{e} + e^2\dot{e})\dot{e}^{-1}(1 - e^2)^{-1/2}[1 - (e - \dot{e})^2]^{-1} + 2\pi[1 - (e - \dot{e})^2]^{-1}.
 \end{aligned}$$

We shall not perform here the tedious algebraic computations, proving in a rigorous mathematical manner, that the written above analytical solution (10) for the integral  $\mathbf{K}_2(e, \dot{e})$  remains valid even in the cases, when

$e(u)$ , and/or  $e(u) - \dot{e}(u)$  are equal to zero. These particular values are preliminary excluded in the derivation of the equality (10). Because they enter as factors into the denominators of some of the intermediate terms. Correspondingly, this situation leads to the necessity to examine the indicated cases in a separate way. The resolving of the designated problem may follow the analogous procedure, which is called to overcome such difficulties, appearing under the analytical solving of the integrals  $\mathbf{K}_1(e, \dot{e})$ ,  $\mathbf{L}_i(e, \dot{e})$ , ( $i = 0, \dots, 3$ ),  $\mathbf{A}_i(e, \dot{e})$ , ( $i = 1, \dots, 5$ ),  $\mathbf{J}_j(e, \dot{e})$ , ( $j = 1, \dots, 4$ ),  $\mathbf{H}_j(e, \dot{e})$ , ( $j = 1, \dots, 4$ ) (see papers [3] and [4]). Especially, the used approach is based on the application of the L'Hospital's rule for resolving of indeterminacies of the type  $0/0$ . We shall return later in this paper to the arising problem.

**3. Analytical computation of the integral  $\mathbf{K}_3(e, \dot{e}) \equiv \int_0^{2\pi} [\ln(1 + e \cos \varphi)] [1 + (e - \dot{e}) \cos \varphi]^{-3} d\varphi$**

Let us compute the integral  $\mathbf{K}_3(e, \dot{e})$ . According to the definition (2):

$$\begin{aligned}
(11) \quad \mathbf{K}_3(e, \dot{e}) &= - (e - \dot{e})^{-2} \int_0^{2\pi} [1 - (e - \dot{e})^2 \cos^2 \varphi] [\ln(1 + e \cos \varphi)] [1 + (e - \dot{e}) \cos \varphi]^{-3} d\varphi + \\
&+ (e - \dot{e})^{-2} \int_0^{2\pi} [\ln(1 + e \cos \varphi)] [1 + (e - \dot{e}) \cos \varphi]^{-3} d\varphi - \\
&- (e - \dot{e})^{-1} \int_0^{2\pi} (\sin \varphi) [\ln(1 + e \cos \varphi)] [1 + (e - \dot{e}) \cos \varphi]^{-3} d[1 + (e - \dot{e}) \cos \varphi] = \\
&= - (e - \dot{e})^{-2} \mathbf{K}_2(e, \dot{e}) + (e - \dot{e})^{-2} \int_0^{2\pi} \{ [1 + (e - \dot{e}) \cos \varphi] - 1 \} [\ln(1 + e \cos \varphi)] [1 + (e - \dot{e}) \cos \varphi]^{-2} d\varphi + \\
&+ (e - \dot{e})^{-2} \mathbf{K}_3(e, \dot{e}) + [2(e - \dot{e})]^{-1} \{ (\sin \varphi) [\ln(1 + e \cos \varphi)] [1 + (e - \dot{e}) \cos \varphi]^{-2} \Big|_0^{2\pi} - \\
&- \int_0^{2\pi} (\cos \varphi) [\ln(1 + e \cos \varphi)] [1 + (e - \dot{e}) \cos \varphi]^{-2} d\varphi + e \int_0^{2\pi} (\sin^2 \varphi) (1 + e \cos \varphi)^{-1} [1 + (e - \dot{e}) \cos \varphi]^{-2} d\varphi \} = \\
&= - (e - \dot{e})^{-2} \mathbf{K}_2(e, \dot{e}) + (e - \dot{e})^{-2} \mathbf{K}_1(e, \dot{e}) - (e - \dot{e})^{-2} \mathbf{K}_2(e, \dot{e}) + (e - \dot{e})^{-2} \mathbf{K}_3(e, \dot{e}) - [2(e - \dot{e})^2]^{-1} \mathbf{K}_1(e, \dot{e}) + \\
&+ [2(e - \dot{e})^2]^{-1} \mathbf{K}_2(e, \dot{e}) + e [2(e - \dot{e})]^{-1} \int_0^{2\pi} (1 + e \cos \varphi)^{-1} [1 + (e - \dot{e}) \cos \varphi]^{-2} d\varphi + \\
&+ [2e(e - \dot{e})]^{-1} \int_0^{2\pi} [(1 - e^2 \cos^2 \varphi) - 1] (1 + e \cos \varphi)^{-1} [1 + (e - \dot{e}) \cos \varphi]^{-2} d\varphi = \\
&= (e - \dot{e})^{-2} [\mathbf{K}_3(e, \dot{e}) - (3/2) \mathbf{K}_2(e, \dot{e}) + (1/2) \mathbf{K}_1(e, \dot{e}) - (1 - e^2) [2e(e - \dot{e})]^{-1} \int_0^{2\pi} [1 + (e - \dot{e}) \cos \varphi]^{-2} d\varphi - \\
&- [e/(e - \dot{e})] \int_0^{2\pi} \{ [1 + (e - \dot{e}) \cos \varphi] - 1 \} (1 + e \cos \varphi)^{-1} [1 + (e - \dot{e}) \cos \varphi]^{-2} d\varphi \} +
\end{aligned}$$

$$\begin{aligned}
& + [2e(e-\dot{e})]^{-1} \int_0^{2\pi} [1 + (e-\dot{e})\cos\varphi]^{-2} d\varphi - [2(e-\dot{e}^2)]^{-1} \int_0^{2\pi} \{[1 + (e-\dot{e})\cos\varphi] - 1\} [1 + (e-\dot{e})\cos\varphi]^{-2} d\varphi = \\
& = (e-\dot{e})^{-2} \{ \mathbf{K}_3(e,\dot{e}) - (3/2)\mathbf{K}_2(e,\dot{e}) + (1/2)\mathbf{K}_1(e,\dot{e}) + [(1+e^2-e\dot{e})/2]\mathbf{A}_2(e,\dot{e}) + \\
& + [(1-e^2)/2][\mathbf{J}_1(e,\dot{e}) - \mathbf{J}_2(e,\dot{e})] - (1/2)\mathbf{A}_1(e,\dot{e}) \}.
\end{aligned}$$

Transferring the *unknown* function  $\mathbf{K}_3(e,\dot{e})$  from the right-hand-side to the left one into the above relation, we can write  $\mathbf{K}_3(e,\dot{e})$  through the *already known* functions:

$$(12) \quad \mathbf{K}_3(e,\dot{e}) = \{2[1 - (e-\dot{e}^2)]\}^{-1} \{3\mathbf{K}_2(e,\dot{e}) - \mathbf{K}_1(e,\dot{e}) - (1+e^2-e\dot{e})\mathbf{A}_2(e,\dot{e}) + \mathbf{A}_1(e,\dot{e}) + (1-e^2)[\mathbf{J}_2(e,\dot{e}) - \mathbf{J}_1(e,\dot{e})]\}.$$

In the above formula, functions  $\mathbf{K}_1(e,\dot{e})$  and  $\mathbf{K}_2(e,\dot{e})$  are given by the analytical solutions (5) and (10), respectively. The other integrals in the right-hand-side of (12) are evaluated in the earlier paper [3], as follows:  $\mathbf{A}_1(e,\dot{e})$  – formula (7),  $\mathbf{A}_2(e,\dot{e})$  – formula (8),  $\mathbf{J}_1(e,\dot{e})$  – formula (27) and  $\mathbf{J}_2(e,\dot{e})$  – formula (34). The numerations of the later formulas correspond to [3]. The substitution of these expressions into (12) gives the explicit form of the solution (12) as a function of the eccentricity  $e(u)$  and its derivative  $\dot{e}(u)$ . After some simple algebraic transformations, we are in a position to write the final analytical solution for the integral  $\mathbf{K}_3(e,\dot{e})$ :

$$(13) \quad \mathbf{K}_3(e,\dot{e}) = \pi[1 - (e-\dot{e}^2)]^{-5/2} (2 + e^2 - 2e\dot{e} + \dot{e}^2) \ln \{ \{2 - 3e^2 + e^4 + 3e\dot{e} - 2e^3\dot{e} - \dot{e}^2 + e^2\dot{e}^2 + (-2 + 2e^2 - 3e\dot{e} + \dot{e}^2)(1-e^2)^{1/2} + (-2 + 2e^2 - e\dot{e})[1 - (e-\dot{e}^2)^2]^{1/2} + (2 - e^2 + e\dot{e})(1-e^2)^{1/2}[1 - (e-\dot{e}^2)^2]^{1/2}\} (e-\dot{e})^{-2} [1 - (1-e^2)^{1/2}]^{-1} \} + \pi(-e^2 + 2e^4 - e^6 - 2e\dot{e} - 2e^3\dot{e} + 4e^5\dot{e} - 2e^2\dot{e}^2 - 6e^4\dot{e}^3 + 2e\dot{e}^3 + 4e^3\dot{e}^3 - e^2\dot{e}^4)\dot{e}^{-2} [1 - (e-\dot{e}^2)^2]^{-5/2} + \pi(e^2 - 2e^4 + e^6 + 2e\dot{e} + e^3\dot{e} - 3e^5\dot{e} - 3\dot{e}^2 + 3e^4\dot{e}^2 + e\dot{e}^3 - e^3\dot{e}^3)\dot{e}^{-2} (1-e^2)^{-1/2} [1 - (e-\dot{e}^2)^2]^{-2} + 3\pi[1 - (e-\dot{e}^2)]^{-2}.$$

$$\begin{aligned}
\mathbf{4. Analytical expressions for the integrals} \quad \mathbf{K}_4(e,\dot{e}) &\equiv \int_0^{2\pi} [\ln(1 + e\cos\varphi)][1 + \\
& + (e-\dot{e})\cos\varphi]^{-4} d\varphi \quad \text{and} \quad \mathbf{K}_5(e,\dot{e}) &\equiv \int_0^{2\pi} [\ln(1 + e\cos\varphi)][1 + (e-\dot{e})\cos\varphi]^{-5} d\varphi
\end{aligned}$$

The computational procedure of the integrals  $\mathbf{K}_4(e,\dot{e})$  and  $\mathbf{K}_5(e,\dot{e})$  exactly resembles to that, which we described earlier in details, when we solved the integrals  $\mathbf{K}_2(e,\dot{e})$  and  $\mathbf{K}_3(e,\dot{e})$ . As it can be established from these calculations, the applied approach is to develop the integrands from the corresponding definitions (2) in such a way that into the right-hand-side to appear the same integral, multiplied by a factor different from unity. The later condition is crucial for the method of computation to work, because the integral, for which we are seeking, may be transferred into the left-hand-side of the equality. The result will be that in the left we shall have only the unknown integral, multiplied by a factor different from zero. Into the right-hand-side remain integrals of the same type (2), but with index  $\mathbf{j}$  less then

that of the integral under resolving. The formers are already solved. This is essentially a recurrent procedure. Of course, into the right-hand-side also present integrals of the types  $\mathbf{A}_i(e, \dot{e})$  (6) and  $\mathbf{J}_j(e, \dot{e})$  (7), but their analytical expressions are successfully computed in an earlier paper [3]. Therefore, it is only a matter of tedious algebra to resolve analytically the integrals  $\mathbf{K}_4(e, \dot{e})$  and  $\mathbf{K}_5(e, \dot{e})$ , starting directly from their definitions (2). For such reasons, we were motivated to skip here the detailed writing (as we have already done for  $\mathbf{K}_2(e, \dot{e})$  and  $\mathbf{K}_3(e, \dot{e})$ ) of the intermediate steps, leading to the solutions of  $\mathbf{K}_4(e, \dot{e})$  and  $\mathbf{K}_5(e, \dot{e})$ . We shall give only their expressions through the integrals  $\mathbf{K}_j(e, \dot{e})$ , ( $j = 1, 2, 3$ ),  $\mathbf{A}_i(e, \dot{e})$ , ( $i = 2, 3, 4$ ) and  $\mathbf{J}_j(e, \dot{e})$ , ( $j = 2, 3, 4$ ), and the corresponding final analytical formulas for them. We underline that the analytical solution for  $\mathbf{K}_j(e, \dot{e})$ , ( $j = 1, \dots, 5$ ),  $\mathbf{L}_i(e, \dot{e})$ , ( $i = 1, 2, 3$ ),  $\mathbf{A}_i(e, \dot{e})$ , ( $i = 1, \dots, 5$ ),  $\mathbf{J}_j(e, \dot{e})$ , ( $j = 1, \dots, 4$ ) and  $\mathbf{H}_j(e, \dot{e})$ , ( $j = 1, \dots, 4$ ) are also tested, by means of numerical methods, for a dense enough two-dimensional lattice with respect to  $(e, \dot{e})$ . In conclusion, we write down the following results:

$$(14) \quad \mathbf{K}_4(e, \dot{e}) = \{3[1 - (e - \dot{e})^2]\}^{-1} \{5\mathbf{K}_3(e, \dot{e}) - 2\mathbf{K}_2(e, \dot{e}) - (1 + e^2 - e\dot{e})\mathbf{A}_3(e, \dot{e}) + \mathbf{A}_2(e, \dot{e}) + (1 - e^2)[\mathbf{J}_3(e, \dot{e}) - \mathbf{J}_2(e, \dot{e})]\}.$$

It remains to substitute the corresponding analytical expressions for  $\mathbf{K}_3(e, \dot{e})$  (formula (13)),  $\mathbf{K}_2(e, \dot{e})$  (formula (10)),  $\mathbf{A}_2(e, \dot{e})$  (formula (8) from [3]),  $\mathbf{A}_3(e, \dot{e})$  (formula (16) from [3]),  $\mathbf{J}_2(e, \dot{e})$  (formula (34) from [3]) and  $\mathbf{J}_3(e, \dot{e})$  (formula (42) from [3]). The conclusive result from such complicated evaluation can be written as follows:

$$(15) \quad \mathbf{K}_4(e, \dot{e}) = \pi(2 + 3e^2 - 6e\dot{e} + 3\dot{e}^2)[1 - (e - \dot{e})^2]^{-7/2} \ln\{[2 - 3e^2 + e^4 + 3e\dot{e} - 2e^3\dot{e} - \dot{e}^2 + e^2\dot{e}^2 + (-2 + 2e^2 - 3e\dot{e} + \dot{e}^2)(1 - e^2)^{1/2} + (-2 + 2e^2 - e\dot{e})[1 - (e - \dot{e})^2]^{1/2} + (2 - e^2 + e\dot{e})(1 - e^2)^{1/2}[1 - (e - \dot{e})^2]^{1/2}(e - \dot{e})^{-2}[1 - (1 - e^2)^{1/2}]^{-1}\} + (\pi/3)(-2e^3 + 4e^5 - 2e^7 - 3e^2\dot{e} - 5e^4\dot{e} + 8e^6\dot{e} - 6e\dot{e}^2 - 5e^3\dot{e}^2 - 12e^5\dot{e}^2 - 2e^3 + 9e^2\dot{e}^3 + 8e^4\dot{e}^3 - 3e\dot{e}^4 - 2e^3\dot{e}^4)\dot{e}^{-3}[1 - (e - \dot{e})^2]^{-5/2} + (\pi/3)(2e^3 - 6e^5 + 6e^7 - 2e^9 + 3e^2\dot{e} + 4e^4\dot{e} - 17e^6\dot{e} + 10e^8\dot{e} + 6e\dot{e}^2 + e^3\dot{e}^2 + 13e^5\dot{e}^2 - 20e^7\dot{e}^2 - 11\dot{e}^3 - 12e^2\dot{e}^3 + 3e^4\dot{e}^3 + 20e^6\dot{e}^3 + 17e\dot{e}^4 - 7e^3\dot{e}^4 - 10e^5\dot{e}^4 - 4e^5 + 2e^2\dot{e}^5 + 2e^4\dot{e}^5)\dot{e}^{-3}(1 - e^2)^{-1/2}[1 - (e - \dot{e})^2]^{-3} + (2\pi/3)[1 - (e - \dot{e})^2]^{-5/2} + (\pi/3)(11 + 4e^2 - 8e\dot{e} + 4\dot{e}^2)[1 - (e - \dot{e})^2]^{-3}.$$

The explicit form of the integral  $\mathbf{K}_5(e, \dot{e})$ , as a function of the eccentricity  $e(u)$  and its derivative  $\dot{e}(u)$ , may be written in a similar way. At first, the direct processing of the definition (2) for the integral  $\mathbf{K}_5(e, \dot{e})$  leads to the intermediate evaluation for  $\mathbf{K}_5(e, \dot{e})$ , analogous to the relation (14) for  $\mathbf{K}_4(e, \dot{e})$ :

$$(16) \quad \mathbf{K}_5(e, \dot{e}) = \{4[1 - (e - \dot{e})^2]\}^{-1} \{7\mathbf{K}_4(e, \dot{e}) - 3\mathbf{K}_3(e, \dot{e}) + (e - \dot{e})(1 - e^2)e^{-1}\mathbf{J}_4(e, \dot{e}) + \mathbf{A}_3(e, \dot{e}) - (2e - \dot{e})e^{-1}\mathbf{A}_4(e, \dot{e})\}.$$

Like to the previous case above, the substitution into the relation (16) of the analytical solutions for  $\mathbf{K}_4(e, \dot{e})$  (formula (15)),  $\mathbf{K}_3(e, \dot{e})$  (formula (13)),  $\mathbf{A}_3(e, \dot{e})$  (formula (16) from [3]),  $\mathbf{A}_4(e, \dot{e})$  (formula (9) from [3]) and

$\mathbf{J}_4(e, \dot{e})$  (formula (47) from [3]), gives, after some tedious algebra, the final explicit analytical evaluation:

$$(17) \quad \mathbf{K}_5(e, \dot{e}) = (\pi/4)(8 + 24e^2 + 3e^4 - 48e\dot{e} - 12e^3\dot{e} + 24\dot{e}^2 + 18e^2\dot{e}^2 - 12e\dot{e}^3 + 3\dot{e}^4)[1 - (e - \dot{e})^2]^{-9/2} \times \\ \times \ln\{2 - 3e^2 + e^4 + 3e\dot{e} - 2e^3\dot{e} - \dot{e}^2 + e^2\dot{e}^2 + (-2 + 2e^2 - 3e\dot{e} + \dot{e}^2)(1 - e^2)^{1/2} + \\ + (-2 + 2e^2 - e\dot{e})[1 - (e - \dot{e})^2]^{1/2} + (2 - e^2 + e\dot{e})(1 - e^2)^{1/2}[1 - (e - \dot{e})^2]^{1/2}\}(e - \dot{e})^{-2} \times \\ \times [1 - (1 - e^2)^{1/2}]^{-1} + (\pi/6)(-3e^4 + 9e^6 - 9e^8 + 3e^{10} - 4e^3\dot{e} - 10e^5\dot{e} + 32e^7\dot{e} - 18e^9\dot{e} - 6e^2\dot{e}^2 - 4e^4\dot{e}^2 - \\ - 35e^6\dot{e}^2 + 45e^8\dot{e}^2 - 12e\dot{e}^3 - 16e^3\dot{e}^3 - 60e^7\dot{e}^3 + 39e^2\dot{e}^4 + 25e^4\dot{e}^4 + 45e^6\dot{e}^4 - 18e\dot{e}^5 - 16e^3\dot{e}^5 - 18e^5\dot{e}^5 + \\ + 3e^2\dot{e}^6 + 3e^4\dot{e}^6)\dot{e}^{-4}[1 - (e - \dot{e})^2]^{-7/2} + (\pi/12)(6e^4 - 24e^6 + 36e^8 - 24e^{10} + 6e^{12} + 8e^3\dot{e} + 18e^5\dot{e} - \\ - 102e^7\dot{e} + 118e^9\dot{e} - 42e^{11}\dot{e} + 12e^2\dot{e}^2 + e^4\dot{e}^2 + 88e^6\dot{e}^2 - 227e^8\dot{e}^2 + 126e^{10}\dot{e}^2 + 24e\dot{e}^3 + 16e^3\dot{e}^3 - \\ - 35e^5\dot{e}^3 + 205e^7\dot{e}^3 - 210e^9\dot{e}^3 - 50e^4\dot{e}^4 - 138e^2\dot{e}^4 + 48e^4\dot{e}^4 - 70e^6\dot{e}^4 + 210e^8\dot{e}^4 + 182e\dot{e}^5 - 40e^3\dot{e}^5 - \\ - 16e^5\dot{e}^5 - 126e^7\dot{e}^5 - 55e^6\dot{e}^5 - 4e^2\dot{e}^6 + 17e^4\dot{e}^6 + 42e^6\dot{e}^6 + 9e\dot{e}^7 - 3e^3\dot{e}^7 - 6e^5\dot{e}^7)\dot{e}^{-4} \times \\ \times (1 - e^2)^{-1/2}[1 - (e - \dot{e})^2]^{-4} + (5\pi/12)(10 + 11e^2 - 22e\dot{e} + 11\dot{e}^2)[1 - (e - \dot{e})^2]^{-4}.$$

$$\mathbf{5. Expressions for the integrals} \quad \mathbf{K}_i(e, \dot{e}) \equiv \int_0^{2\pi} [\ln(1 + e\cos\varphi)][1 + (e - \dot{e})\cos\varphi]^{-i} d\varphi,$$

( $\mathbf{i} = 1, \dots, 5$ ) for some specific values of their arguments  $e(u)$  and  $\dot{e}(u)$

Let us, at first, introduce a useful notation, with a view to shorten (*in some cases*) the writing of the analytical formulas. More specially, we intent to denote with the function  $\mathbf{Z}(e, \dot{e})$  the argument of the logarithmic function, which enters both into the intermediate calculations and the final solutions for the integrals  $\mathbf{K}_i(e, \dot{e})$ , ( $\mathbf{i} = 1, \dots, 5$ ). This argument is *the same for all*  $\mathbf{i} = 1, \dots, 5$ , which makes it reasonable to introduce into use one more notation into the system of notations, used in the present paper. We stress, however, that we shall skip such a shortening of the notations (as we already have done until now), if we want to write, as possible, but more tedious, in the “*most explicit*” form the dependence of the expressions on  $e(u)$  and  $\dot{e}(u)$ .

Therefore, we define that:

$$(18) \quad \mathbf{Z}(e, \dot{e}) \equiv \{2 - 3e^2 + e^4 + 3e\dot{e} - 2e^3\dot{e} - \dot{e}^2 + e^2\dot{e}^2 + (-2 + 2e^2 - 3e\dot{e} + \dot{e}^2)(1 - e^2)^{1/2} + \\ + (-2 + 2e^2 - e\dot{e})[1 - (e - \dot{e})^2]^{1/2} + \\ + (2 - e^2 + e\dot{e})(1 - e^2)^{1/2}[1 - (e - \dot{e})^2]^{1/2}\}(e - \dot{e})^{-2}[1 - (1 - e^2)^{1/2}]^{-1}.$$

We shall write the above function for two different pairs of its arguments, namely:  $\{e, \dot{e} = 0\}$  and  $\{e - \dot{e}, -\dot{e}\}$ . These combinations will arise during the further use of the notation formula (18):

$$(19) \quad \mathbf{Z}(e, \dot{e} = 0) = 2[2 - 3e^2 + e^4 - 2(1 - e^2)^{3/2}]e^{-2}[1 - (1 - e^2)^{1/2}]^{-1},$$

$$(20) \quad \mathbf{Z}(e - \dot{e}, -\dot{e}) = \{2 - 3e^2 + e^4 + 3e\dot{e} - 2e^3\dot{e} - \dot{e}^2 + e^2\dot{e}^2 + (-2 + 2e^2 - 3e\dot{e} + \dot{e}^2)(1 - e^2)^{1/2} + \\ + (-2 + 2e^2 - e\dot{e})[1 - (e - \dot{e})^2]^{1/2} + (2 - e^2 + e\dot{e})(1 - e^2)^{1/2}[1 - (e - \dot{e})^2]^{1/2}\}e^{-2}\{1 - [1 - (e - \\ - \dot{e})^2]^{1/2}\}^{-1}.$$

Until now, we have computed analytically  $\mathbf{K}_i(e, \dot{e})$ , ( $\mathbf{i} = 1, \dots, 5$ ) under the condition  $\dot{e}(u) \neq 0$ . For  $\mathbf{i} = 2, 3, 4$  and 5 the derivative  $\dot{e}(u)$  of the eccentricity  $e(u)$  presents as a factor in the denominators of some of the summands in these expressions. Therefore, it is not reasonable to calculate

$\mathbf{K}_i(e,0)$ , ( $i = 2, \dots, 5$ ) simply setting  $\dot{e}(u) = 0$  into the already calculated results for this functions, valid for  $\dot{e}(u) \neq 0$ . Of course, we may attempt to use the L'Hospital's rule for evaluating of indeterminacies of the type  $0/0$ , but this approach (if it works) will probably be too tedious for our exposition. We shall use the same computational scheme for evaluating of the integrals  $\mathbf{K}_i(e,0)$ , ( $i = 2, \dots, 5$ ), as in the previous cases, when  $\dot{e}(u) \neq 0$ . But the recurrence formulas will now be established for the specific case  $\dot{e}(u) = 0$ . Before to begin with this procedure, we note that the just discussed problem, concerning the nullification of  $\dot{e}(u)$ , does not play a role in deriving of  $\mathbf{K}_1(e,0)$  from the expression (5) for  $\mathbf{K}_1(e,\dot{e})$ . We are able, without any contradictions, to set  $\dot{e}(u) = 0$ , to obtain that:

$$(21) \quad \mathbf{K}_1(e,0) = 2\pi(1-e^2)^{-1/2} \ln\{[2-3e^2+e^4-2(1-e^2)^{3/2}-2(1-e^2)^{3/2} + (2-e^2)(1-e^2)]e^{-2}[1-(1-e^2)^{1/2}]^{-1}\} = 2\pi(1-e^2)^{-1/2} \ln\{2[2-3e^2+e^4-2(1-e^2)^{3/2}] \times e^{-2}[1-(1-e^2)^{1/2}]^{-1}\} = 2\pi(1-e^2)^{-1/2} \ln \mathbf{Z}(e,0).$$

It is easily seen that  $\lim \mathbf{K}_1(e,0) \rightarrow 0$ , when  $e(u)$  approaches zero.

Now, we start to the *direct* evaluation of the integral  $\mathbf{K}_2(e,0)$ :

$$(22) \quad \begin{aligned} \mathbf{K}_2(e,0) &= \int_0^{2\pi} (\cos^2\varphi + \sin^2\varphi) [\ln(1 + e\cos\varphi)] (1 + e\cos\varphi)^{-2} d\varphi = \\ &= -e^{-2} \int_0^{\frac{2\pi}{e}} (1 - e^2 \cos^2\varphi) [\ln(1 + e\cos\varphi)] (1 + e\cos\varphi)^{-2} d\varphi + e^{-2} \int_0^{\frac{2\pi}{e}} [\ln(1 + e\cos\varphi)] (1 + e\cos\varphi)^{-2} d\varphi - \\ &= -e^{-1} \int_0^{\frac{2\pi}{e}} (\sin\varphi) [\ln(1 + e\cos\varphi)] (1 + e\cos\varphi)^{-2} d(1 + e\cos\varphi) = \\ &= -e^{-2} \mathbf{K}_1(e,0) + e^{-2} \mathbf{K}_0(e) - e^{-2} \mathbf{K}_1(e,0) + e^{-2} \mathbf{K}_2(e,0) - \\ &= -e^{-2} \int_0^{\frac{2\pi}{e}} [(1 + e\cos\varphi) - 1] [\ln(1 + e\cos\varphi)] (1 + e\cos\varphi)^{-1} d\varphi + \int_0^{\frac{2\pi}{e}} (1 - \cos^2\varphi) (1 + e\cos\varphi)^{-2} d\varphi = \\ &= e^{-2} \mathbf{K}_2(e,0) - 2e^{-2} \mathbf{K}_1(e,0) + e^{-2} \mathbf{K}_0(e) - e^{-2} \mathbf{K}_0(e) + e^{-2} \mathbf{K}_1(e,0) + \mathbf{J}_1(e,0) + \\ &+ e^{-2} \int_0^{\frac{2\pi}{e}} [(1 - e^2 \cos^2\varphi) - 1] (1 + e\cos\varphi)^{-2} d\varphi = \\ &= -e^{-2} \mathbf{J}_1(e,0) + e^{-2} \mathbf{K}_2(e,0) - e^{-2} \mathbf{K}_1(e,0) + \mathbf{J}_1(e,0) + e^{-2} \mathbf{A}_1(e,0) - 2\pi/e^2 + e^{-2} \mathbf{A}_1(e,0) = \\ &= e^{-2} \mathbf{K}_2(e,0) - e^{-2} \mathbf{K}_1(e,0) + 2e^{-2} \mathbf{A}_1(e,0) + (e^2 - 1)e^{-2} \mathbf{J}_1(e,0) - 2\pi/e^2. \end{aligned}$$

This relation gives a possibility to find an analytical solution for the unknown function  $\mathbf{K}_2(e,0)$ , because the other functions of the eccentricity  $e(u)$  are already known:  $\mathbf{K}_1(e,0)$  from formula (21),  $\mathbf{A}_1(e,0)$  (formula (20) from paper [3]), and  $\mathbf{J}_1(e,0)$  (formula (35) from paper [3]). Taking into account these relations, we obtain:

$$(23) \quad \begin{aligned} \mathbf{K}_2(e,0) &= (1 - e^2)^{-1} [\mathbf{K}_1(e,0) - 2\pi(1 - e^2)^{-1/2} + 2\pi] = \\ &= (1 - e^2)^{-1} [2\pi(1 - e^2)^{-1/2} \ln \mathbf{Z}(e,0) - 2\pi(1 - e^2)^{-1/2} + 2\pi] = \\ &= 2\pi(1 - e^2)^{-3/2} \{ \ln\{2[2 - 3e^2 + e^4 - 2(1 - e^2)^{3/2}]\} e^{-2} [1 - (1 - e^2)^{1/2}]^{-1} - 1 + (1 - e^2)^{1/2} \}. \end{aligned}$$

We underline that this result does not require the condition  $\dot{e}(u) \neq 0$ . Just the opposite is true! At the very beginning of the computations, we set  $\dot{e}(u) = 0$ . We shall not write here the proof that the relation (10) for  $\mathbf{K}_2(e, \dot{e})$  (derived under the suppositions  $e(u) \neq 0$ ,  $\dot{e}(u) \neq 0$  and  $e(u) - \dot{e}(u) \neq 0$ ) in the limit  $\dot{e}(u) \rightarrow 0$  coincides with the above relation (23) for  $\mathbf{K}_2(e, 0)$ . This statement can easily be checked by the means of the L'Hospital's rule. Finally, we note that the transition  $e(u) \rightarrow 0$  in the formula (23) leads to a vanishing result:  $\mathbf{K}_2(0, 0) = 0$ , which corresponds to the expected value from the definition (9). Despite of the our skipping of the detailed considerations of the behavior of the established relations, under the transitions  $e(u) \rightarrow 0$ ,  $\dot{e}(u) \rightarrow 0$  and  $[e(u) - \dot{e}(u)] \rightarrow 0$ , we nevertheless stress that such considerations are important. They give a certainty that the transitions through these singular points are continuous. Such a detailed treatment was done for the integrals  $\mathbf{A}_i(e, \dot{e})$ , ( $i = 1, \dots, 5$ ),  $\mathbf{J}_j(e, \dot{e})$ , ( $j = 1, \dots, 4$ ) and  $\mathbf{H}_j(e, \dot{e})$ , ( $j = 1, \dots, 4$ ) in paper [3]. But with a view to give a shorter description of the procedures of solving of the integrals  $\mathbf{K}_i(e, \dot{e})$ , ( $i = 1, \dots, 5$ ), we do not write out such tedious computations, introducing the use of the L'Hospital's rule for resolving of indeterminacies of the type 0/0. Before to proceed further, we emphasize that the above-mentioned remarks, concerning the solution of the integral  $\mathbf{K}_2(e, \dot{e})$ , are also remaining valid for the solutions of the "higher order" integrals  $\mathbf{K}_i(e, \dot{e})$ , ( $i = 3, 4, 5$ ). We now begin with the description of their computation, and *we shall not return to the discussion of such similar matter later.*

$$\begin{aligned}
(24) \quad \mathbf{K}_3(e, 0) &= \int_0^{2\pi} (\cos^2 \varphi + \sin^2 \varphi) [\ln(1 + e \cos \varphi)] (1 + e \cos \varphi)^{-3} d\varphi = \\
&= -e^2 \int_0^{2\pi} (1 - e^2 \cos^2 \varphi) [\ln(1 + e \cos \varphi)] (1 + e \cos \varphi)^{-3} d\varphi + e^{-2} \int_0^{2\pi} [\ln(1 + e \cos \varphi)] (1 + e \cos \varphi)^{-3} d\varphi - \\
&- e^{-1} \int_0^{2\pi} (\sin \varphi) [\ln(1 + e \cos \varphi)] (1 + e \cos \varphi)^{-3} d(1 + e \cos \varphi) = \dots = \\
&= [2(1 - e^2)]^{-1} \{3\mathbf{K}_2(e, 0) - \mathbf{K}_1(e, 0) - (1 + e^2)\mathbf{A}_2(e, 0) + \mathbf{A}_1(e, 0) + (1 - e^2)[\mathbf{J}_2(e, 0) - \mathbf{J}_1(e, 0)]\} = \\
&= [2(1 - e^2)]^{-1} \{6\pi(1 - e^2)^{-3/2} [\ln \mathbf{Z}(e, 0) - 1 + (1 - e^2)^{1/2}] - 2\pi(1 - e^2)(1 - e^2)^{-3/2} \ln \mathbf{Z}(e, 0) - \\
&- 2\pi(1 + e^2)(1 - e^2)^{-3/2} + 2\pi(1 - e^2)(1 - e^2)^{-3/2} + (1 - e^2)[\pi(2 + e^2)(1 - e^2)^{-5/2} - \\
&- 2\pi(1 - e^2)(1 - e^2)^{-5/2}]\}.
\end{aligned}$$

In the above equality the symbol "... =" denotes some of the skipped intermediate calculations. There are used also the already available solutions (23) for  $\mathbf{K}_2(e, 0)$  and (21) for  $\mathbf{K}_1(e, 0)$ . From paper [3] we apply the following formulas: (20) for  $\mathbf{A}_1(e, 0)$ , (21) for  $\mathbf{A}_2(e, 0)$ , (28) for  $\mathbf{J}_1(e, 0)$  and (35) for  $\mathbf{J}_2(e, 0)$ , respectively. Further evaluations lead to the seeking for final analytical result for the integral  $\mathbf{K}_3(e, \dot{e} = 0)$ :

$$(25) \quad \mathbf{K}_3(e,0) = (\pi/2)(1-e^2)^{-5/2} \{ (4+2e^2) \ln \{ 2[2-3e^2+e^4-2(1-e^2)^{3/2}] e^{-2} [1-(1-e^2)^{1/2}]^{-1} \} - 6 - e^2 + 6(1-e^2)^{1/2} \}.$$

To evaluate analytically the remaining two integrals  $\mathbf{K}_4(e, \dot{e} = 0)$  and  $\mathbf{K}_5(e, \dot{e} = 0)$ , we proceed in a very similar way. Here we only sketch these calculations.

$$(26) \quad \begin{aligned} \mathbf{K}_4(e,0) &= [3(1-e^2)]^{-1} \{ 5\mathbf{K}_3(e,0) - 2\mathbf{K}_2(e,0) - (1+e^2)\mathbf{A}_3(e,0) + \mathbf{A}_2(e,0) + \\ &+ (1-e^2)[\mathbf{J}_3(e,0) - \mathbf{J}_2(e,0)] \} = \\ &= [3(1-e^2)]^{-1} \{ (\pi/2)(1-e^2)^{-5/2} [(20+10e^2) \ln \mathbf{Z}(e,0) - 30 - 5e^2 + 30(1-e^2)^{1/2}] - \\ &- 4\pi(1-e^2)(1-e^2)^{-5/2} \ln \mathbf{Z}(e,0) - 4\pi(1-e^2)(1-e^2)^{-5/2} [-1 + (1-e^2)^{1/2}] - \\ &- \pi(2+e^2)(1+e^2)(1-e^2)^{-5/2} + 2\pi(1-e^2)(1-e^2)^{-5/2} + \\ &+ (1-e^2)[\pi(2+3e^2)(1-e^2)^{-7/2} - \pi(2+e^2)(1-e^2)(1-e^2)^{-7/2}] \}. \end{aligned}$$

As before, we have applied the already computed results: formulas (25) and (23) for  $\mathbf{K}_3(e, \dot{e} = 0)$  and  $\mathbf{K}_2(e, \dot{e} = 0)$ , respectively. From paper [3] we have used the evaluations (21) for  $\mathbf{A}_2(e,0)$ , (22) for  $\mathbf{A}_3(e,0)$ , (35) for  $\mathbf{J}_2(e,0)$  and, finally, (44) for  $\mathbf{J}_3(e,0)$ . Consequently, the simplification of the solution (26) may be expressed as follows:

$$(27) \quad \begin{aligned} \mathbf{K}_4(e,0) &= (\pi/6)(1-e^2)^{-7/2} [(12+18e^2) \ln \mathbf{Z}(e,0) - 22 - 15e^2 + (22+8e^2)(1-e^2)^{1/2}] = \\ &= (\pi/6)(1-e^2)^{-7/2} \{ (12+18e^2) \ln \{ 2[2-3e^2+e^4-2(1-e^2)^{3/2}] e^{-2} [1-(1-e^2)^{1/2}]^{-1} \} - \\ &- 22 - 15e^2 + (22+8e^2)(1-e^2)^{1/2} \}. \end{aligned}$$

Correspondingly, the integral  $\mathbf{K}_5(e, \dot{e} = 0)$  can be computed by means of  $\mathbf{K}_4(e,0)$  (formula (27)),  $\mathbf{K}_3(e,0)$  (formula (25)),  $\mathbf{A}_3(e,0)$  (formula (22) from paper [3]),  $\mathbf{A}_4(e,0)$  (formula (23) from paper [3]) and  $\mathbf{J}_4(e,0)$  (formula (50) from paper [3]).

$$(28) \quad \begin{aligned} \mathbf{K}_5(e,0) &= [4(1-e^2)]^{-1} [7\mathbf{K}_4(e,0) - 3\mathbf{K}_3(e,0) + (1-e^2)\mathbf{J}_4(e,0) - 2\mathbf{A}_4(e,0) + \mathbf{A}_3(e,0)] = \\ &= (\pi/24)(1-e^2)^{-9/2} [(48+144e^2+18e^4) \ln \mathbf{Z}(e,0) - 100 - 150e^2 - 9e^4 - (1/2)(12e^2+3e^4) + \\ &+ (100+110e^2)(1-e^2)^{1/2}]. \end{aligned}$$

Therefore, the final analytical solution for the integral  $\mathbf{K}_5(e,0)$  is:

$$(29) \quad \begin{aligned} \mathbf{K}_5(e,0) &= (\pi/48)(1-e^2)^{-9/2} \{ (96+288e^2+36e^4) \ln \{ 2[2-3e^2+e^4- \\ &- 2(1-e^2)^{3/2}] e^{-2} [1-(1-e^2)^{1/2}]^{-1} \} - 200 - 312e^2 - 21e^4 + (200+220e^2)(1-e^2)^{1/2} \}, \end{aligned}$$

where we, of course, have used the short-notation definition (19) for the function  $\mathbf{Z}(e,0)$ . To conclude the matter, connected with the application of the analytical solutions of the integrals of the type  $\mathbf{K}_i(e, \dot{e})$ , ( $i = 1, \dots, 5$ ), we shall write down in an explicit form some of these expressions (namely, for  $i = 3, 4$  and  $5$ ), when the two-arguments pair  $\{e, \dot{e}\}$  is replaced by  $\{e - \dot{e}, -\dot{e}\}$ . We do not give here the detailed computations, but the only the final results, including also the definition (20) for the function  $\mathbf{Z}(e - \dot{e}, -\dot{e})$ :

$$(30) \quad \begin{aligned} \mathbf{K}_3(e - \dot{e}, -\dot{e}) &= \pi(2+e^2)(1-e^2)^{-5/2} \ln \{ \{ 2-3e^2+e^4+3e\dot{e}-2e^3\dot{e}-\dot{e}^2+e^2\dot{e}^2 + \\ &+ (-2+2e^2-3e\dot{e}+\dot{e}^2)(1-e^2)^{1/2} + (-2+2e^2-e\dot{e})[1-(e-\dot{e})^2]^{1/2} + \\ &+ (2-e^2+e\dot{e})(1-e^2)^{1/2} [1-(e-\dot{e})^2]^{1/2} \} e^{-2} \{ 1 - [1-(e-\dot{e})^2]^{1/2} \}^{-1} \} + \\ &+ \pi(-e^2+2e^4-e^6+4e\dot{e}-6e^3\dot{e}+2e^5\dot{e}-3\dot{e}^2+4e^2\dot{e}^2-e^4\dot{e}^2)\dot{e}^{-2}(1-e^2)^{-5/2} + \pi(e^2-2e^4+e^6-4e\dot{e} + \\ &+ 7e^3\dot{e}-3e^5\dot{e}-9e^2\dot{e}^2+3e^4\dot{e}^2+4e\dot{e}^3-e^3\dot{e}^3)\dot{e}^{-2}(1-e^2)^{-2} [1-(e-\dot{e})^2]^{-1/2} + 3\pi(1-e^2)^{-2}. \end{aligned}$$

$$(31) \quad \mathbf{K}_4(e - \dot{e}, -\dot{e}) = \pi(2+3e^2)(1-e^2)^{-7/2} \ln \{ \{ 2-3e^2+e^4+3e\dot{e}-2e^3\dot{e}-\dot{e}^2+e^2\dot{e}^2 +$$



$$\begin{aligned}
& + (-2 + 2e^2 - 3e\dot{e} + \dot{e}^2)(1 - e^2)^{1/2} + (-2 + 2e^2 - e\dot{e})[1 - (e - \dot{e})^2]^{1/2} + \\
& + (2 - e^2 + e\dot{e})(1 - e^2)^{1/2}[1 - (e - \dot{e})^2]^{1/2} e^{-2} \{1 - [1 - (e - \dot{e})^2]^{1/2}\}^{-1} + (\pi/3)(2e^3 - 4e^5 + 2e^7 - \\
& - 9e^2\dot{e} + 15e^4\dot{e} - 6e^6\dot{e} + 18e\dot{e}^2 - 15e^3\dot{e}^2 + 6e^5\dot{e}^2 - 13\dot{e}^3 + 4e^2\dot{e}^3 - 2e^4\dot{e}^3)\dot{e}^{-3}(1 - e^2)^{-5/2} + \\
& + (\pi/3)(-2e^3 + 6e^5 - 6e^7 + 2e^9 + 9e^2\dot{e} - 26e^4\dot{e} + 25e^6\dot{e} - 8e^8\dot{e} - 18e\dot{e}^2 + 43e^3\dot{e}^2 - \\
& - 37e^5\dot{e}^2 + 12e^7\dot{e}^2 - 45e^2\dot{e}^3 + 23e^4\dot{e}^3 - 8e^6\dot{e}^3 + 18e\dot{e}^4 - 5e^3\dot{e}^4 + 2e^5\dot{e}^4)\dot{e}^{-3}(1 - e^2)^{-3}[1 - (e - \dot{e})^2]^{-1/2} + \\
& + (\pi/3)(11 + 4e^2)(1 - e^2)^{-3} + (2\pi/3)(1 - e^2)^{-5/2}. \\
(32) \quad & \mathbf{K}_5(e - \dot{e}, -\dot{e}) = (\pi/4)(8 + 24e^2 + 3e^4)(1 - e^2)^{-9/2} \ln\{[2 - 3e^2 + e^4 + 3e\dot{e} - 2e^3\dot{e} - \dot{e}^2 + e^2\dot{e}^2 + \\
& + (-2 + 2e^2 - 3e\dot{e} + \dot{e}^2)(1 - e^2)^{1/2} + (-2 + 2e^2 - e\dot{e})[1 - (e - \dot{e})^2]^{1/2} + \\
& + (2 - e^2 + e\dot{e})(1 - e^2)^{1/2}[1 - (e - \dot{e})^2]^{1/2} e^{-2} \{1 - [1 - (e - \dot{e})^2]^{1/2}\}^{-1}\} + \\
& + (\pi/6)(-3e^4 + 9e^6 - 9e^8 + 3e^{10} + 16e^3\dot{e} - 44e^5\dot{e} + 40e^7\dot{e} - 12e^9\dot{e} - 36e^2\dot{e}^2 + 81e^4\dot{e}^2 - 63e^6\dot{e}^2 + \\
& + 18e^8\dot{e}^2 + 48e\dot{e}^3 - 48e^3\dot{e}^3 + 42e^5\dot{e}^3 - 12e^7\dot{e}^3 - 25e^4\dot{e}^4 + 2e^2\dot{e}^4 - 10e^4\dot{e}^4 + 3e^6\dot{e}^4)\dot{e}^{-4}(1 - e^2)^{-7/2} + \\
& + (\pi/12)(6e^4 - 24e^6 + 36e^8 - 24e^{10} + 6e^{12} - 32e^3\dot{e} + 126e^5\dot{e} - 186e^7\dot{e} + 122e^9\dot{e} - 30e^{11}\dot{e} + 72e^2\dot{e}^2 - \\
& - 269e^4\dot{e}^2 + 382e^6\dot{e}^2 - 245e^8\dot{e}^2 + 60e^{10}\dot{e}^2 - 96e\dot{e}^3 + 280e^3\dot{e}^3 - 367e^5\dot{e}^3 + 243e^7\dot{e}^3 - 60e^9\dot{e}^3 - 264e^2\dot{e}^4 + \\
& + 143e^4\dot{e}^4 - 119e^6\dot{e}^4 + 30e^8\dot{e}^4 + 96e\dot{e}^5 - 8e^3\dot{e}^5 + 23e^5\dot{e}^5 - 6e^7\dot{e}^5)\dot{e}^{-4}(1 - e^2)^{-4}[1 - (e - \dot{e})^2]^{-1/2} + \\
& + (5\pi/12)(10 + 11e^2)(1 - e^2)^{-4}.
\end{aligned}$$

## 6. Final analytical explicit evaluations for the integrals

$$\mathbf{L}_i(e, \dot{e}) \equiv \int_0^{2\pi} [\ln(1 + e\cos\varphi)](1 + e\cos\varphi)^{-1} [1 + (e - \dot{e})\cos\varphi]^{-i} d\varphi, \quad (i = 1, 2, 3)$$

We have already obtained in the previous paper [4] the final analytical expressions for the integrals  $\mathbf{L}_0(e)$ ,  $\mathbf{K}_0(e)$  and  $\mathbf{K}_1(e, \dot{e})$  (see formulas (3), (4) and (5), respectively, into the introduction of the present paper). We have also evaluated in an explicit form the integrals  $\mathbf{K}_i(e, \dot{e})$ , ( $i = 2, \dots, 5$ ), (see formulas (10), (13), (15) and (17), respectively). This circumstance enables us to apply the recurrence relations (formulas (13), (12) and (11) from paper [4]), which will be sufficient to write explicitly, as functions of  $e(u)$  and  $\dot{e}(u) \equiv de(u)/du$  the unknown functions  $\mathbf{L}_1(e, \dot{e})$ ,  $\mathbf{L}_2(e, \dot{e})$  and  $\mathbf{L}_3(e, \dot{e})$ . Strictly speaking, here we do not need to know the full analytical solutions of the integrals  $\mathbf{K}_4(e, \dot{e})$  and  $\mathbf{K}_5(e, \dot{e})$ , because we interrupt the recurrence chain at the integral  $\mathbf{L}_3(e, \dot{e})$ , i.e., we need not to calculate for our purposes the integrals  $\mathbf{L}_i(e, \dot{e})$  with  $i \geq 4$ .  $\mathbf{K}_4(e, \dot{e})$  and  $\mathbf{K}_5(e, \dot{e})$  are evaluated for other reasons. Therefore, we can write, according to ((13), paper [4]), that:

$$\begin{aligned}
(33) \quad & \mathbf{L}_1(e, \dot{e}) = (e/\dot{e})\mathbf{L}_0(e) - [(e - \dot{e})/\dot{e}]\mathbf{K}_1(e, \dot{e}) = \\
& = -2\pi e\dot{e}^{-1}(1 - e^2)^{-1/2} \ln\{[1 + (1 - e^2)^{1/2}][2(1 - e^2)]^{-1}\} - 2\pi(e - \dot{e})\dot{e}^{-1}[1 - (e - \dot{e})^2]^{-1/2} \times \\
& \times \ln\{[2 - 3e^2 + e^4 + 3e\dot{e} - 2e^3\dot{e} - \dot{e}^2 + e^2\dot{e}^2 + (-2 + 2e^2 - 3e\dot{e} + \dot{e}^2)(1 - e^2)^{1/2} + \\
& + (-2 + 2e^2 - e\dot{e})[1 - (e - \dot{e})^2]^{1/2} + \\
& + (2 - e^2 + e\dot{e})(1 - e^2)^{1/2}[1 - (e - \dot{e})^2]^{1/2}\}(e - \dot{e})^{-2}[1 - (1 - e^2)^{1/2}]^{-1}\}.
\end{aligned}$$

In a fully analogous way, we are able to evaluate the other integrals  $\mathbf{L}_2(e, \dot{e})$  and  $\mathbf{L}_3(e, \dot{e})$ , for which we are seeking for. After some simple but tedious algebra, without using the notation (18) for  $\mathbf{Z}(e, \dot{e})$ , we shall give the final analytical form for the solutions of  $\mathbf{L}_2(e, \dot{e})$  and  $\mathbf{L}_3(e, \dot{e})$ . Taking into

account the recurrence relation (12) from paper [4] and the solutions (10) for  $\mathbf{K}_2(e, \dot{e})$  and (32) for  $\mathbf{L}_1(e, \dot{e})$ , we have:

$$(34) \quad \mathbf{L}_2(e, \dot{e}) = (e/\dot{e})\mathbf{L}_1(e, \dot{e}) - [(e - \dot{e})/\dot{e}]\mathbf{K}_2(e, \dot{e}) = \\ = -2\pi e^2 \dot{e}^{-2} (1 - e^2)^{-1/2} \ln\{[1 + (1 - e^2)^{1/2}][2(1 - e^2)]^{-1}\} - 2\pi(e^2 - e^4 + 3e^3\dot{e} - \dot{e}^2 - 3e^2\dot{e}^2 + e\dot{e}^3)\dot{e}^{-2} \times \\ \times [1 - (e - \dot{e})^2]^{-3/2} \ln\{[2 - 3e^2 + e^4 + 3e\dot{e} - 2e^3\dot{e} - \dot{e}^2 + e^2\dot{e}^2 + (-2 + 2e^2 - 3e\dot{e} + \dot{e}^2)(1 - e^2)^{1/2} + \\ + (-2 + 2e^2 - e\dot{e})[1 - (e - \dot{e})^2]^{1/2} + (2 - e^2 + e\dot{e})(1 - e^2)^{1/2}[1 - (e - \dot{e})^2]^{1/2}\}(e - \dot{e})^{-2} \times \\ \times [1 - (1 - e^2)^{1/2}]^{-1}\} + 2\pi(e^2 - e\dot{e})\dot{e}^{-2}[1 - (e - \dot{e})^2]^{-1/2} - 2\pi(e^2 - e^4 - 2e\dot{e} + 2e^3\dot{e} + \dot{e}^2 - e^2\dot{e}^2)\dot{e}^{-2} \times \\ \times [1 - (e - \dot{e})^2]^{-1}(1 - e^2)^{-1/2} - 2\pi(e - \dot{e})\dot{e}^{-1}[1 - (e - \dot{e})^2]^{-1}.$$

Similarly, the recurrence formula (11) from paper [4], combined with the solutions (13) for  $\mathbf{K}_3(e, \dot{e})$  and (34) for  $\mathbf{L}_2(e, \dot{e})$ , leads to the following result:

$$(35) \quad \mathbf{L}_3(e, \dot{e}) = (e/\dot{e})\mathbf{L}_2(e, \dot{e}) - [(e - \dot{e})/\dot{e}]\mathbf{K}_3(e, \dot{e}) = \\ = -2\pi e^3 \dot{e}^{-3} (1 - e^2)^{-1/2} \ln\{[1 + (1 - e^2)^{1/2}][2(1 - e^2)]^{-1}\} - \pi(2e^3 - 4e^5 + 2e^7 + 10e^4\dot{e} - 10e^6\dot{e} - \\ - 5e^3\dot{e}^2 + 20e^5\dot{e}^2 - 2\dot{e}^3 - 5e^2\dot{e}^3 - 20e^4\dot{e}^3 + 5e\dot{e}^4 + 10e^3\dot{e}^4 - \dot{e}^5 - 2e^2\dot{e}^5)\dot{e}^{-3}[1 - (e - \dot{e})^2]^{-5/2} \times \\ \times \ln\{[2 - 3e^2 + e^4 + 3e\dot{e} - 2e^3\dot{e} - \dot{e}^2 + e^2\dot{e}^2 + (-2 + 2e^2 - 3e\dot{e} + \dot{e}^2)(1 - e^2)^{1/2} + (-2 + 2e^2 - e\dot{e}) \times \\ \times [1 - (e - \dot{e})^2]^{1/2} + (2 - e^2 + e\dot{e})(1 - e^2)^{1/2}[1 - (e - \dot{e})^2]^{1/2}\}(e - \dot{e})^{-2}[1 - (1 - e^2)^{1/2}]^{-1}\} - \\ - \pi(3e^3 - 6e^5 + 3e^7 - 3e^2\dot{e} + 15e^4\dot{e} - 12e^6\dot{e} - 3e\dot{e}^2 - 15e^3\dot{e}^2 + 18e^5\dot{e}^2 + 3\dot{e}^3 + 9e^2\dot{e}^3 - 12e^4\dot{e}^3 - 3e\dot{e}^4 + \\ + 3e^3\dot{e}^4)\dot{e}^{-3}[1 - (e - \dot{e})^2]^{-2}(1 - e^2)^{-1/2} - \pi(2e^2 - 2e^4 + e\dot{e} + 6e^3\dot{e} - 3\dot{e}^2 - 6e^2\dot{e}^2 + 2e\dot{e}^3)\dot{e}^{-2} \times \\ \times [1 - (e - \dot{e})^2]^{-2} + \pi(3e^3 - 3e^5 - e^2\dot{e} + 9e^4\dot{e} - 2e\dot{e}^2 - 9e^3\dot{e}^2 + 3e^2\dot{e}^3)\dot{e}^{-3}[1 - (e - \dot{e})^2]^{-3/2}.$$

Consequently, the above solution (35) encloses the considered by us system of analytical solutions for the auxiliary integrals  $\mathbf{L}_i(e, \dot{e})$ , ( $i = 0, \dots, 3$ ) (see definitions (1)) and  $\mathbf{K}_j(e, \dot{e})$ , ( $j = 1, \dots, 5$ ) (see definitions (2)). As a rule, these definite integrals turn out to be complicate expressions of the assumed by us independent variables  $e(u)$  and  $\dot{e}(u) \equiv de(u)/du$ . Nevertheless, we are enjoyed to establish the explicit form of the solutions. With a preliminary optimism, we postpone the problem of the simplification of the expressions, where these integrals will enter as auxiliary functions. It is important to note, that during the process of derivations, it becomes clear that the computed solutions are unique. That is to say, the application of the formulas will not lead to bifurcation problems, generated by the established solutions itself. Another good characteristic of the above considered solutions is that they passage continuously through some *suspected* peculiar points like  $e(u) = 0$ ,  $\dot{e}(u) = 0$ ,  $e(u) - \dot{e}(u) = 0$ , etc. This was discussed earlier many times, and the answer to the problem was favorable: these peculiar points do not cause troubles. Such kind of conclusions are essentially proved by the corresponding L'Hospital's rule for resolving of indeterminacies of the type 0/0. Therefore, the established expressions for  $\mathbf{L}_i(e, \dot{e})$ , ( $i = 0, \dots, 3$ ) and  $\mathbf{K}_j(e, \dot{e})$ , ( $j = 1, \dots, 5$ ) may be used without troubles about these singular points.

## 7. Conclusions

The present paper encloses an investigation associated with an analytical solving of several types of definite integrals. They are considered to be functions of the eccentricities  $e(u)$  and their derivatives  $\dot{e}(u) \equiv de(u)/du$  of the particle orbits, moving in the accretion discs with elliptical shapes. These integrals were not found solved in the existing mathematical handbooks and reference books in forms, which are appropriate for use, according to our aspiration to apply them in the theory of elliptical accretion flows. More concretely, the integrals, which we have considered both in the present investigation, and in the papers [3] and [4], are  $\mathbf{L}_i(e, \dot{e})$ , ( $i = 0, \dots, 3$ ) (defined by formula (1)),  $\mathbf{K}_j(e, \dot{e})$ , ( $j = 1, \dots, 5$ ) (defined by formula (2)),  $\mathbf{A}_i(e, \dot{e})$ , ( $i = 1, \dots, 5$ ) (defined by formula (6)),  $\mathbf{J}_j(e, \dot{e})$ , ( $j = 1, \dots, 4$ ) (defined by formula (7)) and  $\mathbf{H}_j(e, \dot{e})$ , ( $j = 1, \dots, 4$ ) (defined by formula (8)). The situation in our case is that the analytical solutions are intended to be set into application for resolving of a **concrete** task. It is connected with the specific model of accretion discs [5], and introduces some limitations on the variables  $e(u)$  and  $\dot{e}(u)$ , which are treated as independent ones. Aside from the circumstance that, by definition,  $\dot{e}(u) \equiv de(u)/du$ . The later must obey three inequalities for all values of the independent variable  $u \equiv \ln(p)$ , where  $p$  is the focal parameter of the particular particle elliptical orbit). Namely, (i)  $|e(u)| < 1$ , (ii)  $|\dot{e}(u)| < 1$  and (iii)  $|e(u) - \dot{e}(u)| < 1$ . These restrictions arise, because the variable  $e(u)$  is considered as an eccentricity and the *stationary* accretion flows in the model of Lyubarskij et al. [5] are *a priori*, by hypothesis, excluding any singular behavior of the accretion disc characteristics. This means that the phenomena like the propagation of shock waves are not taken into account. Therefore, the above mentioned constraints (i) – (iii) are, essentially imposed from physical reasons. Of course, to these must be added also the property that all physical characteristics in the model of Lyubarskij et al. [5] are described by means of *real* quantities. As a consequence, the integrands into the formulas (1), (2), (6), (7) and (8) include only *real* functions, and the corresponding integrals are also *real* functions on  $e(u)$  and  $\dot{e}(u)$ . It has to be mentioned, that such a simplified situation may not occur for models other than [5]. For example, in the paper of Ogilvie [6] is introduced the notion *complex eccentricity*  $\mathbf{E}(\mathbf{r})$  (where  $\mathbf{r}$  is the radius-vector), in order to treat *the more general case*, when the particle orbits of the eccentric accretion discs *are not sharing a common longitude of periastron*. But we are not dealing with this, very probably, much more difficult for analytical solving problem. It is

enough only to mention that in the model of Ogilvie [6], the dynamical equation, governing of the structure of the disc, is, generally speaking, no more ordinary differential equation, but particular one.

We conclude our remarks, stressing that *we have not performed* an analytical solving of the full mathematical problem, concerning the evaluation of the integrals

$\mathbf{L}_i(e, \dot{e})$ ,  $\mathbf{K}_j(e, \dot{e})$ ,  $\mathbf{A}_i(e, \dot{e})$ ,  $\mathbf{J}_j(e, \dot{e})$ , and  $\mathbf{H}_j(e, \dot{e})$ , (the indices  $\mathbf{i}$  and  $\mathbf{j}$  run the corresponding values, accepted by us, in the definitions (1), (2), (6), (7) and (8)). This is done for some particular cases, satisfying the above discussed restriction, imposed on the variables  $e(u)$  and  $\dot{e}(u) \equiv de(u)/du$  from physical reasonings. The so established expressions for these integrals (see also papers [3] and [4]) are presenting a complete system of solutions, which is sufficient for our purposes. It gives a possibility to investigate the behavior of some other integrals, which *directly* enter into the dynamical equation for the elliptical accretion discs, described by the model of Lyubarskij et al. [5]. For this reason, we have named the former five types of integrals “auxiliary integrals”.

## References

1. D i m i t r o v, D. Thin viscous elliptical accretion discs with orbits sharing a common longitude of periastron. V. Linear relations between azimuthal-angle averaged factors in the dynamical equation., Aerospace Research in Bulgaria, 24, 2012, pp. 5–32.
2. D i m i t r o v, D. Thin viscous elliptical accretion discs with orbits sharing a common longitude of periastron. VI . Simplification of the dynamical equation., Aerospace Research in Bulgaria, 24, 2012, pp. 33–59.
3. D i m i t r o v, D. Analytical computation of two integrals, appearing in the theory of elliptical accretion discs. I. Solving of the auxiliary integrals, emerging during their derivations., Aerospace Research in Bulgaria, 25, 2013, 5–34.
4. D i m i t r o v, D. Analytical computation of two integrals, appearing in the theory of elliptical accretion discs. II. Solving of some auxiliary integrals, containing logarithmic functions into their integrands., Aerospace Research in Bulgaria, 25, 2013, 35–61.
5. L y u b a r s k i j, Y u. E., K. A. P o s t n o v, M. E. P r o k h o r o v. Eccentric accretion discs., Monthly Not. Royal Astron. Soc., 266, 1994, № 2, pp. 583–596.
6. O g i l v i e, G. I. Non-linear fluid dynamics of eccentric discs., Monthly Notices Royal Astron. Soc., 325, 2001, № 1, pp. 231–248.

**АНАЛИТИЧНО ПРЕСМЯТАНЕ НА ДВА ИНТЕГРАЛА,  
ВЪЗНИКВАЩИ В ТЕОРИЯТА НА ЕЛИПТИЧНИТЕ АКРЕЦИОННИ  
ДИСКОВЕ. III. РЕШАВАНЕ НА ПЪЛНАТА СИСТЕМА ОТ  
СПОМАГАТЕЛНИ ИНТЕГРАЛИ, СЪДЪРЖАЩИ  
ЛОГАРИТМИЧНИ ФУНКЦИИ В ТЕХНИТЕ ИНТЕГРАНДИ**

*Д. Димитров*

**Резюме**

Настоящото изследване затваря започнатите в по-ранните статии [3] и [4] аналитични оценки на някои видове определени интегралите. Тези решения са необходими стъпки в посока на разкриването на математическата структура на динамичното уравнение, управляващо свойствата на *стационарните* елиптични акреционни дискове, чиито апсидни линии на **всички орбити** лежат върху една и съща линия [5]. Въпреки че разглежданата тук задача може да изглежда, на пръв поглед, като една чисто математическа такава, има някои ограничения от физическо естество върху променливите, влизайки като аргументи в интеграндите. В тази статия ние решаваме аналитично следните два определени интеграла, включващи в техните числителители (като множител) логаритмичната функция  $\ln(1 + e\cos\varphi)$ . Конкретно, ние намираме в явна форма решенията на интегралите

$$\mathbf{L}_i(e, \dot{e}) \equiv \int_0^{2\pi} [\ln(1 + e\cos\varphi)](1 + e\cos\varphi)^{-1} [1 + (e - \dot{e})\cos\varphi]^{-i} d\varphi, \quad (i = 0, \dots, 3) \text{ и } \mathbf{K}_j(e, \dot{e}) \equiv \int_0^{2\pi} [\ln(1 + e\cos\varphi)] [1 + (e - \dot{e})\cos\varphi]^{-j} d\varphi, \quad (j = 1, \dots, 5).$$

Тук ние сме използвали

следните обозначения.  $\varphi$  е азимуталният ъгъл. Интегрирането по  $\varphi$  от 0 до  $2\pi$  означава усредняване върху цялата траектория за всяка една частица от диска. Всяка такава частица се спуска по спирала към центъра на диска, движейки се по (квази-) елиптични орбити с фокални параметри  $p$ . На тези параметри  $p$  е позволено да варират за различните елиптични орбити. В нашия подход на изчисляване, ние третираме  $e(u)$  и  $\dot{e}(u)$  като независими променливи. Физически наложените ограничения (които, до известна степен, водят до опростявания на задачите) са  $|e(u)| < 1$ ,  $|\dot{e}(u)| < 1$  и  $|e(u) - \dot{e}(u)| < 1$  за всички допустими значения на  $u$ . Тоест, между най-вътрешната и най-външната орбита на диска. Следователно, установените в тази статия аналитични решения за интегралите  $\mathbf{L}_i(e, \dot{e})$ , ( $i = 0, \dots, 3$ ) и  $\mathbf{K}_j(e, \dot{e})$ , ( $j = 1, \dots, 5$ ) са, вероятно, не най-общите такива даже в областта на реалния анализ. Въпреки това, те са достатъчни за нашата цел да се опрости динамичното уравнение.

## ANALYTICAL COMPUTATION OF TWO INTEGRALS, APPEARING IN THE THEORY OF ELLIPTICAL ACCRETION DISCS. IV. SOLVING OF THE INTEGRALS, ENSURING THE EVALUATION OF THE DERIVATIVES, ENTERING INTO THE WRONSKI DETERMINANT

*Dimitar Dimitrov*

*Space Research and Technology Institute – Bulgarian Academy of Sciences  
e-mail: dim@mail.space.bas.bg*

### **Abstract**

*The present paper deals with the analytical evaluation of the definite integral  $\int_0^{2\pi} (1 + \cos\varphi)^{n-4} [1 + (e - \dot{e})\cos\varphi]^{-n-1} d\varphi$ , where  $e(u)$  are the eccentricities of the particle orbits,  $\dot{e}(u) \equiv de(u)/du$ ,  $u \equiv \ln(p)$ , with  $p$  being the focal parameter of the corresponding elliptical particle orbits. The parameter  $n$  is the power in the viscosity law  $\eta = \beta \Sigma^n$ , where  $\Sigma$  is the surface density of the accretion disc, and  $\varphi$  is the azimuthal angle. We have fulfilled computations under the following three restrictions: (i)  $|e(u)| < 1$ , (ii)  $|\dot{e}(u)| < 1$  and (iii)  $|e(u) - \dot{e}(u)| < 1$ . They are physically motivated by the accepted for our considerations model of stationary elliptical accretion discs of Lyubarskij et al. [1]. Many particular cases, arising from the singular behavior of some terms for given values of  $e(u)$ ,  $\dot{e}(u)$ , their difference  $e(u) - \dot{e}(u)$  and the power  $n$ , are computed in details. These calculations are performed in two ways: (i) by a direct substitution of the singular value into the initial definition of the integral, and (ii) by a limit transition to this singular value into the already evaluated analytical expression for the integral, obtained for the regular values of the corresponding variables. In the later case, the application of the L'Hospital's rule for resolving of indeterminacies of the type 0/0 is very useful. Both the approaches give the same results in every verified case, which ensures that the transition through the singular value is continuous. This means that the analytical solutions for all the considered (singular and non-singular) cases may be combined into one single formula. Such a prescription of the solution of the above written integral is very suitable to the occasion, when this formula is applied for the verification of the linear dependence/independence of the coefficients, entering into the terms of the dynamical equation of the elliptical accretion disc.*

## 1. Introduction: Some definitions and notations

In the present paper we continue the investigation of the *stationary* elliptical accretion discs, according to the model, developed by Lyubarskij et al. [1]. For more clarity, we shall write down the definitions of the following seven integrals ([2] and the references therein):

$$(1) \quad \mathbf{I}_0(e, \dot{e}, n) \equiv \int_0^{2\pi} (1 + e \cos \varphi)^{n-3} [1 + (e - \dot{e}) \cos \varphi]^{-(n+1)} d\varphi,$$

$$(2) \quad \mathbf{I}_{0+}(e, \dot{e}, n) \equiv \int_0^{2\pi} (1 + e \cos \varphi)^{n-2} [1 + (e - \dot{e}) \cos \varphi]^{-(n+2)} d\varphi,$$

$$(3) \quad \mathbf{I}_j(e, \dot{e}, n) \equiv \int_0^{2\pi} (\cos \varphi)^j (1 + e \cos \varphi)^{n-2} [1 + (e - \dot{e}) \cos \varphi]^{-(n+1)} d\varphi; \quad \mathbf{j} = 0, 1, 2, 3, 4.$$

The appearance of the above written integrals  $\mathbf{I}_0(e, \dot{e}, n)$ ,  $\mathbf{I}_{0+}(e, \dot{e}, n)$  and  $\mathbf{I}_j(e, \dot{e}, n)$ , ( $\mathbf{j} = 0, 1, 2, 3, 4$ ), is evident from the previous considerations (and derivations) of the dynamical equation ([1], [2] and the references therein). For this reason, we shall not discuss now such a subject. We mention only that the integrals  $\mathbf{I}_0(e, \dot{e}, n)$ ,  $\mathbf{I}_{0+}(e, \dot{e}, n)$  and  $\mathbf{I}_j(e, \dot{e}, n)$ , ( $\mathbf{j} = 0, 1, 2, 3, 4$ ) arise, due to the angle-averaging over the azimuthal angle  $\varphi$  in the used system of non-orthogonal curvilinear coordinates  $(p, \varphi)$ . Here  $p$  is the focal parameter of the elliptical orbit for each particle, which changes for the different parts of the accretion disc. Further in the our exposition, like in the paper [1], instead of  $p$  we use its logarithm  $u \equiv \ln(p)$ . Therefore, the eccentricities  $e$  of the particle orbits and their derivatives  $\dot{e} \equiv de/du$  are functions of the parameter/coordinate  $u$ . It is worth to note, that for *circular* orbits in the accretion flow (like the standard  $\alpha$ -disc model [3]), the parameter  $p$  is simply the radius  $r$  of the corresponding particle orbit. To underline that  $u$  is an independent coordinate, we shall often write further that  $e = e(u)$  and  $\dot{e} = \dot{e}(u)$ . It also remains to remark that the parameter  $n$  is the power into the viscosity law  $\eta = \beta \Sigma^n$ , where  $\eta$  is the viscosity,  $\Sigma$  is the surface density of the accretion disc, and  $\beta$  is a constant. We stress that  $n$  is a constant throughout the disc, i.e.,  $n$  does not depend on  $u$ . Of course, under the transition from one model of accretion flow to another one, the power  $n$  may change from a given value to another constant meaning.

During the process of realization of the our program for simplification of the dynamical equation (derived initially by Lyubarskij et al. [1]; *stationary* case), we strike with the problem of the analytical evaluation of the derivatives with respect to  $e(u)$  and  $\dot{e}(u)$  of the integrals  $\mathbf{I}_0(e, \dot{e}, n)$  and  $\mathbf{I}_{0+}(e, \dot{e}, n)$ . It can be shown that the first partial derivatives

$\partial \mathbf{I}_0(e, \dot{e}, n) / \partial e$ ,  $\partial \mathbf{I}_0(e, \dot{e}, n) / \partial \dot{e}$ ,  $\partial \mathbf{I}_{0+}(e, \dot{e}, n) / \partial e$  and  $\partial \mathbf{I}_{0+}(e, \dot{e}, n) / \partial \dot{e}$  may be expressed as linear combinations of the integrals  $\mathbf{I}_0(e, \dot{e}, n)$  and  $\mathbf{I}_{0+}(e, \dot{e}, n)$ . The exact analytical forms of the coefficients of these linear dependences will be derived in a forthcoming paper [4]. We remind that we have accepted the following approach. Until now we do not know the searched for solution  $e(u)$  of the dynamical equation and, consequently, the analytical form of its derivative  $\dot{e}(u) \equiv de(u)/du$  is also unknown. Hence, we are able to consider the eccentricity  $e(u)$  and its derivative  $\dot{e}(u)$  as “independent” variables, having, however, in mind that under differentiation with respect to  $u$ , we must take into account that  $\dot{e}(u) \equiv de(u)/du$ . As we have mentioned earlier, ([2] and the references therein), we insert the following three restrictions: (i)  $|e(u)| < 1$ , (ii)  $|\dot{e}(u)| < 1$  and (iii)  $|e(u) - \dot{e}(u)| < 1$  for all values of the parameter  $u \equiv \ln(p)$  (i.e., in fact, for all admissible values of the focal parameter  $p$ ). Our current problem, which we intend to solve, is the question whether the integrals  $\mathbf{I}_0(e, \dot{e}, n)$  and  $\mathbf{I}_{0+}(e, \dot{e}, n)$  are linearly independent functions with respect to their arguments  $e(u)$ ,  $\dot{e}(u)$  and  $n$ , or not? The standard way to check this is to compute the corresponding *Wronski* determinants. The identical equality to zero of these determinants are *necessary conditions* to be fulfilled the linear relations between the integrals  $\mathbf{I}_0(e, \dot{e}, n)$  and  $\mathbf{I}_{0+}(e, \dot{e}, n)$ . If the opposite is true, then  $\mathbf{I}_0(e, \dot{e}, n)$  and  $\mathbf{I}_{0+}(e, \dot{e}, n)$  must be linearly independent functions of  $e(u)$ ,  $\dot{e}(u)$  and  $n$ , because the pointed out *necessary conditions* would be violated. The analytical evaluations of the *Wronski* determinants require computations of second order partial derivatives like  $\partial^2 \mathbf{I}_0(e, \dot{e}, n) / \partial e^2$ ,  $\partial^2 \mathbf{I}_0(e, \dot{e}, n) / \partial e \partial \dot{e}$ ,  $\partial^2 \mathbf{I}_0(e, \dot{e}, n) / \partial \dot{e}^2$ ,  $\partial^2 \mathbf{I}_{0+}(e, \dot{e}, n) / \partial e^2$ ,  $\partial^2 \mathbf{I}_{0+}(e, \dot{e}, n) / \partial e \partial \dot{e}$  and  $\partial^2 \mathbf{I}_{0+}(e, \dot{e}, n) / \partial \dot{e}^2$ . In view of their analytical evaluation, it is appropriate to compute preliminary two auxiliary integrals, defined by the equalities (4) and (5) below in the next chapter 2.

## 2. Computation of two auxiliary integrals

In our preparation to find explicit analytical expressions for the second order partial derivatives  $\partial^2 \mathbf{I}_0(e, \dot{e}, n) / \partial e^2$ ,  $\partial^2 \mathbf{I}_0(e, \dot{e}, n) / \partial e \partial \dot{e}$ ,  $\partial^2 \mathbf{I}_0(e, \dot{e}, n) / \partial \dot{e}^2$ ,  $\partial^2 \mathbf{I}_{0+}(e, \dot{e}, n) / \partial e^2$ ,  $\partial^2 \mathbf{I}_{0+}(e, \dot{e}, n) / \partial e \partial \dot{e}$  and  $\partial^2 \mathbf{I}_{0+}(e, \dot{e}, n) / \partial \dot{e}^2$ , we encounter with the necessity to evaluate two integrals, namely:

$$(4) \quad \mathbf{I}_{0,-4,+1}(e, \dot{e}, n) \equiv \int_0^{2\pi} (1 + e \cos \varphi)^{n-4} [1 + (e - \dot{e}) \cos \varphi]^{-n-1} d\varphi$$

and



$$(5) \quad \mathbf{I}_{0,-2,+3}(e,\dot{e},n) \equiv \int_0^{2\pi} (1 + e\cos\varphi)^{n-2} [1 + (e - \dot{e})\cos\varphi]^{-n-3} d\varphi.$$

We do not give here a precise designation of the above two integrals. The idea for such (*unconventional*) index notations is that the integrands of the integrals, with which we are dealing, may be represented as a product of three multipliers. Two of them are into the nominator:  $(\cos\varphi)^{\text{first index}}$  and  $(1 + e\cos\varphi)^{n + \text{second index}}$ . The third multiplier is, in fact, the denominator of the integrand:  $[1 + (e - \dot{e})\cos\varphi]^{n + \text{third index}}$ , or, transforming it like a multiplier of the nominator:  $[1 + (e - \dot{e})\cos\varphi]^{- (n + \text{third index})}$ . In particular, if the *first index* = 0, this means that the multiplier  $\cos\varphi$  is absent into the nominator. For example, we would be able to write  $\mathbf{I}_{0,-2,+3}(e,\dot{e},n)$  as  $\mathbf{I}_{0,-3,+1}(e,\dot{e},n)$ , or to write  $\mathbf{I}_{0,+}(e,\dot{e},n)$  as  $\mathbf{I}_{0,-2,+2}(e,\dot{e},n)$ . But we shall not change the “old” system of notations. The reason for this is that the integrals (4) and (5) *only temporarily emerge* into our computations and they must not be considered as frequently struck functions in the evaluated formulas. We also underline that by the term “analytical evaluation of the integrals  $\mathbf{I}_{0,-4,+1}(e,\dot{e},n)$  and  $\mathbf{I}_{0,-2,+3}(e,\dot{e},n)$ ” we do not understand by all means that the evaluation is finished up to some more or less analytical expressions. Instead of that, it may happen to satisfy us with the more modest conclusion that  $\mathbf{I}_{0,-4,+1}(e,\dot{e},n)$  and  $\mathbf{I}_{0,-2,+3}(e,\dot{e},n)$  are linear combinations of the integrals (1) – (3). The establishing of such linear relations is fully sufficient for our purposes.

$$\mathbf{2.1. Evaluation of the integral } \mathbf{I}_{0,-4,+1}(e,\dot{e},n) \equiv \int_0^{2\pi} (1 + e\cos\varphi)^{n-4} [1 + (e - \dot{e})\cos\varphi]^{-n-1} d\varphi$$

### 2.1.1. Case $n \neq 3, e(u) \neq 0, \dot{e}(u) \neq 0$

According to the definition (4), we perform the following transformations of the considered integral  $\mathbf{I}_{0,-4,+1}(e,\dot{e},n)$ :

$$\begin{aligned} (6) \quad \mathbf{I}_{0,-4,+1}(e,\dot{e},n) &= \int_0^{2\pi} (1 + e\cos\varphi)^{n-4} (\cos^2\varphi + \sin^2\varphi) [1 + (e - \dot{e})\cos\varphi]^{-n-1} d\varphi = \\ &= -e^{-2} \int_0^{2\pi} (1 + e\cos\varphi)^{n-3} (1 - e\cos\varphi) [1 + (e - \dot{e})\cos\varphi]^{-n-1} d\varphi + e^{-2} \int_0^{2\pi} (1 + e\cos\varphi)^{n-4} \times \\ &\times [1 + (e - \dot{e})\cos\varphi]^{-n-1} d\varphi - [(n-3)e]^{-1} \int_0^{2\pi} (\sin\varphi) [1 + (e - \dot{e})\cos\varphi]^{-n-1} d[(1 + e\cos\varphi)^{n-3}] = \\ &= e^{-2} \mathbf{I}_{0,-4,+1}(e,\dot{e},n) - e^{-2} \mathbf{I}_{0,-}(e,\dot{e},n) + e^{-2} \int_0^{2\pi} (1 + e\cos\varphi)^{n-2} [1 + (e - \dot{e})\cos\varphi]^{-n-1} d\varphi - \end{aligned}$$

$$\begin{aligned}
& -e^{-2} \int_0^{2\pi} (1 + e \cos \varphi)^{n-3} [1 + (e - \dot{e}) \cos \varphi]^{-n-1} d\varphi + [(n-3)e^2]^{-1} \int_0^{2\pi} (1 + e \cos \varphi)^{n-3} \times \\
& \times [(1 + e \cos \varphi) - 1][1 + (e - \dot{e}) \cos \varphi]^{-n-1} d\varphi + \\
& + (n+1)(e - \dot{e})[(n-3)e]^{-1} \int_0^{2\pi} (1 + e \cos \varphi)^{n-3} (\sin^2 \varphi) [1 + (e - \dot{e}) \cos \varphi]^{-n-2} d\varphi.
\end{aligned}$$

Taking into account in the last integral that  $\sin^2 \varphi = 1 - \cos^2 \varphi$ , we arrive at the next relation:

$$\begin{aligned}
(7) \quad & (1 - e^{-2}) \mathbf{I}_{0,-4,+1}(e, \dot{e}, n) = -2e^{-2} \mathbf{I}_0(e, \dot{e}, n) + e^{-2} \mathbf{I}_0(e, \dot{e}, n) + [(n-3)e^2]^{-1} \mathbf{I}_0(e, \dot{e}, n) - \\
& - [(n-3)e^2]^{-1} \mathbf{I}_0(e, \dot{e}, n) + (n+1)(e - \dot{e})[(n-3)e]^{-1} \int_0^{2\pi} (1 + e \cos \varphi)^{n-3} \times [1 + (e - \dot{e}) \cos \varphi]^{-n-2} d\varphi + \\
& + (n+1)(e - \dot{e})[(n-3)e^3]^{-1} \int_0^{2\pi} (1 + e \cos \varphi)^{n-3} [(1 - e^2 \cos^2 \varphi) - 1][1 + (e - \dot{e}) \cos \varphi]^{-n-2} d\varphi.
\end{aligned}$$

To proceed further, we have to compute the before the last integral in the above equality, namely:

$$\begin{aligned}
(8) \quad & \mathbf{I}_{0,-3,+2}(e, \dot{e}, n) \equiv \int_0^{2\pi} (1 + e \cos \varphi)^{n-3} [1 + (e - \dot{e}) \cos \varphi]^{-n-2} d\varphi = \int_0^{2\pi} (1 + e \cos \varphi)^{n-3} [1 + (e - \dot{e}) \cos \varphi]^{-n-1} d\varphi - \\
& - [(e - \dot{e})/e] \int_0^{2\pi} (1 + e \cos \varphi)^{n-3} [(1 + e \cos \varphi) - 1][1 + (e - \dot{e}) \cos \varphi]^{-n-2} d\varphi = \\
& = \mathbf{I}_0(e, \dot{e}, n) - [(e - \dot{e})/e] \mathbf{I}_0(e, \dot{e}, n) + [(e - \dot{e})/e] \mathbf{I}_{0,-3,+2}(e, \dot{e}, n),
\end{aligned}$$

where we have used the same manner of notations as for the integral  $\mathbf{I}_{0,-4,+1}(e, \dot{e}, n)$  and  $\mathbf{I}_{0,-2,+3}(e, \dot{e}, n)$ . Consequently, from the relation (8) we have:

$$(9) \quad \mathbf{I}_{0,-3,+2}(e, \dot{e}, n) = (e/\dot{e}) \mathbf{I}_0(e, \dot{e}, n) - [(e - \dot{e})/\dot{e}] \mathbf{I}_0(e, \dot{e}, n).$$

We remark that the above relation is derived under the conditions  $e(u) \neq 0$  and  $\dot{e}(u) \neq 0$ , comprised in the Case 2.1.1. Substitution of (9) into (7) gives:

$$\begin{aligned}
(10) \quad & (1 - e^{-2}) \mathbf{I}_{0,-4,+1}(e, \dot{e}, n) = -(2n-5)[(n-3)e^2]^{-1} \mathbf{I}_0(e, \dot{e}, n) + (n-2)[(n-3)e^2]^{-1} \mathbf{I}_0(e, \dot{e}, n) + \\
& + (n+1)(e - \dot{e})[(n-3)\dot{e}]^{-1} \mathbf{I}_0(e, \dot{e}, n) - (n+1)(e - \dot{e})^2[(n-3)e\dot{e}]^{-1} \mathbf{I}_{0,+}(e, \dot{e}, n) + \\
& + (n+1)(e - \dot{e})[(n-3)e^3]^{-1} \int_0^{2\pi} (1 + e \cos \varphi)^{n-2} [1 + (e - \dot{e}) \cos \varphi]^{-n-2} d\varphi - \\
& - (n+1)[(n-3)e^2]^{-1} \int_0^{2\pi} (1 + e \cos \varphi)^{n-2} \{ [1 + (e - \dot{e}) \cos \varphi] - 1 \} [1 + (e - \dot{e}) \cos \varphi]^{-n-2} d\varphi - \\
& - (n+1)(e - \dot{e})[(n-3)e^3]^{-1} \mathbf{I}_{0,-3,+2}(e, \dot{e}, n).
\end{aligned}$$

Applying again the result (9), we obtain that:

$$\begin{aligned}
(11) \quad & (1 - e^{-2}) \mathbf{I}_{0,-4,+1}(e, \dot{e}, n) = (n-3)^{-1} [(-2n+5)/e^2 + (n+1)(e - \dot{e})/\dot{e} - (n+1)(e - \dot{e})(e^2 \dot{e})^{-1}] \mathbf{I}_0(e, \dot{e}, n) + \\
& + (n-3)^{-1} [-(n+1)(e - \dot{e})^2 (e\dot{e})^{-1} + (n+1)(e - \dot{e})e^{-3} + (n+1)e^{-2} + (n+1)(e - \dot{e})^2 (e^3 \dot{e})] \mathbf{I}_{0,+}(e, \dot{e}, n) + \\
& + (n-3)^{-1} [(n-2)e^{-2} - (n+1)e^{-2}] \mathbf{I}_0(e, \dot{e}, n).
\end{aligned}$$

Multiplying the above equality by  $[-(n-3)e^2]$ , we obtain:

$$\begin{aligned}
(12) \quad & (n-3)(1 - e^2) \mathbf{I}_{0,-4,+1}(e, \dot{e}, n) = [(2n-5) + (n+1)(1 - e^2)(e - \dot{e})e^{-1}] \mathbf{I}_0(e, \dot{e}, n) - \\
& - (n+1)[(1 - e^2)(e - \dot{e})^2 (e\dot{e})^{-1} + (2e - \dot{e})/e] \mathbf{I}_{0,+}(e, \dot{e}, n) + 3 \mathbf{I}_0(e, \dot{e}, n).
\end{aligned}$$

This is the wanted representation of the integral  $\mathbf{I}_{0,-4,+1}(e,\dot{e},n)$  through the integrals  $\mathbf{I}_0(e,\dot{e},n)$ ,  $\mathbf{I}_{0+}(e,\dot{e},n)$  and  $\mathbf{I}_0(e,\dot{e},n)$ . Obviously, this dependence is linear and is derived under the conditions  $(n-3) \neq 0$ ,  $e(u) \neq 0$  and  $\dot{e}(u) \neq 0$ . No matter if  $e(u) - \dot{e}(u) \neq 0$  or  $e(u) - \dot{e}(u) = 0$ !

Before to proceed further, we shall remark that we have already computed the analytical expressions for the integrals

$$\mathbf{A}_i(e,\dot{e}) \equiv \int_0^{2\pi} [1 + (e - \dot{e})\cos\varphi]^{-i} d\varphi; \quad (\mathbf{i} = 1, 2, 3, 4, 5),$$

$$\mathbf{J}_i(e,\dot{e}) \equiv \int_0^{2\pi} (1 + e\cos\varphi)^{-1} [1 + (e - \dot{e})\cos\varphi]^{-i} d\varphi; \quad (\mathbf{i} = 1, 2, 3, 4), \quad \mathbf{H}_i(e,\dot{e}) \equiv \int_0^{2\pi} (1 + e\cos\varphi)^{-i} \times \\ \times [1 + (e - \dot{e})\cos\varphi]^{-1} d\varphi; \quad (\mathbf{i} = 1, 2, 3, 4). \text{ Their detailed evaluations are carried out in paper [5].}$$

We also have analytical estimations for the integrals  $\mathbf{L}_i(e,\dot{e}) \equiv \int_0^{2\pi} [\ln(1 + e\cos\varphi)](1 + e\cos\varphi)^{-1} \times$

$$\times [1 + (e - \dot{e})\cos\varphi]^{-i} d\varphi; \quad (\mathbf{i} = 0, 1, 2, 3), \quad \mathbf{K}_i(e,\dot{e}) \equiv \int_0^{2\pi} [\ln(1 + e\cos\varphi)][1 + (e - \dot{e})\cos\varphi]^{-i} d\varphi;$$

$(\mathbf{i} = 1, 2, 3, 4, 5)$ , which derivations are circumstantially described in the papers [6] and [7]. We shall often quote these results, in order to argue our further calculations. Also we shall take into use the expressions of the above integrals for some particular values of their arguments  $e(u)$  and  $\dot{e}(u)$ , which are cited in the above mentioned papers [5], [6] and [7]. *In fact, the later three works were preliminary worked out, in view of their application to the needs of the present paper, i.e., they are in that sense, auxiliary investigations.*

### **2.1.2. Case $n \neq 3$ , $e(u) \neq 0$ , $\dot{e}(u) = 0 \Rightarrow e(u) - \dot{e}(u) \neq 0$**

According to the definitions (1) – (3), we can write for  $\dot{e}(u) = 0$  the following expressions for the integrals  $\mathbf{I}_0(e,\dot{e} = 0,n)$ ,  $\mathbf{I}_{0-}(e,\dot{e} = 0,n)$ ,  $\mathbf{I}_{0+}(e,\dot{e} = 0,n)$  and  $\mathbf{I}_{0,-4,+1}(e,\dot{e} = 0,n)$ :

$$(13) \quad \mathbf{I}_0(e,\dot{e} = 0,n) \equiv \int_0^{2\pi} (1 + e\cos\varphi)^{-3} d\varphi \equiv \mathbf{A}_3(e, 0) = \pi(2 + e^2)(1 - e^2)^{-5/2}, \quad (\text{eq. (22)}$$

from paper [5]),

$$(14) \quad \mathbf{I}_0(e,\dot{e} = 0,n) = \mathbf{I}_{0+}(e,\dot{e} = 0,n) \equiv \int_0^{2\pi} (1 + e\cos\varphi)^{-4} d\varphi \equiv \mathbf{A}_4(e, 0) = \pi(2 + 3e^2)(1 - e^2)^{-7/2},$$

(eq. (23) from paper [5]), and

$$(15) \quad \mathbf{I}_{0,-4,+1}(e, \dot{e} = 0, n) \equiv \int_0^{2\pi} (1 + e \cos \varphi)^{-5} d\varphi \equiv \mathbf{A}_5(e, 0) = (\pi/4)(8 + 24e^2 + 3e^4)(1 - e^2)^{-9/2},$$

(eq. (24) from paper [5]).

Note that the above three evaluations (13) – (15) do not depend on the power  $n$  in the viscosity law  $\eta = \beta \Sigma^n$ . They are valid also for  $n = 3$ ! We can perform the following transformation of the relations (14):

$$(16) \quad \begin{aligned} \mathbf{I}_0(e, \dot{e} = 0, n) &= \mathbf{I}_{0+}(e, \dot{e} = 0, n) = \int_0^{2\pi} (1 + e \cos \varphi)^{-3} d\varphi - e \int_0^{2\pi} (1 + e \cos \varphi)^{-4} d(\sin \varphi) = \mathbf{I}_0(e, \dot{e} = 0, n) + \\ &+ 4e^2 \mathbf{I}_{0,-4,+1}(e, \dot{e} = 0, n) - 4\mathbf{I}_{0,-4,+1}(e, \dot{e} = 0, n) + 4 \int_0^{2\pi} (1 + e \cos \varphi)(1 - e \cos \varphi)(1 + e \cos \varphi)^{-5} d\varphi = \\ &= \mathbf{I}_0(e, \dot{e} = 0, n) + 4(e^2 - 1)\mathbf{I}_{0,-4,+1}(e, \dot{e} = 0, n) + 4\mathbf{I}_0(e, \dot{e} = 0, n) - 4 \int_0^{2\pi} (1 + e \cos \varphi)^{-3} d\varphi + \\ &+ 4 \int_0^{2\pi} (1 + e \cos \varphi)^{-4} d\varphi = \mathbf{I}_0(e, \dot{e} = 0, n) + 4(e^2 - 1)\mathbf{I}_{0,-4,+1}(e, \dot{e} = 0, n) + 4\mathbf{I}_0(e, \dot{e} = 0, n) - 4\mathbf{I}_0(e, \dot{e} = 0, n) + \\ &+ 4\mathbf{I}_0(e, \dot{e} = 0, n) = 8\mathbf{I}_0(e, \dot{e} = 0, n) - 3\mathbf{I}_0(e, \dot{e} = 0, n) + 4(e^2 - 1)\mathbf{I}_{0,-4,+1}(e, \dot{e} = 0, n). \end{aligned}$$

From this equality we are able to express the integral  $\mathbf{I}_{0,-4,+1}(e, \dot{e} = 0, n)$  through the integrals  $\mathbf{I}_0(e, \dot{e} = 0, n) = \mathbf{I}_{0+}(e, \dot{e} = 0, n)$  and  $\mathbf{I}_0(e, \dot{e} = 0, n)$ . Consequently, dividing by  $4(1 - e^2) \neq 0$ , we obtain:

$$(17) \quad \mathbf{I}_{0,-4,+1}(e, \dot{e} = 0, n) = [4(1 - e^2)]^{-1} [7\mathbf{I}_0(e, \dot{e} = 0, n) - 3\mathbf{I}_0(e, \dot{e} = 0, n)].$$

We again note that the above relation (17) is also valid for  $n = 3$ , because under its deduction we do not require anywhere the condition  $n \neq 3$  to be fulfilled. It is evident also that (17) remains valid for  $e(u) = 0$ . In the later case, the equality (17) can be written as:

$$(18) \quad 2\pi = (1/4)[7(2\pi) - 3(2\pi)],$$

which is obviously true.

Let us rewrite the relation (13) in the following way, in order to see its validity under the transition  $\dot{e}(u) \rightarrow 0$ :

$$(19) \quad (n - 3)(1 - e^2)\mathbf{I}_{0,-4,+1}(e, \dot{e}, n) = (2n - 5)\mathbf{I}_0(e, \dot{e}, n) - (n + 1)(2e - \dot{e})e^{-1}\mathbf{I}_{0+}(e, \dot{e}, n) + 3\mathbf{I}_0(e, \dot{e}, n) + (n + 1)(1 - e^2)(e - \dot{e})\dot{e}^{-1}\{\mathbf{I}_{0-}(e, \dot{e}, n) - [(e - \dot{e})/e]\mathbf{I}_{0+}(e, \dot{e}, n)\}.$$

We see that:

$$(20) \quad \lim_{\dot{e}(u) \rightarrow 0} \{\mathbf{I}_0(e, \dot{e}, n) - [(e - \dot{e})/e]\mathbf{I}_{0+}(e, \dot{e}, n)\} = \mathbf{I}_0(e, \dot{e} = 0, n) - \mathbf{I}_{0+}(e, \dot{e} = 0, n) = 0,$$

according to the equalities (14). This result ensures that we may apply the L'Hospital's theorem for computing of indeterminacies of the type 0/0. Because  $\partial \dot{e}(u) / \partial \dot{e} = 1$ , it is enough to evaluate the derivative:

$$(21) \quad \partial \{\mathbf{I}_0(e, \dot{e}, n) - [(e - \dot{e})/e]\mathbf{I}_{0+}(e, \dot{e}, n)\} / \partial \dot{e} = (n + 1) \int_0^{2\pi} (\cos \varphi)(1 + e \cos \varphi)^{n-3} [1 + (e - \dot{e})\cos \varphi]^{-n-2} d\varphi +$$

$$\begin{aligned}
& + e^{-1} \int_0^{2\pi} (1 + e \cos \varphi)^{n-2} [1 + (e - \dot{e}) \cos \varphi]^{-n-2} d\varphi - (n+2) [(e - \dot{e})/e] \int_0^{2\pi} (\cos \varphi) (1 + e \cos \varphi)^{n-2} \times \\
& \times [1 + (e - \dot{e}) \cos \varphi]^{-n-3} d\varphi \xrightarrow{\dot{e}(u) \rightarrow 0} (n+1) \int_0^{2\pi} (\cos \varphi) (1 + e \cos \varphi)^{n-3} (1 + e \cos \varphi)^{-n-2} d\varphi + \\
& + e^{-1} \int_0^{2\pi} (1 + e \cos \varphi)^{n-2} (1 + e \cos \varphi)^{-n-2} d\varphi - (n+2) \int_0^{2\pi} (\cos \varphi) (1 + e \cos \varphi)^{n-2} (1 + e \cos \varphi)^{-n-3} d\varphi = \\
& - e^{-1} \int_0^{2\pi} (1 + e \cos \varphi) (1 + e \cos \varphi)^{-5} d\varphi + e^{-1} \int_0^{2\pi} (1 + e \cos \varphi)^{-5} d\varphi + e^{-1} \int_0^{2\pi} (1 + e \cos \varphi)^{-4} d\varphi = \\
& = e^{-1} \int_0^{2\pi} (1 + e \cos \varphi)^{-5} d\varphi = e^{-1} \mathbf{I}_{0,-4,+1}(e, \dot{e} = 0, n).
\end{aligned}$$

Therefore:

$$(22) \quad \lim_{\dot{e}(u) \rightarrow 0} \{ \dot{e}^{-1} \{ \mathbf{I}_{0_+}(e, \dot{e}, n) - [(e - \dot{e})/e] \mathbf{I}_{0_+}(e, \dot{e}, n) \} \} = e^{-1} \mathbf{I}_{0,-4,+1}(e, \dot{e} = 0, n).$$

So that, we have computed the problematic multiplier, associated with the transition  $\dot{e}(u) \rightarrow 0$ . Now, we take this limit  $\dot{e}(u) \rightarrow 0$  for the whole relation (19), taking into account that  $\mathbf{I}_{0_+}(e, \dot{e} = 0, n) = \mathbf{I}_{0_-}(e, \dot{e} = 0, n)$  (see the equality (14)):

$$(23) \quad 4(1 - e^2) \mathbf{I}_{0,-4,+1}(e, \dot{e} = 0, n) = 7 \mathbf{I}_{0_+}(e, \dot{e} = 0, n) - 3 \mathbf{I}_{0_-}(e, \dot{e} = 0, n).$$

After dividing by  $4(1 - e^2) \neq 0$ , we obtain the relation (17). Consequently, we may consider the equality (12) as valid also for the case  $\dot{e}(u) = 0$ , keeping in mind that we have to perform the limit transition  $\dot{e}(u) \rightarrow 0$  with the help of the L'Hospital's theorem for evaluation of uncertainties of the type 0/0. We again stress that the above results do not use the restriction  $(n - 3) \neq 0$ , and may be applied to the case  $e(u) = 0$ .

### **2.1.3. Case $n \neq 3$ , $e(u) = 0$ , $\dot{e}(u) \neq 0 \Rightarrow e(u) - \dot{e}(u) \neq 0$**

Taking into account the definitions (1) – (4), we can write for the present case the following equalities, as concerns to the integrals  $\mathbf{I}_{0_+}(e = 0, \dot{e}, n)$ ,  $\mathbf{I}_{0_-}(e = 0, \dot{e}, n)$ ,  $\mathbf{I}_{0_+}(e = 0, \dot{e}, n)$  and  $\mathbf{I}_{0,-4,+1}(e = 0, \dot{e}, n)$ :

$$(24) \quad \mathbf{I}_{0_+}(e = 0, \dot{e}, n) = \mathbf{I}_{0_-}(e = 0, \dot{e}, n) = \mathbf{I}_{0,-4,+1}(e = 0, \dot{e}, n) \equiv \int_0^{2\pi} (1 - \dot{e} \cos \varphi)^{-n-1} d\varphi,$$

$$(25) \quad \mathbf{I}_{0_+}(e = 0, \dot{e}, n) \equiv \int_0^{2\pi} (1 - \dot{e} \cos \varphi)^{-n-2} d\varphi > 0.$$

Note that the equalities (24) are valid also for  $n = 3$  and also for  $\dot{e}(u) = 0$ , when  $\mathbf{I}_{0,-4,+1}(e = 0, \dot{e} = 0, n) = 2\pi$ . Let us rewrite the relation (12) in the following way, in order to see its validity under the limit transition

$e(u) \rightarrow 0$ . That is to say, we detach the multiplier, which contains into its denominator the factor  $e(u)$ , causing the troubles under this transition  $e(u) \rightarrow 0$ :

$$(26) \quad (n-3)(1-e^2)\mathbf{I}_{0,-4,+1}(e,\dot{e},n) = [(2n-5) + (n+1)(1-e^2)(e-\dot{e})\dot{e}^{-1}]\mathbf{I}_0(e,\dot{e},n) - (n+1)e^{-1}[(1-e^2)(e-\dot{e})^2\dot{e}^{-1} + 2e-\dot{e}]\mathbf{I}_{0+}(e,\dot{e},n) + 3\mathbf{I}_0(e,\dot{e},n).$$

The problematic term is the coefficient of the integral  $\mathbf{I}_{0+}(e,\dot{e},n)$  in the right-hand-side of (26), which contains into its denominator the multiplier  $e(u)$ . We see that:

$$(27) \quad \lim_{e(u) \rightarrow 0} [(1-e^2)(e-\dot{e})^2\dot{e}^{-1} + 2e-\dot{e}] = \dot{e}^2\dot{e}^{-1} - \dot{e} = 0.$$

Further, we compute the derivative:

$$(28) \quad \frac{\partial[(1-e^2)(e-\dot{e})^2\dot{e}^{-1} + 2e-\dot{e}]/\partial e}{e(u) \rightarrow 0} = \dot{e}^{-1}[-2e(e-\dot{e})^2 + 2(1-e^2)(e-\dot{e})] + 2 \longrightarrow -2\dot{e}/\dot{e} + 2 = 0.$$

We may apply again the L'Hospital's theorem to obtain that:

$$(29) \quad \lim_{e(u) \rightarrow 0} \{e^{-1}[(1-e^2)(e-\dot{e})^2\dot{e}^{-1} + 2e-\dot{e}]\} = 0.$$

This means that, if we take the limit  $e(u) \rightarrow 0$  for the both sides of the equation (26), the coefficient before the integral  $\mathbf{I}_{0+}(e,\dot{e},n)$  will become equal to zero:

$$(30) \quad (n-3)\mathbf{I}_{0,-4,+1}(e=0,\dot{e},n) = (n-6)\mathbf{I}_0(e=0,\dot{e},n) + 3\mathbf{I}_0(e=0,\dot{e},n),$$

or, with the reading of the first equality in (24):

$$(31) \quad (n-3)\mathbf{I}_{0,-4,+1}(e=0,\dot{e},n) = (n-3)\mathbf{I}_0(e=0,\dot{e},n).$$

Taking into account that in the presently considered case  $n \neq 3$ , we may cancel out the factor  $(n-3)$  and to obtain the second equality in the relation (24). As we already mentioned above, it is also valid if we set into it  $\dot{e}(u) = 0$ :

$$(32) \quad \mathbf{I}_{0,-4,+1}(e=0,\dot{e}=0,n) = \mathbf{I}_0(e=0,\dot{e}=0,n) = 2\pi.$$

Therefore, under the limit transition  $e(u) \rightarrow 0$ , the relation (12) leads to the right equality (31). Consequently, we are able to consider (12) to remain valid also for  $e(u) = 0$ , having in mind that then we must apply the L'Hospital's theorem for revealing of uncertainties of the type 0/0.

#### **2.1.4. Case $n \neq 3$ , $e(u) = 0$ , $\dot{e}(u) = 0 \Rightarrow e(u) - \dot{e}(u) = 0$**

It is easily seen that (both for  $n \neq 3$  and  $n = 3$ ):

$$(33) \quad \mathbf{I}_{0,-4,+1}(e=0,\dot{e}=0,n) = \mathbf{I}_0(e=0,\dot{e}=0,n) = \mathbf{I}_0(e=0,\dot{e}=0,n) = \mathbf{I}_{0+}(e=0,\dot{e}=0,n) = 2\pi.$$

Taking into account the correctness of the above equalities, we may apply the analytical representation (12) also in the present case, after performing the transitions

$[e(u) \rightarrow 0] \cap [\dot{e}(u) \rightarrow 0]$  or  $[\dot{e}(u) \rightarrow 0] \cap [e(u) \rightarrow 0]$ . No matter which of the transitions is taken in the first place!

### 2.1.5.1. Case $n = 3$ , $e(u) \neq 0$ , $\dot{e}(u) \neq 0$ , $e(u) - \dot{e}(u) \neq 0$

#### **2.1.5.1.1. A direct computation of the integral $\mathbf{I}_{0,-4,+1}(e,\dot{e},n = 3)$ through the integral $\mathbf{I}_0(e,\dot{e},n = 3)$**

Substituting  $n = 3$  into the definitions (1) – (4), we shall have the following representations for the integrals  $\mathbf{I}_0(e,\dot{e},n = 3)$ ,  $\mathbf{I}_{0,-4,+1}(e,\dot{e},n = 3)$ ,  $\mathbf{I}_{0,+}(e,\dot{e},n = 3)$  and  $\mathbf{I}_0(e,\dot{e},n = 3)$ :

$$(34) \quad \mathbf{I}_0(e,\dot{e},n = 3) = \mathbf{A}_4(e,\dot{e}) = \pi[2 + 3(e - \dot{e})^2][1 - (e - \dot{e})^2]^{-7/2},$$

(formula (9) from paper [5]),

$$(35) \quad \mathbf{I}_{0,+}(e,\dot{e},n = 3) = \int_0^{2\pi} (1 + e \cos \varphi)[1 + (e - \dot{e}) \cos \varphi]^{-5} d\varphi,$$

$$(36) \quad \mathbf{I}_0(e,\dot{e},n = 3) = \int_0^{2\pi} (1 + e \cos \varphi)[1 + (e - \dot{e}) \cos \varphi]^{-4} d\varphi,$$

$$(37) \quad \mathbf{I}_{0,-4,+1}(e,\dot{e},n = 3) = \mathbf{J}_4(e,\dot{e}) = \\ = \pi(-2e^4 + 6e^6 - 6e^8 + 2e^{10} - 14e^5\dot{e} + 28e^7\dot{e} - 14e^9\dot{e} + 7e^4\dot{e}^2 - 49e^6\dot{e}^2 + 42e^8\dot{e}^2 + 35e^5\dot{e}^3 - 70e^7\dot{e}^3 + \\ + 2\dot{e}^4 + 8e^2\dot{e}^4 + 70e^6\dot{e}^4 - 10e\dot{e}^5 - 14e^3\dot{e}^5 - 42e^5\dot{e}^5 + 3\dot{e}^6 + 7e^2\dot{e}^6 + 14e^4\dot{e}^6 - e\dot{e}^7 - 2e^3\dot{e}^7) + \\ + 2\pi e^4 \dot{e}^{-4} (1 - e^2)^{-1/2},$$

(see formula (47) from paper [5] for the explicit writing of the integral  $\mathbf{J}_4(e,\dot{e})$  as a function of the variables  $e(u)$  and  $\dot{e}(u) \equiv de(u)/du$ ).

For the purposes, which will become evident from the consequent exposition of the text, we shall not use directly the above written solution for the integral  $\mathbf{I}_{0,-4,+1}(e,\dot{e},n = 3)$  (37). Instead of that, we begin with a transformation of the first equality in (37), in order to introduce into the right-hand-side of (37) the integral  $\mathbf{I}_0(e,\dot{e},n = 3)$ . We intend further to express the integrals  $\mathbf{I}_{0,+}(e,\dot{e},n = 3)$  and  $\mathbf{I}_0(e,\dot{e},n = 3)$  (for which we do not give until now any explicit solutions in the formulas (35) and (36), respectively) through the later integral  $\mathbf{I}_0(e,\dot{e},n = 3)$ .

$$(38) \quad \mathbf{I}_{0,-4,+1}(e,\dot{e},n = 3) = \int_0^{2\pi} [(1 + e \cos \varphi) - e \cos \varphi](1 + e \cos \varphi)^{-1}[1 + (e - \dot{e}) \cos \varphi]^{-4} d\varphi = \mathbf{I}_0(e,\dot{e},n = 3) - \\ - [e/(e - \dot{e})] \int_0^{2\pi} (1 + e \cos \varphi)^{-1}[1 + (e - \dot{e}) \cos \varphi]^{-3} d\varphi + [e/(e - \dot{e})] \int_0^{2\pi} (1 + e \cos \varphi)^{-1}[1 + (e - \dot{e}) \cos \varphi]^{-4} d\varphi = \\ = \mathbf{I}_0(e,\dot{e},n = 3) - [e/(e - \dot{e})] \mathbf{J}_3(e,\dot{e}) + [e/(e - \dot{e})] \mathbf{I}_{0,-4,+1}(e,\dot{e},n = 3),$$

where we have used the definitions (34) for  $\mathbf{I}_0(e,\dot{e},n = 3) \equiv \mathbf{A}_4(e,\dot{e})$ , (37) for  $\mathbf{I}_{0,-4,+1}(e,\dot{e},n = 3)$  and (40) from paper [5] for the integral  $\mathbf{J}_3(e,\dot{e})$ . Therefore, the above equality (38) gives an expression for the considered integral

$\mathbf{I}_{0,-4,+1}(e,\dot{e},n=3)$ . The division by  $[-\dot{e}/(e-\dot{e})] \neq 0$  (this is ensured for the examined **Case 2.1.5.1**), gives that:

$$(39) \quad \mathbf{I}_{0,-4,+1}(e,\dot{e},n=3) = \mathbf{J}_4(e,\dot{e}) = -[(e-\dot{e})/\dot{e}]\mathbf{I}_{0,(e,\dot{e},n=3)} + (e/\dot{e})\mathbf{J}_3(e,\dot{e}).$$

In the earlier paper [5], we have derived several recurrent relations with respect to the integrals  $\mathbf{J}_1(e,\dot{e})$ ,  $\mathbf{J}_2(e,\dot{e})$  and  $\mathbf{J}_3(e,\dot{e})$ :

$$(40) \quad \mathbf{J}_3(e,\dot{e}) = -[(e-\dot{e})/\dot{e}]\mathbf{A}_3(e,\dot{e}) + (e/\dot{e})\mathbf{J}_2(e,\dot{e}),$$

(first equality from the relation (42) in paper [5]; for brevity's sake, we omit the writing out of the explicit dependence of  $\mathbf{J}_3(e,\dot{e})$  on  $e(u)$  and  $\dot{e}(u)$ , given by the last equality in (42)),

$$(41) \quad \mathbf{J}_2(e,\dot{e}) = -2\pi[(e-\dot{e})/\dot{e}][1-(e-\dot{e})^2]^{-3/2} + (e/\dot{e})\mathbf{J}_1(e,\dot{e}), \quad (\text{formula (33)})$$

from paper [5]).

Of course, we need also of the expression (27) from paper [5], giving the explicit analytical solution for the "initial" integral  $\mathbf{J}_1(e,\dot{e})$ :

$$(42) \quad \mathbf{J}_1(e,\dot{e}) = (2\pi/\dot{e})\{e(1-e^2)^{-1/2} - (e-\dot{e})[1-(e-\dot{e})^2]^{-1/2}\}.$$

It remains to replace, in turn, (42) into (41), and after then (41) into (40), in order to eliminate from the equality (40) the integral  $\mathbf{J}_2(e,\dot{e})$ . But before to make into use this result, intending to resolve for the left-hand-side of the equation (39), we want to derive a presentation of the integral  $\mathbf{A}_3(e,\dot{e})$  through the integral  $\mathbf{I}_{0,(e,\dot{e},n=3)}$ . Let us compute the auxiliary integral  $\mathbf{A}_3(e,\dot{e})$  in the following way:

$$(43) \quad \mathbf{A}_3(e,\dot{e}) = \int_0^{2\pi} [1+(e-\dot{e})\cos\varphi]^{-2} d\varphi - (e-\dot{e}) \int_0^{2\pi} (\cos\varphi)[1+(e-\dot{e})\cos\varphi]^{-3} d\varphi.$$

Earlier we have already found that:

$$(44) \quad \mathbf{A}_2(e,\dot{e}) \equiv \int_0^{2\pi} [1+(e-\dot{e})\cos\varphi]^{-2} d\varphi = 2\pi[1-(e-\dot{e})^2]^{-3/2},$$

(formula (8) from paper [5]). Therefore:

$$(45) \quad \mathbf{A}_3(e,\dot{e}) = 2\pi[1-(e-\dot{e})^2]^{-3/2} - (e-\dot{e}) \int_0^{2\pi} (\cos\varphi)[1+(e-\dot{e})\cos\varphi]^{-3} d\varphi.$$

Developing further the right-hand-side of the above relation (45), we have:

$$(46) \quad \begin{aligned} \mathbf{A}_3(e,\dot{e}) &= 2\pi[1-(e-\dot{e})^2]^{-3/2} - (e-\dot{e}) \int_0^{2\pi} [1+(e-\dot{e})\cos\varphi]^{-3} d(\sin\varphi) = 2\pi[1-(e-\dot{e})^2]^{-3/2} + \\ &+ 3(e-\dot{e})^2 \int_0^{2\pi} [1+(e-\dot{e})\cos\varphi]^{-4} d\varphi + 3 \int_0^{2\pi} \{[1-(e-\dot{e})^2\cos^2\varphi] - 1\} [1+(e-\dot{e})\cos\varphi]^{-4} d\varphi = \\ &= 2\pi[1-(e-\dot{e})^2]^{-3/2} + 3(e-\dot{e})^2 \mathbf{I}_{0,(e,\dot{e},n=3)} + 3 \int_0^{2\pi} [1+(e-\dot{e})\cos\varphi]^{-3} d\varphi - \end{aligned}$$



$$-3(e-\dot{e})\int_0^{2\pi}(\cos\varphi)[1+(e-\dot{e})\cos\varphi]^{-3}d\varphi-3\mathbf{I}_0(e,\dot{e},n=3),$$

where we have used the representation (34) for the integral  $\mathbf{I}_0(e,\dot{e},n=3)$ , when the power  $n=3$ . Consequently, the equalities (46) lead to the result, which can be rewritten as:

$$(47) \quad -2\mathbf{A}_3(e,\dot{e})=2\pi[1-(e-\dot{e})^2]^{-3/2}+3[(e-\dot{e})^2-1]\mathbf{I}_0(e,\dot{e},n=3)-3(e-\dot{e})\int_0^{2\pi}(\cos\varphi)\times \\ \times[1+(e-\dot{e})\cos\varphi]^{-3}d\varphi=-4\pi[1-(e-\dot{e})^2]^{-3/2}+2(e-\dot{e})\int_0^{2\pi}(\cos\varphi)[1+(e-\dot{e})\cos\varphi]^{-3}d\varphi.$$

The second equality in the right-hand-side of (47) follows from (45) (after the multiplication of (45) by  $-2$ ). From (47) we evaluate the integral for which we are looking up. After dividing by  $-5$ , we obtain that:

$$(48) \quad -(e-\dot{e})\int_0^{2\pi}(\cos\varphi)[1+(e-\dot{e})\cos\varphi]^{-3}d\varphi=-(6\pi/5)[1-(e-\dot{e})^2]^{-3/2}+(3/5)[1-(e-\dot{e})^2]\mathbf{I}_0(e,\dot{e},n=3).$$

Substituting the above result (48) into (45), we arrive at the final expression for the integral  $\mathbf{A}_3(e,\dot{e})$ :

$$(49) \quad \mathbf{A}_3(e,\dot{e})=(4\pi/5)[1-(e-\dot{e})^2]^{-3/2}+(3/5)[1-(e-\dot{e})^2]\mathbf{I}_0(e,\dot{e},n=3).$$

Now we are ready to combine the solutions (42), (41) and (49), in order to express the integral  $\mathbf{J}_3(e,\dot{e})$  through the integral  $\mathbf{I}_0(e,\dot{e},n=3)$  by means of the recurrence relation (40). At first, from (42) and (41) it may be evaluated that:

$$(50) \quad \mathbf{J}_2(e,\dot{e})=-2\pi(e-\dot{e})\dot{e}^{-1}[1-(e-\dot{e})^2]^{-3/2}-2\pi e(e-\dot{e})\dot{e}^{-2}[1-(e-\dot{e})^2]^{-1/2}+2\pi e^2\dot{e}^{-2}(1-e^2)^{-1/2}.$$

Then, the relation (40) leads to the expression:

$$(51) \quad \mathbf{J}_3(e,\dot{e})=-\frac{4\pi}{5}(e-\dot{e})\dot{e}^{-1}[1-(e-\dot{e})^2]^{-3/2}-\frac{2\pi e}{5}(e-\dot{e})\dot{e}^{-2}[1-(e-\dot{e})^2]^{-3/2}- \\ -2\pi e^2(e-\dot{e})\dot{e}^{-3}[1-(e-\dot{e})^2]^{-1/2}+2\pi e^3\dot{e}^{-3}(1-e^2)^{-1/2}-(3/5)(e-\dot{e})[1-(e-\dot{e})^2]\dot{e}^{-1}\mathbf{I}_0(e,\dot{e},n=3).$$

Of course, if we replace the analytical expression for the integral  $\mathbf{I}_0(e,\dot{e},n=3)\equiv\mathbf{A}_4(e,\dot{e})=\pi[2+3(e-\dot{e})^2][1-(e-\dot{e})^2]^{-7/2}$  (see the relation (34) in the present paper) into (51), we have to obtain the representation (42) from the paper [5] for the same integral  $\mathbf{J}_3(e,\dot{e})$ . We shall not perform here this checking.

Finally, having available the analytical solution for the integral  $\mathbf{J}_3(e,\dot{e})$ , written into the form (51), we are able to replace it into the equation (39), eliminating thus this integral. Consequently, we conclude that under the conditions, accepted for the considered at present Case 2.1.5.1, the integral  $\mathbf{I}_{0,-4,+1}(e,\dot{e},n=3)$ , which we are seeking for, takes the following form (here we do not use the explicit solution (34)):

$$(52) \quad \mathbf{I}_{0,-4,+1}(e,\dot{e},n=3)=\mathbf{J}_4(e,\dot{e})=-\frac{4\pi}{5}e(e-\dot{e})\dot{e}^{-2}[1-(e-\dot{e})^2]^{-3/2}- \\ -2\pi e^2(e-\dot{e})\dot{e}^{-3}[1-(e-\dot{e})^2]^{-3/2}-2\pi e^3(e-\dot{e})\dot{e}^{-4}[1-(e-\dot{e})^2]^{-1/2}+$$

$$+ 2\pi e^4 \dot{e}^{-4} (1 - e^2)^{-1/2} - [(e - \dot{e})/\dot{e}] \{1 + (3/5)e[1 - (e - \dot{e})^2]\dot{e}^{-1}\} \mathbf{I}_{0,(e,\dot{e},n=3)}.$$

As before, the remark given above, and concerning the replacement in (52) of the integral  $\mathbf{I}_0(e, \dot{e}, n = 3)$  with its analytical solution (34), remains valid also for the present situation. Such a substitution of the relation (34) into (52) leads to the analytical expression for  $\mathbf{J}_4(e, \dot{e})$ , found in the paper [5] (formula (47) in this paper). Again, we shall not check this equivalence of the formulae (52) and (47) in paper [5], because of the brevity reasons.

### 2.1.5.1.2. Evaluation of the integral $\mathbf{I}_{0,-4,+1}(e, \dot{e}, n = 3)$ through the limit transition $n \rightarrow 3$

We have computed the *explicit* analytical expression (52) for the integral  $\mathbf{I}_{0,-4,+1}(e, \dot{e}, n = 3)$ , preserving the existence of the integral  $\mathbf{I}_0(e, \dot{e}, n = 3)$ , unlike the analytical solution (37). Now we ask: are we able to use the relation (12) (derived under the condition  $n \neq 3$ ) in the limit  $n \rightarrow 3$ , to obtain the solution (52)? The later is computed through a *direct* substitution  $n = 3$  into the initial definition (37) for the integral  $\mathbf{I}_{0,-4,+1}(e, \dot{e}, n = 3)$ , in accordance with the *general* definition (4) for the integral  $\mathbf{I}_{0,-4,+1}(e, \dot{e}, n)$ . For this purpose, we shall try to evaluate the integrals  $\mathbf{I}_0(e, \dot{e}, n = 3)$  and  $\mathbf{I}_{0+}(e, \dot{e}, n = 3)$  also by means of the integral  $\mathbf{I}_0(e, \dot{e}, n = 3)$ . This will enable us to check whether the right-hand-side of the equality (12) tends to zero, when  $n$  approaches 3, and then to try to apply the L'Hospital's rule for evaluation of indeterminacies of the type 0/0.

Let us write out the integrals  $\mathbf{I}_0(e, \dot{e}, n = 3)$  and  $\mathbf{I}_{0+}(e, \dot{e}, n = 3)$  through the integral  $\mathbf{I}_0(e, \dot{e}, n = 3)$ . We have the following expression (see definition (36)):

$$(53) \quad \mathbf{I}_0(e, \dot{e}, n = 3) = \int_0^{2\pi} \{ [1 + (e - \dot{e})\cos\varphi] + \dot{e}\cos\varphi \} [1 + (e - \dot{e})\cos\varphi]^{-4} d\varphi = \mathbf{A}_3(e, \dot{e}) + \\ + (\dot{e}/e) \int_0^{2\pi} [(1 + e\cos\varphi) - 1] [1 + (e - \dot{e})\cos\varphi]^{-4} d\varphi = \mathbf{A}_3(e, \dot{e}) + (\dot{e}/e) \mathbf{I}_0(e, \dot{e}, n = 3) - (\dot{e}/e) \mathbf{I}_0(e, \dot{e}, n = 3).$$

From here, we are in a position to find a resolution for the wanted integral  $\mathbf{I}_0(e, \dot{e}, n = 3)$ . After multiplying by  $e/(e - \dot{e}) \neq 0$ , we have:

$$(54) \quad \mathbf{I}_0(e, \dot{e}, n = 3) = [e/(e - \dot{e})] \mathbf{A}_3(e, \dot{e}) - [\dot{e}/(e - \dot{e})] \mathbf{I}_0(e, \dot{e}, n = 3).$$

To finish the solution process, we must replace the analytical representation (49) of the integral  $\mathbf{A}_3(e, \dot{e})$  through the integral  $\mathbf{I}_0(e, \dot{e}, n = 3)$ :

$$(55) \quad \mathbf{I}_0(e, \dot{e}, n = 3) = (4\pi/5)e(e - \dot{e})^{-1} [1 - (e - \dot{e})^2]^{-3/2} + \{ (3/5)e[1 - (e - \dot{e})^2](e - \dot{e})^{-1} - \dot{e}/(e - \dot{e}) \} \mathbf{I}_0(e, \dot{e}, n = 3).$$

Further we compute the integral  $\mathbf{I}_{0+}(e, \dot{e}, n = 3)$  (see definition (35)):

$$(56) \quad \mathbf{I}_{0+}(e, \dot{e}, n = 3) = \int_0^{2\pi} \{ [1 + (e - \dot{e})\cos\varphi] + \dot{e}\cos\varphi \} [1 + (e - \dot{e})\cos\varphi]^{-5} d\varphi = \\ = \mathbf{I}_0(e, \dot{e}, n = 3) + (\dot{e}/e)\mathbf{I}_{0+}(e, \dot{e}, n = 3) - (\dot{e}/e)\mathbf{A}_5(e, \dot{e}),$$

where we have taken into account the definitions (34), (35) and ((19), paper [5]) for the integrals  $\mathbf{I}_0(e, \dot{e}, n = 3)$ ,  $\mathbf{I}_{0+}(e, \dot{e}, n = 3)$  and  $\mathbf{A}_5(e, \dot{e})$ , respectively. From the above derived relation (56) it immediately follows (after a multiplication by  $e/\dot{e}$ ) an expression for the integral  $\mathbf{A}_5(e, \dot{e})$  through the integrals  $\mathbf{I}_0(e, \dot{e}, n = 3)$  and  $\mathbf{I}_{0+}(e, \dot{e}, n = 3)$ :

$$(57) \quad \mathbf{A}_5(e, \dot{e}) \equiv \int_0^{2\pi} [1 + (e - \dot{e})\cos\varphi]^{-5} d\varphi = (e/\dot{e})\mathbf{I}_0(e, \dot{e}, n = 3) - [(e - \dot{e})/\dot{e}]\mathbf{I}_{0+}(e, \dot{e}, n = 3).$$

Let us perform certain transformations of the assumed by us as “basic” integral  $\mathbf{I}_0(e, \dot{e}, n = 3)$ , in order to link it to some other integrals. And thus to establish the sought representation of  $\mathbf{I}_{0+}(e, \dot{e}, n = 3)$  by means of  $\mathbf{I}_0(e, \dot{e}, n = 3)$ . Of course, we may substitute into (57) the already known solution (19) from paper [5] for  $\mathbf{A}_5(e, \dot{e})$ , and express in such a way  $\mathbf{I}_{0+}(e, \dot{e}, n = 3)$  solely by means of  $\mathbf{I}_0(e, \dot{e}, n = 3)$ . But we shall do this in a different manner.

$$(58) \quad \mathbf{I}_0(e, \dot{e}, n = 3) = \int_0^{2\pi} \{ [1 + (e - \dot{e})\cos\varphi] - (e - \dot{e})\cos\varphi \} [1 + (e - \dot{e})\cos\varphi]^{-4} d\varphi = \mathbf{A}_3(e, \dot{e}) + \\ + 4(e - \dot{e})^2 \int_0^{2\pi} (1 - \cos^2\varphi) [1 + (e - \dot{e})\cos\varphi]^{-5} d\varphi = \mathbf{A}_3(e, \dot{e}) + 4(e - \dot{e})^2 \mathbf{A}_5(e, \dot{e}) + 4 \int_0^{2\pi} [1 - (e - \dot{e})\cos\varphi] \times \\ \times [1 + (e - \dot{e})\cos\varphi] [1 + (e - \dot{e})\cos\varphi]^{-5} d\varphi - 4 \int_0^{2\pi} [1 + (e - \dot{e})\cos\varphi]^{-5} d\varphi = \mathbf{A}_3(e, \dot{e}) - \\ - 4[1 - (e - \dot{e})^2] \mathbf{A}_5(e, \dot{e}) + 4 \int_0^{2\pi} [1 + (e - \dot{e})\cos\varphi]^{-4} d\varphi - 4 \int_0^{2\pi} \{ [1 + (e - \dot{e})\cos\varphi] - 1 \} \times \\ \times [1 + (e - \dot{e})\cos\varphi]^{-4} d\varphi = -3\mathbf{A}_3(e, \dot{e}) - 4[1 - (e - \dot{e})^2] \mathbf{A}_5(e, \dot{e}) + 8\mathbf{I}_0(e, \dot{e}, n = 3),$$

where, evidently, we have used the definitions (16) and (19) from paper [5] for  $\mathbf{A}_3(e, \dot{e})$  and  $\mathbf{A}_5(e, \dot{e})$ , and (34) for  $\mathbf{I}_0(e, \dot{e}, n = 3) \equiv \mathbf{A}_4(e, \dot{e})$ . Consequently, we have:

$$(59) \quad 7\mathbf{I}_0(e, \dot{e}, n = 3) = 3\mathbf{A}_3(e, \dot{e}) + 4[1 - (e - \dot{e})^2] \mathbf{A}_5(e, \dot{e}).$$

At present, it remains to substitute into this equality (59) the earlier derived results (49) for  $\mathbf{A}_3(e, \dot{e})$  and (57) for  $\mathbf{A}_5(e, \dot{e})$ . The division by  $4[1 - (e - \dot{e})^2] \neq 0$  gives:

$$(60) \quad (7/4)[1 - (e - \dot{e})^2]^{-1} \mathbf{I}_0(e, \dot{e}, n = 3) - (3\pi/5)[1 - (e - \dot{e})^2]^{-5/2} - (9/20) \mathbf{I}_0(e, \dot{e}, n = 3) - \\ - (e/\dot{e})\mathbf{I}_0(e, \dot{e}, n = 3) = -[(e - \dot{e})/\dot{e}]\mathbf{I}_{0+}(e, \dot{e}, n = 3).$$

From here, it is easy to establish the following linear relation between the integrals  $\mathbf{I}_0(e, \dot{e}, n = 3)$  and  $\mathbf{I}_{0+}(e, \dot{e}, n = 3)$ :

$$(61) \quad \mathbf{I}_{0+}(e, \dot{e}, n = 3) = (3\pi/5)\dot{e}(e - \dot{e})^{-1}[1 - (e - \dot{e})^2]^{-5/2} +$$

$$+ [\dot{e}/(e - \dot{e})]\{(9/20) + (e/\dot{e}) - (7/4)[1 - (e - \dot{e})^2]^{-1}\}\mathbf{I}_{0_{-}}(e, \dot{e}, n = 3).$$

The derived above linear dependence (61) between the integrals  $\mathbf{I}_{0_{-}}(e, \dot{e}, n = 3)$  and  $\mathbf{I}_{0_{+}}(e, \dot{e}, n = 3)$  is remarkable with the conclusion that at least under the conditions (which are supposed during the evaluation (61))  $n = 3$ ,  $e(u) \neq 0$ ,  $\dot{e}(u) \neq 0$  and  $e(u) - \dot{e}(u) \neq 0$  (i.e., Case 2.1.5.1) we already know the answer of the problem, which we are seeking for. Yes, the integrals  $\mathbf{I}_{0_{-}}(e, \dot{e}, n = 3)$  and  $\mathbf{I}_{0_{+}}(e, \dot{e}, n = 3)$  are linearly depended! Such a finding is not surprising in view of the established earlier [8] analytical solutions for the integrals  $\mathbf{I}_{0_{-}}(e, \dot{e}, n)$  and  $\mathbf{I}_{0_{+}}(e, \dot{e}, n)$  for integer powers  $n$  ( $n = -1, 0, 1, 2, 3$ ). If we take the results for  $n = 3$ :

$$(62) \quad \mathbf{I}_{0_{+}}(e, \dot{e}, n = 3) = (\pi/4)(8e + 4e^3 - 12e^5 - 8\dot{e} - 32e^2\dot{e} + 45e^4\dot{e} + 52e\dot{e}^2 - 60e^3\dot{e}^2 - 24\dot{e}^3 + 30e^2\dot{e}^3 - 3\dot{e}^5)(e - \dot{e})^{-1}[1 - (e - \dot{e})^2]^{-9/2}, \quad (\text{formula (6g)})$$

from paper [8]),

$$(63) \quad \mathbf{I}_{0_{-}}(e, \dot{e}, n = 3) = \pi[2 + 3(e - \dot{e})^2][1 - (e - \dot{e})^2]^{-7/2}, \quad (\text{formula (6h)})$$

from paper [8]).

The linear relation (61) between the integrals  $\mathbf{I}_{0_{-}}(e, \dot{e}, n = 3)$  and  $\mathbf{I}_{0_{+}}(e, \dot{e}, n = 3)$  is fully consistent with the analytical expressions (62) and (63) for these functions of  $e(u)$ ,  $\dot{e}(u)$  and the (fixed) power  $n = 3$ . Similar conclusions about the existence of a linear dependence between  $\mathbf{I}_{0_{-}}(e, \dot{e}, n)$  and  $\mathbf{I}_{0_{+}}(e, \dot{e}, n)$  can be made also for the other (fixed) integer values of the power  $n$  in the viscosity law  $\eta = \beta\Sigma^n$ : for  $n = -1$  (see formulas (2g) and (2h) from paper [8]; for  $n = 0$  (see formulas (3g) and (3h) from paper [8]); for  $n = +1$  (see formulas (4g) and (4h) from paper [8]) and  $n = +2$  (see formulas (5g) and (5h) from paper [8]). *We shall not enter here into a discussion about the explicit analytical form of the later pointed out linear functional dependences. Nor yet about their validity, as regards to the possible troubles for "peculiar" (i.e., vanishing some denominators of the expressions) values  $e(u) = 0$ ,  $\dot{e}(u) = 0$ , and  $e(u) - \dot{e}(u) = 0$ .* We postpone such a debate for later considerations. Our dominant aim now is to prepare to solve the problem of the existence of linear relation between the integrals  $\mathbf{I}_{0_{-}}(e, \dot{e}, n)$  and  $\mathbf{I}_{0_{+}}(e, \dot{e}, n)$  for *arbitrary* (physically reasonable) values of the power  $n$ . Of course, we remind that for every concrete accretion disc model,  $n$  remains a *preliminary fixed quantity* throughout the *whole* disc [1].

Let us compute the right-hand-side of the relation (12), in order to check its nullification for the *particular value*  $n = 3$ . We shall apply the results (55) and (61) for the integrals  $\mathbf{I}_{0_{-}}(e, \dot{e}, n = 3)$  and  $\mathbf{I}_{0_{+}}(e, \dot{e}, n = 3)$ , respectively:

$$(64) \quad [1 + 4(1 - e^2)(e - \dot{e})\dot{e}^{-1}]\mathbf{I}_{0_{-}}(e, \dot{e}, n = 3) - 4[(1 - e^2)(e - \dot{e})^2e^{-1}\dot{e}^{-1} + (2e - \dot{e})e^{-1}]\mathbf{I}_{0_{+}}(e, \dot{e}, n = 3) + 3\mathbf{I}_{0_{-}}(e, \dot{e}, n = 3) = - (12\pi/5)(e^2 - 2e\dot{e} + \dot{e}^2 - e^4 + 2e^3\dot{e} - e^2\dot{e}^2 + 2e\dot{e} - \dot{e}^2)e^{-1}(e - \dot{e})^{-1} \times$$

$$\begin{aligned}
& \times [1 - (e - \dot{e})^2]^{-5/2} + (12\pi/5)e(1 - e^2 + 2e\dot{e} - \dot{e}^2)(e - \dot{e})^{-1}[1 - (e - \dot{e})^2]^{-5/2} + \\
& + \{(\dot{e} + 4e - 4\dot{e} - 4e^3 + 4e^2\dot{e})\dot{e}^{-1} - 4(e^2 - e^4 + 2e^3\dot{e} - e^2\dot{e}^2)e^{-1}(e - \dot{e})^{-1}\} \times \\
& \times \{(9/20) + (e/\dot{e}) - (7/4)[1 - (e - \dot{e})^2]^{-1}\} + (9/5)e[1 - (e - \dot{e})^2](e - \dot{e})^{-1} - 3\dot{e}(e - \dot{e})^{-1}\} \mathbf{I}_0(e, \dot{e}, n = 3) = \\
& = \{20\dot{e}^2(e - \dot{e})[1 - (e - \dot{e})^2]^{-1}\}^{-1} \{20\dot{e}(e - \dot{e})[1 - (e - \dot{e})^2](4e - 4e^3 - 3\dot{e} + 4e\dot{e}) + \\
& + 4\dot{e}(-e + e^3 - 2e^2\dot{e} + e\dot{e}^2)\{9\dot{e}[1 - (e - \dot{e})^2] + 20e[1 - (e - \dot{e})^2] - 35\dot{e}\} + 36e\dot{e}^2(1 - e^2 + 2e\dot{e} - \dot{e}^2)^2 - \\
& - 60\dot{e}^3[1 - (e - \dot{e})^2]\} \mathbf{I}_0(e, \dot{e}, n = 3) = \{20\dot{e}^2(e - \dot{e})[1 - (e - \dot{e})^2]^{-1}\} \times 0 \times \mathbf{I}_0(e, \dot{e}, n = 3) \equiv 0.
\end{aligned}$$

To arrive to this zero result, we have taken into account (after some elementary algebra), that the multiplier of the integral  $\mathbf{I}_0(e, \dot{e}, n = 3)$  into the square brackets is identically equal to zero. The same conclusion can be made also for the “free” term (i.e., the term without the integral  $\mathbf{I}_0(e, \dot{e}, n = 3)$ ) in view of the identity:  $(-e + e^3 - 2e^2\dot{e} + e\dot{e}^2 + e - e^3 + 2e^2\dot{e} - e\dot{e}^2) \equiv 0$ .

That is why, the combination of these two equal to zero multipliers leads to the final nullification of the right-hand-side of the equality (12) for  $n = 3$ :

$$\begin{aligned}
(65) \quad \lim_{n \rightarrow 3} \{ & [(2n - 5) + (n + 1)(1 - e^2)(e - \dot{e})\dot{e}^{-1}] \mathbf{I}_0(e, \dot{e}, n) - (n + 1)[(1 - e^2)(e - \dot{e})^2(e\dot{e})^{-1} + \\
& + (2e - \dot{e})/e] \mathbf{I}_{0+}(e, \dot{e}, n) + 3\mathbf{I}_0(e, \dot{e}, n) \} = 0.
\end{aligned}$$

This evaluation (65) indicates that we are able to attempt to compute the integral  $\mathbf{I}_{0,-4,+1}(e, \dot{e}, n = 3)$  not only through a *direct* substitution  $n = 3$  into its definition (4) (see also formula (37)), but also from the relation (12), using the limit transition  $n \rightarrow 3$ , in order to overcome the indeterminacy of the type 0/0. The reasoning to perform such a *duplicating* evaluation of the integral  $\mathbf{I}_{0,-4,+1}(e, \dot{e}, n = 3)$  is to show the *universality* of (12), i.e., that it remains valuable even in the case  $n = 3$ , despite of the necessity to interpret it through the limit transition  $n \rightarrow 3$ . With the invitation of the L’Hospital’s rule for resolving of the indeterminacies of the type 0/0. The conditions for applicability of this theorem are formulated in the textbooks on analysis and are also adduced for clearness in paper [5]. One of them (in our concrete task) is fulfilled by virtue of the established result (65). Other condition concerns the multiplier  $(n - 3)(1 - e^2)$  into the left-hand-side of the equality (12), which, in fact, must be considered as a factor into the denominator in the right-hand-side of (12). If we regard (12) as a solution for the integral  $\mathbf{I}_{0,-4,+1}(e, \dot{e}, n = 3)$ . Specifically:

$$(66) \quad \lim_{n \rightarrow 3} \{ \partial[(n - 3)(1 - e^2)] / \partial n \} = \lim_{n \rightarrow 3} (1 - e^2) = 1 - e^2 \neq 0,$$

because  $|e(u)| < 1$ . It is easily verified that the remaining conditions, for the applicability of the L’Hospital’s theorem, are available. But only if, at first, we have already computed the limit transition  $n \rightarrow 3$  of the derivative with respect to  $n$  of the right-hand-side of the solution (12) for  $\mathbf{I}_{0,-4,+1}(e, \dot{e}, n)$ . As we shall see now, the later evaluations *are not* too problemless for resolving. We just now start to resolve this task. We begin with the finding

of the derivative with respect to the power  $n$  of the right-hand-side of the equality (12) and then take the limit  $n \rightarrow 3$ :

$$\begin{aligned}
(67) \quad & \partial/\partial n \{ [(2n-5) + (n+1)(1-e^2)(e-\dot{e})\dot{e}^{-1}] \mathbf{I}_0(e, \dot{e}, n) - (n+1)[(1-e^2)(e-\dot{e})^2(e\dot{e})^{-1} + \\
& + (2e-\dot{e})/e] \mathbf{I}_{0+}(e, \dot{e}, n) + 3\mathbf{I}_0(e, \dot{e}, n) \} \xrightarrow{n \rightarrow 3} [2 + (1-e^2)(e-\dot{e})\dot{e}^{-1}] \int_0^{2\pi} [1 + (e-\dot{e})\cos\varphi]^{-4} d\varphi - \\
& - [(1-e^2)(e-\dot{e})^2(e\dot{e})^{-1} + (2e-\dot{e})/e] \int_0^{2\pi} (1 + e\cos\varphi)[1 + (e-\dot{e})\cos\varphi]^{-5} d\varphi + \\
& + [1 + (1-e^2)(e-\dot{e})\dot{e}^{-1}] \int_0^{2\pi} [1 + (e-\dot{e})\cos\varphi]^{-4} \{ \ln\{(1 + e\cos\varphi)[1 + (e-\dot{e})\cos\varphi]^{-1}\} \} d\varphi - \\
& - 4[(1-e^2)(e-\dot{e})^2(e\dot{e})^{-1} + (2e-\dot{e})/e] \int_0^{2\pi} (1 + e\cos\varphi)[1 + (e-\dot{e})\cos\varphi]^{-5} \times \\
& \times \{ \ln\{(1 + e\cos\varphi)[1 + (e-\dot{e})\cos\varphi]^{-1}\} \} d\varphi + 3 \int_0^{2\pi} (1 + e\cos\varphi)[1 + (e-\dot{e})\cos\varphi]^{-4} \times \\
& \times \{ \ln\{(1 + e\cos\varphi)[1 + (e-\dot{e})\cos\varphi]^{-1}\} \} d\varphi \equiv \mathbf{C}(e, \dot{e}).
\end{aligned}$$

In deriving of the above equality, we have taken into account the definitions (1), (2) and (3) for the integrals  $\mathbf{I}_0(e, \dot{e}, n)$ ,  $\mathbf{I}_{0+}(e, \dot{e}, n)$  and  $\mathbf{I}_0(e, \dot{e}, n)$ , respectively. We also have used from the analysis the well-known differentiation formula:

$$(68) \quad d(a^x)/dx = a^x \ln(a); \quad a > 0,$$

where the basis  $a > 0$  does not depend on the variable  $x$ . From this rule immediately follows that if we have the constants  $a > 0$ ,  $b > 0$ ,  $y$  and  $z$ , then we can write:

$$\begin{aligned}
(69) \quad & d/dx(a^{y+x}/b^{z+x}) \equiv d/dx(a^{y+x}b^{-z-x}) = (a^{y+x}/b^{z+x})\ln(a) + (a^{y+x}/b^{z+x})[\ln(b)]d(-x)/dx = \\
& = (a^{y+x}/b^{z+x})[\ln(a) - \ln(b)] \equiv (a^{y+x}/b^{z+x})\ln(a/b).
\end{aligned}$$

The above rule is applied, when the differentiation with respect to the power  $n$  of the integrands of the integrals  $\mathbf{I}_0(e, \dot{e}, n)$ ,  $\mathbf{I}_{0+}(e, \dot{e}, n)$  and  $\mathbf{I}_0(e, \dot{e}, n)$  has been performed. To continue the analytical evaluation of the right-hand-side of the relation (67) (which, after the transition  $n \rightarrow 3$ , we denote briefly by  $\mathbf{C}(e, \dot{e})$ ), we have to return to certain auxiliary results, *derived especially for the present investigation*. They are published in papers [6] and [7], and are dealing with the analytical computations of the integrals  $\mathbf{L}_i(e, \dot{e})$  ( $i = 0, 1, 2, 3$ ) and  $\mathbf{K}_i(e, \dot{e})$  ( $i = 1, 2, 3, 4, 5$ ), (see their definitions (17) and (18), respectively). We do not rewrite here these solutions, and also the expressions for some of the *particular* values for the first and second arguments of  $\mathbf{K}_i(e, \dot{e})$  ( $i = 1, 2, 3, 4, 5$ ). Namely,  $\mathbf{K}_i(e, 0)$  ( $i = 1, 2, 3, 4, 5$ ) and  $\mathbf{K}_i(e - \dot{e}, 0)$  ( $i = 3, 4, 5$ ) [7]. We only refer to these (to some extend) long formulas in paper [7], in order to avoid the unnecessary

overload of the our exposition. With the above remarks, we write from (67) that:

$$(70) \quad \begin{aligned} \mathbf{C}(e, \dot{e}) &= (e - e^3 + \dot{e} + e^2 \dot{e}) \dot{e}^{-1} \mathbf{A}_4(e, \dot{e}) + (-e + e^3 - 2e^2 \dot{e} + e \dot{e}^2) \dot{e}^{-1} \mathbf{A}_5(e, \dot{e}) + \\ &+ \{e/[\dot{e}(e - \dot{e})]\}(-e + e^3 - 2e^2 \dot{e} + e \dot{e}^2) \mathbf{A}_4(e, \dot{e}) - \{e/[\dot{e}(e - \dot{e})]\}(-e + e^3 - 2e^2 \dot{e} + e \dot{e}^2) \mathbf{A}_5(e, \dot{e}) + \\ &+ (4e - 4e^3 - 3\dot{e} + 4e^2 \dot{e}) \dot{e}^{-1} \mathbf{K}_4(e, \dot{e}) - (4e - 4e^3 - 3\dot{e} + 4e^2 \dot{e}) \dot{e}^{-1} \mathbf{K}_4(e, \dot{e}) + \\ &+ (-4e + 4e^3 - 8e^2 \dot{e} + 4e \dot{e}^2) \dot{e}^{-1} \mathbf{K}_5(e, \dot{e}) + \\ &+ \{e/[\dot{e}(e - \dot{e})]\}(-4e + 4e^3 - 8e^2 \dot{e} + 4e \dot{e}^2) \mathbf{K}_4(e, \dot{e}) - \{e/[\dot{e}(e - \dot{e})]\}(-4e + 4e^3 - 8e^2 \dot{e} + \\ &+ 4e \dot{e}^2) \mathbf{K}_5(e, \dot{e}) - \\ &- (-4e + 4e^3 - 8e^2 \dot{e} + 4e \dot{e}^2) \dot{e}^{-1} \mathbf{K}_5(e - \dot{e}, 0) - \\ &- \{e/[\dot{e}(e - \dot{e})]\}(-4e + 4e^3 - 8e^2 \dot{e} + 4e \dot{e}^2) \mathbf{K}_4(e - \dot{e}, 0) + \\ &+ \{e/[\dot{e}(e - \dot{e})]\}(-4e + 4e^3 - 8e^2 \dot{e} + 4e \dot{e}^2) \mathbf{K}_5(e - \dot{e}, 0) + 3\mathbf{K}_4(e, \dot{e}) + 3\{e/(e - \dot{e})\} \mathbf{K}_3(e, \dot{e}) - \\ &- 3\{e/(e - \dot{e})\} \mathbf{K}_4(e, \dot{e}) - 3\mathbf{K}_4(e - \dot{e}, 0) - 3\{e/(e - \dot{e})\} \mathbf{K}_3(e - \dot{e}, 0) + 3\{e/(e - \dot{e})\} \mathbf{K}_4(e - \dot{e}, 0) = \\ &= [e/(e - \dot{e})][1 - (e - \dot{e})^2] \mathbf{A}_5(e, \dot{e}) - [\dot{e}/(e - \dot{e})] \mathbf{A}_4(e, \dot{e}) + 4\{e/(e - \dot{e})\}[1 - (e - \dot{e})^2] \mathbf{K}_5(e, \dot{e}) - \\ &- 7\{e/(e - \dot{e})\} \mathbf{K}_4(e, \dot{e}) + 3\{e/(e - \dot{e})\} \mathbf{K}_3(e, \dot{e}) - 4\{e/(e - \dot{e})\}[1 - (e - \dot{e})^2] \mathbf{K}_5(e - \dot{e}, 0) + \\ &+ 7\{e/(e - \dot{e})\} \mathbf{K}_4(e - \dot{e}, 0) - 3\{e/(e - \dot{e})\} \mathbf{K}_3(e - \dot{e}, 0). \end{aligned}$$

At present, we are in a position to substitute into the last equality of the above relation the corresponding analytical evaluations for the integrals  $\mathbf{A}_4(e, \dot{e})$  (formula (9) from paper [5]),  $\mathbf{A}_5(e, \dot{e})$  (formula (19) from paper [5]),  $\mathbf{K}_3(e, \dot{e})$  (formula (18) from paper [7]),  $\mathbf{K}_4(e, \dot{e})$  (formula (20) from paper [7]),  $\mathbf{K}_5(e, \dot{e})$  (formula (22) from paper [7]),  $\mathbf{K}_3(e - \dot{e}, 0)$  (formula (31) from paper [7] with the replacement  $e \rightarrow e - \dot{e}$ ),  $\mathbf{K}_4(e - \dot{e}, 0)$  (formula (34) from paper [7] with the replacement  $e \rightarrow e - \dot{e}$ ) and  $\mathbf{K}_5(e - \dot{e}, 0)$  (formula (36) from paper [7] with the replacement  $e \rightarrow e - \dot{e}$ ). Therefore:

$$(71) \quad \begin{aligned} \mathbf{C}(e, \dot{e}) &= (e - \dot{e})^{-1} \{(\pi/4)e[1 - (e - \dot{e})^2][8 + 24(e - \dot{e})^2 + 3(e - \dot{e})^4][1 - (e - \dot{e})^2]^{-9/2} - \\ &- \pi \dot{e}[2 + 3(e - \dot{e})^2][1 - (e - \dot{e})^2]^{-7/2} + 4e(\pi/4)[1 - (e - \dot{e})^2](8 + 24e^2 + 3e^4 - 48e\dot{e} - \\ &- 12e^3 \dot{e} + 24\dot{e}^2 + 18e^2 \dot{e}^2 - 12e\dot{e}^3 + 3\dot{e}^4)[1 - (e - \dot{e})^2]^{-9/2} \ln \mathbf{Z}(e - \dot{e}, 0) + (4\pi/6)e[1 - (e - \dot{e})^2] \times \\ &\times (-3e^4 + 9e^6 - 9e^8 + 3e^{10} - 4e^3 \dot{e} - 10e^5 \dot{e} + 32e^7 \dot{e} - 18e^9 \dot{e} - 6e^2 \dot{e}^2 - 4e^4 \dot{e}^2 - 35e^6 \dot{e}^2 + 45e^8 \dot{e}^2 - \\ &- 12e\dot{e}^3 - 16e^3 \dot{e}^3 - 60e^5 \dot{e}^3 + 39e^7 \dot{e}^4 + 25e^9 \dot{e}^4 + 45e^5 \dot{e}^4 - 18e\dot{e}^5 - 16e^3 \dot{e}^5 - 18e^5 \dot{e}^5 + 3e^2 \dot{e}^6 + 3e^4 \dot{e}^6) \times \\ &\times \dot{e}^{-4} [1 - (e - \dot{e})^2]^{-7/2} + (4\pi/12)e[1 - (e - \dot{e})^2](6e^4 - 24e^6 + 36e^8 - 24e^{10} + 6e^{12} + 8e^3 \dot{e} + 18e^5 \dot{e} - \\ &- 102e^7 \dot{e} + 118e^9 \dot{e} - 42e^{11} \dot{e} + 12e^2 \dot{e}^2 + e^4 \dot{e}^2 + 88e^6 \dot{e}^2 - 227e^8 \dot{e}^2 + 126e^{10} \dot{e}^2 + 24e\dot{e}^3 + 16e^3 \dot{e}^3 - \\ &- 35e^5 \dot{e}^3 + 205e^7 \dot{e}^3 - 210e^9 \dot{e}^3 - 50\dot{e}^4 - 138e^2 \dot{e}^4 + 48e^4 \dot{e}^4 - 70e^6 \dot{e}^4 + 210e^8 \dot{e}^4 + 182e\dot{e}^5 - 40e^3 \dot{e}^5 - \\ &- 16e^5 \dot{e}^5 - 126e^7 \dot{e}^5 - 55\dot{e}^6 - 4e^2 \dot{e}^6 + 17e^4 \dot{e}^6 + 42e^6 \dot{e}^6 + 9e\dot{e}^7 - 3e^3 \dot{e}^7 - 6e^5 \dot{e}^7) \dot{e}^{-4} [1 - (e - \dot{e})^2]^{-4} \times \\ &\times (1 - e^2)^{-1/2} + (20\pi/12)e[1 - (e - \dot{e})^2](10 + 11e^2 - 22e\dot{e} + 11\dot{e}^2)[1 - (e - \dot{e})^2]^{-4} - \\ &- 7\pi e(2 + 3e^2 - 6e\dot{e} + 3\dot{e}^2)[1 - (e - \dot{e})^2]^{-7/2} \ln \mathbf{Z}(e - \dot{e}, 0) - (7\pi/3)e(-2e^3 + 4e^5 - 2e^7 - 3e^2 \dot{e} - 5e^4 \dot{e} + \\ &+ 8e^6 \dot{e} - 6e\dot{e}^2 - 5e^3 \dot{e}^2 - 12e^5 \dot{e}^2 - 2e^3 + 9e^2 \dot{e}^3 + 8e^4 \dot{e}^3 - 3e\dot{e}^4 - 2e^3 \dot{e}^4) \dot{e}^{-3} [1 - (e - \dot{e})^2]^{-5/2} - \\ &- (7\pi/3)e(2e^3 - 6e^5 + 6e^7 - 2e^9 + 3e^2 \dot{e} + 4e^4 \dot{e} - 17e^6 \dot{e} + 10e^8 \dot{e} + 6e\dot{e}^2 + e^3 \dot{e}^2 + 13e^5 \dot{e}^2 - 20e^7 \dot{e}^2 - 11\dot{e}^3 - \\ &- 12e^2 \dot{e}^3 + 3e^4 \dot{e}^3 + 20e^6 \dot{e}^3 + 17e\dot{e}^4 - 7e^3 \dot{e}^4 - 10e^5 \dot{e}^4 - 4e^5 + 2e^2 \dot{e}^5 + 2e^4 \dot{e}^5) \dot{e}^{-3} [1 - (e - \dot{e})^2]^{-3} \times \\ &\times (1 - e^2)^{-1/2} - (14\pi/3)e[1 - (e - \dot{e})^2]^{-5/2} - (7\pi/3)e(11 + 4e^2 - 8e\dot{e} + 4\dot{e}^2)[1 - (e - \dot{e})^2]^{-3} + \\ &+ 3\pi e(2 + e^2 - 2e\dot{e} + \dot{e}^2)[1 - (e - \dot{e})^2]^{-5/2} \ln \mathbf{Z}(e - \dot{e}, 0) + 3\pi e(-e^2 + 2e^4 - e^6 - 2e\dot{e} - 2e^3 \dot{e} + 4e^5 \dot{e} - \\ &- 2e^2 \dot{e}^2 - 6e^4 \dot{e}^2 + 2e\dot{e}^3 + 4e^3 \dot{e}^3 - e^2 \dot{e}^4) \dot{e}^{-2} [1 - (e - \dot{e})^2]^{-5/2} + \\ &+ 3\pi e(e^2 - 2e^4 + e^6 + 2e\dot{e} + e^3 \dot{e} - 3e^5 \dot{e} - 3e^2 + 3e^4 \dot{e}^2 + e\dot{e}^3 - e^3 \dot{e}^3) \dot{e}^{-2} [1 - (e - \dot{e})^2]^{-2} (1 - e^2)^{-1/2} + \\ &+ 9\pi e[1 - (e - \dot{e})^2]^{-2} - (4\pi/48)e[1 - (e - \dot{e})^2][(96 + 288(e - \dot{e})^2 + 36(e - \dot{e})^4)][1 - (e - \dot{e})^2]^{-9/2} \times \\ &\times \ln \mathbf{Z}(e - \dot{e}, 0) - (4\pi/48)e[1 - (e - \dot{e})^2]\{-200 - 312(e - \dot{e})^2 - 21(e - \dot{e})^4 + [200 + 220(e - \dot{e})^2] \times \\ &\times [1 - (e - \dot{e})^2]^{1/2}\}[1 - (e - \dot{e})^2]^{-9/2} + (7\pi/6)e[12 + 18(e - \dot{e})^2][1 - (e - \dot{e})^2]^{-7/2} \ln \mathbf{Z}(e - \dot{e}, 0) + \\ &+ (7\pi/6)e\{-22 - 15(e - \dot{e})^2 + [22 + 8(e - \dot{e})^2][1 - (e - \dot{e})^2]^{1/2}\}[1 - (e - \dot{e})^2]^{-7/2} - \\ &- (3\pi/2)e[4 + 2(e - \dot{e})^2][1 - (e - \dot{e})^2]^{-5/2} \ln \mathbf{Z}(e - \dot{e}, 0) - (3\pi/2)e\{-6 - (e - \dot{e})^2 + 6[1 - (e - \dot{e})^2]^{1/2}\} \times \\ &\times [1 - (e - \dot{e})^2]^{-5/2}\}. \end{aligned}$$

In the above equality we have used the notation  $\mathbf{Z}(e, \dot{e})$ , introduced in the paper [7] (formula (23) in paper [7]). If we accept for the first argument of this function the difference  $e(u) - \dot{e}(u)$ , and a constant zero value for the second argument, it is easy to see (formula (24) from paper [7] with the replacement  $e \rightarrow e - \dot{e}$ ) that:

$$(72) \quad \mathbf{Z}(e - \dot{e}, 0) = 2\{2 - 3(e - \dot{e})^2 + (e - \dot{e})^4 - 2[1 - (e - \dot{e})^2]^{3/2}\}(e - \dot{e})^{-2}\{1 - [1 - (e - \dot{e})^2]^{1/2}\}^{-1}.$$

The long expression (71) for the function  $\mathbf{C}(e, \dot{e})$  may be simplified, if we notice that the coefficient, multiplying the sum of the six terms with the logarithmic function  $\ln \mathbf{Z}(e - \dot{e}, 0)$ , is *exactly equal to zero*. Even more: the coupling of such terms by triplets with common coefficients shows that the later are also with zero values. Let us prove this statement. Combining in (71) the 3<sup>rd</sup>, the 7<sup>th</sup> and the 12<sup>th</sup> terms together, and also the 16<sup>th</sup>, the 18<sup>th</sup> the 20<sup>th</sup> terms by triplets, we obtain also a zero sum.

Rejecting the above mentioned six terms (because of their zero contribution), we further simplify the expression for  $\mathbf{C}(e, \dot{e})$ , which already does not contain any logarithmic functions. After some algebraic transformations of the remaining 15 terms, we arrive at the final conclusion:

$$(73) \quad \lim_{n \rightarrow 3} \{\partial/\partial n \{[(2n - 5) + (n + 1)(1 - e^2)(e - \dot{e})e^{-1}] \mathbf{I}_0(e, \dot{e}, n) - (n + 1)[(1 - e^2)(e - \dot{e})^2(e\dot{e})^{-1} + (2e - \dot{e})/e] \mathbf{I}_0(e, \dot{e}, n) + 3 \mathbf{I}_0(e, \dot{e}, n)\} \} \equiv \mathbf{C}(e, \dot{e}) = \pi(1 - e^2)(e - \dot{e})(-2e^3 + 6e^5 - 6e^7 + 2e^9 - 2e^2\dot{e} - 8e^4\dot{e} + 22e^6\dot{e} - 12e^8\dot{e} - 2e\dot{e}^2 - e^3\dot{e}^2 - 27e^5\dot{e}^2 + 30e^7\dot{e}^2 - 2e^3\dot{e}^3 - e^2\dot{e}^3 + 8e^4\dot{e}^3 - 40e^6\dot{e}^3 + 7e\dot{e}^4 + 8e^3\dot{e}^4 + 30e^5\dot{e}^4 - 3\dot{e}^5 - 6e^2\dot{e}^5 - 12e^4\dot{e}^5 + e\dot{e}^6 + 2e^3\dot{e}^6)\dot{e}^{-4}[1 - (e - \dot{e})^2]^{-7/2} + 2\pi e^4(1 - e^2)\dot{e}^{-4}(1 - e^2)^{-1/2}.$$

Taking into account the transition (66), we have from the relation (12) (after a division by  $(1 - e^2) \neq 0$ ), that:

$$(74) \quad \lim_{n \rightarrow 3} \mathbf{I}_{0,-4,+1}(e, \dot{e}, n) \equiv \lim_{n \rightarrow 3} \{ \int_0^{2\pi} (1 + e \cos \varphi)^{n-4} [1 + (e - \dot{e}) \cos \varphi]^{-n-1} d\varphi \} = \pi(e - \dot{e})(-2e^3 + 6e^5 - 6e^7 + 2e^9 - 2e^2\dot{e} - 8e^4\dot{e} + 22e^6\dot{e} - 12e^8\dot{e} - 2e\dot{e}^2 - e^3\dot{e}^2 - 27e^5\dot{e}^2 + 30e^7\dot{e}^2 - 2e^3\dot{e}^3 - e^2\dot{e}^3 + 8e^4\dot{e}^3 - 40e^6\dot{e}^3 + 7e\dot{e}^4 + 8e^3\dot{e}^4 + 30e^5\dot{e}^4 - 3\dot{e}^5 - 6e^2\dot{e}^5 - 12e^4\dot{e}^5 + e\dot{e}^6 + 2e^3\dot{e}^6)\dot{e}^{-4}[1 - (e - \dot{e})^2]^{-7/2} + 2\pi e^4\dot{e}^{-4}(1 - e^2)^{-1/2} \int_0^{2\pi} (1 + e \cos \varphi)^{-1} [1 + (e - \dot{e}) \cos \varphi]^{-4} d\varphi \equiv \mathbf{I}_{0,-4,+1}(e, \dot{e}, n = 3).$$

The above expression coincides with the expression for the integral  $\mathbf{I}_{0,-4,+1}(e, \dot{e}, n = 3) \equiv \mathbf{J}_4(e, \dot{e})$  (formula (37), which is, in fact, the result (47), derived in the paper [5]). This means that the transition  $n \rightarrow 3$  in the solution (13) is continuous. And it is possible to use this linear relation even for  $n = 3$ , having in mind that we have to apply, in this connection, the L'Hospital's rule for resolving of indeterminacies of the type 0/0.



**2.1.5.2. Case  $n = 3, e(u) \neq 0, \dot{e}(u) = e(u) \neq 0 \Rightarrow e(u) - \dot{e}(u) = 0$**

A direct computation from the definition (4) gives that:

$$(75) \quad \mathbf{I}_{0,-4,+1}(e, \dot{e} = e, n = 3) \equiv \int_0^{2\pi} (1 + e \cos \varphi)^{-1} d\varphi = 2\pi(1 - e^2)^{-1/2} = \mathbf{A}_1(e, 0),$$

(see, for example, formula (20) from paper [5]).

This result follows also from the above just derived expression (74), if we substitute into it  $\dot{e}(u) = e(u)$ . It is also in agreement with the relation (12), because (74) is derived as a consequence from (12) in the limit  $n \rightarrow 3$ .

**2.1.6. Case  $n = 3, e(u) \neq 0, \dot{e}(u) = 0 \Rightarrow e(u) - \dot{e}(u) \neq 0$**

A direct computation from the definition (4) gives that:

$$(76) \quad \mathbf{I}_{0,-4,+1}(e, \dot{e} = e, n = 3) = \mathbf{A}_5(e, 0) = (\pi/4)(8 + 24e^2 + 3e^4)(1 - e^2)^{-9/2},$$

(formula (24) from paper [5]).

In deriving of the above expression (76), we have at first taken the limit  $\dot{e}(u) \rightarrow 0$ , and after then we have performed the transition  $n \rightarrow 0$ . The solutions (75) and (76) coincide with the solutions  $\mathbf{A}_1(e, 0)$  and  $\mathbf{A}_5(e, 0)$ , respectively, and we note that the later do not depend on the power  $n$  in the viscosity law  $\eta = \beta \Sigma^n$ . We now shall show that we may change the order of the transitions: at first we may take into (4) the transition  $n \rightarrow 3$  and after that substitute  $\dot{e}(u) = 0$ . The final result will be the same as (76). In the expression (74) the transition  $n \rightarrow 3$  is already performed and it remains to evaluate it in the limit  $\dot{e}(u) \rightarrow 0$ . Performing into the first term the multiplication by  $(e - \dot{e}) \neq 0$  (in the our Case 2.1.6  $e(u) - \dot{e}(u) \neq 0$  !) and reducing to a common denominator the two terms of the solution (74), we want, in fact, to evaluate the limit:

$$(78) \quad \pi(1 - e^2)^{-1/2} \lim_{\dot{e}(u) \rightarrow 0} \{ (-2e^4 + 6e^6 - 6e^8 + 2e^{10} - 14e^5\dot{e} + 28e^7\dot{e} - 14e^9\dot{e} + 7e^4\dot{e}^2 - 49e^6\dot{e}^2 + 42e^8\dot{e}^2 + 35e^5\dot{e}^3 - 70e^7\dot{e}^3 + 2e^4 + 8e^2\dot{e}^4 + 70e^6\dot{e}^4 - 10e\dot{e}^5 - 14e^3\dot{e}^5 - 42e^5\dot{e}^5 + 3\dot{e}^6 + 7e^2\dot{e}^6 + 14e^4\dot{e}^6 - e\dot{e}^7 - 2e^3\dot{e}^7)(1 - e^2)^{1/2} + 2e^4[1 - (e - \dot{e})^2]^{7/2} \} \dot{e}^{-4}[1 - (e - \dot{e})^2]^{-7/2}.$$

To apply the L'Hospital's rule for evaluating of indeterminasies of the type 0/0, we must compute the derivatives with respect to  $\dot{e}(u)$  from the denominator and the dominator of the above expression (78).

It is easily checked that the other conditions for the application of the L'Hospital's rule (see paper [5]) are also fulfilled. It turns out, that this rule has to be used *four* times, because only after the *fourth* differentiation with respect to  $\dot{e}(u)$  of the denominator

$\dot{e}^4[1 - (e - \dot{e})^2]^{7/2}$  into (78) ensures non-zero value for  $\dot{e}(u) = 0$ . We here *temporarily* neglect the multiplier  $\pi(1 - e^2)^{-1/2}$  into the left-hand-side of

the equality (78), because it does not make sense under the limit transition  $\dot{e}(u) \rightarrow 0$ . Therefore, we successively compute the following derivatives with respect to  $\dot{e}(u)$  under the transition  $\dot{e}(u) \rightarrow 0$ :

$$(79) \quad \lim_{\dot{e}(u) \rightarrow 0} \{\partial/\partial \dot{e}\{e^4[1 - (e - \dot{e})^2]^{7/2}\}\} = 0.$$

$$(80) \quad \lim_{\dot{e}(u) \rightarrow 0} \{\partial/\partial \dot{e}\{4e^3[1 - (e - \dot{e})^2]^{7/2} + 7\dot{e}^4(e - \dot{e})[1 - (e - \dot{e})^2]^{5/2}\}\} = 0.$$

$$(81) \quad \lim_{\dot{e}(u) \rightarrow 0} \{\partial/\partial \dot{e}\{12e^2[1 - (e - \dot{e})^2]^{7/2} + 56\dot{e}^3(e - \dot{e})[1 - (e - \dot{e})^2]^{5/2} - 7\dot{e}^4[1 - (e - \dot{e})^2]^{5/2} + 35\dot{e}^4(e - \dot{e})^2[1 - (e - \dot{e})^2]^{3/2}\}\} = 0.$$

Finally, we compute analytically that:

$$(82) \quad \lim_{\dot{e}(u) \rightarrow 0} \{\partial/\partial \dot{e}\{24\dot{e}[1 - (e - \dot{e})^2]^{7/2} + 252\dot{e}^2(e - \dot{e})[1 - (e - \dot{e})^2]^{5/2} - 84\dot{e}^3[1 - (e - \dot{e})^2]^{5/2} + 420\dot{e}^3(e - \dot{e})^2[1 - (e - \dot{e})^2]^{3/2} - 105\dot{e}^4(e - \dot{e})[1 - (e - \dot{e})^2]^{3/2} + 105\dot{e}^4(e - \dot{e})^3[1 - (e - \dot{e})^2]^{1/2}\}\} = 24(1 - e^2)^{7/2}.$$

Therefore, we have to differentiate with respect to  $\dot{e}(u)$  *four times*, until we arrive at an expression in the *denominator*, which tends to non-zero value, when  $\dot{e}(u) \rightarrow 0$ .

Let us now compute the limits of the derivatives of the *nominator* of the expression (78), when  $\dot{e}(u)$  approaches zero:

$$(83) \quad \lim_{\dot{e}(u) \rightarrow 0} \{\partial/\partial \dot{e}\{(-2e^4 + 6e^6 - 6e^8 + 2e^{10} - 14e^5\dot{e} + 28e^7\dot{e} - 14e^9\dot{e} + 7e^4\dot{e}^2 - 49e^6\dot{e}^2 + 42e^8\dot{e}^2 + 35e^5\dot{e}^3 - 70e^7\dot{e}^3 + 2e^4 + 8e^2\dot{e}^4 + 70e^6\dot{e}^4 - 10e\dot{e}^5 - 14e^3\dot{e}^5 - 42e^5\dot{e}^5 + 3e^6 + 7e^2\dot{e}^6 + 14e^4\dot{e}^6 - e\dot{e}^7 - 2e^3\dot{e}^7) \times (1 - e^2)^{1/2} + 2e^4[1 - (e - \dot{e})^2]^{7/2}\}\} = 0,$$

$$(84) \quad \lim_{\dot{e}(u) \rightarrow 0} \{\partial/\partial \dot{e}\{(-14e^5 + 28e^7 - 14e^9 + 14e^4\dot{e} - 98e^6\dot{e} + 84e^8\dot{e} + 105e^5\dot{e}^2 - 210e^7\dot{e}^2 + \dots) \times (1 - e^2)^{1/2} + (14e^5 - 28e^7 + 14e^9 - 14e^4\dot{e} + 84e^6\dot{e} - 70e^8\dot{e} - 84e^5\dot{e}^2 + 140e^7\dot{e}^2 + \dots)[1 - (e - \dot{e})^2]^{1/2}\}\} = 0.$$

$$(85) \quad \lim_{\dot{e}(u) \rightarrow 0} \{\partial/\partial \dot{e}\{(14e^4 - 98e^6 + 84e^8 + 210e^5\dot{e} - 420e^7\dot{e} + \dots)(1 - e^2)^{1/2} + (14e^4 + 98e^6 - 84e^8 - 196e^5\dot{e} + \dots)[1 - (e - \dot{e})^2]^{1/2}\}\} = 0,$$

$$(86) \quad \lim_{\dot{e}(u) \rightarrow 0} \{\partial/\partial \dot{e}\{(210e^5 - 420e^7 + 48\dot{e} + 192e^2\dot{e} + 1680e^6\dot{e} - \dots)(1 - e^2)^{1/2} + (-196e^5 + 336e^7 + 196e^4\dot{e} - 1008e^6\dot{e} + \dots)[1 - (e - \dot{e})^2]^{1/2} + (-14e^5 + 98e^7 - 84e^9 + 14e^4\dot{e} - 294e^6\dot{e} + 420e^8\dot{e} + \dots) \times [1 - (e - \dot{e})^2]^{-1/2}\}\} = 6(8 + 24e^2 + 3e^4)(1 - e^2)^{-1/2}.$$

This is the *fourth* differentiation of the *nominator* of the expression (78). Consequently, the L'Hospital's rule for resolving of indeterminacies of the type 0/0, enables us to compute the two-limits transition:

$$(87) \quad \lim_{\dot{e}(u) \rightarrow 0} [\lim_{n \rightarrow 3} \mathbf{I}_{0,-4,+1}(e, \dot{e}, n)] = \lim_{\dot{e}(u) \rightarrow 0} \mathbf{I}_{0,-4,+1}(e, \dot{e}, n = 3) = \mathbf{I}_{0,-4,+1}(e, \dot{e} = 0, n = 3) = (6\pi/24)(8 + 24e^2 + 3e^4)(1 - e^2)^{-1}(1 - e^2)^{-7/2} = (\pi/4)(8 + 24e^2 + 3e^4)(1 - e^2)^{-9/2},$$

where the above solution (87) follows from the equalities (82) and (86). And also we have recovered the multiplier  $\pi(1 - e^2)^{-1/2}$ , according to the expression (78). The evaluation (87) coincides with the right-hand-side of the solution (76) and implies that *no matter* which limit transition  $\dot{e}(u) \rightarrow 0$

or  $n \rightarrow 3$  will be taken first. That is to say, the two-limits transitions  $\lim_{\dot{e}(u) \rightarrow 0} \lim_{n \rightarrow 3}$  and  $\lim_{n \rightarrow 3} \lim_{\dot{e}(u) \rightarrow 0}$  are equivalent in the considered by us situations. This also confirms again, that the relation (12) may be used for evaluation of the integral  $\mathbf{I}_{0,-4,+1}(e, \dot{e}, n)$  in the cases when  $n = 3$  and/or  $\dot{e}(u) = 0$  through the application of the L'Hospital's rule for computing of indeterminacies of the type  $0/0$ .

### **2.1.7. Case $n = 3, e(u) = 0, \dot{e}(u) \neq 0 \Rightarrow e(u) - \dot{e}(u) \neq 0$**

A direct computation from the definition (4) gives:

$$(88) \quad \mathbf{I}_{0,-4,+1}(e = 0, \dot{e}, n = 3) \equiv \int_0^{2\pi} (1 - \dot{e} \cos \varphi)^{-4} d\varphi = \mathbf{A}_4(-\dot{e}, 0) = \pi(2 + 3\dot{e}^2)(1 - \dot{e}^2)^{-7/2},$$

(formula (23) from paper [5] with the replacement  $e(u) \rightarrow -\dot{e}(u)$ ).

We may also evaluate this integral by another way, using the solution (74), where the transition  $n \rightarrow 3$  is already performed. And where we are allowed directly to set  $e(u) = 0$  (simultaneously preserving  $\dot{e}(u) \neq 0$ ), because  $e(u)$  does not take place as a factor into the denominators. The result is:

$$(89) \quad \lim_{e(u) \rightarrow 0} [\lim_{n \rightarrow 3} \mathbf{I}_{0,-4,+1}(e, \dot{e}, n)] = -\pi \dot{e} (-2\dot{e}^3 - 3\dot{e}^5) \dot{e}^{-4} (1 - \dot{e}^2)^{-7/2} = \pi(2 + 3\dot{e}^2)(1 - \dot{e}^2)^{-7/2},$$

which coincides with the above evaluation (88). Consequently, we again arrive at the conclusion that *no matter* which of the transitions  $n \rightarrow 3$  or  $e(u) \rightarrow 0$  must be realized at first. The expression (12) also may be useful (i.e., to make sense) for the analytical evaluation of the integral  $\mathbf{I}_{0,-4,+1}(e, \dot{e}, n)$  for  $n = 3$  and/or  $e(u) = 0$ , if the corresponding two-limits  $n \rightarrow 3$  and  $e(u) \rightarrow 0$  are performed.

### **2.1.8. Case $n = 3, e(u) = \dot{e}(u) = 0 \Rightarrow e(u) - \dot{e}(u) = 0$**

Obviously, in this most simple case  $\mathbf{I}_{0,-4,+1}(e = 0, \dot{e} = 0, n = 3) = 2\pi$ . The same result follows from the expressions (76) and (88), if we take  $e(u) \rightarrow 0$ , or  $\dot{e}(u) \rightarrow 0$ , respectively.

All the above considerations, made in the **Cases 2.1.1 – 2.1.8**, support the statement that the *linear relation* (12) may be used also in the situations when some or all of the quantities  $e(u)$ ,  $\dot{e}(u)$  and  $n - 3$  are equal to zero. It is enough only to apply the L'Hospital's rule (theorem) for resolving of indeterminacies of the type  $0/0$ . It seems out, that there is *no matter* what must be the order of performing of the needed transitions  $e(u) \rightarrow 0$ ,  $\dot{e}(u) \rightarrow 0$  and  $n \rightarrow 3$ .

### 3. Conclusions

In the present paper we have resolved analytically the integral  $\mathbf{I}_{0,-4,+1}(e,\dot{e},n)$ , given by the definition (4). A similar approach for an analytical evaluation of the other integral  $\mathbf{I}_{0,-2,+3}(e,\dot{e},n)$ , described by the definition (5), will be applied in a forthcoming paper [9]. Such calculations split into many particular cases. This situation is caused by the vanishing of the denominators of some terms in the final or/and intermediate results for certain values of the eccentricity  $e(u)$ , its derivative  $\dot{e}(u)$  and the power  $n$ . It is remarkable that all these solutions can be expressed by means of a single common formula. The essential point is that such divergences may be overcome with the help of the L'Hospital's rule for resolving of indeterminacies of the type  $0/0$ . For this reason, the application of the solutions into the subsequent calculations is simplified to some extent, because there is not already need to consider every case in a separate way. Of course, having in mind the corresponding limit transitions, when we have dealing with the singular points. The generalized in such a manner solution for the integral  $\mathbf{I}_{0,-4,+1}(e,\dot{e},n)$  is given by the formula (12). The corresponding to the integral  $\mathbf{I}_{0,-2,+3}(e,\dot{e},n)$  solution is derived in paper [9].

The basic motivation to establish the analytical solutions of the integrals  $\mathbf{I}_{0,-4,+1}(e,\dot{e},n)$  (definition (4)) and  $\mathbf{I}_{0,-2,+3}(e,\dot{e},n)$  (definition (5)) is to give the answer of the question whether the integrals  $\mathbf{I}_0(e,\dot{e},n)$  (definition (1)) and  $\mathbf{I}_{0+}(e,\dot{e},n)$  (definition (2)) are linearly dependent functions of  $e(u)$ ,  $\dot{e}(u)$  and  $n$  or not. The standard approach to resolve this problem is to compute the corresponding Wronski determinant and to evaluate its equalization/non-equalization to zero value. In the process of realization of this procedure, there arises the necessity of knowledge of the analytical solutions of these integrals  $\mathbf{I}_{0,-4,+1}(e,\dot{e},n)$  and  $\mathbf{I}_{0,-2,+3}(e,\dot{e},n)$ . It is worth to note, that in the present investigation we already encounter with the property that for *integer*  $n$  ( $n = -1, 0, 1, 2, 3$ ) the integrals  $\mathbf{I}_0(e,\dot{e},n)$  and  $\mathbf{I}_{0+}(e,\dot{e},n)$  are linearly dependent functions. In particular, formula (61) clearly demonstrates such a linear relation for  $n = 3$ . Therefore, we have a hint to expect also the existence of linear dependencies between  $\mathbf{I}_0(e,\dot{e},n)$  and  $\mathbf{I}_{0+}(e,\dot{e},n)$  in the general case, including the *non-integer* values of the power  $n$ . Such an expectation follows from the property that the viscosity law  $\eta = \beta\Sigma^n$  does not impose or require any physically motivated separations of the powers  $n$  (for different families of models of Lyubarskij et al. [1]) into *integer* and *non-integer* values. That is to say, between models with (fixed) *integer*  $n$  and models with (fixed) *non-integer*  $n$ .

## References

1. L y u b a r s k i j, Y u. E., K. A. P o s t n o v, M. E. P r o k h o r o v. Eccentric accretion discs., Monthly Not. Royal Astron. Soc., 266, 1994, № 2, pp. 583–596.
2. D i m i t r o v, D. Thin viscous elliptical accretion discs with orbits sharing a common longitude of periastron. IV. Proof of the homogeneity of the dynamical equation, governing the disc structure for arbitrary powers  $n$  in the viscosity law  $\eta = \beta \Sigma^n$ ., Aerospace research in Bulgaria, 23, 2009, pp. 19–35.
3. S h a k u r a, N. I., R. A. S u n y a e v. Black holes in binary systems. Observational appearance., Astron. & Astrophys., 24, 1973, № 3, pp. 337–355.
4. D i m i t r o v, D. Thin viscous elliptical accretion discs with orbits sharing a common longitude of periastron. VII. Do we have a truncation of the chain of linear relations between the integrals, entering into the dynamical equation?, Aerospace research in Bulgaria, 26, 2014, (to appear).
5. D i m i t r o v, D. Analytical computation of two integrals, appearing in the theory of elliptical accretion discs. I. Solving of the auxiliary integrals, emerging during their derivations., Aerospace Research in Bulgaria, 25, 2013, pp. 5–34.
6. D i m i t r o v, D. Analytical computation of two integrals, appearing in the theory of elliptical accretion discs. II. Solving of some auxiliary integrals, containing logarithmic functions into their integrands., Aerospace Research in Bulgaria, 25, 2013, pp. 35–61.
7. D i m i t r o v, D. V. Analytical computation of two integrals, appearing in the theory of elliptical accretion discs. III. Solving of the full set of auxiliary integrals, containing logarithmic functions into their integrands., Aerospace Research in Bulgaria, 26, 2013, (to appear).
8. D i m i t r o v, D. Thin viscous elliptical accretion discs with orbits sharing a common longitude of periastron. I. Dynamical equation for integer values of the powers in the viscosity law., Aerospace Research in Bulgaria, 19, 2006, pp. 16–28.
9. D i m i t r o v, D. Analytical computation of two integrals, appearing in the theory of elliptical accretion discs. V. Solving of the supplement integral, needed for the analytical evaluation of the Wronski determinant., Aerospace Research in Bulgaria, 28, 2015, (to appear).

**АНАЛИТИЧНО ПРЕСМЯТАНЕ НА ДВА ИНТЕГРАЛА,  
ВЪЗНИКВАЩИ В ТЕОРИЯТА НА ЕЛИПТИЧНИТЕ АКРЕЦИОННИ  
ДИСКОВЕ. IV. РЕШАВАНЕ НА ЕДИН ИНТЕГРАЛ,  
ОБЕЗПЕЧАВАЩ ОЦЕНЯВАНЕТО НА ПРОИЗВОДНИТЕ,  
ВЛИЗАЩИ В ДЕТЕРМИНАНТАТА НА ВРОНСКИ**

*Д. Димитров*

**Резюме**

Настоящата статия се занимава с аналитичното пресмятане на определения интеграл

$$\int_0^{2\pi} (1 + e \cos \varphi)^{n-4} [1 + (e - \dot{e}) \cos \varphi]^{-n-1} d\varphi, \text{ където } e(u) \text{ са}$$

ексцентрицитетите на орбитите на частиците,  $\dot{e}(u) \equiv de(u)/du$ ,  $u \equiv \ln(p)$ , като  $p$  е фокалният параметър на съответните елиптични орбити на частиците. Параметърът  $n$  е степента в закона за вискозитета  $\eta = \beta \Sigma^n$ , където  $\Sigma$  е повърхностната плътност на акреционния диск и  $\varphi$  е азимуталният ъгъл. Ние сме извършили изчисленията при следните три ограничения: (i)  $|e(u)| < 1$ , (ii)  $|\dot{e}(u)| < 1$  и (iii)  $|e(u) - \dot{e}(u)| < 1$ . Те са физически мотивирани от възприетия за нашите разглеждания модел на *стационарни* елиптични акреционни дискове на Любарски и др. [1]. Голям брой частни случаи, възникващи поради сингулярното поведение на някои членове за дадени значения на  $e(u)$ ,  $\dot{e}(u)$ , тяхната разлика  $e(u) - \dot{e}(u)$  и степенния показател  $n$ , са детайлно изчислени. Тези пресмятания са извършени по два способа: (i) чрез *директно* полагане на сингулярното значение в първоначалната дефиниция на интеграла, и (ii) чрез граничен преход към това сингулярно значение във вече оценения аналитичен израз за интеграла, получен за регулярни стойности на съответните променливи. В последния случай е твърде полезно прилагането на правилото на Лъопитал за решаването на неопределености от вида 0/0. Двата подхода дават едни и същи резултати във всеки проверяван случай, което осигурява щото преходът през сингулярното значение да е непрекъснат. Това означава, че аналитичните решения за всички (сингулярни и несингулярни) случаи могат да бъдат комбинирани в една единствена формула. Такова едно описание на решението на горенаписания интеграл, е твърде удобно за случая, когато тази формула се прилага за проверяването на линейната зависимост/независимост на коефициентите, влизащи в членовете на динамичното уравнение на елиптичния акреционен диск.

## **DESCRIPTION OF THE LIULIN TYPE INSTRUMENTS AND MAIN SCIENTIFIC RESULTS**

***Tsvetan Dachev, Jordanka Semkova, Borislav Tomov, Yury Matviichuk,  
Plamen Dimitrov, Nikolay Bankov, Rositsa Koleva, Stefan Malchev***

*Space Research and Technology Institute – Bulgarian Academy of Sciences  
e-mail: tdachev@bas.bg*

### ***Abstract***

*Ionizing radiation has been recognized as one of the main health concerns for the humans in the near Earth and space radiation environment. The estimation of the radiation effect on health requires at first order accurate knowledge of the accumulated absorbed dose, which depend on the global space radiation distribution, solar cycle and local variations generated by the 3D mass distribution surrounding the space vehicle. This paper presents an overview of the Bulgarian-built spectrometer-dosimeters of Liulin-type and their main scientific results, which was obtained in space, at aircraft, balloon and rocket since 1988.*

## **1. Introduction**

The radiation field around the Earth is complex, composed of GCRs, trapped particles of the Earth's radiation belts, solar energetic particles, albedo particles from Earth's atmosphere and secondary radiation produced in the shielding materials around the biological objects [1-4]. Dose characteristics in near Earth and space radiation environment also depend on many other parameters such as the orbit parameters, solar cycle phase and current helio-and geophysical conditions.

### ***1.1. Galactic cosmic rays***

The dominant radiation component in the near Earth and free space environment are the galactic cosmic rays (GCR). The GCR are charged particles that originate from sources beyond our solar system. GCR are the

most penetrating of the major types of ionizing radiation. The energies of GCR particles range from several tens up to  $10^{12}$  MeV nucleon<sup>-1</sup>. The GCR spectrum consists of 98 % protons and heavier ions (baryon component) and 2 % electrons and positrons (lepton component). The baryon component is composed of 87 % protons, 12 % helium ions (alpha particles) and 1 % heavy ions [5]. Highly energetic particles in the heavy ion component, typically referred to as high Z and energy (HZE) particles, play a particularly important role in space dosimetry [2]. HZE particles, especially iron, possess high-LET (Linear energy transfer) and are highly penetrating, giving them a large potential for radiobiological damage [6]. Up to 1 GeV energy, the flux and spectra of GCR particles show modulation that is anti-correlated with solar activity.

### ***1.2. Trapped radiation belts***

Radiation belts are the regions of high concentration of the energetic electrons and protons trapped within the Earth's magnetosphere. There are two distinct belts of toroidal shape surrounding the Earth where the high energy charged particles get trapped in the Earth's magnetic field. The inner radiation belt (IRB), located between about 0.1 to 2 Earth radii, consists of both electrons with energies up to 10 MeV and protons with energies up to ~700 MeV. The outer radiation belt (ORB) starts from about 4 Earth radii and extends to about 9-10 Earth radii in the anti-sun direction. The outer belt mostly consists of electrons whose energy is not larger than 10 MeV. The electron flux may cause problems for components located outside a spacecraft (e.g. solar cell degradation). They do not have enough energy to penetrate a heavily shielded spacecraft such as the International space station (ISS) wall, but may deliver large additional doses to astronauts during extra vehicular activity [7-9]. The South-Atlantic Anomaly (SAA) is an area where the IRB comes closer to the Earth surface due to a displacement of the magnetic dipole axes from the Earth's center. The daily average SAA doses reported by Reitz et al., (2005) [10] inside of the ISS vary in the range 74-215  $\mu\text{Gy d}^{-1}$  for the absorbed dose rates and in the range 130-258  $\mu\text{Sv d}^{-1}$  for the averaged equivalent daily dose rates.

### ***1.3. Solar Energetic Particles (SEP)***

The SEP are mainly produced by solar flares, sudden sporadic eruptions of the chromosphere of the Sun. High fluxes of charged particles (mostly protons, some electrons and helium and heavier ions) with energies



up to several GeV are emitted by processes of acceleration outside the Sun. It is now generally understood that SEP events arise from coronal mass ejections (CME) from active regions of the solar surface. The CME propagates through interplanetary space carrying along with it the local surface magnetic field frozen into the ejected mass. There is a transition (shock) region between the normal sectored magnetic structure of interplanetary space and the fields frozen into the ejected mass, which forms a transition region (shock) where the interplanetary gas is accelerated forming the SEP. As the accelerated region passes an observation point, the flux intensity is observed to increase dramatically [11]. The time profile of a typical SEP starts off with a rapid exponential increase in flux, reaching a peak in minutes to hours. The energy emitted lies between 15 and 500 MeV nucleon<sup>-1</sup> and the intensity can reach 10<sup>4</sup> cm<sup>-2</sup> s<sup>-1</sup> sr<sup>-1</sup>. Electrons with energies of ~0.5 to 1 MeV arrive at the Earth, usually traveling along interplanetary field lines, within tens of minutes to tens of hours. Protons with energies of 20 to 80 MeV arrive within a few to ~10 hours, although some high energy protons can arrive in as early as 20 minutes. SEP are relatively rare and occur most often during the solar maximum phase of the 11-year solar cycle. In the years of maximum solar activity up to 10 flares can occur, during the years of minimum solar activity only one event can be observed on average [12].

#### ***1.4. Atmospheric Ionizing Radiation***

The natural radiation level at cruising aircraft altitudes is much higher than it is at ground level. The radiation field arises as a result of the interaction of primary GCR particles with the Earth's atmosphere. An additional flux of albedo secondary GCR is observed at altitudes below 3 km, which contributes to the forming of the flux minimum around 1.6 km altitude [13]. The intensity of the atmospheric radiations, composed of GCR primary and secondary particles and their energy distribution vary with altitude, location in the geomagnetic field, and the time in the sun's magnetic activity (solar) cycle [11]. The atmosphere provides shielding, which depends on the overhead atmospheric depth. The geomagnetic field provides a different kind of shielding, by deflecting low-momentum charged particles back to space. Because of the orientation of the geomagnetic field, which is predominately dipolar in nature, the Polar Regions are susceptible to penetrating GCR (and SEP) particles. At each geographic location, the minimum momentum per unit charge (magnetic rigidity) a vertically

incident particle can have and still reach a given location above the Earth is called the geomagnetic vertical cutoff rigidity [14]. The local flux of incident GCR at a given time varies widely with geomagnetic location and the solar modulation level. When the solar activity is high, the GCR flux is low, and vice versa.

### ***1.5. Natural radioactivity***

The larger fractions of the Earth's surface where people live and work has as natural soil cover resulting from weathering processes. The lower atmospheric radiation and the associated external exposure are mainly from gamma rays emitted from the top 25 cm of the surface layer of the Earth and the construction materials of the buildings [15]. At ground level the space radiation (originating from outside the Earth's atmosphere, including solar radiation) generate about 11 % of the effective dose which the average US population, is exposed to, while the terrestrial one (radiation emitted by radionuclides in soil and rocks) is 7 %. The major amount of the effective dose is produced by inhaled Radon and ingested Potassium, Thorium and Uranium [16].

## **2. Instrumentation**

All Liulin type dosimetric instruments use one or more silicon detectors and measure the deposited energy and number of particles into the detector/s when charged particles hit the detector, that allow to calculate the dose rate and particle flux.

The first used in space Bulgarian build dosimetry instrument named LIULIN (see Table 1, Item No 1) was developed for the scientific program of the second Bulgarian astronaut [17].

The measurements in the LIULIN instrument were based on a single silicon detector followed by a charge-sensitive and shaping amplifier (CSA). The number of the pulses at the output of CSA above a given threshold was proportional to the particle flux hitting the detector; the amplitude of the pulses at the output of CSA was proportional to the particles deposited energy and further to the deposited dose. The same measurement procedure was used for the RADIUS-MD instrument (see Table 1, Item No 2). The instrument was developed and qualified for space together with French and Russian colleagues for the unsuccessful Mars-96 mission [18]. LIULIN and RADIUS-MD instruments were designed to

provide data just for the dose rate and particle flux in a single detector, but not data for the deposited energy spectrum. Later this design was no more used, that is why in this paper we will not describe comprehensively it but will summarize the major results obtained during the operation of the LIULIN instrument on MIR space station between April 1988 and September 1994.

Many other instruments was developed and used in space, on ground, aircraft and balloons since then. The paper aims to review the major milestones of their development, calibrations and scientific results.

Table 1 collect information for the all developed and build in Bulgaria instruments that have been used in near Earth radiation environment or around the Moon.

Totally 14 different space instruments were developed, build and qualified for space between 1988 and 2014. 3 of them were lost because of problems with the rockets of the Mars-96, Foton-M1 and Phobos-Grunt missions. R3D-B1 instrument for Foton-M1 mission is not shown in the table because it was very similar to the R3D-B2/B3 instruments for Foton-M2/M3 missions.

The first column of the Table 1 gives information about the name of the satellite, begin and end time and number of available measurements. The second column lists the name of the experiment, Principal investigator (PI) and Co-PIs. Also major references describing the instrument and obtained data are listed. The third column gives the name of the instrument, technical specifications, location, shielding and resolution of the instrument. The last 2 columns present images of the instruments and their locations (carriers).

There are 2 major measurement systems developed by the team till this moment. The first one is based on one detector and is known as Liulin type Deposited Energy Spectrometer (DES) [19, 20], while the second one is dosimetric telescope (DT) by 2/3 detectors [21, 22]).

## ***2.1. DES instrumentation***

### ***2.1.1. DES description***

The main purpose of the Liulin type Deposited Energy Spectrometer (DES) is to measure the spectrum (in 256 channels) of the deposited energy in a silicon detector from primary and secondary particles at the aircraft and

balloons altitudes, at low earth orbits, outside of the Earth magnetosphere on the route, around and on the surface of the planets of the solar system.

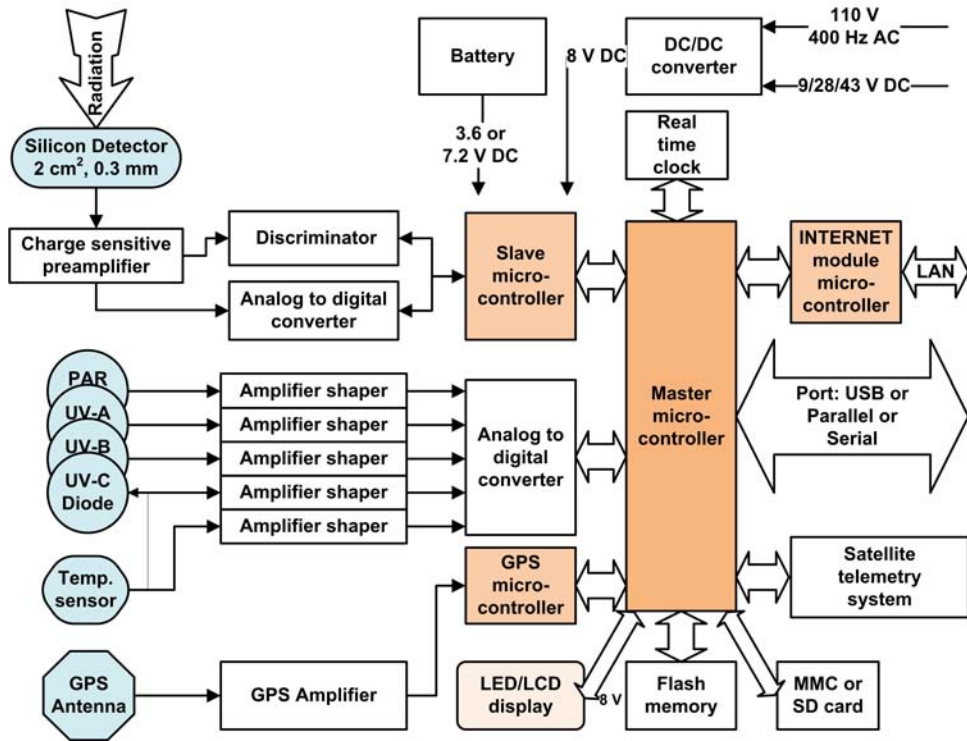


Fig. 1. Generalized block diagram of Liulin-type DES instruments

Historically the first development of DES was for the Liulin-3M instrument [19] for use on aircraft and balloons [23] and for BION-11/12 missions. Later the redevelopment of the Liulin-3M instrument was named Liulin-4 or Liulin-6, which are synonyms of DES.

Fig. 1 presents a generalized block diagram of Liulin type DESs [24]. DES usually contains: one semiconductor detector, one charge-sensitive preamplifier, a fast 256 channel analog-to-digital converter (ADC), discriminator, real time clock, 2 or more microcontrollers and a flash memory. Different modifications of DESs use additional modules such as: UV sensitive photo diodes, temperature sensor, Global Positioning System

(GPS) module with antenna and receiver, LED or LCD display, multimedia card (MMC) or SD card.

Pulse analysis technique is used to obtain the deposited energy from each photon/particle crossing partially or fully the silicon detector. The deposited energies organised in 256 channels form the deposited energy spectrum for each measurement cycle. It is further used for the calculation of the absorbed dose and flux in the silicon detector from primary and secondary particles. The analysis of the shape of the spectrum and the dose to flux ratio, known also as specific dose (SD), permits the characterization of the predominant radiation source in the DES environment [25].

The unit is managed by the microcontrollers through specially developed firmware. The ADC and the slave microcontroller measure organize and keep in RAM memory the 256 channels deposited energy spectrum. The master microcontroller (seen in the right part of Figure 1.) manages the whole work of the spectrometer and data outputs. The developed modifications permits: store of the spectrum data on flash memory or on SD/MMC card; transmission of the spectra data toward parallel, serial or USB port; transmission of spectra data toward internet module and further to LAN network; dose and flux data visualization on alpha numeric or graphic display.

For the two R3D-B2/B3 instruments on Foton satellites and for the R3DE/R instrument on ISS (see Table 1, Item No 4/7 and Item No 9/11), 4 photodiode with filters in different wavelengths and 1 temperature input channels were also developed and used.

Another type of input is the GPS tract, which consists of GPS antenna, receiver and microcontroller unit (MCU). This is used by aircraft instruments for positioning of the measurements versus the geographic longitude, latitude, altitude above the sea level and Universal Time (UT).

Different power supplies were used in the different instruments. They are presented on the upper part of Figure 1 and include 3.6 V or 7.2 V rechargeable or primary batteries, 28 V or 43 V DC aircraft and satellite power and 110 V, 400 Hz AC aircraft power line.

The main measured parameter in the DESs is the amplitude of the pulse after the CSA, generated by a particle or a photon crossing partially or fully the detector [20]. The amplitude of the pulse is proportional by a factor of  $240 \text{ mV MeV}^{-1}$  to the energy deposited in the detector and to the dose,

respectively. By 8 bit ADC these amplitudes are digitized and organized in a 256-channel deposited energy spectrum.

By definition the dose in the silicon detector  $D_{Si}$  [Gy] is one Joule deposited in 1 kg of matter. The DES absorbed dose is calculated by dividing the summarized energy deposition in the spectrum in Joules to the mass of the detector in kilograms:

$$(1) \quad D_{Si} [Gy] = K \sum_{i=1}^{255} (EL_i i) [J] / MD [kg]$$

$K$  is a coefficient.  $MD$  is the mass of the detector, and  $EL_i$  is the energy loss in Joules in the channel  $i$ . The energy in MeV is proportional to the amplitude  $A$  of the pulse:  $EL_i [MeV] = A [V] / 0.24 [V/MeV]$ , where  $0.24 [V/MeV]$  is a coefficient dependent on the preamplifier used and its sensitivity.

All 255 deposited dose values, depending on the deposited energy for one exposure time, form the deposited energy spectrum. The energy channel number 256 accumulates all pulses with amplitudes higher than the upper energy-of 20.83 MeV measured by the spectrometer. The methods for characterization of the type of incoming space radiation are described in [25, 26].

### 2.1.2. DES calibrations

Fig. 2 presents deposited energy spectra from different calibrations of DES, which are compared with proton, electron and GCR spectra obtained at aircraft altitudes and on spacecraft. The individual spectra seen in the figure are obtained after averaging of various numbers of primary spectra and are plotted in coordinates Deposited energy per channel/Deposited per channel dose rate. This allows better understanding of the process of formation of the spectra in the different deposited energy ranges. According to formula (1) the absorbed dose in Si is the area between the curve of the deposited energy spectrum and the abscissa. That is why from bottom to top the spectra position against the ordinate axes depends on the value of the deposited dose rates in Si seen in the legend at the top of the figure.

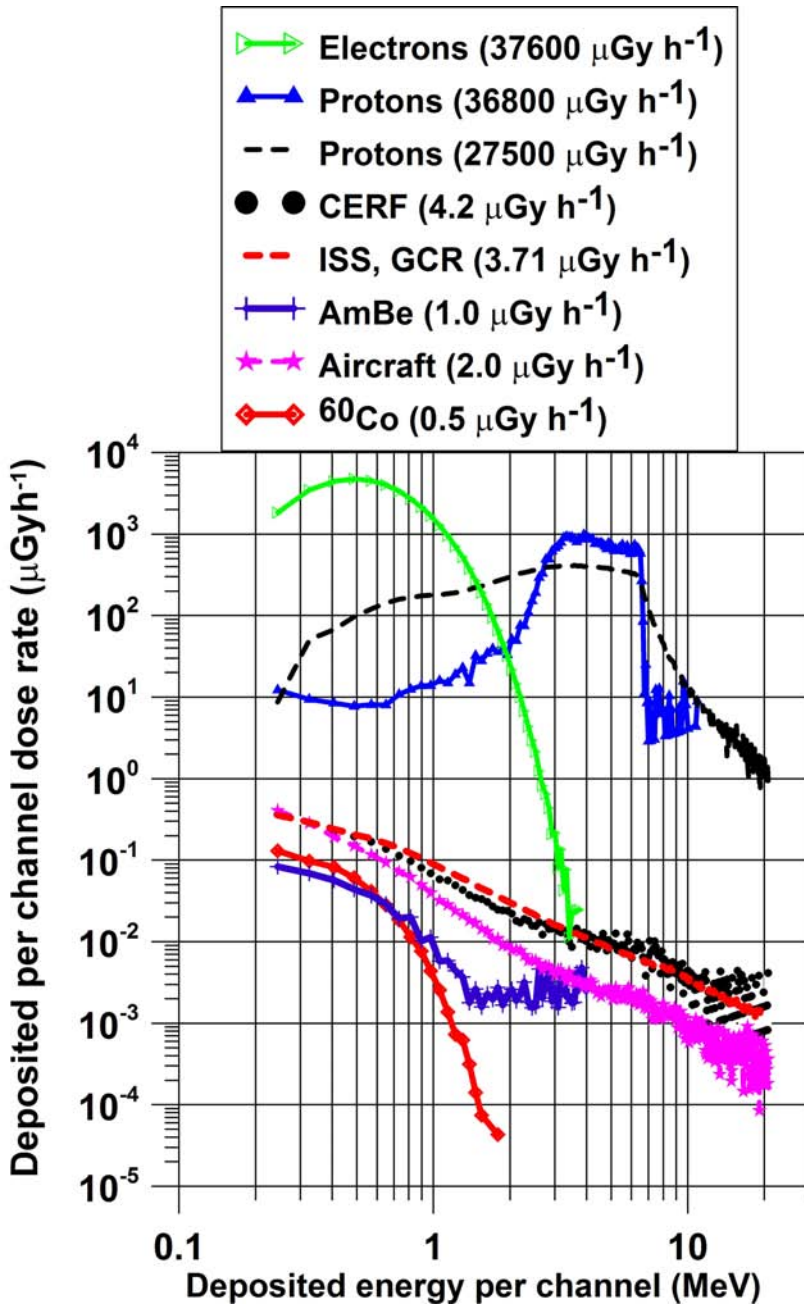


Fig. 2. Different spectrum shapes obtained by Liulin type instruments during calibrations and on aircraft and spacecraft

Lowest diamonds line spectrum in Fig. 2 ( $D=0.5 \mu\text{Gy h}^{-1}$ ) was obtained by Prof. Frantisek Spurny during the calibrations of the Liulin-4C MDU#2 (see Table 2, Item No 1) with  $^{60}\text{Co}$  reference radiation source in Nuclear Physics Institute of Czech Academy of Sciences [27]. This spectrum is the shortest because  $^{60}\text{Co}$  photons delivered relatively small energy depositions. The absolute values of the dose rates obtained from the spectra are in very good agreement with the dose rates calculated by means of EGS 4 transport code (<http://rcwww.kek.jp/research/egs/>). The values of the measured doses were found to be with 2.8% difference than the reference value for  $^{137}\text{Cs}$  source and with 8% difference for  $^{60}\text{Co}$  source [27]. The calibrations revealed that except for charged energetic particles, the DES has high effectivity towards gamma rays, which allowed monitoring the natural background radiation.

Next above - crosses line spectrum in Fig. 2 is again by reference radiation source of AmBe emitting neutrons with average energy of 4.4 MeV. This spectrum continues up to about 4 MeV deposited energy with very well seen change of the curve slope around 1.2 MeV deposited energy. The neutrons sensitivity of the DES was further studied in CERN-EU high-energy reference field (CERF) facility [28] on aircraft and in near Earth radiation environment. The spectrum with heavy dots in Fig. 2 is obtained in the CERF facility field, which generates a spectrum containing events in all channels of DES including the 256<sup>th</sup> channel devoted for energy depositions above the upper level of the spectrometer of 20.83 MeV. The events seen below 1 MeV in AmBe and CERF was supposed to represent the contribution of low LET radiation (electrons, muons, etc), while the events above 1 MeV that of high LET component (neutrons). This idea was further developed and allows from the deposited energy spectrum in the Silicon detector to be calculated the ambient dose equivalent  $H^*(10)$  at aircraft altitudes [29, 30].

The CERF energy deposition spectrum is very similar to the averaged aircraft spectrum shown with asterisks line in Fig. 2. This spectrum is obtained by averaging Czech airlines aircraft data during mean solar activity at altitudes close to 10.6 km on routes between Prague and North America towns New York and Montreal [31]. The International Space Station (ISS) R3DE instrument (see Table 2, Item No 5) mean GCR deposited energy spectrum shown with heavy dashed line did have shape even closer to the CERF spectrum. The spectrum was obtained by R3DE



instrument outside ISS by averaging of all measurements with 10 sec resolution for 2418 hours in the period 20 February-31 December 2008 [32].

CERF, ISS and aircraft spectra in Fig. 2 show similar knee around 6.5-7 MeV deposited energy. To explain this knee on Fig. 2 is added the heavy triangle line spectrum ( $36800 \mu\text{Gy h}^{-1}$ ), that was obtained during calibrations of DES (non-shielded detector) with 7.8 MeV protons beam at the Cyclotron facilities of the University of Louvain, Belgium [20]. The knee seen at about 6.3 MeV corresponds to the place where the incident energy of the normally falling to the 0.3 mm thick detector protons is equal to the deposited energy. All normally falling protons, which have smaller energies than 6.3 MeV are stopped inside of the detector. The exact value of the CSDA (continuous-slowng-down approximation) range in  $\text{g/cm}^2$  for 0.3 mm silicon is 6.04 MeV [33].

The light dashed line spectrum in Fig. 2 with  $27500 \mu\text{Gy h}^{-1}$  absorbed dose rate is obtained by RADOM instrument (see Table 1, Item No 10) on Chandrayaan-1 satellite after averaging of 60 primary 10 seconds resolution spectra [34]. This spectrum shows very similar shape to the cyclotron facilities spectrum shape (see the  $36800 \mu\text{Gy h}^{-1}$  full triangle spectrum) and the knee is at the same position. This is so because the energy of the inner belt protons falling on the detector is calculated to be 7-8 MeV e.g. equal to the energy of the cyclotron facilities mono energetic protons falling on the non-shielded detector. Main differences of both spectra are seen in the deposited energy range 0.244 – 2.8 MeV where except protons in space is observed large amount of low LET depositing particles and electrons. Smaller slope of the space spectrum after the knee can be explained with additional amount of ions heavier than protons in space.

The open triangle spectrum is the highest one in Fig. 2. It is obtained on Chandrayaan-1 satellite at altitudes of the ORB (22000 km). This spectrum with predominant electron population is the result of averaging of 120 spectra with 10 seconds resolution. Only the part, in the deposited energies up to 4.0 MeV is shown. Further the spectrum continue with form and shape similar to the ISS GCR spectrum (shown with thick line without symbols in Fig. 2) but here because of the very high count rate of the spectrometer and respectively large dead time the incoming CGR particles are not well detected and presented.

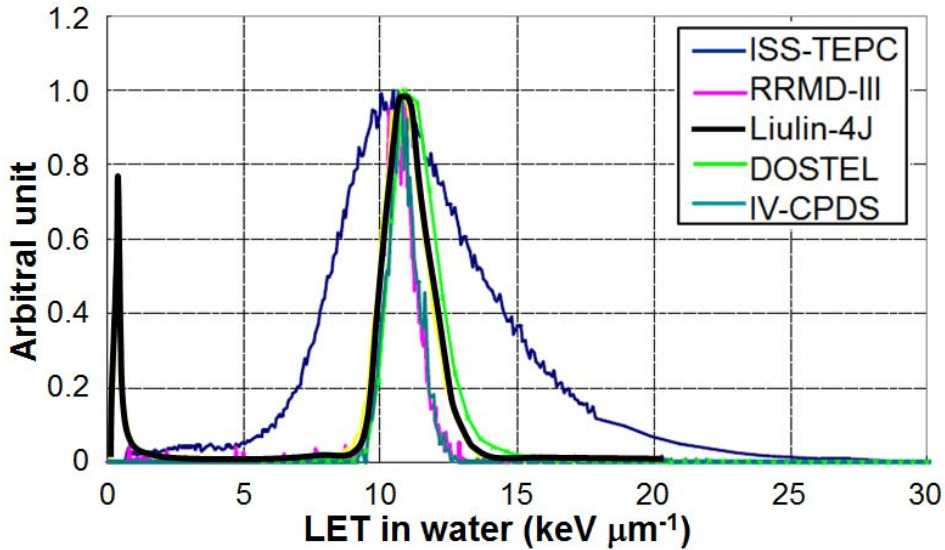
The exact position of the knee depends from the thickness of the detector's shielding and from the exact detector thickness, which are different for the different instruments. As larger these values are as larger is the value of the knee in the spectrum. That is why on Figure 2 the knee is observed above the calculated value of 6.04 MeV in the range 6.0-7.0 MeV. The average value of 6.2 MeV deposited energy is responsible for the channel number 78, which means that all other channels up to 256 of the spectrometer are populated by long pathlength low LET particles (protons) or by neutrons and heavier ions.

More comprehensive the DES calibrations with protons in the Louvain la-Neuve cyclotron facility are presented in [20]. Uchihori et al. in 2002 [35] performed calibrations with protons and heavy ions at Heavy Ion Accelerator at the National Institute of Radiological Sciences (NIRS) in Chiba, Japan (HIMAC) facility in Japan. In both cases of proton calibrations good agreement was found between the measured and the spectra predicted by the GEANT code. Nice coincidence between the predicted and obtained by Liulin-4J (MDU-3) response function was reported by Uchihori et al. [36] (Please see Figure 2 there). The response function was accumulated by points obtained in  $H^+$ ,  $He^+$ ,  $C^+(400\text{ MeV})$  and  $Ca^+(400\text{ MeV})$  beams.

The DES effectiveness for neutrons depends on their energy, being minimal for neutrons with energy 0.5 MeV and has a maximum of a few percent for neutrons with energy of 50 MeV in the CERN field [29]. According to the "neutron induced nuclear counter effect" introduced for the Hamamatsu PIN diodes of type S2744-08 (same are used in all DESs) [37] neutrons could be observed in all channels of the spectrum with a probability at least one order of magnitude higher in first 14 channels.

### ***2.1.3. DES data intercomparison with other instruments data***

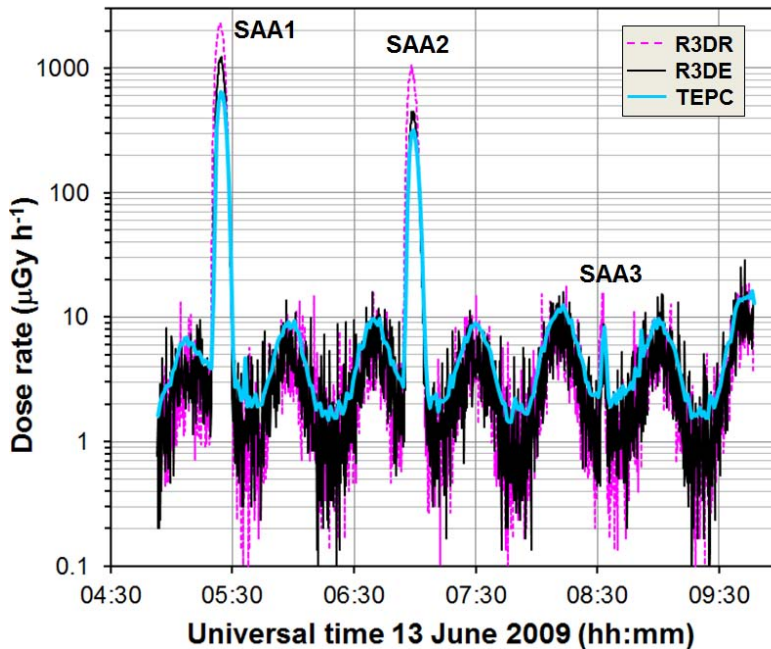
Post-flight calibrations with Liulin-E094 MDUs (see Table 1, Item No 3) were performed in HIMAC heavy ion accelerator during the 1st ICCHIBAN (Inter Comparison for Cosmic-ray with Heavy Ion Beams At NIRS) Project run in Chiba Japan in February 2002 with 400 MeV/u Carbon ions. The deposited energy spectra obtained with all 4 MDUs show a sharp maximum close to 6.1 MeV, that is in good agreement with theoretical prediction and with measurements of the same source with the DOSTEL-1 instrument [38].



*Fig. 3. Comparison of the deposited energy spectra obtained by Liulin-4J instrument with another 3 Si telescopes and ISS-TEPC obtained during the ICCHIBAN-1 test run with 400 MeV/u Carbon ions*

Fig. 3 presents comparison of the deposited energy spectra obtained by Liulin-4J instrument (see Table 2, Item No 2) with another 3 Si telescopes (RRMD-III, DOSTEL, IV-CPDOS) and ISS-TEPC obtained during the ICCHIBAN-1 run with 400 MeV/u Carbon ions [39]. It is seen that the silicon detectors show good agreement of LET spectrum. The ISS-TEPC spectrum is wider but it comes from its structure (chord length).

For the purpose of in-space intercomparison between Liulin data with data from another instrument was prepared Fig. 4, which contains data from tissue equivalent proportional counter (TEPC) and 2 Liulin DES instruments - R3DE/R (see Table 1, Item No 9 and 11). The TEPC data are plotted in Fig. 4 using the opportunity provided by Zapp (2013) [40] and by the ‘Coordinated Data Analysis Web’ at the Goddard Space Flight Center (<http://cdaweb.gsfc.nasa.gov/>).



*Fig. 4. Comparison of the dose rates measured simultaneously by the R3DE/R instruments and NASA TEPC for a period on 13 June 2009 between 4:53 and 9:46 UT*

The dose rate data presented in Fig. 4 is plotted versus the UT and show three passes across the SAA region, which is denoted with labels SAA1-SAA3, seven passes across the high latitude GCR regions in both hemispheres and six passes across the magnetic equator. The analysis of the dose rate dynamics in Fig. 4 shows the following: 1) The R3DR SAA dose rates are the largest and reach  $2304 \mu\text{Gy h}^{-1}$  during the SAA1 maximum because R3DR is the lightest shielded instrument [41]. The more shielded by surrounding masses R3DE dose rates are about half that ( $1222 \mu\text{Gy h}^{-1}$ ), whereas the TEPC dose rates (heaviest shielded inside ISS) are the smallest ( $645 \mu\text{Gy h}^{-1}$ ). 2) The TEPC GCR dose rates are higher than the most of the dose rates measured with the R3DE/R instruments. This is because secondary particles build up additional doses in it. In the regions of the magnetic equator the smallest dose rate values are obtained by the R3DR instrument. The R3DE dose rates are in the middle, whereas the TEPC dose rates are the highest. The doses accumulated by the three instruments for 4 h and 56 m are  $261 \mu\text{Gy}$  (R3DR),  $132 \mu\text{Gy}$  (R3DE) and  $100 \mu\text{Gy}$  (TEPC).

DES intercomparison of dose rate measurements on aircraft was performed in a lot of cases. Below in the text we will report some of the more significant.

The exposure of aircraft crew to cosmic radiation has received a great deal of attention after the recommendation by the International Commission on Radiological Protection (ICRP) in 1990, that exposure to cosmic radiation in the operation of jet aircraft should be recognized as occupational exposure, initiated a number of new dose measurements onboard aircraft [42]. In the cited above report there is a large amount of DES dose rate measurements performed by Prof. Frantisek Spurny and compared with other instruments and computer codes, which confirm the ability of DES to characterize the radiation field at aircraft altitudes.

The response of a LIULIN-4 spectrometer was compared by Green et al. [43] to that of the HAWK TEPC <http://www.npl.co.uk/science-+-technology/ionising-radiation/neutron-metrology/hawk-tepc> on 42 aircraft flights in 2003–2004 covering the full range of cutoff rigidity values. On all flights, the absorbed dose measured by both instruments agreed to within 5%. These data provide an in-flight validation of the calibration factor determined by us in ground-based studies.

Getley et al. [44, 44a] performed intercomparison measurements by different detectors including TEPC and Liulin-4SA (see Table 2, Item No 5) on board Boeing 747-400 Qantas Airways flights from August 2008 to March 2009. The flight routes involved cross-equatorial flights between Sydney, Melbourne, and Los Angeles. A northern latitude flight traveled between Sydney, Hong Kong, London, and Singapore, and numerous high southern latitude flights were flown between Sydney and Johannesburg and Sydney and Buenos Aires. In the summary of the paper they wrote: “Comprehensive testing of both the Liulin and QinetiQ QDOS/Rayhound over a 6 month period, at both high northern and southern latitudes as well as in crossequatorial flights, suggests that both of these spectrometers have the ability to provide reliable dose assessments for aircrew monitoring.”

The boxes and additional constructive materials of the most of the DES instruments described in this paper provide between 0.41 and 0.6  $\text{g cm}^{-2}$  shielding. For the lower boundary of 0.41  $\text{g cm}^{-2}$  shielding the calculated stopping energy of normally incident particles to the detector is 0.78 MeV for electrons and 15.8 MeV for protons [33]. For 0.6  $\text{g cm}^{-2}$  shielding these values are 1.18 MeV for electrons and 27.5 MeV for protons. This means

that only protons and electrons with energies higher than the above mentioned values can reach the detector of the instrument.

## ***2.2. Dosimetric telescope (DT) instrumentation***

### ***2.2.1. DT description***

First application of the Liulin DT method was for the Liulin-5 instrument on ISS. Liulin-5 (see Table 1, Item No 6) is an active experiment in the spherical phantom [45]. The aim of Liulin-5 experiment is long-term investigation of the depth-dose distribution and continuous monitoring of the particle fluxes, dose rates, energy deposition and LET spectra in a radial channel of the Russian spherical tissue-equivalent phantom MATROSHKA-R [46, 47], using a telescope of three silicon detectors. Liulin -5 is sensitive to photons, electrons, protons and heavy ions. Liulin-5 charged particle telescope was launched to ISS by Progress-60 cargo craft in May 2007.

The investigation of the radiation environment in the phantom on ISS by Liulin-5 experiment envisages: i) measurement of the depth distributions of the energy deposition spectra, flux and dose rate, and absorbed dose  $D$ ; ii) measurement of the LET spectrum in silicon, and then calculation of LET spectrum in water and  $Q$ , according to the  $Q(L)$  relationship given in ICRP – 60, where  $L$  stays for LET.  $Q(L)$  is related functionally to the unrestricted LET of a given radiation, and is multiplied by the absorbed dose to derive the dose equivalent  $H$ .  $H$ ,  $D$  and  $Q$  are related by:

$$(2) \quad H = Q_{av}D ,$$

where  $D$  is the absorbed (integrated over all particles) dose, and  $Q_{av}$  is the dose averaged quality factor, given by:

$$(3) \quad Q_{av} = \int Q(L)D(L)dL /D$$

Liulin-5 consists of two units: a detector module and an electronics module (see Table 1, Item No 6). The detector module is mounted in the radial channel of the phantom, while the electronics is outside the phantom. More detailed description of Liulin-5 method and instrument can be found in [45, 48]. The detector module contains 3 silicon detectors (D1-D3) arranged as a particle telescope.

Fig. 5 is a schematic diagram of Liulin-5 and the spherical phantom. The sensitive thickness of the detectors D1 and D3 is 370  $\mu\text{m}$ , of D2 it is 360  $\mu\text{m}$  and the detectors' diameter is 17.2 mm. The D1 detector is placed at 40 mm depth in the phantom, D2 is at 60 mm and D3 is at 165 mm distance from its surface.

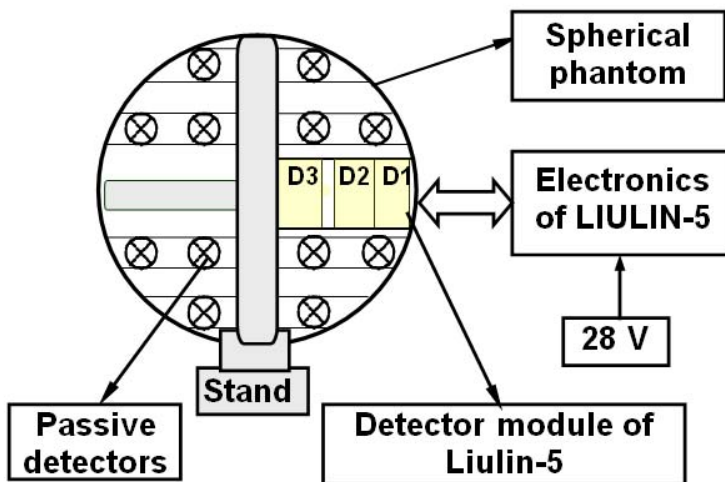


Fig. 5. Schematic diagram of Liulin-5 experiment in the spherical phantom

From each detector the energy deposition spectrum for a cycle of measurement is recorded in two 256 channels' sub-ranges. Then the overall energy deposition spectrum is constructed in 512 channels. The amount of energy  $\Delta E$  deposited in the detector is proportional to the value  $k1\sum(iN_i)+k2\sum(jN_j)$ , and the incident particle flux is proportional to  $\sum N_i+\sum N_j$ . Here  $i$  and  $j$  are the spectral channel numbers in the two sub-ranges (LLET and HLET),  $N_i$  and  $N_j$  are the amount of particles registered in channels  $i$  and  $j$  of the corresponding sub-ranges,  $k1$  and  $k2$  are coefficients. The values  $\sum(iN_i)$ ,  $\sum(jN_j)$ ,  $\sum N_i$ ,  $\sum N_j$  are recorded for given time intervals and are used for calculation of the doses and particle fluxes rates.

The absorbed dose in the detector is calculated as

$$(4) \quad D = \Delta E/m,$$

where  $m$  is the detector's mass.

The geometry factor for converting the measured in a single detector amount of particles into differential flux is  $14.6 \text{ cm}^2 \text{ sr}$ , assuming the incident flux is isotropic.

Detectors D1 and D2 operate in coincidence mode. The distance between D1 and D2 is 20 mm. The viewing angle of D1-D2 assembly is  $81.4^\circ$ . When a particle enters the telescope within the  $81.4^\circ$ -degree sensitivity cone, with energy enough to make it through both the D1 and D2 detectors, it is considered a coincident event. The energy deposition spectrum measured in the D1 detector in coincidence mode with the D2 is recorded and used to obtain LET spectrum. Since the incidence angle of the particles is not measured, the energy deposition is converted into mean LET in silicon as:

$$(5) \quad \text{LET}(\text{Si}_i) = \Delta E_i / h_{D1},$$

where  $\Delta E_i$  is the deposited energy in channel  $i$ ,  $\text{LET}(\text{Si}_i)$  is the LET in silicon in channel  $i$  (here  $i = 1-512$ ), and  $h_{D1}$  is the D1 thickness. Calculations show that the dependence of the telescope's effective area on particle incident angle is practically linear and decreases from  $2.324 \text{ cm}^2$  at  $0^\circ$  between the telescope axis and flux to  $0 \text{ cm}^2$  at  $40.7^\circ$ . The average increasing of particle range in the detector in case of nonparallel to the axis incidence is 7 %.

The LET spectra in silicon obtained are used for calculation of the differential and integral LET spectra in water, the absorbed dose rates and the quality factors. The geometry factor for converting the measured by the D1-D2 telescope amount of particles into differential isotropically incident flux is  $2.01 \text{ cm}^2 \cdot \text{sr}$ . The energy deposition in water (tissue) relative to that in silicon is taken to be 1.24, independent of particle energy. LET for water  $\text{LET}(\text{H}_2\text{O})$  is then found by the following relation:

$$(6) \quad \text{LET}(\text{H}_2\text{O}) = 1.24 \times \text{LET}(\text{Si}) / 2.34$$

Taking into account that the relation between  $\text{LET}(\text{H}_2\text{O})$  and  $\text{LET}(\text{Si})$  changes with proton energy  $E_p$  from 1.27 for  $E_p = 30 \text{ MeV}$  to 1.21 for  $E_p = 1000 \text{ MeV}$ , and that for a typical energy  $E_p = 100 \text{ MeV}$  the conversion coefficient is 1.24, the maximum difference of  $\text{LET}(\text{H}_2\text{O})$  obtained by using real conversion function and the simple conversion factor is less than 3 %.



To obtain the LET spectrum dose of isotropically incident particles, the dose calculated from the D1-D2 coincidences spectrum is multiplied by 13.5.

The instrument provides time resolved: Absorbed dose rate in each detector; Flux rate in the range  $0 - 4 \times 10^2 \text{ (cm}^2 \text{ s}^{-1}\text{)}$ , measured in each of the detectors; Energy deposition spectra in D1 detector in the range 0.45-63 MeV in 512 spectral channels; Energy deposition spectra in D2 detector in the range 0.45-60 MeV in 512 spectral channels; Energy deposition spectra in D3 detector in the range 0.2-10 MeV in 512 spectral channels; LET(H<sub>2</sub>O) spectra in the range 0.65-90 keV  $\mu\text{m}^{-1}$  in 512 spectral channels. The events exceeding the upper energy deposition or LET limit of each detector are recorded in the corresponding 512-th channel.

Second application of the DT method was for the Liulin-Phobos instrument (see Table 1, Item No 12) developed for the Phobos-Grunt mission [22]. The main goal of the Liulin-Phobos experiment was the investigation of the radiation environment and doses in the heliosphere at distances of 1 to 1.5 AU from the Sun and in the near-Mars space.

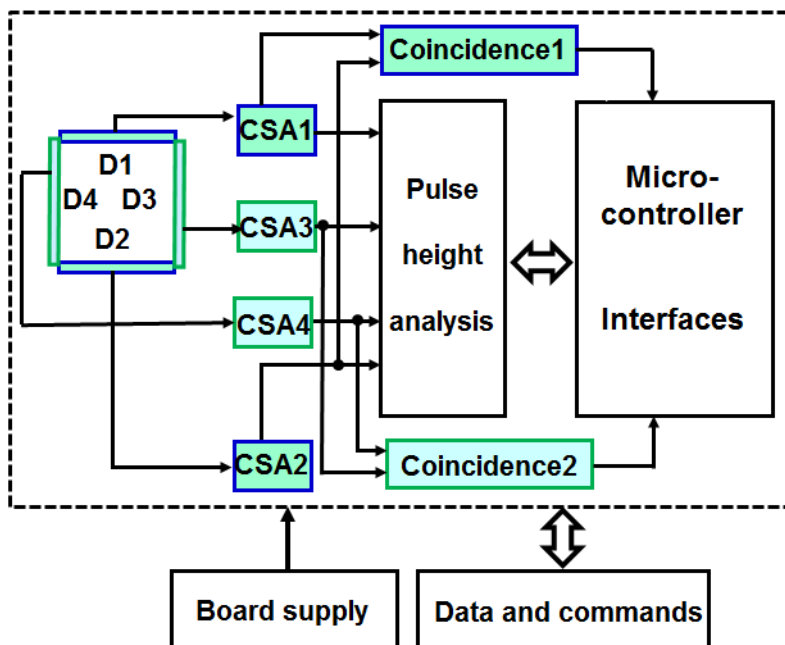


Fig. 6. Block-scheme of Liulin-Phobos charged particle telescope

Liulin-Phobos instrument consisted of two dosimetric telescopes - D1&D2, and D3&D4 arranged at two perpendicular directions. The block-schema of the instrument is shown in Fig. 6. Every pair of telescopes consists of two 0.3 mm thick Si PIN photodiodes, operating in coincidence mode to obtain LET. One of the detectors in every telescope measures the energy deposition spectrum in the range 0.1-10 MeV, and the other in the range 0.45-90 MeV. In that way every dosimetric telescope provides data in the energy deposition range 0.1 - 90 MeV. The instrument was designed to measure absorbed dose rate and particle flux every 60s, energy deposition spectra and LET spectrum every 60 min.

The parameters featured by Liulin-Phobos DT was: Absorbed dose rate in the range  $4 \times 10^{-8}$ -0.1 Gy h<sup>-1</sup>, and absorbed dose D, measured by every single detector; Particle flux in the range 0-10<sup>4</sup> cm<sup>-2</sup> s<sup>-1</sup>, measured by every single detector; Energy deposition spectra in the range 0.1-90 MeV, measured by every dosimetric telescope; LET spectrum (in H<sub>2</sub>O) in range 0.75–155 keV/μm, measured by every DT; Quality factor Q = f(LET) and average quality Q<sub>av</sub>; Dose equivalents H = Q<sub>av</sub> D, measured by two DT.

A similar to the Liulin-Phobos DT instrument is now under development for the ExoMars mission [49].

### **2.2.2. DT calibrations**

Liulin-5 was exposed to 400 MeV/n <sup>16</sup>O and 300 MeV/n <sup>56</sup>Fe beams during the ICCHIBAN-7 experiments [50] at the HIMAC in September 2005.

Fig. 7 shows the deposited energy distribution in the silicon detectors of Liulin-5 obtained during the exposures to 400 MeV/n <sup>16</sup>O [45]. At first the detector module of Liulin-5 was exposed perpendicular to the beam with beam center at the center of the detectors (0° inclinations). After that detector module of Liulin-5 was inclined at angles of 30° and 60° relative to the beam line and rotation was made around the centre of D1 detector. On each plot two distributions are seen – the left represents measured spectra in LLET range and the right represents measured spectra in HLET range of the detectors. We assume that HLET peaks correspond to the distribution of the main <sup>16</sup>O beam, and the LLET peaks correspond to scattered background beams. Most of HLET events registered in D3 detector exceed the upper energy loss range limit of that detector and were registered in the highest spectral channel as events of 10 MeV.

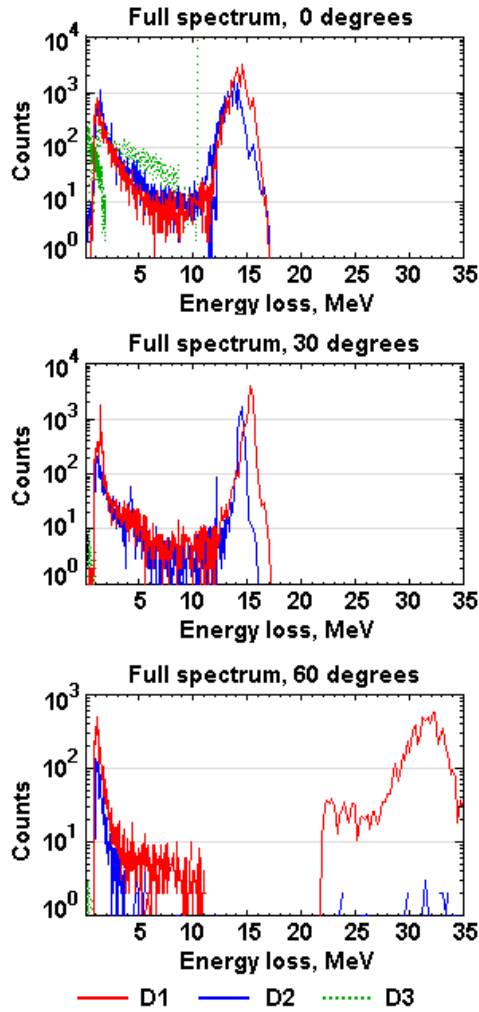
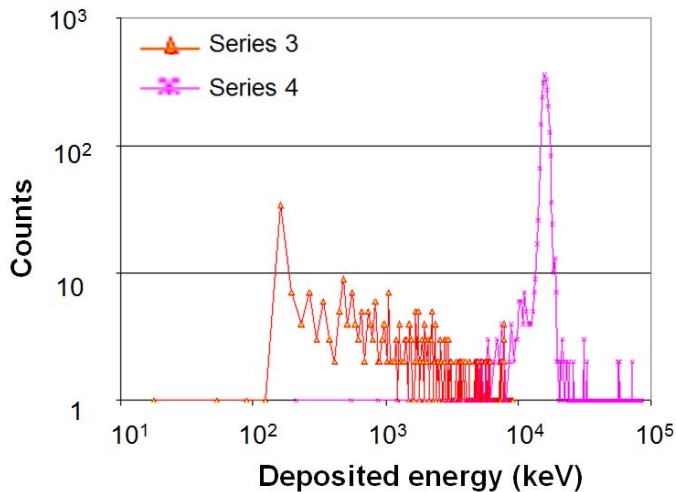


Fig. 7. Deposition energy distributions of  $^{16}\text{O}$  beam in the silicon detectors D1–D3 of Liulin-5

For the  $30^\circ$  exposure D3 detector was outside the main beam, and for the  $60^\circ$  exposure both D2 and D3 detectors were outside the main beam. That is why only scattered background beams in LLET ranges were registered in them.

As a result of the calibrations the Liulin-5 measurement range of LET(H<sub>2</sub>O) was estimated to be 0.65 –90 keVμm<sup>-1</sup>. This makes it possible for Liulin-5 to measure the low-LET components of cosmic radiation, as well as a significant part of biologically relevant high-LET heavy ion component of GCR that contribute to the radiation doses on ISS.

The Liulin-Phobos flight unit was calibrated with proton and heavy ion beams at the cyclotron and at the HIMAC accelerator at the NIRS, Japan in January-February 2009. The calibrations were performed in agreement with the Memorandum of Understanding on collaboration concerning development, calibration, space flight measurements and data analysis of the Liulin-F instrument onboard the Phobos-Soil mission, which was signed between STII-BAS, IBMP-RAS NIRS, Chiba, Japan.



*Fig. 8. LET spectrum of <sup>20</sup>Ne 600 MeV/u, obtained in D1&D2 telescope at 0° inclination of the telescope axis to the incident beam*

As an example of the obtained results Fig. 8 shows the energy deposition spectrum in the D2 detector in a coincidence mode with D1 (LET spectrum) of <sup>20</sup>Ne ions with energy 600 MeV/n [51]. The distribution was obtained at 0° inclination of the telescope's D1-D2 axis to the ion beam. The left part of the LET distribution was measured in low LET range of the detector and is mainly due to secondary radiation, resulting from interactions of primary neon beam with surrounding materials. The main peak represents the LET distribution of the neon ions and was measured in high LET range of this detector. The obtained LET(H<sub>2</sub>O) of <sup>20</sup>Ne 600

MeV/n is 26.7 keV/ $\mu\text{m}$  –it is in good agreement with the theoretically calculated value of 25.5 keV/ $\mu\text{m}$ , having in mind the shielding of the detectors. The results of the Liulin-Phobos calibrations at NIRS confirm the correctness of the electronic calibrations made preliminary.

### **3. Main experiments and results in space**

#### ***3.1. LIULIN experiment on MIR space station***

The Bulgarian-Russian dosimeter-radiometer LIULIN (see Table 1, Item No 1) was installed in the working compartment of the MIR space station [17]. The effective mass thickness of screening matter inside the working compartment of MIR is evaluated to be 6-15g cm<sup>-2</sup>. Thus the main contribution to the count rate is given by protons and electrons that, outside MIR space station, have energy large than 100 MeV and 10 MeV respectively. It uses a silicon detector with a thickness of 306 microns and area of 1.8 cm<sup>2</sup>. Simultaneous measurement of the energy absorbed in the detector and of the flux of particles are recorded and transmitted to Earth. The noise level of the detector and electronics was 83 keV. The dose sensitivity is 1 nGy/pulse. The detector unit (see Table 1, Item No 1) is a miniature, portable, self-indicating devise. LIULIN-Microcomputer unit (MCU) is an eight-bit microprocessor unit.

Main results obtained by the LIULIN device can be listed as follows:

- During the declining phase of 22nd solar cycle the GCR fluxes observed at  $L > 4$  have been enhanced from 50-70  $\mu\text{Gy day}^{-1}$  in 1989-1990 up to 130-140  $\mu\text{Gy day}^{-1}$  in 1993-1994. In same time the GCR flux increased from an average value of 0.58 cm<sup>-2</sup> s<sup>-1</sup> in 1991 up to 1.53 cm<sup>-2</sup> s<sup>-1</sup> in 1991 [52];
- The peak value of the dose rate and flux of particles measured by LIULIN in the SAA increase gradually by a factor of 2 between 1991 and 1994 at the altitude of 410 km. The increase is attributed to the decrease of the atmospheric density during the declining phase of solar activity, which is due to the lower rate of heating of the upper atmosphere when the solar UV and EUV radiation diminishes during the minimum of solar cycle A power law relationship has been deduced between local atmospheric density at the altitude of MIR station and the maximum dose rate in the center of the SAA when the neutral density decreased from  $8 \times 10^{-15}$  g cm<sup>-3</sup> to  $6 \times 10^{-16}$  g cm<sup>-3</sup> the maximum dose increases from 200 to 1200 mGy h<sup>-1</sup>, while the flux of particles increased from 30 to 120 cm<sup>-2</sup> s<sup>-1</sup> [52];

- LIULIN measurements represent the low altitude manifestation of radiation belts dynamics. Before the 23-26 March 1991 solar-geomagnetic events LIULIN dose and flux data exhibited one maximum located at  $L \sim 1.4$  the region of the SAA. It is due to the particles from the inner radiation belt. After the March 23 1991 geomagnetic storm a “new” maximum in LIULIN flux data was created at  $1.8 < L < 2.2$ . This was an unique phenomenon, not reported previously and after [http://www.stp.isas.jaxa.jp/akebono/RDM/rdm/rdmflux\\_1989\\_2010.gif](http://www.stp.isas.jaxa.jp/akebono/RDM/rdm/rdmflux_1989_2010.gif). It was a relatively stable configuration observed during the whole of 1991 independently of the geomagnetic conditions. It was identified in LIULIN data till the middle of 1993. The outer radiation belt maximum was frequently observed after geomagnetic disturbances as a dynamic structure for 1-3 months. ORB in MIR data was usually located at  $2.5 < L < 3.2$ . After long quiet conditions it disappeared [53];
- Several outstanding SEP took place during the LIULIN observations. SEP data are available for September 29, 1989, October 18, 1989, March 23, 1991, June 8 and 15, 1991, and June 26, 1992. Data analysis of them is presented in the paper by Shurshakov et al. [54].

### ***3.2. Experiments and results on ISS***

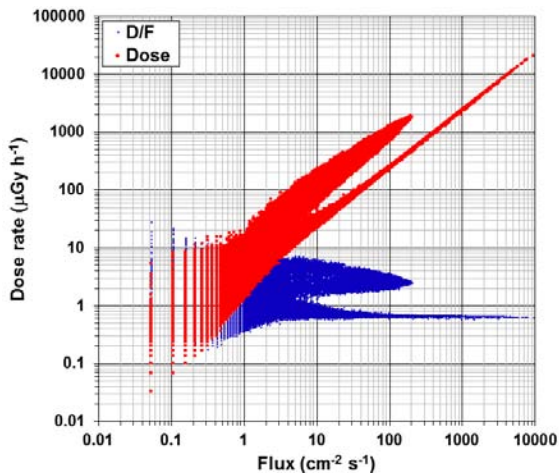
The largest amount of Liulin experiments in space since 2001 was performed on ISS. Listing them we have to mention: Liulin-E094 (April-August 2001), Liulin-ISS (September 2005-till now), Liulin-5 (May 2007-till now), R3DE (February 2008-September 2009) and R3DR (March 2009-August 2010) (see Table 1, Items No 3, 5, 6, 9, 11). Two of them Liulin-ISS and Liulin-5 are working until now. R3DR experiment is scheduled to be repeated as part of EXPOSE-R2 mission for 1.5 years since June 2014 at Russian Zvezda module of ISS [http://www.nasa.gov/mission\\_pages/station/research/experiments/211.html](http://www.nasa.gov/mission_pages/station/research/experiments/211.html).

#### ***3.2.1. DES data selection procedure***

The data selection procedure was established for DES instruments to distinguish between the three expected radiation sources: (i) GCR particles, (ii) protons with more than 15.8 MeV energy in the SAA region of the IRB and (iii) relativistic electrons with energies above 0.78 MeV in the ORB [25].

Fig. 9 is prepared to confirm these features with the R3DR data. The abscissa plots the measured flux in  $\text{cm}^{-2} \text{s}^{-1}$ , while the ordinate shows the dose rate in  $\mu\text{Gy h}^{-1}$  and dose rate to flux ratio (D/F) (or specific dose SD) in  $\text{nGy cm}^{-2} \text{particle}^{-1}$  [25, 55] for the period 1 April–7 May 2010, which is remarkable with very high ORB fluxes and respectively dose rates [8]. The large amount of experimental points (295374 points) in the diagonal of the figure is responsible for the dose rate values, which, as expected, are in linear dependence from the flux, while the almost horizontally plotted points present the D/F ratio.

Three branches in each graphic are differentiated and they look as a left hand wrist with two fingers. The wrist represents a highly populated part in the diagonal bunch of points: (1) it takes a large amount of the measured points in the range  $0.03\text{--}30 \mu\text{Gy h}^{-1}$ ; (2) for a fixed flux a wide range of doses is observed. These two features could be explained only by the GCR particles, which, being with small statistical relevance and high LET, are able to deposit various doses for fixed flux value. The smallest dose rates ( $0.03\text{--}0.4 \mu\text{Gy h}^{-1}$ ) are observed close to the magnetic equator, while the largest are at high latitudes. In the horizontal graphic this part of the data is represented with a similar large amount of points, which in large scale overlap the dose rate diagonal points.



*Fig. 9. Characterization of the R3DR predominant radiation sources by the dose rate from flux and dose to flux (D/F) dependencies*

The “index” finger is in the dose rate range 9–22,000  $\mu\text{Gy h}^{-1}$  and looks as a straight line. Its representation in the horizontal graphic is a finger extending up to 10,000 in  $\text{cm}^{-2} \text{s}^{-1}$ , with dose to flux values below 1  $\text{nGy cm}^{-2} \text{particle}^{-1}$ . This finger is based on low LET particles and could be formed only by the relativistic electrons [7] in the outer radiation belt.

The “big” finger in the diagonal graphic has a different source compared to the previous two because it is characterized by a high range of doses for fixed flux but the dose rates are in the range 30–1900  $\mu\text{Gy h}^{-1}$ . This amount of points could be formed only by protons from the IRB (The region of South Atlantic Anomaly (SAA)) whose dose depositions depend on the energy. The lower energy protons are depositing higher doses. In the horizontal graphic this finger has a similar form and is situated in the range 1.2–8.  $\text{nGy cm}^{-2} \text{particle}^{-1}$ . Both IRB and ORB fingers can be approximated by straight lines. From these approximations we obtain that 1 proton in IRB produces in the Silicon detector on average a dose of 1.4  $\text{nGy}$ , while 1 electron in ORB produces a dose of 0.33  $\text{nGy}$ , which is in good agreement with Heffner’s formulae [55].

The conclusion which can be drawn from Fig. 9 is that the data can be simply split in two parts by the requirements for the ratio  $D/F < 1$  and  $D/F > \text{nGy cm}^{-2} \text{particle}^{-1}$ . This will generate graphics, which will divide the IRB and ORB sources. GCR protons in equatorial and low latitude regions have very small fluxes of less than 1  $\text{particle cm}^{-2} \text{s}^{-1}$ , that is why the  $D/F$  ratio is not stable and varies in the range from 0.03 to 30  $\text{nGy cm}^{-2} \text{particle}^{-1}$  [8]. This variation makes the  $D/F$  ratio inapplicable for the characterization of the GCR radiation source.

### ***3.2.2. Liulin-E094 results***

The first use of DES in space was in the Liulin-E094 instrument (see Table 1, Item No 3), that was developed, qualified for space and used in the ESA Dosimetric Mapping-E094 experiment [10] on the US Laboratory module of the ISS as a part of the Human Research Facility in May-August, 2001 [18]. The main purpose of this experiment was to investigate the dose rate distribution inside the US Laboratory module and Node-1 of ISS.

In the paper by Dachev et al., 2006 [56] was developed a 3-D shielding model of the MDU unit and located it at the four locations in the ISS shielding model. Using the trapped proton differential spectra generated from the SPENVIS on-line capability for calculation of AP8 trapped proton



spectra and the high-energy proton transport code PDOSE we was able to calculate the doses at each locations of MDUs. The differences between the observed Liulin-E094 MDUs doses and calculated do not exceed 15%. The obtained data were also used for statistical validation of the high-charge and energy (HZE) transport computer (HZETRN) code [57-59].

### **3.2.3. *Liulin-ISS results***

Liulin-ISS instrument (see Table 1, Item No 3) was launched to the Russian segment (RS) of ISS in September 2005. It contains four Mobile Dosimetry Units (MDU) with displays and Control and interface unit and was used in the Service Radiation Monitoring System of the RS of ISS [60]. Following information may be displayed: Current dose in  $\mu\text{Gy h}^{-1}$ , Current event rate (Flux)  $\text{cm}^{-2} \text{s}^{-1}$ , Accumulated from the “Switch ON” dose mGy. The battery operation time of the MDU is about 7 days. The 4 MDU can be used as personal dosimeters in case of dangerous SEP. Because some problems with the telemetry system connections the instrument was not used as planned and now under development is a new instrument with similar functions, which is expected to be in space in the next 2-3 years.

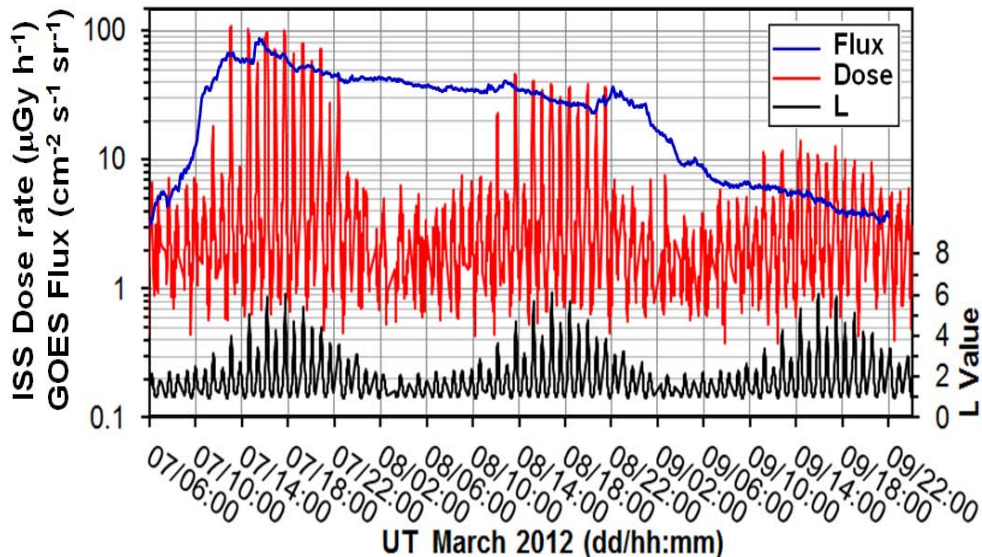
### **3.2.4. *Liulin-5 results***

Liulin-5 DT instrument (see Table 1, Item No 5) [21] was launched to the RS of ISS in May 2007. Measurements with Liulin-5 were conducted in the spherical tissue equivalent phantom of Matroshka- R experiment located in the PIRS-1 module of ISS in the period July 2007 – March 2010, corresponding to the minimum of solar activity in 23rd solar cycle. Also measurements corresponding to the maximum of 24th solar cycle have been conducted since December 2011 till now (April 2014) both inside and outside the phantom located in the MIM1 module of ISS. The main results obtained during the minimum of 23rd solar cycle were published in [61-63]. (Semkova et al., 2012, 2013a, 2013b)

During the SEP events of 7-12 March 2012 (see Fig. 10) at  $L > 3$  the particle flux and dose rates increased in all three detectors of Liulin-5 charged particle telescope located at 40, 60 and 165 mm depths along the radius of the tissue-equivalent spherical phantom in MIM1 module of ISS [63a].

The additional absorbed dose at 40 mm depth in the phantom received from SEP event on 7-9 March 2012 was approximately 180  $\mu\text{Gy}$ . The additional dose equivalent at 40 mm depth in the phantom received

from that event was about 448  $\mu\text{Sv}$ . The additional exposures received from SEP event are comparable to the average daily absorbed dose and dose equivalent measured in the spherical phantom in ISS during quite periods.



*Fig. 10. Proton flux with energies  $\geq 100$  MeV measured by GOES-13 (blue curve), the dose rate in D1 detector of Liulin -5 measured outside the SAA (red curve), and the corresponding L-values (black curve) versus time during the March 2012 SEP event*

In Figure 10 it is seen that there is a good agreement of Liulin-5 dose rates trend during the SEP event with the proton flux of energies  $\geq 100$  MeV (able to penetrate inside ISS) measured by GOES – 13 satellite (blue line).

### 3.2.5. R3DE instrument results

R3DE instrument (see Table 1, Item No 9) with 256 channels ionizing radiation monitoring spectrometer and 4 channels UV spectrometer worked on the ESA European Technology Exposure Facility (EuTEF) platform inside of EXPOSE-E facility outside of the European Columbus module of the ISS between 20 February 2008 and 1 September 2009 with 10-s resolution behind  $0.45 \text{ g cm}^2$  of shielding [25, 32].

There are 2 major discoveries connected with the R3DE instrument. The first one is the already mentioned large relativistic electrons doses

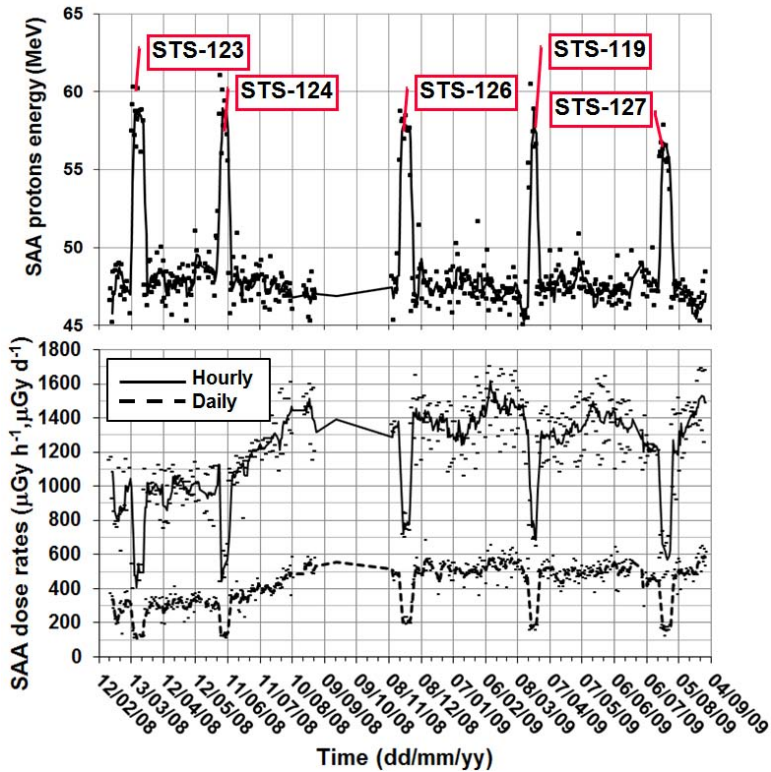
[32, 41], while the second one is the decrease of the SAA dose rate during the dockings of the USA space shuttle with ISS [64].

Figure 11 shows the result of measurements of the SAA doses for the time span between 22/03/2008 and 01/09/ 2009. SAA proton energies in MeV, maximal dose rates in  $\mu\text{Gy h}^{-1}$ , and daily dose rates in  $\mu\text{Gy d}^{-1}$  are presented in the two panels. The maximal dose rates are the value in the interval from 00:00 to 24:00 h, which is larger than any other SAA 10 s measurement. The largest value here was  $1708 \mu\text{Gy h}^{-1}$ , and the average was  $1218 \mu\text{Gy h}^{-1}$ .

The relatively low dose rates at the left side of Fig. 11 have to do with the ISS altitudes in the range of 350—365 km. The increase of the station altitude up to 365—375 km after 21 June 2008 led to an increase of the maximal SAA dose rate above  $1200 \mu\text{Gy h}^{-1}$ .

The main feature seen in Fig. 11 is that during the five space shuttle docking times the SAA maximal doses fall by  $600 \mu\text{Gy h}^{-1}$  and reach an average level of 400—500  $\mu\text{Gy h}^{-1}$  for the STS-123 and STS-124 missions. For STS-126, STS-119, and STS-127, the drop was also  $600 \mu\text{Gy h}^{-1}$  from an average level of  $1400 \mu\text{Gy h}^{-1}$ .

The analysis of the daily average SAA dose rate for the studied period shows that before 21 June 2008 it was around  $300 \mu\text{Gy d}^{-1}$ , after 21 June 2008 it started to increase, and on 31 July it reached a value of  $500 \mu\text{Gy d}^{-1}$ , the level at which the daily average SAA dose rate stayed until the end of the observations in September 2009. The dockings of the space shuttles decreased the daily average SAA dose rate by about  $200 \mu\text{Gy d}^{-1}$ . Similar reductions of the SAA dose rates were observed by Semones (2008) [65] with the TEPC in the Columbus module for the period 4—24 March 2008. Because of the larger shielding inside the Columbus module, the reduction reported in [65] was from 120 to  $97 \mu\text{Gy d}^{-1}$  during the STS-123 docking time. Benghin et al. (2008) [66] also reported changes in the ratio of daily dose rates of the unshielded detectors numbers 2 and 3 of the DB-8 system during the shuttle dockings.



*Fig. 11. Daily and hourly SAA dose rates and SAA proton energies measured with the R3DE instrument during the EXPOSE-E mission. The space shuttle dockings at the ISS create strong decreases in the hourly and daily dose rates due to the additional shielding effect of the space shuttle body on the R3DE detector. At the same time the energy of the protons in the SAA increases. The space shuttle visits are marked with the STS number of flight*

The investigation of the averaged energy of the protons in the SAA region is shown in the upper panel of Fig. 12, which reveals that the shuttle dockings increased this energy from about 48 MeV to 58 MeV. The energy of the protons incident normally to the detector is calculated by using the experimental formula described by Heffner (1971) [55]. The increase of the averaged proton energy in the SAA region during the shuttle dockings can be explained with the increase of the values in the entire energy range caused by the stopping of the lowest-energy protons in the mass of the space shuttle.

Figure 12 shows the dose rate dynamics observed by 3 different instruments around the time of Space Shuttle (STS-123) docking and

undocking in the time frame 5-31 March 2008. The measured absorbed doses in each exposure interval are presented by black diamonds, while the obtained statistically moving average doses are shown with heavy (red) lines. The numbers there correspond to the number of single measurements used in the moving average calculation.

The 3 panels contain data as follows: In Figure 12a there are the NASA TEPC absorbed dose rate data, which by the selection to be higher than  $100 \mu\text{Gy h}^{-1}$  present only the SAA maxima. First part of the data between 5 March and 14:03:37 at 10 March are from position SM-410, while second part till 31 March is from position COL1A3. Data are obtained from <http://cdaweb.gsfc.nasa.gov/> server and prepared by N. Zapp [40]; Figure 12b contains Liulin-5 [45] dose rate data from the first detector selected in same way as the TEPC data; Figure 12c contains R3DE dose rate data selected as the other 2 data sets. Only here the lowest dose rates are  $200 \mu\text{Gy h}^{-1}$ .

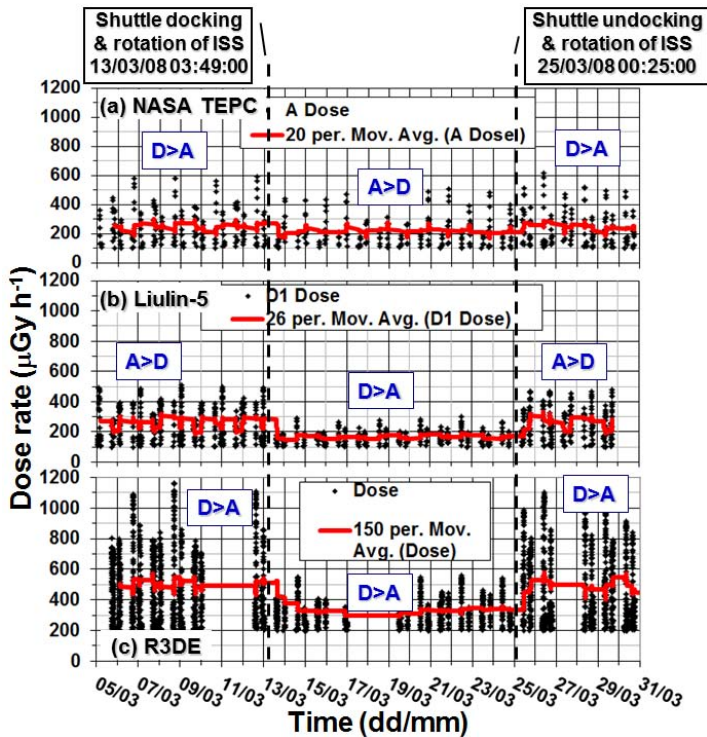


Fig. 12. Variations of the dose rates by NASA TEPC, R3DE and Liulin-5 instruments close to STS-123 docking in the time frame 5-31 March 2008

Because of the large time interval on the X axis in Figure 6 the 6-8 ascending and descending crossings of the SAA anomaly per day are presented by a pair of 2 bars. The first one corresponds to the descending orbits, while the second one to the ascending orbits during one series of 6-8 crossings. The differences in the dose rate amplitudes are produced by the east-west asymmetries of the proton fluxes in the region of the SAA [57]. These amplitudes are additionally stimulated to changes by the attitude of the ISS, which changes by 180° during the Shuttle docking period and reversed after it [67].

The relations between ascending and descending amplitudes of the dose rates for each instruments before, during and after the Shuttle docking are underlined by text boxes, which contain inequalities labelled by  $D > A$  when the descending dose rates were greater than ascending ones and in reverse with  $A > D$  when the other relation was fulfilled. For the R3DE instrument there were no changes of the amplitudes relations. At any time the descending dose rate value was greater than the ascending one. This behaviour can be explained by the position of the R3DE instrument on the top of EuTEF where it is not shadowed by the Columbus body from SAA protons drifting to the west. The other 2 instruments showed rotation of the ascending descending inequalities connected with the Shuttle docking. These relations are explained more precisely in the next paragraph.

It is well seen that all 3 data sets recorded a decrease in the dose rates after the docking of Space Shuttle at 03:49 on 13<sup>th</sup> of March 2008. To emphasize the decreases moving averages lines are calculated and presented by heavy lines in each panel of figure 6. For R3DE the decrease in moving averages was from 500 to 300  $\mu\text{Gy h}^{-1}$  or about 40% from the value before the docking. The Liulin-5 data decreased from 300 to 180  $\mu\text{Gy h}^{-1}$  or again about 40% from the value before the docking. TEPC dose rates obtain the smallest decrease from 280 to about 200  $\mu\text{Gy h}^{-1}$ , which is about 30% decrease. Dose rates measured by all 3 instruments returned to the values before the docking of STS-123 after 00:25 on 25<sup>th</sup> of March, when the undocking of Space Shuttle occurred.

### ***3.2.6. R3DR instrument results***

The R3DR spectrometer (see Table 1, Item No 11) was launched inside of the EXPOSE-R facility to the ISS in December 2008 and was mounted at the outside platform of the Russian Zvezda module of the ISS.

The first data were received on March 11, 2009. Until the end of August 2010 the instrument worked almost continuously with 10 seconds resolution; the data were recorded on the ISS. Comprehensive presentation of the R3DR results inside of the EXPOSE-R facility can be found in [68].

In Figure 4 there was already presented a comparison of data obtained simultaneously by R3DE/R instruments and NASA TEPC. The main conclusion from the comparisons of data between R3DE and R3DR instruments [41] is that the values of the dose rates produced by different radiation sources around the ISS did have large and rapid variations in space and time. All obtained data can be interpreted as possible doses obtained by cosmonauts and astronauts during Extra Vehicular Activities (EVA) because the R3DE/R instrument shielding is very similar to the Russian and American space suits' average shielding [3]. Fast, active measurements at the body of each astronaut to obtain the exact dynamics of the dose accumulation during EVA are required.

An instrumental solution was proposed in [69], where the possible hardware and software improvements for a new Liulin type dosimeter were proposed. New instruments will be able, on the basis of the analysis of the shape of the deposited energy spectrum and the value of the dose to flux ratio, to distinguish the different types of radiation sources in the ISS radiation environment as GCR, IRB protons and outer radiation belt electrons. They will measure, calculate, store and present on display the fast variations of the absorbed and ambient dose equivalent doses in any of the possible surrounding mass distributions.

### ***3.3. Experiments and results on satellites***

#### ***3.3.1. Results obtained at Foton M2/M3 satellites***

Radiation Risks Radiometer-Dosimeter (R3D) for Biopan (R3D-B) with 256 channels ionizing radiation monitoring spectrometer and four channels UV spectrometer known as R3D-B2 (see Table 1, Item No 3) was successfully flown 31 May–16 June 2005 inside of the ESA Biopan 5 facilities on Foton M2 satellite. The operation time of the instrument was about 20 days for fulfilling of the total 1.0 MB flash memory with 30 s resolution [70]. R3D-B3 spectrometer (see Table 1, Item No 7) was with almost same mechanical characteristics as R3D-B2. Larger 2.0 MB flash memory was used for about 30 days measurements. It was successfully flown 14–29 September 2007 inside of the ESA Biopan 6 facilities on Foton

M3 satellite. Together with R3D-B3, the Liulin-Photo instrument (see Table 1, Item No 8) was flown but inside of the capsule of the Foton M3 satellite [70a]. Most important findings in the R3D-B2/B3 data were the measurements of high doses delivered by relativistic electrons at altitudes below 300 km and latitudes above 50° geographic latitude in both hemispheres [7].

### 3.3.2. Results obtained at Chandrayaan satellite

RADOM spectrometer-dosimeter (see Table 1, Item No 10) was successfully used on the Indian Chandrayaan-1 Moon satellite from 22 October 2008-30 August 2009. It started working 2 h after the launch with 10 seconds resolution behind about 0.45 g cm<sup>-2</sup> shielding. The instrument sent data for a number of crossings of the Earth radiation belts and continued to work on 100 and 200 km circular lunar orbits measuring mainly the GCR environment [34].

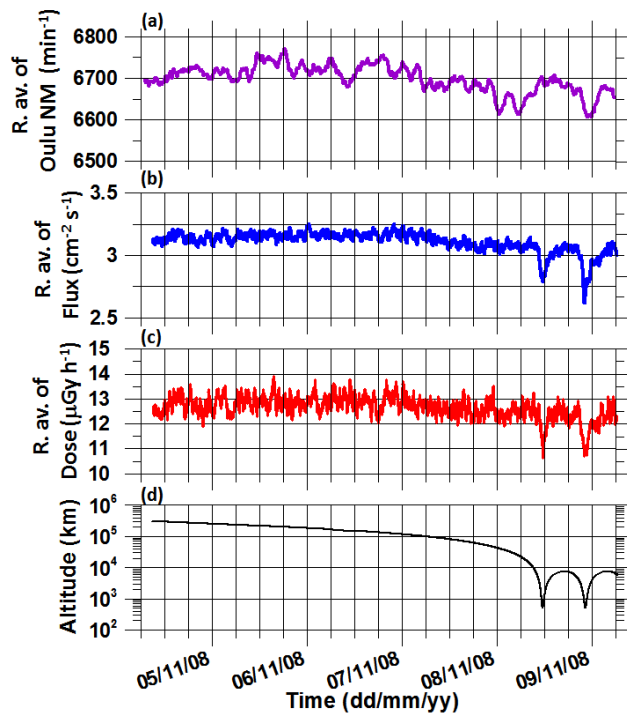


Fig. 13. RADOM observations during lunar transfer trajectory and lunar orbit capture. The distance is from the Moon. The trends in particle flux coincide with the Oulu neutron monitor data trends



Chandrayaan-1 was placed into the lunar transfer trajectory on 3rd November 2008 (13th day after launch) and a lunar orbit capture manoeuvre was carried out on 8th November (18th day after the launch). Fig. 13 shows RADOM observations for about 3 days before the lunar orbit capture and about one day after it. More than 40000 measurements with 10 s resolution are used for the figure. Figures 13b and 13c show the moving average over 200 points of measured particle flux and the absorbed dose rate respectively. Figure 13d shows the distance from the Moon (in km), while the Figure 9a shows the Oulu Neutron Monitor running average of measured count rate per minute averaged over 10 minutes. The average dose rate from more than 33000 measurements in the altitudinal range between 308000-20000 km from the Moon is  $\sim 12.76 \mu\text{Gy h}^{-1}$ . The range of the real measured dose rates is between 3.34 and 41.34  $\mu\text{Gy h}^{-1}$  with a standard deviation of 4.25  $\mu\text{Gy h}^{-1}$ . The average flux is 3.14 particles  $\text{cm}^{-2} \text{s}^{-1}$ , while the real flux range is between 1.71 and 4.82 particles  $\text{cm}^{-2} \text{s}^{-1}$  with a standard deviation of 0.41  $\text{cm}^{-2} \text{s}^{-1}$ . Figures 13b and 13c don't show this real dynamics of the values because the moving averages are plotted there. These values of the dose rate and flux may be used as referee values for the "deep space" radiation conditions at this very low level of solar activity and respectively.

For the above mentioned altitudinal range the flux correlates with the Oulu NM count rate and respectively with the solar activity. Later on during the two closer approaches to the Moon at an altitude about 508 km the flux and the dose rate decrease because the enhanced shielding of the cosmic rays by the Moon body itself. A closer look at the Figure 13a reveals that the second periselene crossing is deeper than the first one. This is mostly related with a local increase of the solar activity as evident from the simultaneous decrease of the Oulu NM count rate.

RADOM observations which began within two hours after launch of the Chandrayaan-1 and continued until the end of the mission demonstrated that it could successfully characterize different radiation fields in the Earth and Moon environments. Signature and intensity of proton and electron radiation belts, relativistic electrons in the Earth magnetosphere as well as galactic cosmic rays were well recognized and measured. Effect of solar modulation of galactic cosmic rays could also be discerned in the data. The electron radiation belt doses reached  $\sim 40000 \mu\text{Gy h}^{-1}$ , while the maximum flux recorded was  $\sim 15000 \text{cm}^{-2} \text{s}^{-1}$ . The proton radiation belt doses reached the highest values of  $\sim 130000 \mu\text{Gy h}^{-1}$ , while the maximum flux was  $\sim 9600 \text{particle cm}^{-2} \text{s}^{-1}$ . Comparison of these results with other similar instruments

on board ISS shows good consistency, indicating nominal performance RADOM. Outside the radiation belts, en-route to the Moon, the particle flux ( $\sim 3$  particle  $\text{cm}^{-2} \text{s}^{-1}$ ) and corresponding dose were very small ( $\sim 12 \mu\text{Gy h}^{-1}$ ) which further decreased slightly in the lunar orbit because of the shielding effect of the Moon. Average flux and dose in lunar orbit were  $\sim 2.45 \text{ cm}^{-2} \text{ s}^{-1}$ , and the corresponding absorbed dose rate was  $9.46 \text{ cm}^{-2} \text{ s}^{-1}$  respectively at 100 km orbit. These increased to  $2.73$  particles  $\text{cm}^{-2} \text{ s}^{-1}$  and  $10.7 \mu\text{Gy h}^{-1}$  respectively, at 200 km orbit. The total accumulated dose during the transfer from Earth to Moon was found to  $\sim 1.3$  Gy.

### ***3.3.3. Results obtained at “BION-M” №1 spacecraft***

“BION-M” №1 was a low Earth orbit satellite that orbited the Earth with a period of 89.9 min, an inclination of  $65^\circ$  with respect to the Earth’s equator, and with an altitude above the Earth surface in the range 253–585 km. The final orbit of the satellite was almost circular with an apogee of 585 km and a perigee of 555 km altitude. The final orbital parameters were reached after 21 April 2013 [71]. Space radiation has been monitored using the RD3-B3 spectrometer-dosimeter (see Table 1, Item No 13), which was mounted inside of the satellite in a pressurized volume together with biological objects and samples. The RD3-B3 instrument is a battery operated version of the spare model of the R3D-B3 instrument developed and built for the ESA BIOPAN-6 facility on Foton M3 satellite in September 2007 [70].

The observed hourly and daily IRB dose rates at the “BION-M” №1 satellite are the highest seen by us during our measurements on “Mir” and the ISS space station and on Foton-M2/M3 satellites because the altitude of the “BION-M” №1 orbit was the highest in comparison with all missions mentioned above. The same is valid for the GCR doses. The observed ORB doses are smaller than the ones measured outside the ISS because of the higher shielding on the “BION-M” №1 satellite.

### ***3.4. Main experiments and results at aircraft balloon and rocket***

Table 2 lists DES Liulin type experiments on aircraft, balloon, rocket and mountains peaks. The pictures shown for items 2 and 8 are the latest versions of the instruments used in this category. For some of the mentioned in these rows references the instruments was housed in different that the shown in the pictures.

The Liulin-4C, MDU#2 instrument (see Table 2, Item No 1) worked successfully during the flight of French balloon up to 32 km altitude in the region of the Gap town in Southern France on 14<sup>th</sup> of June 2000. This experiment was performed by the Nuclear Physics Institute, Czech Academy of Sciences [72].

One battery-powered DES of Liulin-4J (see Table 2, Item No 1) type performed dosimetric measurements of the ionizing radiation environment at ~20 km altitude aboard NASA's Lockheed ER-2 high altitude research aircraft in October-November 2000 from Edwards Air Force Base (AFB) in Southern California and flew over the border region dividing Central California from Central Nevada [73].

Mobile Dosimetry Units MDU-5 and 6 (see Table 2, Item No 2) was used for long-term measurements between 2001 and 2014 on Czech Airlines (CSA) aircraft at different routes. Data obtained were used for comparison with model calculated doses for the purposes of individual monitoring of aircrew [30, 31]. Fig. 14 presents almost one solar cycle data from these flights, which are publicly available in database of measurements. (<http://hroch.ujf.cas.cz/~aircraft/>) [74, 74a]. Please see Fig. 14 captions for more details.

Very similar instruments to the Mobile Dosimetry Units MDU-5 and 6 was used by scientific groups in Spain [76] and Korea [77] for radiation measurements at aircrafts.

Three battery-powered DES (see Table 2, Item No 3) were operated during the 8 June 2005 certification flight of the NASA Deep Space Test Bed (DSTB) balloon at Ft. Sumner, New Mexico, USA. The duration of the flight was about 10 hours ([http://wrmiss.org/workshops/tenth/pdf/08\\_benton.pdf](http://wrmiss.org/workshops/tenth/pdf/08_benton.pdf)).

Liulin-6S, Lilun-M, Liulin-6MB and Liulin-6R (see Table 2, Item No 4) are internet based instruments [78]. They use internet module to generate web page. The obtained deposited energy spectra data are transmitted via LAN interface by HTTP and FTP protocols. They worked for different periods since 2005 at Jungfrau (Switzerland) 3453 meters Above Mean Sea Level (AMSL) <http://130.92.231.184/>, Moussala (Bulgaria) 2925 meters AMSL <http://beo-db.inrne.bas.bg/moussala/> and Lomnický štít (Slovakia) 2633 meters AMSL <http://147.213.218.13/> peaks and at ALOMAR observatory in Norway (<http://128.39.135.6/>) [17]. The three peak instruments are working well till now (April 2014) and their data can be obtained online on the mentioned above addresses.

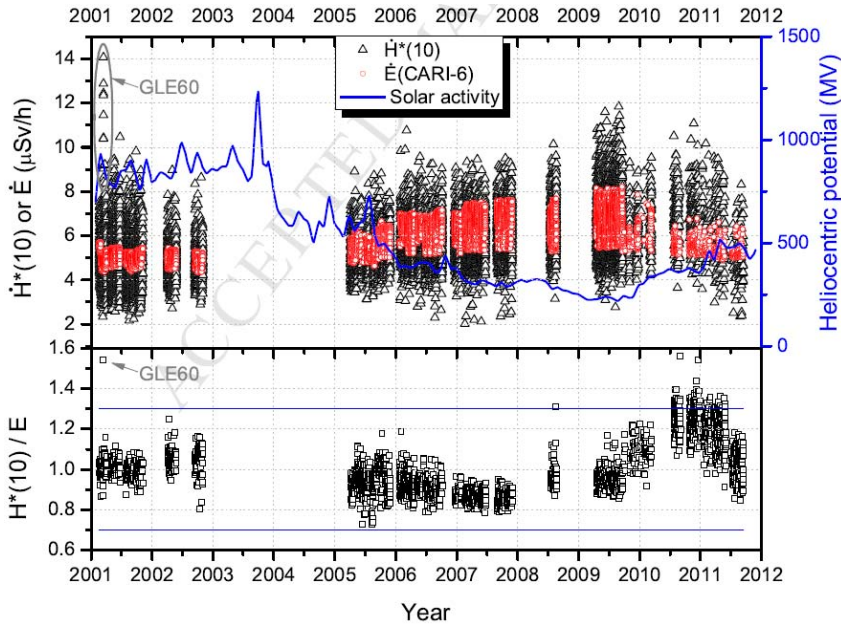


Fig. 14. Top panel: Ambient dose equivalent ( $H^*(10)$  - black triangle) dose rates determined by Liulin and effective dose rates ( $E(\text{Cari-6})$  – red circles) calculated with CARI-6 code [75] plotted as a function of time (only data at 35000 (10.67 km) and effective vertical cut-off rigidity [14] ( $VCR \leq 3.5$  GV) are shown).

Solar activity is expressed via the heliocentric potential).

Bottom panel: Ratios of integral values per whole flight between ambient dose equivalents,  $H^*(10)$ , estimated with Liulin, and effective doses,  $E$ , calculated with CARI-6 plotted as a function of time.  $\pm 30\%$  confidence band is plotted with 2 horizontal blue lines

Liulin-4SA (see Table 2, Item No 5) spectrometer was designed in 2005 under the request of Captain Ian Getley pilot of Boeing 747-400, Qantas Airways aircraft [44]. Liulin-4SA was used inside of the cockpit of Boeing 747-400 aircraft and provided on LCD display data for the local dose rate and flux simultaneously with the flight altitude, longitude and latitude, obtained from build-in GPS receiver for each measurements interval (usually 60 sec). Pre-programmed alert signals was able to be initiated when the measured dose rate exceed preliminary set levels for 3 subsequent measurement intervals.

The presented in Table 2, Item No 6 two Liulin DES systems consists of 4 dosimetry units (DU) and 1 control and interface unit (CIU).

The Liulin-6U instrument was delivered to NASA, Marshall Space Flight Center, USA in 2005. It was planned to be used in a balloon experiment [79]. The second one is delivered to the Skobeltsyn Institute of Nuclear Physics at Lomonosov Moscow State University in 2010. It was planned to be used in the RAZREZ system for RADIOSCAF experiment on ISS [80, 81].

Liulin-R instrument (see Table 2, Item No 7) was successfully launched on HotPay2 rocket from Andoya Rocket Range (ARR), Norway, on 31<sup>st</sup> of January, 2008 at 19:14:00 and rising up to 380 km altitude, as a part of an EU financed scientific program called eARI (ALOMAR eARI project) [82].

Wissmann et al. [83] performed 5 balloon experiments up to 30 km altitude using Liulin-6RG spectrometers (see Table 2, Item No 8) between July 2011 and August 2012. The Liulin instruments were powered and transmitted the obtained in 30 sec deposited energy spectrum to data logger, developed in Physikalisch-Technische Bundesanstalt (PTB), Germany.

The presented in Table 2, Item No 9 Liulin spectrometer is the last generation of series of instruments with build-in GPS receiver and 1 or 2 MB SD card. First this type of instruments (LIULIN-4N) was used by colleagues from Department of Chemistry and Chemical Engineering, Royal Military College of Canada in 2003-2005 [43, 84]. Two different methods of determining the route  $H^*(10)$  value from the LIULIN data were examined, which agree very well the  $H^*(10)$  values measured by the TEPC (within the 20% error inherent within both instruments).

### ***3.5. Profile of the ionizing radiation exposure between the Earth surface and free space***

Fig. 15 presents the synthesized altitudinal profiles of the moving averages (over 4 points) of 3 parameters: absorbed dose rate in  $\mu\text{Gy h}^{-1}$  (heavy line), flux in  $\text{cm}^{-2} \text{s}^{-1}$  (long (red) dashed line) and specific dose (SD) in  $\text{nGy cm}^2 \text{particle}^{-1}$  (short (blue) dashed line). On the left side of the figure are listed the carriers, instruments, time, averaged geographic coordinates of the measured values and their altitudinal range in km. On the right side are listed the conditions and predominant radiation sources for the places pointed with the arrows. The figure is similar to the published in [86] Fig.2 but improved with the new data obtained with RD3-R3 instrument on

“BION-M” No1 satellite and Liulin-5 data on ISS for the period of flight of “BION-M” No1 satellite - 21/04/-13/05/2013.

Fig. 15 contains original experimental data, which are compared and plotted to reveal a unified picture how the different ionizing radiation sources contribute and build the space radiation exposure altitudinal profile from the Earth surface up to the free space. The dose rate and flux data cover 7 orders of magnitude and can be used for educational purposes and also as reference values for new models. The presentation of data in kilometers above the Earth surface instead in L values allows space agencies medical staff and that not specialized in the geophysics support to use them for a first approach for the expected human exposure at different altitudes and also the general public and students to have a simple knowledge about the position of the most common maxima of exposure around the Earth and up to free space.

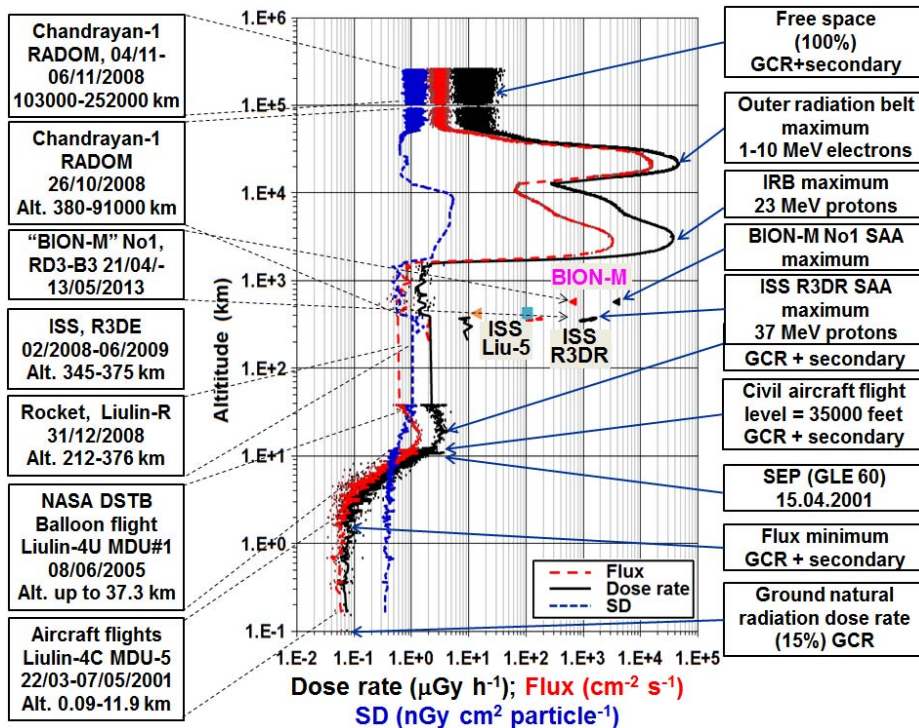


Fig. 15. Variations of the absorbed dose rate, flux and specific dose for altitudinal range from 0.1 to 250,000 km. (For interpretation of the references to color in this figure legend, the reader is referred to the web version of this article.)





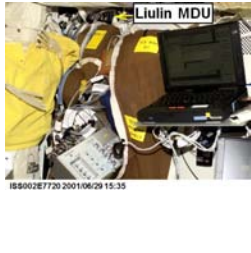

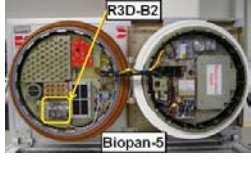



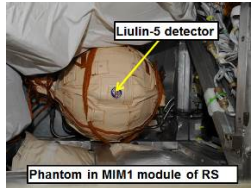

## Conclusions

The Liulin type low mass, dimension and price instruments during the period 1989-2014 proved their ability to characterize the radiation environment at the: ground, mountain peaks, aircraft, balloon, rocket and spacecraft.



## Acknowledgements

The authors would like to thank to: V. Petrov, V. Shurshakov, V. Benghin and I. Chernykh from Institute of Biomedical Problems, Moscow, Russia for the long lasting and fruitful scientific cooperation since the development of the first LIULIN instrument in 1986; G. Horneck and G. Reitz from DLR, Institute of Aerospace Medicine, Germany, D.-P. Häder, M. Lebert and M. Schuster from Department für Biology der Friedrich-Alexander-Universität, Germany for the leadership and cooperation in the experiments on ESA Foton-M2/M3 spacecraft and ISS; F. Spurny, and O. Ploc from Nuclear Physics Institute, Czech Republic for work on the radiological interpretation of Liulin data and for the leadership in the use of Liulin instruments on aircraft; K. Fujitaka, Y. Uchihori and H. Kitamura from National Institute of Radiological Sciences, Chiba, Japan for the leadership in the calibrations of Liulin instruments on protons and heavy ions; J. Lemaire, from Institut d'Aeronomie Spatiale de Belgique for the help in the interpretation of LIULIN data; Gh. Gregoire and H. Schnitz from Institut de Physique, Universite Catholique de Louvaln, Belgique, for the Liulin-ISS calibrations; E.G. Stassinopoulos, former Director of NASA-GSFC Radiation Physics Office for the support and help in the Liulin-3M calibrations; E. Benton from Department of Physics, Oklahoma State University, USA for the support and NASA balloon data; J. Miller, Lawrence Berkeley National Laboratory, Berkeley, USA for the post-calibrations of LIULIN instrument; ISRO staff and more specially to: M. Annadurai, Project Director and J.N. Goswami, Project scientist of Chandrayaan-1 satellite, P. Sreekumar and V. Sharan, Space Astronomy & Instrument Division, ISRO, Bangalore, India for the RADOM instrument support; M.T. Giardi and M. Damasso, Institute of Crystallography-National Research Council, Roma, Italy for the Liulin-Photo cooperation.

Table 1. Liulin type experiments performed during satellite missions

Item No	Satellite Date begin-Date end Available number of measurements	Experiment name PI CoPI References	Instrument Size [mm]/Mass [kg] Place Shielding [g cm <sup>-2</sup> ] Resolution [sec]/[min]	Instrument Location image	External view of the instrument
1	MIR SS 04/1988-06/1994 > >2,000,000 measurements	LIULIN V. Petrov, IMBP; Ts. Dachev, SRTL.  Dachev, et al., 1989. [17]; Shurshakov et al., 1999. [54].	LIULIN 1 DU (109x149x40 mm, 0.45 kg); 1 MCU (300x220x187 mm, 6.5 kg)  Inside different modules of MIR SS >5 g cm <sup>-2</sup> 30 sec		
2	Mars-96 16/11/1996  (The satellite was lost because of rocket booster malfunctioning)	RADIUS-MD V. Petrov, IMBP; Ts. Dachev, SRTL.  Semkova et al., 1994. [18].	2 Solid State Detectors (SSD) (154x80x70 mm, 0.38 kg)  Outside and inside Mars-96 satellite > >2 g cm <sup>-2</sup> ; 10 min		
3	ISS  05/05/2001- 26/08/2001/  1,267,200	Dosimetric Mapping G. Reitz, DLR; Ts. Dachev, SRTL.  Dachev et al., 2002. [20]; Reitz et al., 2005. [10]; Nealy et al., 2007. [58]; Slaba et al., 2011. [59].	Liulin-E094 1 CIU (120x80x60 mm, 0.4 kg) 4 MDU (100x64x24 mm, 0.23 kg) Inside of the American Lab. and Node 1 of ISS >  >20 g cm <sup>-2</sup> ; 30 sec		
4	Foton M2  01/06/2005- 12/06/2005  17,280	Biopan 5 G. Horneck, DLR; D. Häder, UE; Ts. Dachev, SRTL.  Häder et al., 2009. [70]; Dachev et al., 2009. [7].	R3D-B2 (57x82x24 mm, 0.12 kg)  1 DU outside of the satellite and inside of Biopan-5 facility  1.75 g cm <sup>-2</sup> ; 60 sec		
5	ISS Since Sept. 2005 13/08/2008- 29/08/2008 Service system in next 15 years  149,760 spectra	Liulin-ISS V. Petrov, IMBP; Ts. Dachev, SRTL.  Dachev, et al., 2005. [60].	Liulin-MKS 1 CIU (120x80x20 mm, 0.4 kg) 4 MDU (110x80x25 mm, 0.23 kg)  Inside Russian segment of ISS >20 g cm <sup>-2</sup> ; 10-3599 sec		
6	ISS 17/05/2007-  Working permanently against flash memory card >2,500,000 measurements	Matroska-R V. Petrov, IMBP; J. Semkova, SRTL.  Semkova, et al., 2003. [21]; Semkova, et al., 2008. [22].	Liulin-5, Dosimetric telescope by 3 detectors ( 50/30x191 mm, 0.4 kg) Electronic block (160x90x30 mm, 0.8 kg)  Inside Russian segment of ISS >20 [g cm <sup>-2</sup> ]; 90 sec		



7	Foton M3 14/09/2007- 26/09/2007  18,720	Biopan 6  G. Horneck, DLR; D. Häder, UE; Ts. Dachev, SRTL.  Damasso et al., 2009. [70a]; Häder et al., 2009. [70].	R3D-B3 1 DU (57x82x24 mm, 0.12 kg)  outside of the satellite and inside of Biopan-6 facility  0.8 g cm <sup>-2</sup> ; 60 sec		
8	Foton M3 14/09/2007- 26/09/2007  27,360	PHOTO-II  M.-T. Giardy, IC- AR, Rome, Italy; Ts. Dachev, SRTL.  Damasso et al., 2009. [70a].	Liulin-Photo, 1 DU (57x82x24 mm, 0.5 kg)  Above Photo instrument, inside of the satellite, > >5.0 g cm <sup>-2</sup> ; 60 sec		
9	ISS, Columbus module  17/02/2008- 03/09/2009  4,406,400	EXPOSE-E  G. Horneck, DLR; D. Häder, UE; Ts. Dachev, SRTL.  Häder and Dachev, 2003. [70] Dachev et al., 2012. [32]	R3DE 1 DU (76x76x36 mm, 0.19 kg)  Outside of ISS in EXPOSE-E facility in EuTEF >  >0.6 g cm <sup>-2</sup> ; 10 sec		
10	Chandrayaan-1 satellite around the Moon 22/10/2008- 29/09/2009  1,209,600 spectra	RADOM  Ts. Dachev, SRTL  Dachev et al., 2011. [34]; Dachev, 2013. [85].	RADOM 1 DU (110x40x20 mm, 0.098 kg)  Outside of the Chandrayaan-1 satellite > >0.6 g cm <sup>-2</sup> ; 10 and 30 sec		
11	ISS, Zvezda module  11/03/2009- 20/08/2010  3,540,000	EXPOSE-R  G. Horneck, DLR; D. Häder, UE; Ts. Dachev, SRTL.  Dachev et al., 2013. [8] Dachev 2013. Dachev et al., 2014	R3DR 1 DU (76x76x36 mm, 0.19 kg)  Outside of ISS in EXPOSE-E facility outside of Zvezda module > >0.6 g cm <sup>-2</sup> ; 10 sec		
12	Phobos-Grunt 09/11/2011  (The satellite was lost because of rocket booster malfunctioning)	Liulin-Phobos  V. Petrov, IMBP; J. Semkova, SRTL.  Semkova, et al., 2008. [22].	Liulin-Phobos 2x2 dosimetric telescopes (172x114x45 mm 0.5 kg)  Outside Phobos-Grunt satellite; >2 g cm <sup>-2</sup>  Dose and flux 60 sec Spectrum 60 min		

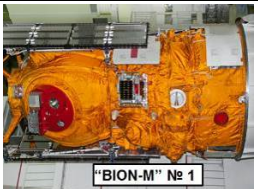
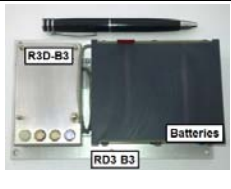









13	<p>"BION-M" №1 19/04/2013- 1305.2013</p> <p>In space 34, 391 spectra</p>	<p>RD3-B3</p> <p>V. Shurshakov, IMBP; Ts. Dachev, SRTI</p> <p>Dachev et al., 2014. [71].</p>	<p>RD3-B3 (110x80x44 mm, 0.3 kg)</p> <p>1 battery operated DU Inside "BION-M" №1 satellite/ &gt;</p> <p>&gt;2 [g cm<sup>-2</sup>]; 60 sec</p>		
----	--	--	---	---	--

Table 2. Liulin type experiments at aircraft, balloon, rocket and mountains peaks

Item No	Experiment description Date begin-Date end	Person performing the experiment References	Instrument Size [mm]/Mass [kg] Place Resolution [sec]	External view of the instrument
1	<p>1. Balloon experiment at Gap-Tallard aerodrome, France, 14/06/2000;</p> <p>2. NASA's Lockheed ER-2 high altitude research aircraft, Oct.-Nov. 2000.</p>	<p>1. CNES balloon technological flight program, F. Spurny, NPI-CAS, Prague, Czech Republic;</p> <p>2. Y. Uchihori, NIRS, Japan;</p> <p>Spurny, F., 2000. [72]. Uchihori et al., 2003. [73].</p>	<p>Liulin-4C/4J, MDU-2 (100x64x24 mm, 0.23 kg with rechargeable Li-Ion battery pack)</p> <p>Inside of the balloon gondola or the ER-2 cockpit, 60 sec.</p>	
2	<p>Long-term (&gt;60 days) measurements at aircraft altitudes for different airlines. 28 V DC/DC converter.</p> <p>Since 2001 up to 2014.</p>	<p>F. Spurny and O. Ploc, NPI, Czech Rep; Ploc et al., 2013. [74]</p> <p>J.C. Saez Vergara and R. Dominguez-Mompell Roman, CIEMAT and IBERIA, Spain [76].</p> <p>Hwang et al, KASI, Korea [77]</p>	<p>DU (110x100x45 mm, 0.48 kg including 2 D size Lithium-Ion batteries)</p> <p>Inside of the aircraft</p> <p>300/600 sec.</p>	
3	<p>Deep Space Test Bed (DSTB) certification flight</p> <p>8 June 2005 at Ft. Sumner, New Mexico, USA. ~10 hours</p>	<p>E. R. Benton, ERIL Research Inc.</p> <p>Benton, 2005. <a href="http://wrmiss.org/workshops/tenth/pdf/08_benton.pdf">http://wrmiss.org/workshops/tenth/pdf/08_benton.pdf</a></p>	<p>3 Liulin MDU (100x64x24 mm, 0.23 kg with rechargeable Li-Ion battery pack)</p> <p>Inside of the balloon gondola 60 sec.</p>	
4	<p>Measurements at mountain peaks. The Liulin instrument contains Internet module to post, store and transmit the obtained results via FTP protocol in Internet.</p>	<p>Bern university, Jungfrau, Switzerland: <a href="http://130.92.231.184/">http://130.92.231.184/</a></p> <p>Lomnitski Shtit: <a href="http://147.213.218.13/">http://147.213.218.13/</a></p> <p>INRNE-BAS, BEO-Moussala: <a href="http://beo-db.inrne.bas.bg/moussala/">http://beo-db.inrne.bas.bg/moussala/</a></p>	<p>DU (84x40x40 mm, 0.12 kg.</p> <p>Internet module with 22 MHz microprocessor, 512K flash and 512K SRAM memory.</p> <p>600 sec.</p>	
5	<p>Measurements at aircraft altitudes. A built in GPS receiver record: UT, Longitude, Latitude and Altitude, which together with the dose rate data are shown on the display.</p>	<p>I. Getley, University of New South Wales, Australia</p> <p>Getley et al., 2010. [44].</p>	<p>Spectrometer (110x55x45 mm; 0.38 kg); Display (115x40x20 mm; weight 0.12 kg); Rechargeable battery package (90x60x40 mm; 0.18 kg). Inside of the cockpit of Boeing 747-400 Qantas Airways flights. 60 sec.</p>	

6	1. NASA balloon experiment for radiation studies. 2. RAZREZ system on ISS (The both systems are already delivered but both exp. are not performed.)	1. J. Adams et al., 2007. [79]. NASA/Marshall Space Flight Center, USA.  2. Petrov et al., 2009. [80] <a href="http://wrmiss.org/workshops/fourteenth/Petrov.pdf">http://wrmiss.org/workshops/fourteenth/Petrov.pdf</a>	4 DU (74x40x20 mm, 0.065 kg; 1 CIU (144x60x20 mm, 0.21 kg) Total 0.47 kg.  Powered from 28 V DC, 0.72 mA. Data transmission trough RS485 interface.	
7	Under the HotPay2 project from Andoya Rocket Range, Norway was launched a rocket up to 380 km altitude on January 31, 2008.	Tomov et al., 2009. [82]. <a href="http://www.stil.bas.bg/FSR/PDF/TOP5_Tomov_Borislav2242058.pdf">http://www.stil.bas.bg/FSR/PDF/TOP5_Tomov_Borislav2242058.pdf</a>	(110x40x20 mm, 0.098 kg)  Inside of the rocket payload  60 sec.	
8	5 balloon flights up to 30 km altitude between July 2011 and August 2012	F.Wissmann et al., Physikalisch-Technische Bundesanstalt (PTB), Germany  F.Wissmann et al., 2013. [83]	Liulin-RG4/5 2 DU (110x40x20 mm 0.092 kg). With serial readout of the data measured with the Si-detector. On the gondola of the balloon. 30 sec.	
9	Long-term (>60 days) measurements at aircraft altitudes. A built in GPS receiver record: UT, Longitude, Latitude and Altitude. Data are stored at 1 or 2 GB SD card. 28 V DC/DC converter. Since 2005 up to 2014.	A.R. Green et al., Royal Military College of Canada, Canada.  Green et al., 2005. [43]; Kitching, 2004. [84].	1 DU (110x100x45 mm, 0.48 kg including 2 D size Lithium-Ion batteries)  inside of the aircraft  300/600 sec	

## References

1. Badhwar, G.D., W. Atwell, B. Cash, V.M. Petrov, Yu.A. Akatov, I.V. Tchernykh, V.A. Shurshakov, V.A. Arkhangelsky, Radiation environment on the MIR orbital station during solar minimum. *Adv. Space. Res.* 22 (4), 1998, 501-510.
2. Benton, E.R., E.V. Benton, Space radiation dosimetry in low-Earth orbit and beyond, *Nucl. Instrum. and Methods in Physics Research, B*, 184, (1-2), 2001, 255-294.
3. Benton, E.R., E.V. Benton, A.L. Frank, M.F. Moyers, Characterization of the radiation shielding properties of US and Russian EVA suits using passive detectors, *Radiation Measurements*, 41, 2006, 1191-1201.
4. NCRP, Report No. 142, Operational Radiation Safety Program for Astronauts in Low-Earth Orbit: A Basic Framework - Report No. 142, Bethesda, MD, 2002.
5. Simpson, J.A., Composition and origin of cosmic rays. In: Shapiro, M.M. (Ed.), *NATO ASI Series, Series C Mathematical and Physical Sciences*, 1983, 107. Reidel, Dordrecht.

6. Kim, M.-H.Y., G., De Angelis, F.A. Cucinotta, Probabilistic assessment of radiation risk for astronauts in space missions. *Acta Astronautica* 68 (7–8), 2010, 747–759.
7. Dachev, Ts.P., B.T. Tomov, Yu.N. Matviichuk, P.G. Dimitrov, N.G. Bankov, Relativistic electrons high doses at international space station and Foton M2/M3 satellites. *Advances in Space Research* 44, 2009, 1433–1440. <http://dx.doi.org/10.1016/j.asr.2009.09.023>.
8. Dachev Ts.P., B.T. Tomov, Yu.N. Matviichuk, Pl.G. Dimitrov, N.G. Bankov, G. Reitz, G. Horneck, D.-P. Häder, M. Lebert, M. Schuster, Relativistic Electron Fluxes and Dose Rate Variations during April-May 2010 Geomagnetic Disturbances in the R3DR Data on ISS, *Adv. Space Res.* 50, 2012, 282-292. <http://dx.doi.org/10.1016/j.asr.2012.03.028>.
9. Dachev Ts.P., B.T. Tomov, Yu.N. Matviichuk, Pl.G. Dimitrov, N.G. Bankov, G. Reitz, G. Horneck, D.-P. Häder, M. Lebert, M. Schuster, Relativistic Electron Fluxes and Dose Rate Variations Observed on the International Space Station. *J. Atmospheric and Solar-Terrestrial Physics*, 99, 2013, 150-156. <http://dx.doi.org/10.1016/j.jastp.2012.07.007>.
10. Reitz G., R. Beaujean, E. Benton, S. Burmeister, Ts. Dachev, S. Deme, M. Luszik-Bhadra, and P. Olko, Space radiation measurements on-board ISS—the DOSMAP experiment. *Radiat Prot Dosimetry*. 116, 2005, 374-379. <http://rpd.oxfordjournals.org/cgi/content/abstract/116/1-4/374>.
11. Mertens, C.J., J.W. Wilson, S.R. Blattinig, S.C. Solomon, M.J. Wiltberger, J. Kunches, B.T. Kress, J.J. Murray, Space weather nowcasting of atmospheric ionizing radiation for aviation safety, NASA Langley Research Center, 2007. Available online at: [http://ntrs.nasa.gov/archive/nasa/casi.ntrs.nasa.gov/20070005803\\_2007005368.pdf](http://ntrs.nasa.gov/archive/nasa/casi.ntrs.nasa.gov/20070005803_2007005368.pdf)
12. Lantos, P., The Sun and its effects on the terrestrial environment. *Radiation Protection Dosimetry* 48 (1), 1993, 27–32.
13. Bazilevskaya, G.A., Y.I. Stozhkov, A.K. Svirzhevskaya, N.S. Svirzhevsky, Cosmic rays and radioactivity in the near-ground level of the atmosphere. *Journal of Physics* 409, 2013, 012213. <http://dx.doi.org/10.1088/1742-6596/409/1/012213>.
14. Shea M.A., D.F. Smart, Vertical cutoff rigidities for cosmic ray stations since 1955. In: 27th International Cosmic Ray Conference. *Contributed Papers*, 10, 2001, 4063–4066.
15. Wilson, J.W., D.L. Maiden, P. Goldhagen, H. Tai, J.L. Shinn, Overview of Atmospheric Ionizing Radiation (AIR). NASA Langley Research Center, 2003. Available online at: [http://ntrs.nasa.gov/archive/nasa/casi.ntrs.nasa.gov/20030063010\\_2003072785.pdf](http://ntrs.nasa.gov/archive/nasa/casi.ntrs.nasa.gov/20030063010_2003072785.pdf)
16. Wahl, L.E., Environmental Radiation, 2010. Available online at: [http://hps.org/documents/environmental\\_radiation\\_fact\\_sheet.pdf](http://hps.org/documents/environmental_radiation_fact_sheet.pdf), Fig 1., reprinted from <http://www.ncrppublications.org/Reports/160>).

17. Dachev, Ts.P., Yu.N. Matviichuk, J.V. Semkova, R.T. Koleva, B. Boichev, P. Baynov, N.A. Kanchev, P. Lakov, Ya.J. Ivanov, P.T. Tomov, V.M. Petrov, V.I. Redko, V.I. Kojarinov, R. Tykva, Space radiation dosimetry with active detections for the scientific program of the second bulgarian cosmonaut on board the Mir space station, *Adv. Space Res.*, 9, 10, 1989, 247-251. [http://dx.doi.org/10.1016/0273-1177\(89\)90445-6](http://dx.doi.org/10.1016/0273-1177(89)90445-6).
18. Semkova, J., Ts. Dachev, Yu. Matviichuk, R. Koleva, B. Tomov, P. Bajnov, V. Petrov, V. Nguyen, M. Siegrist, J. Chene, C. d'Uston, F. Cotin, Dosimetric investigation on MARS-96 missions, *Adv. Space Res.*, V 14, No.10, 1994, 707-710. [http://dx.doi.org/10.1016/0273-1177\(94\)90530-4](http://dx.doi.org/10.1016/0273-1177(94)90530-4).
19. Dachev, Ts.P., E.G. Stassinopoulos, B.T. Tomov, Pl.G. Dimitrov, Yu.N. Matviichuk, V.A. Shurshakov, V.M. Petrov, Analysis of the Cyclotron Facility Calibration and Aircraft Results Obtained by LIULIN-3M Instrument, *Adv. Space Res.*, 32, 2003, 67-71. doi:10.1016/S0273-1177(03)90372-3.
20. Dachev Ts., B. Tomov, Yu. Matviichuk, Pl. Dimitrov, J. Lemaire, Gh. Gregoire, M. Cyamukungu, H. Schmitz, K. Fujitaka, Y. Uchihori, H. Kitamura, G. Reitz, R. Beaujean, V. Petrov, V. Shurshakov, V. Benghin, F. Spurny, Calibration Results Obtained With Liulin-4 Type Dosimeters. *Adv. Space Res.* V 30, No 4, 2002, 917-925. [http://dx.doi.org/10.1016/S0273-1177\(02\)00411-8](http://dx.doi.org/10.1016/S0273-1177(02)00411-8).
21. Semkova, J, R. Koleva, G. Todorova, N. Kanchev, V. Petrov, V. Shurshakov, V. Benghin, I. Tchhernykh, Yu. Akatov, V. Redko, Yu. Ivanov, Investigation of dose and flux dynamics in the Liulin-5 dosimeter of the tissue-equivalent phantom onboard the Russian segment of the International Space Station, *Adv. Space Res.*, 31, 2003, 1383-1388.
22. Semkova, J., S. Maltchev, B. Tomov, Yu. Matviichuk, Ts. Dachev, R. Koleva, V. Benghin, I. Chernykh, V. Shurshakov, V. Petrov, Charged particle telescope Liulin-Phobos for radiation environment study during upcoming Phobos Sample Return Mission, *Proceedings of the International Conference on Fundamental Space Research, Sunny Beach, Bulgaria, 23-28 September 2008*, ISBN 978-954-322-316-9, 351-354. Available online at: <http://www.stil.bas.bg/FSR2009/>.
23. Stassinopoulos E.G., C.A. Stauffer, T.P. Dachev, C.J. Brucker, B.T. Tomov, P.G. Dimitrov, The LIULIN-3M Radiometer for Measuring Particle Doses in Space and on Aircraft, *NASA/TM-2002-210003*, February, 2002. Available online at: [http://ntrs.nasa.gov/archive/nasa/casi.ntrs.nasa.gov/20020045343\\_2002075693.pdf](http://ntrs.nasa.gov/archive/nasa/casi.ntrs.nasa.gov/20020045343_2002075693.pdf)
24. Dachev, Ts.P., B.T. Tomov, Yu.N. Matviichuk, Pl.G. Dimitrov, F. Spurny, O. Ploc, K. Brabkova, I. Jadrnickova, Liulin type spectrometry-dosemetri instruments, *Radiat Prot. Dosimetry*, 2011, 675-679. <http://dx.doi.org/10.1093/rpd/ncq506>

25. Dachev Ts.P., Characterization of near Earth radiation environment by Liulin type instruments. *Adv. Space Res.* 44, 2009, 1441-1449. doi:10.1016/j.asr.2009.08.007.
26. Dachev, Ts.P., F. Spurny, O. Ploc, Characterization of radiation environment by Liulin type spectrometers, *Radiat Prot Dosimetry*, 144 (1-4), 2011, 680-683. <http://dx.doi.org/10.1093/rpd/ncq534>
27. Spurny, F. and Ts. Dachev, Long-Term Monitoring of the Onboard Aircraft Exposure Level With a Si-Diode Based Spectrometer. *Adv. Space Res.*, 32, No.1, 2003, 53-58. [http://dx.doi.org/10.1016/S0273-1177\(03\)90370-X](http://dx.doi.org/10.1016/S0273-1177(03)90370-X)
28. Mitaroff, A., M. Silari, The CERN-EU high energy reference field (CERF) facility for dosimetry at commercial flight altitudes and in space. *Radiat. Prot. Dosim.* 102, 2002, 7–22.
29. Spurny, F., Response of a Si-diode-based device to fast neutrons, *Radiation Measurements* 39, 2005, 219-223. <http://dx.doi.org/10.1016/j.radmeas.2004.05.006>.
30. Ploc, O., F. Spurny, Ts.P. Dachev, Use of Energy Depositing Spectrometer for Individual Monitoring of Aircrew, *Radiat Prot Dosimetry*, 144 (1-4), 2011, 611-614. <http://dx.doi.org/10.1093/rpd/ncq505>
31. Spurny, F., O. Ploc, and I. Jadrníková, Spectrometry of linear energy transfer and dosimetry measurements onboard spacecrafts and aircrafts. *Phys. Part. Nuclei Lett.*, 6, 70–77, # Pleiades Publishing, Ltd. ISSN 2009, 1547-4771.
32. Dachev, Ts., G. Horneck, D.-P. Häder, M. Lebert, P. Richter, M. Schuster, R. Demets, Time profile of cosmic radiation exposure during the EXPOSE-E mission: the R3D instrument. *Journal of Astrobiology*, 12, 5, 2012, 403-411. <http://eea.spaceflight.esa.int/attachments/spacestations/ID501800a9c26c2.pdf>.
33. Berger M.J., J.S. Coursey, M.A. Zucker, and J. Chang, Stopping-Power and Range Tables for Electrons, Protons, and Helium Ions., NIST Standard Reference Database 124. Available online at: <http://physics.nist.gov/PhysRefData/Star/Text/contents.html>.
34. Dachev, Ts.P., B.T. Tomov, Yu.N. Matviichuk, Pl.G. Dimitrov, S.V. Vadawale, J.N. Goswami, V. Girish, G. de Angelis, An overview of RADOM results for Earth and Moon Radiation Environment on Chandrayan-1 Satellite, *Adv. Space Res.*, 48, 5, 2011, 779-791. <http://dx.doi.org/10.1016/j.asr.2011.05.009>
35. Uchihori, Y., H. Kitamura, K. Fujitaka, Ts.P. Dachev, B.T. Tomov, P.G. Dimitrov, Y. Matviichuk, Analysis of the calibration results obtained with Liulin-4J spectrometer–dosimeter on protons and heavy ions. *Radiat. Meas.* 35, 2002, 127–134.
36. Uchihori, Y, T. Dachev, H. Kitamura, H. Kentaro, K. Yajima, Chapter VII — Liulin-4J Silicon Portable Spectrometer, Report, HIMAC-078, 2003, 56-63.
37. Zhang, L., R. Mao, R. Zhu, Fast neutron induced nuclear counter effect in Hamamatsu silicon PIN diodes and APDs, *IEEE Transactions on Nuclear Science* 58 (3), 2011, 1249–1256.

38. Burmeister, S., R. Beaujean, F. Petersen, G. Reitz, Post Flight, Calibration of DOSTEL with Heavy Ions During the First and Third, ICCHIBAN, Run at HIMAC, Chiba. 8th Workshop on Radiation Monitoring for the International Space Station 3–5 September 2003, LBNL, Berkeley, USA. Available online at: <http://wrmiss.org/workshops/eighth/burmeister.pdf>
39. Uchihori, Y., H. Kitamura, K. Fujitaka, N. Yasuda, E. Benton, Comparison of results from the 1st ICCHIBAN experiment and current status of the 3<sup>rd</sup> ICCHIBAN experiment. In: 8th Workshop on Radiation Monitoring for the International Space Station 3–5 September, LBNL, Berkeley, USA, 2003. Available online at: <http://wrmiss.org/workshops/eighth/uchihori.pdf>
40. Zapp, NASA GSFC, by 'Coordinated Data Analysis Web' at Goddard Space Flight Center, May, 2013. <http://cdaweb.gsfc.nasa.gov/tmp/>.
41. Dachev Ts., Analysis of the space radiation doses obtained simultaneously at 2 different locations outside ISS, *Adv. Space Res.*, 52, 2013, 1902-1910. <http://dx.doi.org/10.1016/j.asr.2013.08.011>.
42. Radiation Protection 140, 2004. Cosmic Radiation Exposure of Aircraft Crew, Compilation of Measured and Calculated Data, Edited by L. Lindborg, D.T. Bartlett, P. Beck, I.R. McAulay, K. Schnuer, H. Schraube and F. Spurný, Final Report of EURADOS WG 5, Group of Experts established under Article 31 of the Euratom treaty, Directorate-General for Energy and Transport, Directorate H - Nuclear Energy, Unit H.4 - Radiation Protection Available online at: [http://ec.europa.eu/energy/nuclear/radiation\\_protection/doc/publication/140.pdf](http://ec.europa.eu/energy/nuclear/radiation_protection/doc/publication/140.pdf)
43. Green, A.R., L.G.I. Bennett, B.J. Lewis, F. Kitching, M.J. McCall, M. Desormeaux, A. Butler, An empirical approach to the measurement of the cosmic radiation field at jet aircraft altitudes, *Advances in Space Research*, 36, 2005, 1618-1626.
44. Getley, I. L., L.G.I. Bennett, B.J. Lewis, B. Bennett, C.S. Dyer, A.D.P. Hands, and M.L. Duldig, Evaluation of new cosmic radiation monitors designed for aircrew exposure assessment, *Space Weather*, 8, 2010. S01001. <http://dx.doi.org/doi:10.1029/2009SW000492>.
- 44a. Getley, I. L., Cosmic and solar radiation monitoring of Australian commercial flight crew at high southern latitudes as measured and compared to predictive computer modelling, A Doctoral Thesis Submitted in Fulfilment of the Requirements for the Award of Doctor of Philosophy of The University of New South Wales, June 2007.
45. Semkova, J., R. Koleva, V. Shurshakov, V. Beninghin, St. Maltchev, N. Kanchev, V. Petrov, E. Yarmanova, I. Chernykh, Status and calibration results of Liulin-5 charged particle telescope designed for radiation measurements in a human phantom onboard the ISS, *Advances in Space Research*, 40, 2007, 1586–1592. <http://dx.doi.org/doi:10.1016/j.asr.2007.01.008>.
46. Akatov, Yu.A., V.G. Eremenko, I.S. Kartsev, et al., Spherical phantom for studying radiation conditions in outer space. *Nuclear Measurement & Information Technologies*, 3, 2002, 67-71.
47. Shurshakov, V., Y. Akatov, I.S. Kartsev, et al., Measurements of the absorbed dose distribution in the spherical tissue equivalent phantom in

- MATROSHKA-R space experiment, 11th WRMISS, United Kingdom, Oxford, 2006, Available online at: <http://www.wrmiss.org/workshops/eleveth>
48. Semkova, J., R. Koleva, St. Maltchev et al., Radiation measurements inside a human phantom aboard the International Space Station using Liulin-5 charged particle telescope, *Advances in space research*, 45, Issue 7, 2010, 858-865. <http://dx.doi.org/doi:10.1016/j.asr.2009.08.027>.
  49. Dachev, Ts., J. Semkova, B. Tomov, Y. Matviichuk, P. Dimitrov, N. Bankov, R. Koleva, L. Zelenyi, I. Mitrofanov, A. Malakhov, M. Mokrousov, V. Tretyakov, V. Petrov, V. Shurshakov, V. Benghin, Bulgarian Participation in Future Interplanetary Missions, *Proceedings of Seventh Scientific Conference with International Participation SES*, Sofia, 4-6 December 2012, ISSN 1313-3888, 2013, 55-63. <http://www.space.bas.bg/SES2012/Ph-5.pdf>.
  50. Uchihori Y., E.R. Benton, N. Yasuda, et al., ICCHIBAN Working Group and ICCHIBAN participants NSRL-ICCHIBAN Brief Report, ICCHIBAN-7&8 Announcement and Future ICCHIBAN experiments, 10th WRMISS, Chiba, Japan, 2005. Available online at: [http://wrmiss.org/workshops/tenth/pdf/01\\_uchihori.pdf](http://wrmiss.org/workshops/tenth/pdf/01_uchihori.pdf).
  51. Semkova, J., St. Maltchev, V. Benghin, Y. Uchihori, N. Yasuda, H. Kitamura, Results of Liulin-F particle telescope pre-flight calibrations with protons and heavy ions *Proceedings of Fundamental Space Research conference 2009*, 211-214. <http://www.stil.bas.bg/FSR2009/>.
  52. Dachev, Ts.P. B.T. Tomov, Yu.N. Matviichuk, R.T. Koleva, J.V. Semkova, V.M. Petrov, V.V. Benghin, Yu.V. Ivanov, V.A. Shurshakov, J. Lemaire, Solar Cycle Variations of MIR Radiation Environment as Observed by the LIULIN Dosimeter, *Radiation Measurements*, 30 (3), 1999, 269-274. [http://dx.doi.org/10.1016/S1350-4487\(99\)00061-X](http://dx.doi.org/10.1016/S1350-4487(99)00061-X).
  53. Dachev Ts.P., J.V. Semkova, Yu.N. Matviichuk, B.T. Tomov, R.T. Koleva, P.T. Baynov, V.M. Petrov, V.V. Shurshakov, Yu. Ivanov, Inner Magnetosphere Variations after Solar Proton Events. Observations on Mir Space Station In 1989-1994 Time Period, *Adv. Space Res.*, 22, No 4, 1998, 521-526. [http://dx.doi.org/10.1016/S0273-1177\(98\)01073-4](http://dx.doi.org/10.1016/S0273-1177(98)01073-4).
  54. Shurshakov, V.A., V.M. Petrov, Yu.V. Ivanov, V.A. Bondarenko, V.V. Tzetlin, V.S. Makhmutov, Ts.P. Dachev and J.V. Semkova, Solar particle events observed on MIR station, *Radiation Measurements*, 30, 1999, 317-325. [http://dx.doi.org/10.1016/S1350-4487\(99\)00058-X](http://dx.doi.org/10.1016/S1350-4487(99)00058-X).
  55. Heffner J., Nuclear radiation and safety in space. M, Atomizdat, 1971, pp 115. (in Russian)
  56. Dachev, T., W. Atwell, E. Semones, B. Tomov, B. Reddell, ISS Observations of SAA radiation distribution by Liulin-E094 instrument on ISS, *Adv. Space Res.*, 37, 2006, 1672-1677. doi:10.1016/j.asr.2006.01.001.
  57. Wilson J.W., J.E. Nealy, T. Dachev, B.T. Tomov, F.A. Cucinotta, F.F. Badavi, G. De Angelis, N. Leutke, W.



- Atwell, Time serial analysis of the induced LEO environment within the ISS 6A. *Adv. Space Res.*, 40, 11, 2007, 1562-1570. doi:10.1016/j.asr.2006.12.030.
58. Nealy J.E., F.A. Cucinotta, J.W. Wilson, F.F. Badavi, N. Zapp, T. Dachev, B.T. Tomov, E. Semones, S.A. Walker, G.De Angelis, S.R. Blattnig, W. Atwell, Pre-engineering spaceflight validation of environmental models and the 2005 HZETRN simulation code. *Adv. Space Res.*, 40, 11, 2007, 1593-1610. doi:10.1016/j.asr.2006.12.030.
  59. Slaba, T.C., S.R. Blattnig, F.F. Badavi, N.N. Stoffle, R.D. Rutledge, K.T. Lee, E.N. Zapp, T.P. Dachev and B.T. Tomov, Statistical Validation of HZETRN as a Function of Vertical Cutoff Rigidity using ISS Measurements. *Adv. Space Res.*, 47, 2011, 600-610. doi:10.1016/j.asr.2010.10.021.
  60. Dachev, Ts., B. Tomov, Yu. Matviichuk, Pl. Dimitrov, R. Koleva, J. Semkova, J. Lemaire, V. Petrov, V. Shurshakov, Overview on the MIR radiation environment results obtained by LIULIN instrument in 1988–1994 time period. Description of LIULIN-4 subsystem for the Russian segment of the ISS. In: *Risk Evaluation of Cosmic-ray Exposure in Long-term Manned Space Mission*, Tokyo, Japan, 1999, 127–150.
  61. Semkova, J., R. Koleva, St. Maltchev, N. Bankov, V. Benghin, et al., Depth dose measurements with the Liulin-5 experiment inside the spherical phantom of the Matroshka-R project onboard the International Space Station, *Adv. Space Res.*, 49, 2012, 471–478. <http://dx.doi.org/10.1016/j.asr.2011.10.005>.
  62. Semkova, J., R. Koleva, St. Maltchev, N. Bankov, V. Benghin, et al., Radiation characteristics in the spherical tissue-equivalent phantom on the ISS during solar activity minimum according the data from Liulin-5 experiment, *J. Atm. Solar-Terr. Phys.*, 99, July 2013, 157–163. <http://dx.doi.org/10.1016/j.jastp.2012.07.006>.
  63. Semkova, J., R. Koleva, N. Bankov, St. Malchev, V.M. Petrov, et al., Study of radiation conditions onboard the International space station by means of the Liulin-5 dosimeter, *Cosmic Research*, 51 (2), 2013, 124-132. <http://dx.doi.org/doi:10.1134/S0010952512060068>.
  - 63a. Semkova, J., T. Dachev, R. Koleva, S. Maltchev, N. Bankov, et al., Radiation Environment on the International Space Station During the Solar Particle Events in March 2012, *Astrol. Outreach*, 1, 2013, 102. <http://dx.doi.org/doi:10.4172/jao.1000102>.
  64. Dachev T.P., Semkova J., Tomov B., Matviichuk Yu., Dimitrov Pl., Koleva R., Malchev St., Reitz G., Horneck G., Angelis G. De, Häder D.-P., Petrov V., Shurshakov V., Benghin V., Chernykh I., Drobyshev S., Bankov N. G. Space Shuttle drops down the SAA doses on ISS. *Adv. Space Res.* 47, 2011, 2030-2038. doi:10.1016/j.asr.2011.01.034.
  65. Semones, E., ISS TEPC measurement results, 13th Workshop on Radiation Monitoring for the International Space Station (WRMISS), Krakow, Poland,

- September 8–10, 2008. Available online at: [http://wrmiss.org/workshops/thirteenth/Semones\\_TEPC.pdf](http://wrmiss.org/workshops/thirteenth/Semones_TEPC.pdf).
66. Benghin, V.V., V.M. Petrov, S.G. Drobyshev, M.I. Panasyuk, O.Yu. Nechaev, A.G. Miasnikov, and A.N. Volkov, Results of the radiation monitoring system onboard the service module of ISS, 13th Workshop on Radiation Monitoring for the International Space Station (WRMISS), Krakow, Poland, September 8–10, 2008. Available online at: <http://wrmiss.org/workshops/thirteenth/Benghin.pdf>.
  67. Chernykh, I., Petrov, V., Shurshakov, V., et al., ISS attitude influence on the dose rate measured with Liulin-5 instrument, Workshop on Radiation Measurements on ISS, Krakow, Poland, 8-10 September 2008, <http://www.wrmiss.org/workshops/thirteenth/Chernykh.pdf>.
  68. Dachev, Ts., G. Horneck, D.-P. Häder, M. Schuster, and M. Lebert, EXPOSE-R cosmic radiation time profile, *Jornal of Astrobiology*, available on CJO20142014. [http://journals.cambridge.org/article\\_S1473550414000093](http://journals.cambridge.org/article_S1473550414000093).
  69. Dachev T., B. Tomov, Y. Matviichuk, P. Dimitrov, G. De Angelis, Y. Uchihori, O. Ploc, Main Specifications of New Liulin Type Intelligent Crew Personal Dosimeter, Proceedings of Sixth Scientific Conference with International Participation SES, Sofia, ISSN 13131-3888, 2011, 76-82. [http://www.space.bas.bg/SENS/SES2010/1\\_SpPh/10.pdf](http://www.space.bas.bg/SENS/SES2010/1_SpPh/10.pdf).
  70. Häder D.P., P. Richter, M. Schuster, Ts. Dachev, B. Tomov, Pl. Dimitrov, Yu. Matviichuk, R3D-B2 - Measurement of ionizing and solar radiation in open space in the BIOPAN 5 facility outside the FOTON M2 satellite, *Adv. Space Res.* 43, 8, 2009, 1200-1211. doi:10.1016/j.asr.2009.01.021.
  - 70a. Damasso M., Ts. Dachev, G. Falzetta, M.T. Giardi, G. Rea, A. Zanini, The radiation environment observed by Liulin-Photo and R3D-B3 spectrum-dosimeters inside and outside Foton-M3 spacecraft, *Radiation Measurements*, V. 44, N0 3, 2009, 263-272. doi:10.1016/j.radmeas.2009.03.007.
  71. Dachev, T.P., B.T. Tomov, Yu.N. Matviichuk, Pl.G. Dimitrov, NG. Bankov, V. V. Shurshakov, O.A. Ivanova, D.-P. Häder, M.T. Schuster, G. Reitz, G. Horneck, “BION-M” №1 spacecraft radiation environment as observed by the RD3-B3 radiometer-dosimeter in April-May 2013, *Journal of Atmospheric and Solar-Terrestrial Physics*, Paper ATP-S-14-00142, 2014. (in print)
  72. Spurny, F., Dosimetry Measurements during a Balloon Flight – June 2000, Report DRD NPI AS CR 488/00, September 2000.
  73. Uchihori, Y., E. Benton, J. Moeller, G. Bendrick, Radiation measurements aboard NASA ER-2 high altitude aircraft with the Liulin-4J portable spectrometer, *Advances in Space Research*, 32, 2003, 41-46.
  74. Ploc, O., Measurement of Exposure to Cosmic Radiation at Near-Earth Vicinity with Energy Deposition Spectrometer Liulin onboard Aircraft and Spacecraft, PhD Thesis, September 2009.
  - 74a. Ploc, O., I. Ambrožová, J. Kubančák, I. Kovář, Ts. Dachev, Publicly available database of measurements with the silicon

- spectrometer Liulin on board aircraft, *Radiation measurements*, 58, 2013, 107-112. <http://dx.doi.org/10.1016/j.radmeas.2013.09.002>.
75. Friedberg, W., Snyder, W., Faulkner, D.N., US FAA Report DOT/FAA/AM-92-2, 1992.
  76. Sáez Vergara, J.C., and R. Dominguez-Mompell, The implementation of cosmic radiation monitoring in routine flight operation of IBERIA airline of Spain: 1 y of experience of in-flight permanent monitoring, *Radiation Protection Dosimetry*, 136, 2009, 291-296.
  77. Hwang, J., J. Lee1, K.-S. Cho, H.-S. Choi, S. Rho, and I.-H. Cho, Space Radiation Measurement on the Polar Route onboard the Korean Commercial Flights, *J. Astron. Space Sci.*, 27(1), 2010, 43–54.
  78. Матвийчук, Ю., Димитров Пл., Томов Б., Дачев Цв., Мониторинг радиационной обстановки в реальном масштабе времени с использованием сети Интернет, *Proceedings of Fundamental Space Research Conference*, 343-346, Slanchev Briag, September 23-28, 2008. [http://www.stil.bas.bg/FSR/PDF/TOP5Matviichuk\\_Yuriy2211249.pdf](http://www.stil.bas.bg/FSR/PDF/TOP5Matviichuk_Yuriy2211249.pdf)
  79. Adams, J.H., L. Adcock, J. Apple, M. Christl, W. Cleveand, M. Cox, K. Dietz, C. Ferguson, W. Fountain, B. Ghita, E. Kuznetsov, M. Milton, J. Myers, S. O'Brien, J. Seaquist, E. A. Smith, G. Smith, L. Warden and J. Watts, *Nuclear Instruments and Methods in Physics Research Section A: Accelerators, Spectrometers, Detectors and Associated Equipment*, 579, 2007, 522-525.
  80. Grigoriev, A. V., O. R. Grigoryan, A. Y. Drozdov, Y. M. Malyshkin, Y. V. Popov, E. A. Mareev, and D. I. Iudin Thunderstorm neutrons in near space: Analyses and numerical simulation, *J. Geophys. Res.*, 2010, 115, A00E52, doi:10.1029/2009JA014870.
  81. Petrov V.L., M.I. Panasyuk, A.M. Amelyushkin, A.Yu. Drozdov, O.Yu. Nechaev, RAZREZ system for RADIOSCAF experiment, Fourteenth WRMISS Workshop, Dublin, UK, 7–9 September 2010. Available online at: <http://www.wrmiss.org/workshops/fourteenth/Petrov.pdf>.
  82. Tomov B., Pl. Dimitrov, Yu. Matviichuk, Ts. Dachev, Galactic and Solar Cosmic Rays Study by Ground and Rocketborne Space Radiation Spectrometers-Dosimeters- Liulin-6R and Liulin-R, *Proceedings of Fundamental Space Research Conference*, ISSN 978-954-322-316-9, 2008, 252-257. , [http://www.stil.bas.bg/FSR/PDF/TOP5Tomov\\_Borislav2242058.pdf](http://www.stil.bas.bg/FSR/PDF/TOP5Tomov_Borislav2242058.pdf).
  83. Wissmann, F., O. Burda, S. Khurana, T. Klages, and F. Langner, Dosimetry of secondary cosmic radiation up to an altitude of 30 km, *Radiat. Prot. Dosimetry*, First published online December 16, 2013. doi:10.1093/rpd/nct329.
  84. Kitching, F., Use of a Liulin Detector for the Determination of Aircrew Radiation Exposure, Master's Thesis, Royal Military College of Canada, Kingston, Ont., Canada, November 2004.
  85. Dachev, T.P., Profile of the ionizing radiation exposure between the Earth surface and free space, *Journal of Atmospheric and Solar-Terrestrial Physics*, 102, September 2013, 148–156, 2013. <http://dx.doi.org/10.1016/j.jastp.2013.05.015>

## ОПИСАНИЕ НА ПРИБОРИТЕ ОТ ТИПА „ЛЮЛИН“ И ГЛАВНИ НАУЧНИ РЕЗУЛТАТИ

*Цв. Дачев, Й. Семкова, Б. Томов, Ю. Матвийчук,  
Пл. Димитров, Н. Банков, Р. Колева, Ст. Малчев*

### Резюме

Йонизиращата радиация създава здравни проблеми за хората на повърхността, в атмосферата и в околоземното космическо пространство. Оценката на радиационното въздействие върху здравето изисква точно познаване на натрупаната погълната доза, която зависи от глобалното разпределение на космическата радиация, фазата на слънчевия цикъл и от локалните вариации, генерирани от разпределението на масата около точката на измерване. В статията е направен обзор на създадените в България спектрометри-дозиметри от типа „Люлин“ и основните научни резултати, които са получени с тях от 1988 г. досега на самолети, балони, ракети и спътници, включително станцията „Мир“ и международната космическа станция (МКС).

## **ROBUST SMOOTHING OF TIME SERIES BY SIMPLE FAST ALGORITHM. TRACING OF TREND IN STELLAR FLICKERING AND CONTINUUM OF STELLAR SPECTRUM**

*Tsvetan Georgiev*

*New Bulgarian University,  
Institute of Astronomy and NAO, 1784 Sofia  
e-mail: tsgeorgiev@nbu.bg*

### ***Abstract***

*The method of the moving data window has been widely used for tracing the behavior of time series on a large scale where the estimation of the central point of the window is based on the Method of the Least Squares (MLS). However, the ordinary MLS minimizes the scatter of all  $n$  squares of the deviations and it is extremely sensitive to strong outliers. One alternative is the Method of the Least Trimmed Squares (MLTS) of Rousseeuw that minimizes only the left part of the squares of the deviations, ordered increasingly, including at least  $h = n/2+1$  data points. Strong outliers may be present in the right part of this order, but the MLTS ignores them. Thus the MLTS has an asymptotic robustness of 50% against strong outliers in the data, while the robustness of the MLS is definitely 0%. Apart from that the MLS ordinary regression is derived by direct formulas with respect to the coefficients while the MLTS robust regression is derived by testing all the available patterns of possible solutions: single data points in 1D case, lines through pairs of points in 2D case, planes through triplets of points in 3D case, etc. The pattern that has the shortest MLTS scatter is revealed as a solution. The main disadvantage of the MLTS is that in 2D, 3D, etc. it needs huge computing time in order to check all the available patterns. It may take a few million – billion times longer than it takes for the calculation of the respective ordinary regression. This work presents (i) a simple fast algorithm for the MLTS that omits progressively numerous patterns and may reduce the computing time a few thousand – million times. It presents also (ii) the capability of the MLTS applied in processing time series, especially with respect to the task of tracing stellar light curves in the presence of flares and tracing continuum stellar spectra in the presence of many spectral lines. Here we deal with equally spaced time series, but the method can be applied for all cases as a general solution.*

## 1. Smoothing by the Method of the Moving Polynomial (MMP)

A time series is an ordered discrete sequence of values that are dependent on time or other argument. Examples of a time series are a stellar variability curve, a stellar spectrum, a photometric section of a galaxy image, an index of a geophysical activity, etc. Usually the procedures applied on a time series aims (i) to decompose it into a trend and short scale variations, or (ii) to forecast some intermediate or further values of the time series. In many real cases the noise contamination disturbs the time series and at least a preliminary smoothing for suppressing the noise is needed. Theory and recommendations for time series smoothing are given in many books [1,2,3,4], as well as in many contemporary manual.

A common and widely used method for suppressing the noise is based on the so called moving data window. Let us define a time series  $z_k$ ,  $k=1, \dots, n$  and a data window of size  $w$ . We suppose  $w$  is an odd number and  $1 \ll w \ll n$ . Then the smoothing method works, as follows. The center of the data window moves along the time series step by step along the input time series. For every fixed position of the window, centered on the data point  $k$ , a numerical method uses the data in the window and estimates a “better” value  $\langle z_k \rangle$ , corresponding to  $z_k$ . In the output time series  $\langle z_k \rangle$  replaces  $z_k$ . Usually the estimation of  $z_k$  is based on the Method of the Least Squares (MLS) and the estimation  $\langle z_k \rangle$  is the central value of a regression polynomial of a low degree  $p$ ,  $F_p(z)$ , describing the large scale trend of the window data:  $\langle z_k \rangle = F_p(z_k)$ . In the simplest case,  $p=0$ , the estimation  $\langle z_k \rangle$  is the average of the data in the window. In other cases, a regression line,  $p=1$ , a regression quadratic polynomial,  $p=2$ , etc., are used in the sense of an average line, an average quadratic polynomial, etc. Let us call this common method “Method of the Moving Polynomial” (MMP).

The MMP based on the MLS produces an output (a result) time series that has been smoothed at a scale shorter than the window size. At a fixed window size  $w$ , when the polynomial degree  $p$  increases, the smoothing effect decreases, i.e. more details stands out in the output (result) time series. Otherwise, at a fixed polynomial degree  $p$ , when the window size  $w$  increases, the smoothing effect increases too.

In the case of equally spaced data, explored here, a significant simplification of the calculations of the MLS estimation of the current value (the central value of the window) exists: (i) the regression coefficients ahead the odd powered polynomial terms are definitely zero and (ii) the MLS procedure may be changed by convolution of the time series with

preliminary calculated kernel coefficients [5]. Formulas for deriving the coefficients in 1D and 2D cases for  $p=2$  and  $p=4$ , as well as an application for smoothing of digital image of a galaxy has been published [6]. So, excluding the average (with  $p = 0$ ) that causes too strong smoothness, the simplest tracing of a complicated time series may be based on the MLS parabola (with  $p = 2$ ):  $\langle z \rangle = b_0 + b_2.t^2$ .

Theoretically, the MLS is applicable over a system of statistical assumptions. The main of them is that the observed values of the dependent variable ( $z$ ) are subject to errors with zero mean and a finite variance, common for all observations. On the contrary, if only one strong outlier is present among the data, the MLS is practically useless. The problem is very serious (i) when the number of outliers is large, e. g. 40% of the data, (ii) when the number of the arguments (independent variables) is larger than unit when the visual control is almost impossible, and (iii) in time series processing or image processing, when the program code should be able to ignore automatically numerous outliers.

Furthermore, the MMP (based on the MLS), being a linear transformation of the time series, saves the “total energy” (entropy, self-information) of the data. For this reason the strong impulses in the data spread and disturb the behavior of the time series at scales compatible with a double-sized window. The high sensitivity to impulse noise is the most fundamental disadvantage of the MLS. Though, the MLS is the best (i) when the supposed intrinsic behavior of the time series at large scales is simple (naturally smooth) and (ii) when the noise distribution is close to the normal distribution. Otherwise, a method that is robust against numerous strong outliers is urgently needed.

A wide spread robust method gives an estimation of  $z_k$  as the median of the values in the moving data window [7]. The median is a robust estimation of the population mean with an asymptotic robustness of 50 % against outliers. Again, when the window size increases, the smoothing effect increases too. However, the median method saves sharp edges and produces result time series which are jagged at the shortest scale. For these reasons an additional smoothing by the MMP after the median smoothing is recommended. Unfortunately, simple methods for building median line, median plane or median are not certain.

It is very attractive to have a smoothing method that combines the flexibility of the MLS and the robustness of the median smoothing. Moreover, while the MLS estimates average means, average lines, average

planes, average polynomials, etc., this method has to estimate mode means, mode lines, mode planes, mode polynomials, etc.

The application of the MMP presented here is based on an extremely robust method, described in Section 2. Because of its specific character the MLTS may take millions – billions times longer in respect of the MLS and for this reason the MLTS is not widely spread. Therefore in Section 3 we present a simple fast algorithm for applying of the MLTS that may reduce the computing time thousands – millions of times. In Section 4 we apply the MMP based on the MLTS to trace the stellar light curves with flares and in Section 5 we apply this approach to trace the continuum in the stellar spectrum with many lines.

## **2. The Method of the Least Trimmed Squares (MLTS)**

The ordinary method of the least squares (MLS) is based on the principle of the least squares, introduced by Legendre and Gauss at the end of XVIII century. The MLS estimator minimizes the sum of all  $n$  squares of deviations. Its two most important particularities are: (i) the estimations are presented by formulas for direct calculation of the coefficients and their standard errors (advantage) and (ii) the estimations have zero robustness against outliers (disadvantage).

Different improvements of the MLS, aiming robustness against impulse noise, are proposed in the scientific literature, but we concentrate on the extremely robust method based on another principle. It has been introduced by Peter Rousseeuw in 1984 [8] and it is known as “Method of the Least Trimmed Squares” (MLTS). The principle of this method that changes the principle of the MLS is: the best estimation minimizes the sum of the left half of the squares of the deviations ordered in an ascending order (ordered by the increasing), no less then  $h = n/2+1$  for  $n$  data points.

The MLTS differs very significantly from the MLS in two respects: (i) The estimations are not to be presented by formulas for direct calculation of the coefficients and the standard deviations of the coefficients. For this reason any estimation should be made testing numerous patterns and this can be extremely time-consuming; (ii) The MLS estimation has an asymptotic robustness of 50% against outliers. For this reason practically up to 40% of the outliers do not change the estimation. Beside this, while  $h$  increases, the robustness of the MLTS decreases. In the case of  $h = n$  the estimation through the MLTS coincides with the estimation through the MLS. However, if  $h < n/2+1$ , the MLTS may recognize wrongly a small



part of the distribution as a keeper of the mode value. In the present paper we explore only the number  $h = n/2+1$ .

The MLTS is widely discussed and illustrated by Rousseeuw & Leroy in 1987 [9]. Some astronomical applications have been presented as illustrations of the power of this method by Georgiev in 2008 [10].

The simplest application of the MLTS is the estimation of the mode mean of a 1D population. Let us take the sample  $z_j$ ,  $j = 1, \dots, n$  into account. Then the MLTS works, as follows.

0. It takes into consideration consequently each value  $z_j$ , regarding it as a possible mode estimation. (The number of all checked points is  $N = n$ .)

1. It derives for every  $z_j$  all the  $n$  squares of the deviations  $\Delta z_{jk}^2 = (z_j - z_k)^2$ ,  $k = 1, \dots, n$ .

2. It sorts the values  $\Delta z_{jk}^2$  increasingly and trims the first  $h = n/2+1$  of them, ignoring the others.

3. It calculates the sum  $S_j$  of the trimmed squares of deviations and uses this sum as a label of the goodness of the data  $z_j$  as an estimation of the sample mean value;

4. It announces the value of  $z_j$  which has the shortest sum  $S_j$  to be the estimation of the mode of the 1D population;

5. It announces the value  $s = 2 \times [S_j / (h-1)]^{1/2}$  as an estimation of the standard deviation of the population. Multiplying by 2 is necessary for compatibility with the standard deviation estimation, that is based on half the deviations, with such an estimation by the MLS, that is based on all the deviations.

Figure 1 show an example composed of 138 measurements of the atmosphere extinction of the *Rozhen* NAO with a standard error of a single value of about 0.01 mag (about 1%) (courtesy of Dimitrov [11]; see for details Fig. 5 in [10]). Three estimations of the population mean are shown as average, median and mode. Note that the derivation of the MLTS mode is based on a clear mathematical principle and it does not need a histogram presentation of the data.

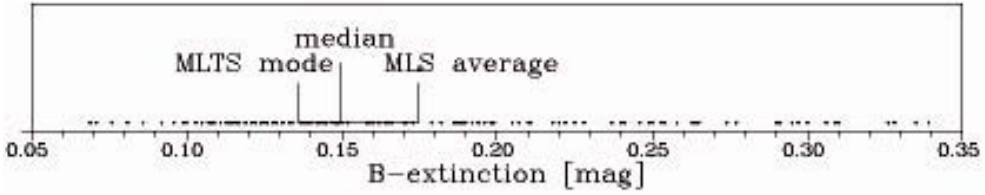


Fig. 1. Comparison of the positions MLTS mode, median and MLS average on a random value with a heavy right tail: atmosphere B-extinction over the Rozhen NAO. The mode estimation by the MLTS does not need visual (histogram) presentation of the data

Further, searching for the mode in 2D, 3D, etc., discrete distributions, MLTS checks every point (vector)  $r_j$ , as a possible mode estimation in 2D, 3D, etc. space. MLTS applies the same scheme, as in the 1D case, using the respective squares of deviations  $\Delta r_{jk}^2 = |r_j - r_k|^2$ ,  $k=1, \dots, n$ ; The number of the checks in these applications is always  $N = n$ .

The MLTS is designed mainly to derive the robust (mode) regression line  $\langle z \rangle = b_0 + b_1.t$ . In this case MLTS checks the lines through all pairs of points as a possible solution:

0. It derives the parameters  $b_0$  and  $b_1$  of the line  $z = b_0 + b_1.t$  through every pair of points.

The number of checked pairs (combinations) is  $N = n.(n-1)/2$ .

1. It derives all  $n$  squares of deviations  $\Delta z_{jk}^2$  (for each pint  $k$ ,  $k=1, \dots, n$ , of the sample) with respect to every checked line  $j$ ,  $j=1, \dots, N$ .

Furthermore the MLTS follows the steps 2 – 5 in the previous example and derives the line that is best among the available line patterns.

Searching for 2nd degree (mode) regression curve (or mode regression plane  $\langle z \rangle = a.x + b.y + c$ ), the MLTS follows the same scheme, checking every triad of points. Than the number of combinations is  $N = n.(n-1).(n-2)/6$ . In the case of 3 arguments MLTS checks every four points and the number of the combinations is  $N = n.(n-1).(n-2).(n-3)/24$ , etc.

In this work we show applications of fitting or smoothing of time series or data rows using four kinds of low degree polynomials:

$$(2.1a) \quad \langle z \rangle = b_0 + b_1.t$$

$$(2.1b) \quad \langle z \rangle = b_0 + b_2.t^2$$

$$(2.2) \quad \langle z \rangle = b_0 + b_1.t + b_2.t^2$$

$$(2.3) \quad \langle z \rangle = b_0 + b_1.t + b_2.t^2 + b_3.t^3$$

Figure 2 shows examples with light curves (LCs) of the variable stars V 425 Cas and KR Aur that contain irregular fast light variations (flickering). The LC are obtained with the 2 m telescope of the Rozhen NAO, [12] and [13], with 162 and 64 data points, respectively. The levels of the MLS average, median and MLTS, as well as the regression polynomials of 2<sup>nd</sup> and 3<sup>rd</sup> degree, derived by the MLS and MLTS, fit all data.

In Fig.2a the general trend of the data follows the shape of a 2<sup>nd</sup> degree polynomial. By this reason both polynomials of the type (2.2) are closely situated. In this case the MLTS does not show some advantages. However, in Fig.2b the general (calm) trend follows an approximately horizontal line and both 3<sup>rd</sup> degree polynomials of the type (2.3) are essentially different. The MLS polynomial is deviated by a large flare, while the MLTS polynomial recognizes and elucidates the horizontal trend, ignoring the flare. In this case the MLTS shows clearly its robustness against outliers.

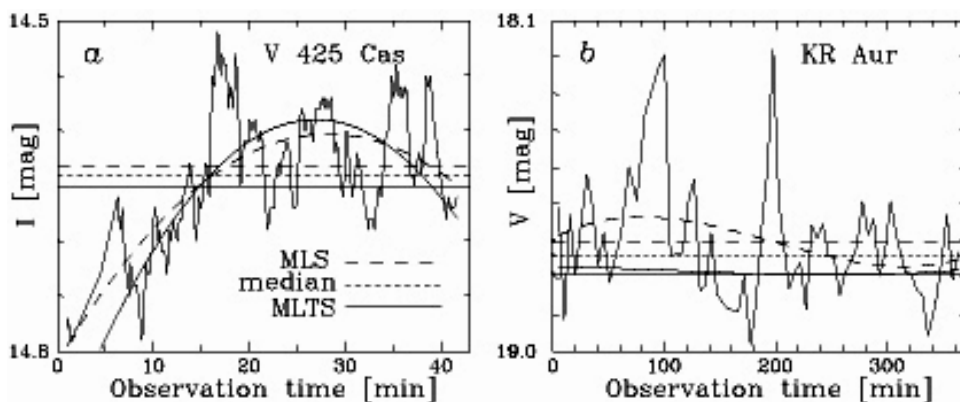


Fig. 2. Fitting of light curves of flickering stars with comparison of the MLTS mode, median and MLS average (horizontal lines), as well as of polynomial curves of 2<sup>nd</sup> degree (2.2) in the case a and 3<sup>rd</sup> degree (2.3) in the case b. In the case b The MLTS mode line or the MLTS 3<sup>rd</sup> degree polynomial may be used for detach of a residual curve and an estimation of the energy of the flares

### 3. Simple fast method for the application of the MMP though MLTS

Searching for the best polynomial, the MLTS must check a large number of combinations. This number increases fast with the increase in the

polynomial degree:  $N \sim n^2$  for the 1<sup>st</sup> degree (2.1a) or (2.1b),  $N \sim n^3$  for the 2<sup>nd</sup> degree (2.2),  $N \sim n^4$  for the 3<sup>rd</sup> degree (2.3) etc. That is why the building of 3<sup>rd</sup> degree polynomial by the MLTS over 100 points needs to test  $\approx 15.7 \times 10^6$  combinations, but over 1000 points it needs to check  $44.2 \times 10^9$  combinations (Fig.3a, upper dashed line). Such tasks may take decades of computation time.

However, such a consecutive test of millions – billions combinations is not necessary. The practice shows that the number of the combinations that have to be checked in order to obtain an optimal result may be reduced thousands – millions times. In particular, a random number generator may be used to trim a high enough number of arbitrary combinations, but the simplest way is omitting numerous combinations, by attributing smaller importance to them. The simple fast method, described below, is based on omitting the neighboring combinations and it needs data that is preliminary sorted in an ascending order by argument  $t$ . When the number of arguments is larger than one, the data must be sorted in an ascending order by the first argument, and if need by the second, etc., arguments.

Let us concentrate on the simplest case (2.1a) or (2.1b) with a full number of combinations (pairs of points)  $N = n(n-1)/2$ . All such combinations may be counted and tested by the following C-code

```
(3.1) N=0; for (i=0; i<n-1; i++) for (j=i+1; j<n; j++) { N++;
/* Here is the place of the code that tests and labels the line patterns */ }
```

However, the neighboring pairs of points, numbered as  $(i,j)$ , like  $(0,1)$   $(1,2)$ ,  $(2,3)$ , etc.,  $(0,2)$ ,  $(2,4)$ ,  $(4,6)$ , etc., or, generally,  $(0,0+m)$ ,  $(0+m, 0+2m)$ ,  $(0+2m, 0+3m)$ , etc., may be omitted as close neighbors and less useful. Generally, beginning with the point numbered 0 and using only the pairs of points that have difference divisible by  $m$  between their numbers, we may thin out the number of combinations about  $m^2$  times. We could use all the points, testing also for the cases  $(k, k+m)$ ,  $(k+m, k+2m)$ ,  $(k+2m, k+3m)$ , etc., for  $k = 0, \dots, m$ , i.e, about  $m$  more times . So, such thin out procedure must be applied by the C-code

```
(3.2) M=0; for (k=0; k<m; k++) for (i=k; i<n-m; i+=m) for (j=i+m; j<n;
j+=m) { M++;
/* The code that tests and labels the line patterns must be written here */ }
```

Here  $M$  is the number of the used combinations. Thus the reduction gain becomes  $(N/M) \sim m$  in the case of (2.1a) or (2.1b),  $(N/M) \sim m^2$  in the case of (2.2) and  $(N/M) \sim m^3$  in the case of (2.3).

For example, in the case of  $n = 13$  points, numbered as 0, 1, 2, ..., 12,  $p=1$  and  $m = 1$ , we have to check the full number of combinations,  $N = 78$ . However, if we use  $m = 3$ , we have to check  $M \approx N/3$  combinations. Really in respect to (3.2) the combinations are 21. These combinations are shown in Fig. 3.

(0,3)	(0,6)	(0,9)	(0,12)	(3,6)	(3,9)	(3,12)	(6,9)	(6,12)	(9,12)
(1,4)	(1,7)	(1,10)		(4,7)	(4,10)		(7,10)		
(2,5)	(2,8)	(2,11)		(5,8)	(5,11)		(8,11)		

*Fig. 3. Inventory of the combination used with applying of the fast method for MLTS regression line ( $p = 1$ ) on  $n=13$  points with thin out step  $m = 3$ . The number of these “good” combinations is  $M = 21$ , while the number of all combinations is  $N = 78$*

Here we present a method for automatic progressive increase of the thin out step  $m$  in dependence on  $n$ . The increasing is shown in Fig.4a. The user must supply a suitable supporting number, f.e.  $n_0 = 21$ . In that case, if  $n \leq n_0$ , the computer program will use all combinations, corresponding to  $n$ , as in the general case (3.1), with  $m = 1$ . If the number of points in the current application of the MLTS occurs  $n > n_0$ , a suitable thin out step of  $m > 1$  will be derived and used, so that it reduces the number of the used combination as in (3.2).

The C-code, given below, shows the automatic derivation of  $m$ , in dependence of  $n$  and a supporting number supplied by a user  $n_0$ , with a respective number of combinations  $N_0$ , derived by (3.1). This code increases the thin out step  $m$  (Fig. 4a) and defines the number of checked combinations  $M$  to be more and more large than  $N_0$ , but with enough slow increasing (Fig.4,b, thick graphs).

```

/* Here is the part of the program that calculates  $N_0$  from  $n_0$  though
(3.1) */
(3.3) M=0; m=1; if(n>n0) {
      N=(n0-1)*n0/2.; for(l=n0; l<=n; l+=2) {
      M=0; for(k=0; k<=m; k++) for(i=k; i<l-nd; i+=k) for(j=i+k; j<l;
      j+=k) { M++;

```

if ( $M > N_0$  &&  $1/k > 2$ ) {  $N_0 = M$ ;  $m++$ ; } }

The result is the thin out step  $m$  that will be used for C-code (3.2), as well as the preliminary derived number  $M$  of the combinations to be used. In this approach the thin out step  $m$  increases slowly but progressively with the increasing number of points  $n$ . The reduction gain  $N/M$  increases rapidly.

Figure 4a shows the increasing of the thin out step  $m$  number in dependence on  $n$ , after the code (3.3). Figure 4b presents the slow increase of the used combinations  $M$  (thick jagged curves) and the fast increase in gain ( $N/M$ ) (jagged curves at the bottom down corner).

In the examples given in Fig.4 the user-supplied supporting number  $n_0$ , that starts the increase of  $m$  and the increase of  $N/M$ , is 75, 32 and 22, respectively. There in the case of  $n=1000$  points the thin out step tends to  $m=100$  (Fig.4a). In the same time in the cases of polynomials of 1<sup>st</sup>, 2<sup>nd</sup> and 3<sup>rd</sup> degree the gain  $N/M$  is about 100, 3000 and 110 000 times, respectively (Fig. 4b).

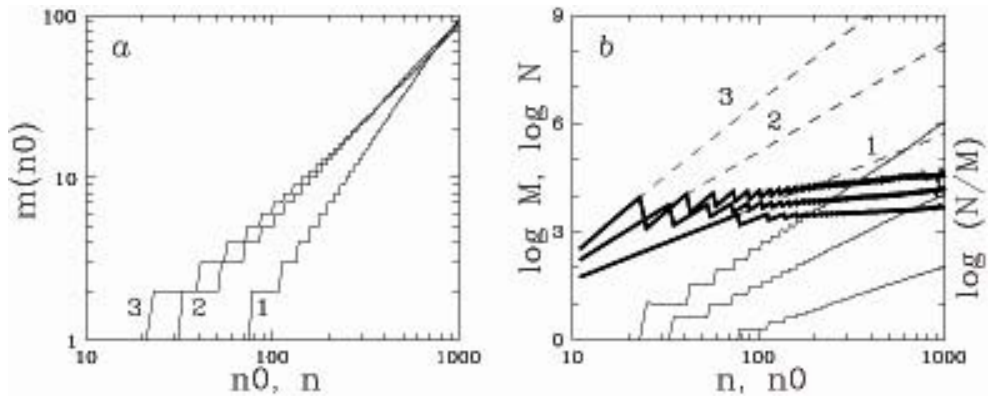


Fig. 4. a. Increasing of the thin out step  $m$  in dependence on the data number  $n$  and user supplied beginning number  $n_0$ , where the numbers 1, 2 and 3 correspond to the models (2.1), (2.2) and (2.3). b. Increasing of the full combination number  $N$  (dashed lines), used number of combinations  $M$  (thick graphs) the gain  $N/M$  (graphs in the right-down corner) in dependence on  $n$ . The numbers correspond, as in a, to polynomials of 1<sup>st</sup> (1), 2<sup>nd</sup> (2) or 3<sup>rd</sup> (3) degree

Figure 4 shows that the proposed fast method, based on omitting of combinations, makes the MLTS and the MMP based on the MLTS really useable. Some applications are given below.

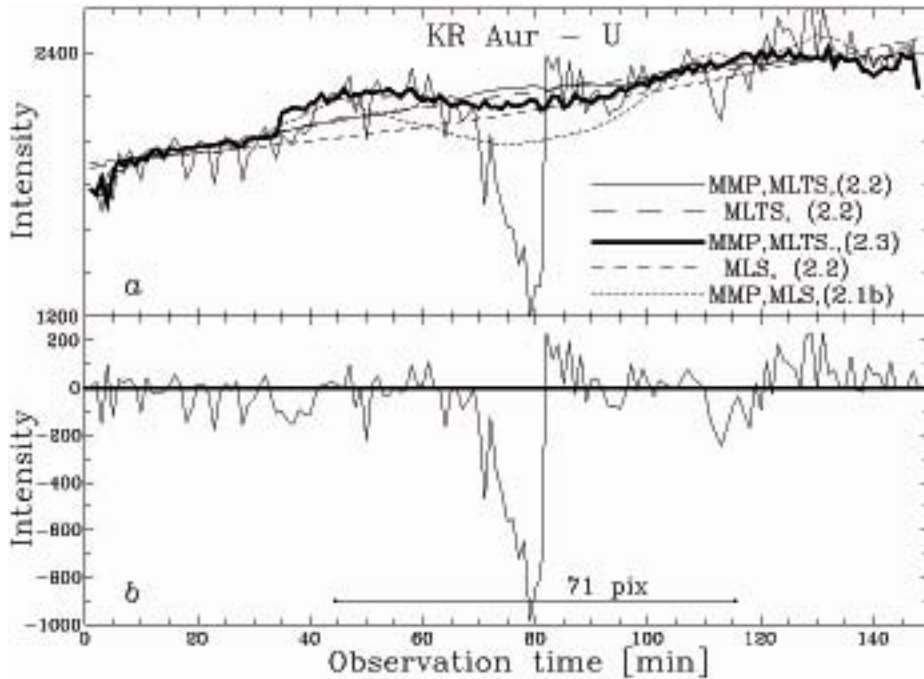


Fig. 5. a. Results of tracing of a light curve of the cataclysmic star KR Aur by various methods, signed in the picture. In the cases 2 and 4 the regression curve over all points is build. In the other 3 cases different smoothing methods with window size 71 pix (points) are used; b. Residual light curve with respect to the MMP smoothing by the MLTS (2.3) in a. (thick curve)

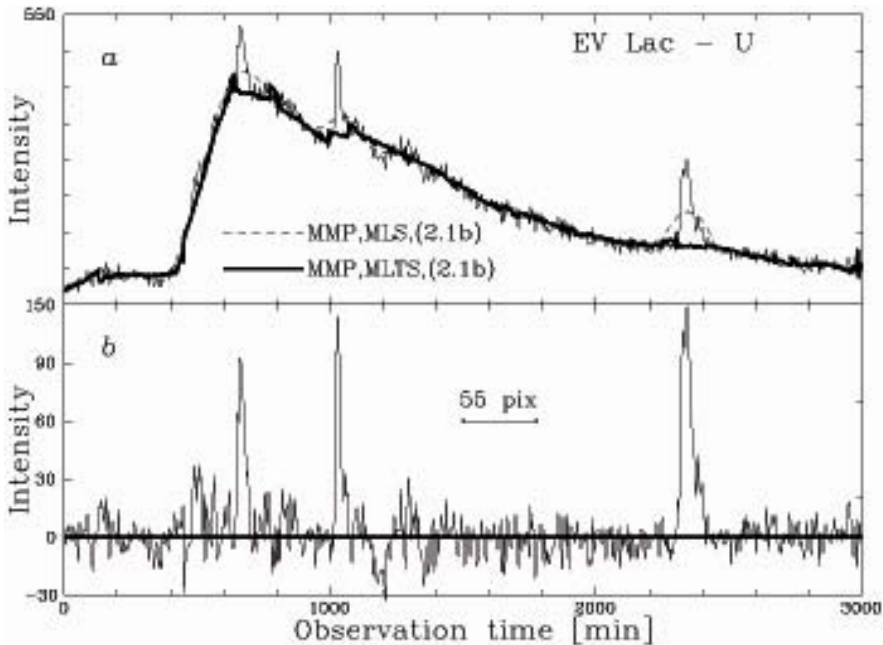
#### 4. Tracing a large scale trend in stellar light curves with flickering

The flickering of symbiotic and cataclysmic stars produces complicated light curves where both large scale trends and short scale variations are of astrophysical interest.

Figure 5a shows a light curve (LC) of the cataclysmic variable KR Aur with 148 points (60 cm telescope of the Belogradchik AO, [13]). A significant sink of a 2-fold light decrease and duration of about 15 min dominates in the LC. The general behavior of the LC is fitted by a 2<sup>nd</sup> degree polynomial (2.2) through the MLS and through the MLTS. Note that the MLS polynomial is affected by the sink of the LC and it has a concave curve, but the MLTS polynomial ignores the sink and shows a more realistic convex curve. The LC is also smoothed by the MMP with a window size 71

pix (points) through the MLS (2.1b), as well as through the MLTS (2.2) and MLTS (2.3). (For visualizing of the jaggedness of the MLTS result additional smoothing by the MLS has not been applied.)

The last mentioned smoothing may be considered the best and useful for deriving the “energy” of the sink: Figure 5b shows the residual LC with respect to the MMP, made though the MLTS (2.3).



*Fig. 6 a: Results of smoothing of the LC of a strong and continuous outburst of EV Lac with a window of 55 pix (points) by 2 methods, signed in the picture.  
b. Residual LC with respect to the MMP smoothing by the MLTS (2.3)*

Figure 6a represents the LC with 600 points of a remarkable power outburst of the active red dwarf star EV Lac (60 cm telescope of the Rozhen NAO, [14]). The general photometric behavior of the outburst is presented by smoothing with a window size of 55 points (275 min) by use of the MLS and the MLTS of type (2.1b). Note that the MLS smoothens and spreads the local short outbursts, while the MLTS ignores them.

Figure 6b shows that the residual LC with respect to MLTS is smoothened. (Additional LMS smoothing of the MLTS smooth is not applied). The residual LC elucidates clearly at least three well pronounced short time outbursts with a duration of 100 – 200 min. The applied MLTS



method gives possibility of deriving the energy of the main outburst as well as the energy of the flickering outbursts.

### 5. Tracing the spectral continuum among many spectral lines

The deriving of the continuum of a stellar spectrum containing numerous spectral lines is an important and difficult task. The MMP based on the MLTS gives a reasonable solution.

Figure 7a presents a part of the spectrum of the AM star HD 033254 through 900 data points with a step of  $0.1 \text{ \AA}$  (2 m telescope of the *Rozhen* NAO [15]). The continuum seems to be linear and the regression line, build by the MLTS (2.1b), confirms clearly this impression. The respective LTS regression line is deviated down by the absorption spectral lines and it is useless. Furthermore, the smoothening by a window size of 71 pix (points) through the polynomial (2.1b) is applied by MLS and MLTS. The MLS curve twists accounting for the intensities of the lines, but the MLTS curve follows confidently the line of the continuum.

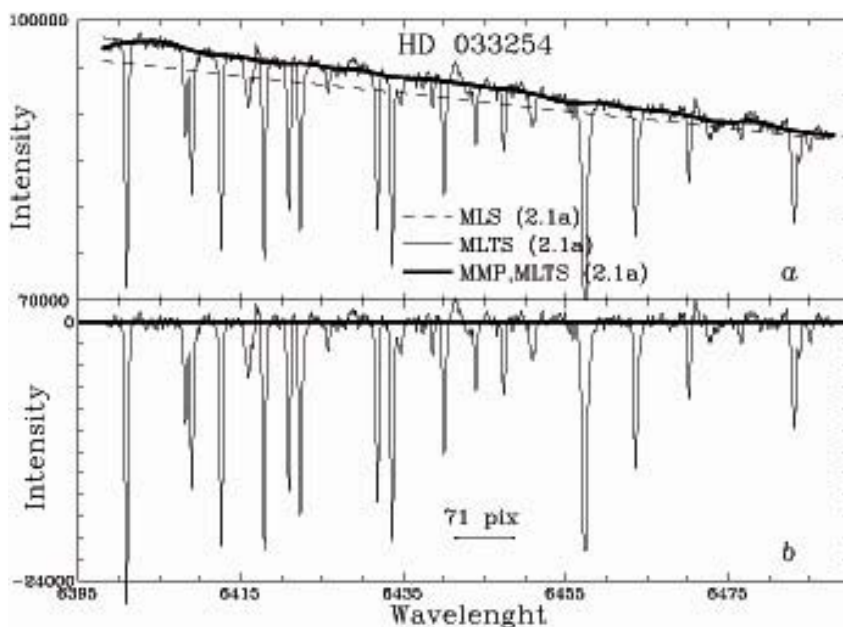
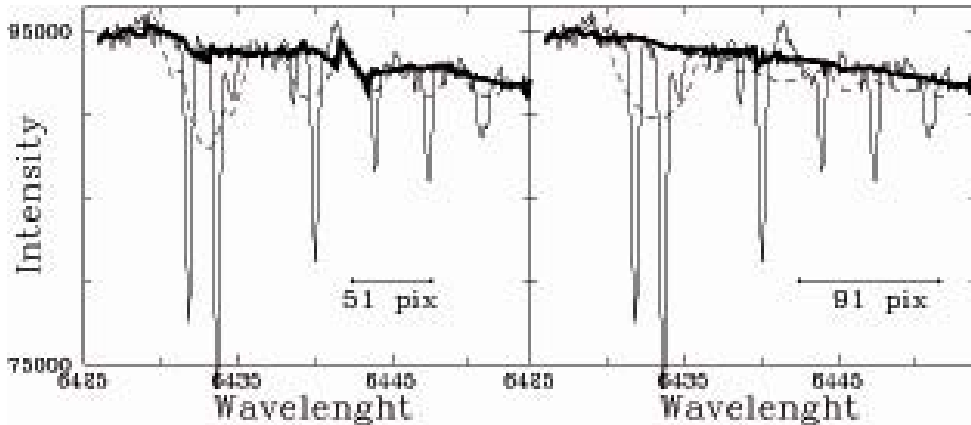


Fig. 7. a: Results of processing of a spectrum of the Am star HD 033254 by various methods, signed in the picture. In 2 cases, signed by “full”, a regression line over all points is built. In the rest cases smoothing window size of 71 pix (7.1 Å) is applied; b. Residual light curve with respect to the MMP smoothing by the MLTS (2.1b)

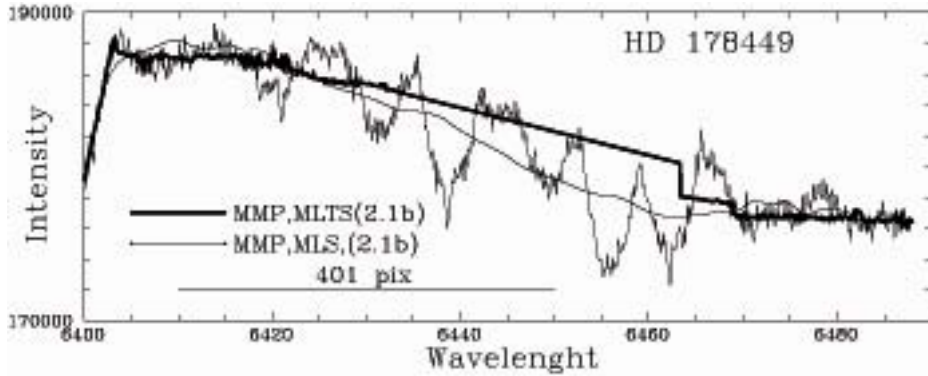
Figure 7b shows the residual spectrum with respect to the MLTS smooth and the equivalent widths of the spectral lines may be easy derived.

Figure 8 shows the central part of the spectrum, given in Fig.7. Smoothing with 2 different window sizes is applied and the results are practically identical. These examples show that the window size is not too crucial.



*Fig. 8. Smoothing of the central part of the spectrum of HD 033254, given in Fig.7a by the MMP (2.1b) through MLS (dashed curve) or MLTS (thick curve) with a window of 51 pix or 91 pix. In both cases the MLTS (2.1b) follows the majority of the points, which are placed in the band of the continuum*

Figure 9 shows an attempt for tracing the continuum in the complicated spectrum of the star HD 178449 with 900 points (2 m telescope of the *Rozhen* NAO, [15]). A MMP smoothing with a window size of 401 pix is applied through the MLS or MLTS. The MLS polynomial follows the middle part of the band of the data. On the contrary, the MLTS attempts to find and to follow the trend of some majority of points. This attempt is about to be successful up to 6000 Å, but the right tail of the data is too short and the derived trend occurs broken. Essentially, this attempt for tracing some spectral continuum is not successful.



*Fig. 9. Results of smoothing the spectrum of the star HD 178449 by application of a very large window of 401 pix (points). The right edge of the MLTS curve is broken because the spectrum is complicated and short*

Figure 9 shows the significant difference between the results of MMP smoothing by the MLS or by the MLTS. It elucidates also the fact that the result of the MLTS smoothing cannot be easily predicted.

In the end, note that in the last example the computing time for the MLTS smoothing by means of the C-code (3.2) with the implementation of the algorithm (3.3) took about 10 min (roughly one second per data point), while when applying of the direct method (3.1) only the computing time should be about 100 times larger.

## **Conclusion**

The main known advantage of the MLTS (Rousseeuw, 1984; Rousseeuw &, Leroy, 1987) in comparison with the MLS is its extremely high robustness with respect to outliers. Really the MLTS is able to ignore up to about 40% of the data, providing with a “mode” regression model. However, this method is not widely spread even when strong outliers are present because of its extremely high time consumption. This is understandable. When the data amount is not large, the user is able to reject the outliers that cannot be taken into consideration and to apply the ordinary MLS. However, in the case of many outliers or of many consecutive applications of a chosen regression model in the presence of outliers, the MLTS may be recommended. Apart from the examples given here, the MLTS may be useful in image processing and galaxy photometry.

We must note that we call the MLTS estimation to be “mode” but it is not just the mode, it must be slightly shifted toward the ignored large deviations. We consider this shift is very small.

**Acknowledgements.** The author is thankful to Dr. A. Antov and Dr. I. Kh. Iliev for the kindly allowed data, as well as for the valuable discussions about the text and the context of this paper.

## References

1. Anderson, T. W., The statistical analysis of time series. 1971. New York: John Wiley & Sons
2. Brillinger, D. R., Time series: Data analysis and theory. 1975. New York: Holt, Rinehart. & Winston.
3. Otnes, R. K., Enochson, L., Applied time series analysis. 1978.,New York: John Wiley & Sons
4. Shumway, R. H., Applied statistical time series analysis. 1988. Englewood Cliffs, NJ: Prentice Hall.
5. Heasley, J. N., Publ. Astron. Soc. Pacific 96, 1984, 767
6. Georgiev, Ts. B., Bull. Spec. Astrophys. Obs. 39, 1996, 131
7. Tukey, J. W., Exploratory Data Analysis. 1977. Addison Wesley Publ. Co.
8. Rousseeuw, P. J., J. Am. Stat. Assoc. 79, 1984, 871
9. Rousseeuw, P. J., Leroy A. M., Robust Regression and Oulier Detection. 1987. John Willy & Sons
10. Georgiev, Ts. B., Bulg. Astron. J. 10, 2008. 93
11. Dimitrov, D., Private communication. 2007
12. Tsvetkova, S., Bоеva S., Bulg. Astron. J. 12, 2009, 43
13. Antov, A., Private communication. 2012
14. Bogdanovskii, R., Konstantinova – Antova R., Private communication. 2013
15. Budaj, J., Iliev, I. Kh., Mon. Not. Roy. Astron. Soc. 346, 2003, 27-36

## **РОБАСТО ИЗГЛАЖДАНЕ НА РЕДОВЕ ОТ ДАННИ ЧРЕЗ ПРОСТ БЪРЗ АЛГОРИТЪМ. ПРЕКАРВАНЕ НА ТРЕНДА ПРИ ЗВЕЗДЕН ФЛИКЕРИНГ И КОНТИНУУМ ПРИ ЗВЕЗДЕН СПЕКТЪР**

**Цв. Георгиев**

### **Резюме**

Методът на движещия се прозорец от данни се използва широко при трасиране на едромащабното поведение на времеви редове, като оценката на централната точка на прозореца се базира на Метода на

най-малките квадрати (МНК). Обаче, обичайният МНК минимизира разсейването на всичките  $n$  квадрати на отклонения и затова е екстремално чувствителен към силно отклоняващи се данни. Една алтернатива е Методът на отбраните най-малки квадрати (МОНК) на Русю. Той минимизира само лявата част на квадратите на отклоненията, наредени по нарастване, включвайки поне  $h = n/2+1$  данни. В дясната част на наредените квадрати на отклоненията може да присъстват произволно големи квадрати на отклонения, но МОНК ги игнорира. Така МОНК има асимптотична 50 % робастност спрямо силно отклоняващи се данни, докато робастността на МНК е определено 0 %. Обаче, докато коефициентите на обичайната МНК регресия се изчисляват чрез аналитично изведени формули, при МОНК това става чрез тестване на достъпни образци на възможни решения. Такива са: В едномерния случай – всяка данна; В двумерния случай – правата през всяка двойка точки; В тримерния случай – равнината през всяка тройка точки и т.н. Образецът, който има най-малко МОНК-разсейване се избира за решение. Главният недостатък на МОНК е, че в 2D, 3D и т.н. случаи той се нуждае от огромно изчислително време за да провери всички достъпни образци. Това може да отнеме милион-милиард пъти повече компютърно време отколкото времето за изчисляване на обичайна регресия. В тази работа е представен (i) прост бърз алгоритъм, който пропуска съседни комбинации с прогресивно увеличаваща се стъпка и може да редуцира изчислителното време хиляда – милион пъти. Представени са и (ii) възможностите на МОНК при изглаждане на редове от данни в два примера – за трасиране на кривата на блясъка на звезда в присъствието на избухвания и за прекарване на континуума на звезден спектър в присъствието на множество спектрални линии. Тук се имат предвид еквиливантни редове от данни но методът е приложим във всички случаи.

## **FRACTAL APPROACH TO SPACE STRUCTURES, OBJECTS AND DYNAMIC PHENOMENA**

***Filip Filipov***

*e-mail: fyfilipov@gmail.com*

### ***Abstract***

*This paper presents the fractal theory and the definition of a fractal. It dwells on the basic features of abstract and natural fractals, as well as on the mathematical instruments used to describe these sophisticated, complex and nonlinear shapes and phenomena in the Universe. The study examines some of the earliest attempts to apply the fractal theory in astrophysics and particularly the processes related to gravitational singularities, the shape of spiral galaxies and the dynamic organization and structure of the Universe.*

### **1. Introduction**

In his visionary work the American scientist, Benoit Mandelbrot, opened new vistas in mathematics and all sections of physics by discovering the fractal set of geometric shapes. In the preface to the second revised edition of his book, titled *The Fractal Geometry of Nature*<sup>1</sup>, he pointed out that he was in search for a new natural geometry, which would not leave out the huge diversity of “irregular” shapes to be seen everywhere in the physical reality, but would rather describe and include them in mathematical studies. This had to be done, because “Clouds are not spheres, mountains are not cones, coastlines are not circles, and bark is not smooth, nor does lightning travel in a straight line.” He considered his mathematical research both a philosophic and aesthetic drive to a more complex and profound understanding of the forms and processes in reality. The fractal theory has been widely used in the pursuit to attain a new understanding of the complex nonlinear and dynamic processes in astrophysics, geophysics, and even in

the sciences examining the human body, brain and consciousness. Since mathematic studies in fractal geometry and the practical application of these studies in specific sciences started only after 1975, there are still many areas, as well as space phenomena and processes, which can benefit substantially from the application of fractal analysis.

## **2. Purpose**

The present paper is an attempt to present the fractal theory and some of the early experiments to apply it to astrophysics. The main point is to approach the widely spread nonlinear dynamic processes in the Universe with the latest mathematical descriptive tools and furthermore to perform a structural analysis of the existing shapes and objects in space.

## **3. Results and Discussion**

### **3.1. Fractal – definition and characteristics**

If we are to use one of the most general definitions, *fractal* is an object which is *self-similar* in one way or another<sup>2</sup>. From a strict mathematical point of view this self-similarity is relevant only to the structure or shape of the object, however, from a more abstract and philosophical point of view a fractal can be considered in a more universal aspect – every time there is a complex *self-similarity, manifested in a single hierarchically structured whole*. Mathematically the fractal refers to equations related to *iteration, recursion* or any form of *feedback*.<sup>3</sup> Mathematics and informatics define iteration as algorithmic repetition of any process or function, and recursion – as a particular type of functions referring to themselves or put in other words each member of a recursive function is derived from previous members of the same function. In turn the self-similarity of fractals can be realized by an iterative, recursive or stochastic mathematical method. Fractals of exact self-similarity are most often realized by an iterative method; the quasi-self-similar fractals are usually realized by recursive functions, while the accidental fractals exhibit numeric or statistical characteristics persistent in certain proportions. From a mathematical point of view fractals have the following characteristics<sup>4</sup>:

- The whole projects and manifests itself in itself – each part of the whole is similar to the whole, whereas the self-similarity can be exact, approximate or stochastic;

- Abstract fractals organized mathematically have a fine pattern structure in random small scale, and naturally generated fractals have a self-similar structure and properties in broad but still limited scale;
- Rather high irregularity, difficult to describe using the standard Euclid's geometry language;
- Non-whole (Hausdorff) dimensions which as a rule are bigger than the topological dimensions;
- Simple and recursive definition;
- The so called natural dynamic fractals exhibit a characteristic typical for the complex dynamic systems – self-organisation and natural emergence, which occurs because of the very essential properties of the fractals, and also because of the fact that a form of cyclic causality generates fractality.

### 3.2. Mathematical definition of fractal structures

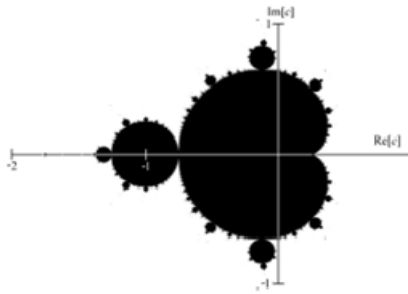


Fig. 1. Graphic image of the Mandelbrot Set <sup>5</sup>

If one examines *the Mandelbrot set* with the purpose to clarify the mathematical aspect of the fractal concept, one will arrive at the conclusion that this set is identified as a fractal determined by a set of points  $C$  in the complex plane characterized by the following iterative sequence:

$$Z_0=0; \quad Z_{n+1}=Z_n^2 + c$$

so that this sequence does not converge to infinity. The several opening iterative lines look like this:



if  $c = X + i.Y$ , where  $X$  and  $Y$  are real numbers, and  $i$  is the imaginary number  $\sqrt{-1}$  and  $Z_0 = 0$ , then:

$$Z_1 = Z_0^2 + c = X + i.Y$$

$$Z_2 = Z_1^2 + c = (X + i.Y)^2 + X + i.Y = X^2 - Y^2 + X + (2.X.Y + Y). i$$

$$Z_3 = Z_2^2 + c = \dots$$

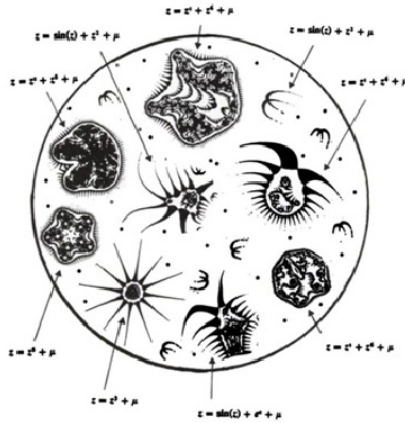


Fig. 2. Biomorphic fractal patterns of a quadratic functional definition different from the classic one<sup>6</sup>

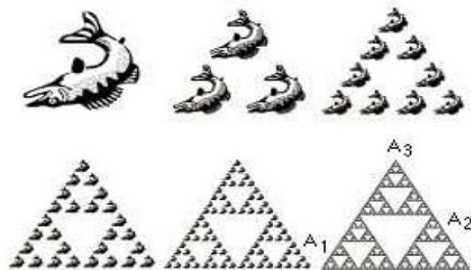


Fig. 3. Sierpinski's triangle constructed by multiple reduction of image prototype<sup>7</sup>

Graphically this set is displayed by a complex coordinate system and by taking into account whether a certain point in the coordinate system belongs to the Mandelbrot set or not (*Fig. 1*). The point is that various functions can be placed in an iterative sequence and their *Mandelbrot sets* can be obtained. Put in other words different functional models can be placed in the specific mathematical feedback (the iterative sequence) and this will construct different fractals. *Fig.2* shows fractal forms quite similar to the forms of living organisms or to forms existing in the Universe. The particular functional equations of the displayed fractals are as follows:  $z=z^3+\mu$ ;  $z=z^5+\mu$ ;  $z=z^3+z^5+\mu$ ;  $z=\sin(z)+z^2+\mu$ ;  $z= z^3+z^6+\mu$ , etc., where  $\mu$  is constant.

There are other types of fractals not related to complex numbers. One of the commonly quoted classic examples of a non-complex, iterative fractal is Serpinski's Triangle S (ref. *Fig.3*). It is worth noting that when constructing this fractal, during the first recursive steps, it has a rather rough and formless structure, but the progressing recursion results in a gradual perfection of each detail of the fractal. Thus original rough properties are shaped by recursive construction, and are transformed into fine patterns. One can trace the mathematical formalization behind this special property of fractals. The S set has three components each of which is a reduced image of S. Each of these components has three sub-components thus resulting in a nine-fold reduced image on the next level and this goes on infinitely. A simple observation of this iterative fractal leads to the functional correlation:  $S = f_1(S) \cup f_2(S) \cup f_3(S)$ , where  $f_1, f_2, f_3$  are reductions of the S space by a factor of  $\frac{1}{2}$ , and the three main components of S are as follows:  $f_1(S), f_2(S), f_3(S)$ . This definition is applicable to any set of objects. If the collection of prototype cards is  $F = (f_1, f_2, f_3)$ , referred to as *Iterative functional system*, then in respect of each set  $F(T) = f_1(T) \cup f_2(T) \cup f_3(T)$ , it can be evidenced that S is of core significance: by starting with a certain compact set  $T_0$  and  $K \geq 1$ , we can describe recursively  $T_K = F(T_{K-1})$ ; then  $T_K \rightarrow S$  with  $K \rightarrow \infty$ , in other words  $T_K$  tends to *Serpinski's triangle S* in Hausdorff dimensions with K tending to infinity and at that independently from the type of the initial set  $T_0$  (ref. *Fig.3*, where *Serpinski's triangle S* is realized, made of a set of fishes). Therefore, S is referred to as a *fractal set attractor* of the iterative-functional system, described by the equation:  $S = f_1(S) \cup f_2(S) \cup f_3(S)$ , and the initially rough form, from which the fractal structure gradually moves away systematically by each new step of the iteration, is referred to as a *fractal set repeller*<sup>8</sup>.

For the sake of clear and unambiguous visualization, we shall write down the following expression:

$$FR(\text{pattern/function}) \xrightarrow{\text{iteration}} \text{Attractor}$$

The presented notation should be interpreted as follows:

*Fractality with a certain pattern and/or with a particular mathematically definable function, after a certain number of iterations, transforms into its attractor.*

If the *Mandelbrot set* is examined as attractor and it is denoted as M, then its complex fractality may be displayed in the following way:

$$FR(Z_{n+1}=Z_n^2 + c) \xrightarrow{\text{iteration}} M.$$

And if *Serpinski's triangle* is examined under this scheme, as a typical non-complex fractal, with its S, the result will be as follows:

$$FR(f_1(S) \cup f_2(S) \cup f_3(S)) \xrightarrow{\text{iteration}} S.$$

In a more generic way it can also be expressed as follows:

$$FR(\text{Triplexity}) \xrightarrow{\text{iteration}} S,$$

because as was already shown each image, characterized by triplicity, can become a pattern of this fractality and according to the above-mention iteration method can be transformed into a fractal attractor – *Serpinski's triangle*.

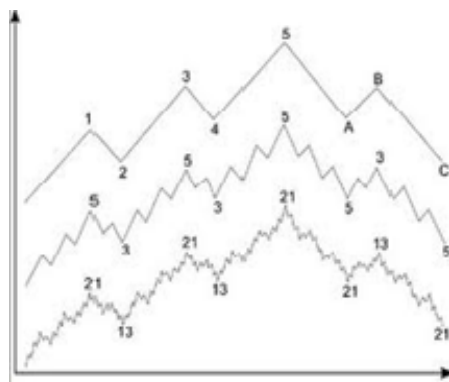


Fig. 4. Fractality of the stock exchange index

The main property of a fractal – its self-similarity, can be used to calculate its dimensions<sup>9</sup>. If we use simple geometric figures and if we create a degree of self-similarity within them, e.g. if a segment is increased twice, we will obtain two copies of the segment; if a square is increased twice, four copies of the first square will be obtained; if a triangle is increased twice again 4 copies of the first triangle will be obtained; if a cube is increased twice 8 copies of the first cube will be obtained. On the basis of these examples the following can be argued: if D is dimensions, K is the rate of increase, and N is the number of the obtained identical figures, then the following correlation is valid:  $K^D = N$ . Hence D is derived from the following formula:  $D = \log N / \log K$ . If this formula is applied to *Serpinski's triangle* with the already used random set of fishes, it can be seen that upon the first iteration of self-similarity 3 identical images are obtained ( $N = 3$ ), each of which is 1/2 of the prototype, hence  $K = 2$ . Then the Hausdorff dimensions of the fractal called *Serpinski's triangle* are:  $D = \log 3 / \log 2 = 1.5849625$ .

Then again in his subsequent works Mandelbrot goes on to discuss the so called *multifractal*. What is meant is a fractal structure with more than one base pattern. In other words not only singular fractals (fractals with a single pattern) can be observed in reality, but also multifractals – complex fractal structures with more than one functional patterns. An example of such a naturally generated, but already mathematically abstract fractal is the functional trajectory of the stock exchange movements. It has for a long time been established, on the basis of the so called *technical analysis*, that there is a fractal similarity in the charts of stock exchange indexes between the different time intervals which are visualized (*Fig. 4*). The daily chart of the EURUSD index may be constructed by several iterations of the model set out by the chart of the same index, but visualized subsequently on a 4-hour or 15-minute chart. In this case it can be noticed that different patterns evolve: W-image, N-image, И-image or V-image and so on. Indeed, these are the so called different patterns of the multifractal, developing in the form of the particular stock exchange index. According to the above mentioned more general notation any particular multifractal may be expressed in the following way:

$mFR(W\text{-патерн, N-патерн, И-патерн, V-патерн...}) \rightsquigarrow \text{EURUSD,}$

Which is to say that the EURUSD is a *multifractal* (this is denoted by  $m$ ), obtained by iterating the following patterns: W-pattern, N-pattern, И-pattern, V-pattern and so on.

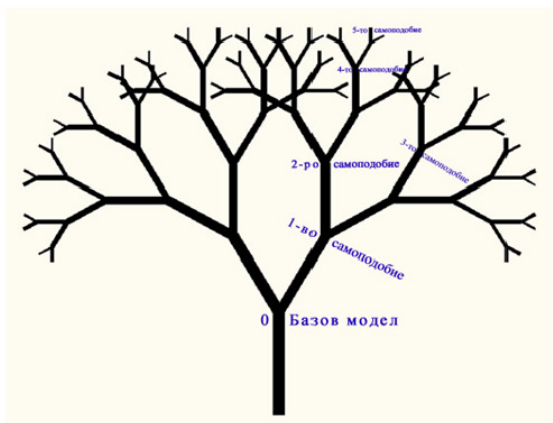


Fig. 5. Degree of self-similarity of natural fractals

According to the author of this paper, when analyzing the naturally originating fractals, one specific new value may also be introduced – degree of self-similarity. Fig.5 shows the typical form of the natural fractals of trees. It reveals how the basic pattern – fork ( $Y$ ) is realized in this particular tree-like structure by degree of self-similarity 5. This whole-number positive variable in fact indicates how many hierarchical levels there are in a particular natural fractal and also how many degrees of recursive self-reference were realized through the basic pattern in order to achieve the structure of the particular object. If a certain natural fractal structure is multifractal, it will exhibit several degrees of self-similarity, each one manifested at different hierarchical depth. If in this particular case of a non-complex fractal we denote its attractor by  $Y$ , the result will be the following:

$$FR(f_1(Y) \cup f_2(Y)) \rightsquigarrow Y,$$

or put in a more general way, but anyway expressed adequately, indicating the existence of a *natural fractal of a specific degree of self-similarity 5* we will obtain:

$$nFR(\text{fork}_5) \rightsquigarrow Y.$$

Here the sign  $n$  must be understood exactly in this way: *there exists a natural fractal*, and *index 5* of the *fork* pattern stands for *the degree of self-similarity* of the particular fractal in *Fig.5*. The potential application of the fractal analysis and descriptive method to astrophysical objects and to the objects distribution structure in the Universe will be demonstrated on the basis of fairly easy to understand mathematical definitions.

### 3.3. Fractality of the natural forms in the Universe related to waves, convection and turbulence. Elaboration of the fractal analysis

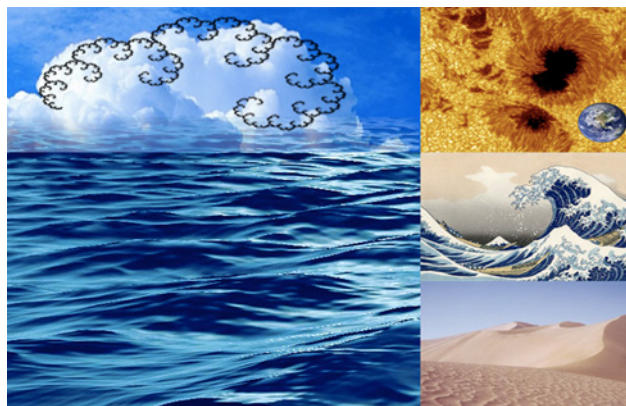


Fig. 6. Naturally generated fractal patterns

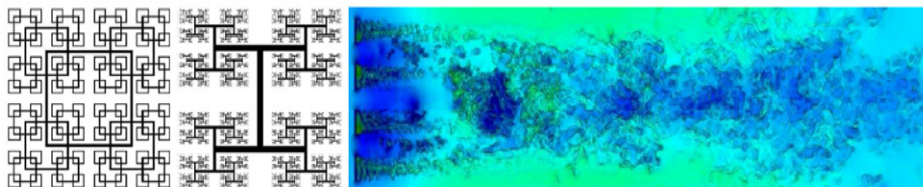


Fig. 7. Fractals and turbulence

The wave process was contemplated in the environment of its natural emergence and its self-similarity was noticed as early as ancient times (ref. *Fig. 6*). The big ocean waves are made of smaller waves, which in turn are further furrowed in waves. The same process is to be observed in the desert too, where the gigantic sand dunes have a wave-like structure in several levels. If the convection flows of matter are observed for instance in the clouds of the Earth or Jupiter or on the surface of the Sun, fractal patterns are easy to discern in their intensive turbulence. One of the important new ideas in the fluids science is the fact that turbulence is modelled through fractal patterns (*Fig. 7*).<sup>10</sup> Each natural movement of fluid in space or earth environment has, generally expressed, two states: laminar flow and turbulent flow. Under certain conditions the laminar flow having parallel current lines naturally transforms into a turbulent flow. Turbulence structures are similar at various space levels of observation and here again what can be seen is a dynamic fractality. Turbulence causes the imaging of vortex cores varying in scale which represent the basic dissipative mechanism<sup>11</sup> for the transmission and dissipation of energy in the flows. The big vortex cores start the fractal expansion process and at the same time they dissipate energy, causing turbulence of a lower magnitude, and it is exactly in this way that fractality is realized at smaller hierarchical levels in the whole of the fractal. This process evolves structurally and after a certain “life”-time and stability it starts gradually to subside (if no more energy enters the system) by the process of dissipating energy to the intermolecular level.

However, if energy keeps entering the system where the turbulence occurred, fractality is stabilized and this is easy to observe as a stable turbulence picture. The following notation can be produced:

$$FR(\text{Vortex core}) \rightsquigarrow \text{Turbulence} \rightarrow \text{Energy dissipation}$$

According to the author of this study in this way a conclusion can be reached that matter, manifested in different physical states, is entirely penetrated by fractality, i.e. actually everywhere in the Universe matter is organized on the basis of self-similarity generated by cyclic causality. Using the above example, taken from nature, demonstrating by turbulence not only single cyclic vortexes, but also a structural texture of fractally recurrent vortex cycles, which transmit and dissipate energy, the scope of the causal analysis of the examined processes can be significantly expanded.

The causal fabric of the Universe is not composed only of simple, complex and cyclic causal links, but also of vortex causal processes which are essentially fractals. In other words the cyclic causal link as one singular closed cycle transforms into a nucleus and pattern of a causal vortex-fractal, which means that the following notation can be formulated:

$$FR(\text{Cyclic causality}) \rightsquigarrow \text{Causal fractal} \rightarrow \text{Energy dissipation.}$$

Moreover, the presented example of the turbulence process evidences that the emergence and transformation of the dynamic fractality in the Universe passes through four stages:

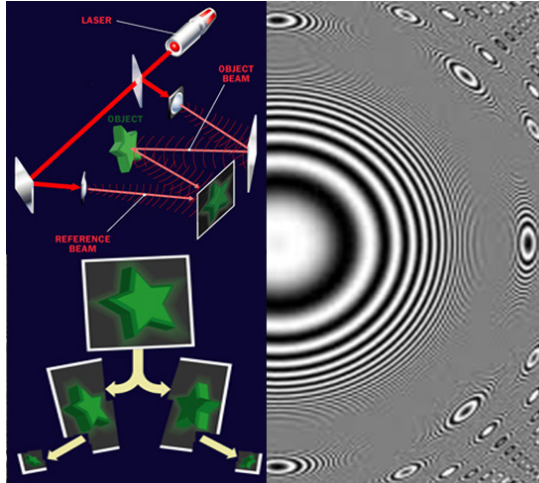
- (i) *emergence* – natural switching from non-fractal (i.e. non-self-similar structure) into fractal structure or put in other words the beginning of the self-organisation of the fractal process, at which there is already one degree of self-similarity;
- (ii) *evolution* – unfolding of the fractality pattern to ever smaller hierarchical levels in the fractal totality or put in other words, fractal „growth” during which the degree of self-similarity increases;
- (iii) *subsiding* – discontinuation of the realization of the fractal pattern to lower levels in the self-similar hierarchy and gradual fading away of entire hierarchical branches of the fractal, where the degree of self-similarity starts decreasing;
- (iv) *liquidation* – the fading away of different hierarchical levels of the fractal reaches a critical phase which causes the self-similarity in a given structure to disappear, i.e. the degree of self-similarity is equal to zero.

It is important to note that while there is a strong and constant causal impulse bringing in a steady inflow of energy, the fractal is evolving and trying to attain its attractor – its proportional and hierarchically self-similar manifested form and structure, which is simultaneously a balanced and steady energy state of the system. Conversely, it has to be emphasized that the above described four stages in the evolution of the dynamic fractal should not be examined only in single-model fractal structures. These are to be seen in the so called *multifractals*, whereas with them it is possible one pattern to be at the emergence and evolution stage in the overall structure of the multifractal, and another pattern to be at the subsiding and liquidation stage, at that the dynamics of the first pattern may and may not be contingent on the dynamics of the second one.



### 3.4. Application of the fractal approach in astrophysics

#### 3.4.1. Holography, structural fractality and the holographic principle in astrophysics



*Fig. 8. Hologram flow chart. Retaining the model of the whole upon breaking a holo-plate<sup>12</sup>*

In case a demonstration is needed on how fractal structures evolve naturally as a result of a certain cyclic-causal process, then the holographic phenomenon seems to be the best option. When a particular wave phenomenon is included in a cyclic causal link to itself, e.g. a ray of coherent light, it is split into a primary ray and a referent ray, and while the two rays are interacting between each other interference occurs that can cause a fractalised record of the environment where the interference took place. In the holo-process the referent ray interferes with the primary ray and the latter has been dissipated repeatedly under different angles by a particular object. The interesting point with this instance of wave cyclic causality is that fractality can be detected not only in the fixed interference picture itself, usually recorded on a holographic plate, but also in the very particle structure of this picture – no matter how many pieces the holographic plate is broken into, it retains the model and information recorded in the whole plate anyway (ref. *Fig.8*). Thus a kind of fractality is reached, which is not based on the geometry of forms, but on the very internal structure of the object. If the plate is exposed to a suitable laser beam, a 3D holo-image will emerge out of it because the interaction between

the laser beam and the fractally structured plate will create a cascade of a huge number of light refractions, as a result of which a 3D image appears, which was recorded initially on one 2D object – the holo-plate. Thus it becomes clear that the holographic setup can be used to record and present the entire information concerning the shape of a n-dimensional object on (n-1)-dimensional plate. This in contemporary theoretical physics and astrophysics appears to be the so called *holographic principle*, which was first formulated by Hooft and Susskind<sup>13,14</sup>. This principle was inspired by the black holes thermodynamics and the insight with them is that the information contents of all objects that have fallen into a particular black hole may be entirely located in the surface fluctuations of the gravitational singularity event horizon. Hence the theory assumes that the entire Universe can be seen as a 2D information structure “displayed” on the cosmologic horizon in a way that the three dimensions that we observe are only an effective description of the macro level. Susskind applies the holographic principle and the fractal ideas to substantiate the so called *Principle for information conservation in the Universe* – a concept derived from astrophysics which is of crucial significance in modern science.

### 3.4.2. Fractal approach to gravitational singularity

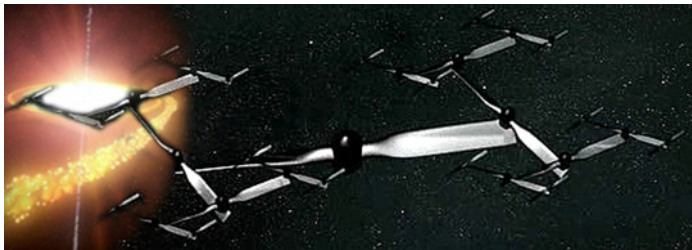


Fig. 9. A still from the film „Through the Wormhole. The Riddle of Black Holes”- 16.06.2010, visualising Susskind’s ideas

In his book *The Black Hole War*<sup>15</sup>, as well as in his interview presented by Morgan Freeman in the *Through the Wormhole. The Riddle of Black Holes* series, Susskind demonstrated the application of the fractal approach to the gravitational singularities. In scientific circles *The Black Hole War* is understood to stand for the long lasting scientific dispute with Hawking where Susskind presents witty thought experiments and mathematical constructs in

order to show that no information about the cause-and-effect processes is lost at the physical level even at the black hole boundaries. After a series of twists and turns Susskind nonetheless “won” the war and Hawking accepted his arguments. By a thought experiment examining the different points of view of observers moving in reference to a black hole, Susskind demonstrated the fractal structure of matter, and its transformation into an image on the holographic plate covering the entire surface of a given black hole. In order to visualize his idea he described a dynamic fractal with a moving propeller of an airplane falling into a black hole (ref. *Fig.9*).

The conclusion that can be drawn is that a fractal structure, similar in form to the fractality on the holographic plate, appears on the surface of the gravitational singularity; this fractal structure is a record and a dynamic reflection of the entire reality. This situation visualizes through *the holographic principle* how the macro-cosmic structures in the Universe, which have distinct fractal characteristics, touch, determine and interact with the fractal structure of the holographic patterns shaped on the event horizon of the black hole by the specific radiation of Hawking<sup>17,18</sup>, emanating from this gravitational singularity. According to theoretic physics virtual particles and anti-particles exist in the texture of the Universe and they are constantly emerging and disappearing. They appear on the basis of a particular emitted quantum of energy and afterwards they re-merge and re-emit the initial quantum of energy. This process is not disrupted in the absence of gravitational singularity, but in the presence of gravitational singularity it is possible for a particle after emerging to sink into the black hole and its antipode to break free from the gravitational vortex. This is exactly what produces Hawking’s radiation, which according to Susskind realizes the information conservation law, also under these extreme conditions.



*Fig. 10. The "heart pulsation" of a black hole<sup>16</sup>*

Nonetheless, fractal processes taking place on the boundary of gravitational singularity may be accessed and perceived in their reality by our

senses as well. The peak astrophysics facility – the Chandra observatory – provides opportunities to investigate X-ray radiation in deep space including radiation coming also from systems with probable black holes. Thanks to this facility the American scientists have detected a specific pulsation generated by the self-regulating feedback system of jet and the accretion disk of a black hole about 14 times the Sun’s mass, also known by the name of: GRS 1915+105.<sup>19</sup> It turned out that it’s not only the supermass black holes in the centre of galaxies that have a self-regulatory cyclic-causal mechanism<sup>20</sup>, but black holes of relatively normal size also possess such a mechanism. Exactly this regulatory mechanism is the cause of the “heart pulsation” of GRS 1915+105<sup>21</sup>(ref. *Fig.10*). It has a typical fractal form and bears a close resemblance to the proven fractal morphology of the electrocardiogram of the human heart pulsation. This fractality may be represented graphically or in audio form<sup>22</sup>, however, it is essentially part of the fractal process taking place on the boundary of gravitational singularity.

### 3.4.3. Fractal approach to the structure of spiral galaxies



*Fig. 11. Fractal spiral structure quite similar to the structure of spiral galaxies.*<sup>23</sup>

There is another example of fractal approach to astrophysic structures. This is easy to do by computer simulation of vortex movements and shapes similar to the ones visible for instance in our Galaxy (ref. *Fig. 11*). It is evident that matter in the Universe is distributed fractally: hundreds of milliards of stars, grouped together, form a galaxy, groups of galaxies are attracted to one another and form galaxy clusters, and these merge and form super-clusters.<sup>24</sup> What matters here is the fact that the different or similar levels of these structures, often interact among each other thus realizing different phenomena of a causal-cyclic nature. For example a particular energy radiation of our Galactic centre may totally re-structure the spiral organization of our Galaxy or of any particular star system – this is an interaction between two different

hierarchical levels in the fractal structure of the Milky Way. Nonetheless the different star systems influence one another so in some cases this leads also to the birth of new solar systems – e.g. a particular star explodes and compresses a gas cloud up to an adequate condition required for the subsequent birth of a solar system – this is an interaction between two similar hierarchical levels in the fractal structure of the *Milky Way*.

### 3.4.4. The Universe as a self-reproducing fractal – the theory of Linde, Penrose and Gurzadian

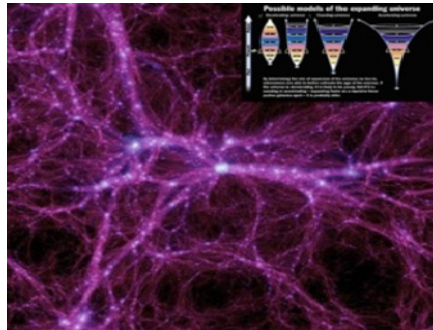


Fig. 12. Fractal pattern of the Universe – cosmic net<sup>26,27</sup>

It was mentioned in the foregoing section that the Universe represents a macrocosmic fractal structure. This is due to the fact that the fractal forms have an exceptionally wide distribution in the Universe. This can be noticed not only in the observed levels close to us, but also in its grand structure appearing at the level of super-galactic clusters<sup>25</sup>(ref. Fig.12).

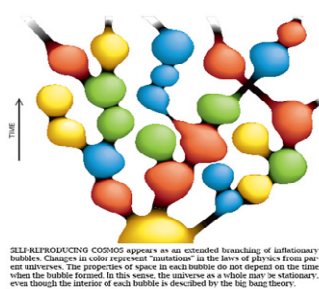


Fig. 13. Visualized fractal structure of the Multiverse: published in Scientific American - "The Self-Reproducing Inflationary Universe", A.Linde<sup>29</sup>

Some basic questions can be asked: *why is there such a densely saturated dissemination of fractal forms in the Universe and why they emerge in the first place?* This inevitably leads contemporary cosmologists to fractal scenarios of the global evolution and organization of the Universe. The simplified idea of the so called *Big Bang* has been put to intensive criticism because it cannot explain a number of phenomena observed in the astrophysics and physics of elementary particles, including the fact that seen on a grand scale the visible space exhibits clearly discernible fluctuations in the distribution of matter, easily definable by fractal geometry. Therefore Andrej Linde, professor in Physics at Stanford University, proposed to examine the Universe as a constantly evolving self-reproducing fractal<sup>28</sup>. This concept developed on the basis of the so called *inflationary universe scenario*, directly relevant to its accelerated inflation, assumes that the Universe consists of multiple big explosions each representing a different sub-universe with specific laws of physics. According to Professor Linde, however, the entire structure is united in a self-reproducing tree-like fractal (ref. *Fig.13*). This was substantiated by Penrose and Gurzadian in 2010 when they announced that structures were discovered in the cosmic microwave background which are most probably related to events preceding the Big Bang.<sup>30</sup>

#### **4. Conclusion**

This paper demonstrated the mathematical tools of the fractal theory. Thanks to the introduced notation of the fractal processes and the mathematical concept of the *degree of self-similarity* the complex dynamic processes in the Universe, as well as their trajectory of appearance, can be analysed structurally. This is to pinpoint the significance of the fractal theory in the field of astrophysics and in the investigation of the nonlinear properties and manifestations of some key objects and processes in space.

#### **References**

1. Манделброт, Б., *Фрактальная геометрия природы*, Москва, 2002, ИКИ, ISBN 5-93972-108-7, с.13-19
2. Briggs, J., *Fractals: The Patterns of Chaos*, London, UK, 1992, PH "Thames and Hudson", p. 148
3. Ibid
4. Falconer, K., *Fractal Geometry: Mathematical Foundations and Applications*, 2003, pp.7-20

5. Манделброт, Б., *Фрактальная геометрия природы*, Москва, 2002, ИКИ, ISBN 5-93972-108-7, с.268
6. Pickover, C., *Accident, Evolution, and Art*, Chaos, Complexity, And Accident: Nov.-Dec. 1999, p.3
7. Barnsley, M., Hutchinson J., Stenflo O., *V -variable fractals and superfractals*, [http://maths.anu.edu.au/~barnsley/pdfs/V-var\\_super\\_fractals.pdf](http://maths.anu.edu.au/~barnsley/pdfs/V-var_super_fractals.pdf), Retrieved on 12.01.2014
8. Манделброт, Б., *Фрактальная геометрия природы*, Москва, 2002, ИКИ, ISBN 5-93972-108-7, с.276-277; Barnsley M., Hutchinson J., Stenflo O., *V -variable fractals and superfractals*, [http://maths.anu.edu.au/~barnsley/pdfs/V-var\\_super\\_fractals.pdf](http://maths.anu.edu.au/~barnsley/pdfs/V-var_super_fractals.pdf), Retrieved on 12.01.2014
9. Bradley, L., *Fractals*, Space Telescope Science Institute, <http://www.stsci.edu/~lbradley/seminar/fractals.html> Retrieved on 12.01.2014
10. Takayasu, H., *Fractals in the physical sciences*, Manchester Univ Pr., 1990, p. 45
11. Nicolis, G., Prigogine I., *In Exploring Complexity: An Introduction*, WH Freeman, New York, 1989, p. 15
12. Колектив от автори към статията *Hologram*, към енциклопедичното съдържание на адрес: <http://science.howstuffworks.com/hologram.htm> Retrieved on 12.01.2014
13. Susskind, L., *The World as a Hologram*. Journal of Mathematical Physics 1995, 36 (11): 6377–6396
14. Raphael, B., *The Holographic Principle*. Reviews of Modern Physics 2002, 74 (3): 825–874
15. Susskind, L., *The Black Hole War*, Little, Brown and Company, NY 2009, pp. 354-365
16. Neilsen, J., *GRS 1915+105: Taking the Pulse of a Black Hole System*, <http://chandra.harvard.edu/photo/2011/g1915/> ; [http://chandra.harvard.edu/resources/podcasts/media/pod290111\\_hd.m4v](http://chandra.harvard.edu/resources/podcasts/media/pod290111_hd.m4v) Retrieved on 12.01.2014
17. Hawking, S., *Black hole explosions?*, 1974, Nature 248 (5443): 30
18. Hamilton, A., *Hawking Radiation*, <http://casa.colorado.edu/~ajsh/hawk.html> Retrieved on 12.01.2014
19. Neilsen, J. & Lee J., *GRS 1915+105: Erratic Black Hole Regulates Itself* , <http://chandra.harvard.edu/photo/2009/g1915/> Retrieved on 12.01.2014
20. Matteo, T.D. and co-writers, *Direct cosmological simulations of the growth of black holes and galaxies*, [http://lanl.arxiv.org/PS\\_cache/arxiv/pdf/0705/0705.2269v1.pdf](http://lanl.arxiv.org/PS_cache/arxiv/pdf/0705/0705.2269v1.pdf) Retrieved on 12.01.2014
21. Neilsen, J., *GRS 1915+105: Taking the Pulse of a Black Hole System*, <http://chandra.harvard.edu/photo/2011/g1915/> , [http://chandra.harvard.edu/resources/podcasts/media/pod290111\\_hd.m4v](http://chandra.harvard.edu/resources/podcasts/media/pod290111_hd.m4v) Retrieved on 12.01.2014
22. Newman, P., *Listen to a Black Hole*, [http://heasarc.nasa.gov/docs/xte/learning\\_center/listen.html](http://heasarc.nasa.gov/docs/xte/learning_center/listen.html) , Retrieved on 12.01.2014

23. Gefter, A., *Galaxy map hints at fractal universe*, New scientist web site, <http://www.newscientist.com/article/dn14200-galaxy-map-hints-at-fractal-universe.html> Retrieved on 12.01.2014
24. Ibid
25. Baryshev, Y., Teerikorpi E., Mandelbrot B., *Discovery of Cosmic Fractals*, 2002 Singapore, World Scientific Publishing Co. Pte. Ltd., p.340-343
26. Perlmutter, S. & Levi M., *Dark Energy* <http://snap.lbl.gov/science/darkenergy.php> Retrieved on 12.01.2014;
27. Колектив от автори към статията *The Wide Angle: Dark Energy*, Discovery Space Special Feature: <http://dsc.discovery.com/space/wide-angle/dark-energy.html> Retrieved on 12.01.2014
28. Linde A., *The Self-Reproducing Inflationary Universe*, Scientific American, November 1994, p.48-54
29. Ibid
30. Gurzadyan, V.G., Penrose R., *Concentric circles in WMAP data may provide evidence of violent pre-Big-Bang activity*, <http://arxiv.org/ftp/arxiv/papers/1011/1011.3706.pdf> , Retrieved on 27.02.2011

## **ФРАКТАЛЕН ПОДХОД КЪМ КОСМИЧЕСКИ СТРУКТУРИ, ОБЕКТИ И ДИНАМИЧНИ ЯВЛЕНИЯ**

***Ф. Филипов***

### ***Резюме***

Представя се фракталната теория и определението за това що е фрактал. Показани са основните свойства на абстрактните и естествени фрактали, както и математическия инструментариум, използван за описание на тези сложни, комплексни и нелинейни форми и явления във Вселената. Демонстрират се някои от първите опити за приложение на фракталната теория в областта на астрофизиката и по-специално процесите, свързани с гравитационните сингулярности, формата на спиралните галактики и динамичната организация и структура в Космоса.



## **HYPOTHESIS OF A COSMOLOGICAL MODEL OF THE UNIVERSE WITHOUT GRAVITATION**

***Velko Velkov***

*e-mail: velvel@mail.bg*

### ***Abstract***

*The paper presents a hypothesis of a Cosmological Model of the Universe without Gravitation as a factor and a reason for the attraction of the material bodies. It is justified a physical Essence availability in the Space and its parameters, defined for the first time at the paper, and their evolution to be accepted as a basis of emergence of the matter and the processes in the Universe.*

### **Introduction**

The present-day physicists and scientists of different field of knowledge are trying hard to achieve the so called “Great unification” of the gravitation with other three fundamental forces of hard interaction in the frames of the Standard Model. Many theories of gravitation have been proposed for this aim. The gravitational waves and dark matter registration have been announced lately. At the present stage, approximately 100 years after the General Theory of Gravitation had been created, which is considered as a final theory of gravitation, there is no explanation of it. Why is it so? Why we seek for gravitational waves and dark matter as a proof of the gravitation existence, that is the bodies attraction? Maybe the analogues with the electromagnetic and mechanical waves mislead us.

Meeting the difficulties, concerning the nature of the gravitation and its relation with other forces and interactions, it should be considered as an option the possibility of gravitation not existence, contrary to our views and scientific theories. At first, such idea seems paradoxical and insolent but the trying to find an answer of several basic questions in this direction,

predisposes in thoughts about such possibility. Generally they are as follows:

- why the contemporary science with its high level theoretical and experimental development, can't unify the gravitational interaction with the three other basic interactions;

- why and how the electrically neutral material bodies attract each other;

- why the gravitational interaction force is on order of 37 to 40 or approximately  $10^{40}$  times weaker than the rest three interactions;

- why, despite the development of contemporary high-tech measuring equipment and technology, it can't be registered the gravitational waves and the corresponding graviton, which according to the science, is considered as a gravitational energy quantum of spin 2;

- why the gravitational interaction is an exception from the other three interactions and is only attraction, without repulsion.

The uniting of the possible answers of these and other related questions in a single information massif gives rise to the assumption that gravity, that is the bodies attraction to each other may not actually exist. But then logically comes the question what could be the reason for the bodies trend towards each other, the reality which led to the Newton's law of Universal attraction.

### **Hypothesis**

The seeking for the answer of the posed questions, relating to the gravitation, and many years of persistent efforts for their clarifying, have resulted in and reinforced the idea that what we define and perceive as gravity is not an attraction of the bodies at all, e.g. gravity as a phenomenon is absent, and the attraction effect is due to other factors. The development of the concept has led to the search for the reason of the material bodies tend to each other. The logic leads to the conclusion, that, if the bodies actually do not attract, according to the assumption of the hypothesis, they should be pushed towards each other. Assuming that the admission is well founded, it should also be a reason for their pushing, therefore, there must be some force that pushes them. This force could be due to the pressure, caused by a real physical factor with certain physical parameters, occupying the universal space (Here it should be noted, that the modern science assumes with high degree of credibility, that a small part of the so-called "dark" matter has converted into a substance of the known physical parameters

(bright matter).

Second branch of the point leads to the same conclusion, namely, that the universal space is not empty, and is occupied entirely by dense and continuous reality. Evidence about this and a direct consequence is the genesis and formation of the material entities. It is not logical to believe and accept that the matter and, in particular, the substance come from nothing, from empty space. (Let us recall one of the main issues, concerning contemporary physics, namely - what gives mass of the material particles, according to the hypothesis that this is Higgs - boson or "god particle", which is also increasingly being looked for like the "dark" matter, spending huge funds).

Once we have come to the conclusion through two independent branches of reasoning, that universal space is filled with something real of inherent physical properties, we should name it and reveal its physical parameters. Then this unintelligible reality will emerge from anonymity and be legitimized. The term "Essence" is the most appropriate about the name.

According to the hypothesis, this Essence adopted by us for the objective existence with its physical properties, is a source of pressure, leading to suppression of material bodies toward each other. Prior to clarify the pressure process principles it should be revealed the physical properties and parameters of the Essence.

It is logical to assume, that the likely physical parameters of the Essence are the known primary physical parameters - density, temperature, energy and their derivatives. To determine the values of these parameters, it is appropriate to adopt as a base some fundamental values. For example, for the Essence density determination, which should relate with the pressure, it is suitable, as a fundamental value, the Newton's gravitational constant to be used  $\text{cm}^3/\text{g}\cdot\text{s}^2$ , (In cgs units, centimeters cubed per gram per second squared). Physically, it is known as a specific volume in thermodynamics – the volume per unit mass of the Essence. The specific volume is the reciprocal of the density, which is a prerequisite for the determination of the density of the Essence. As is known, the value of the gravitational constant, determined experimentally for the first time by Cavendish [1] is  $6,67 \cdot 10^{-8}$ , ie in this volume expressed in cubic centimeters [ $\text{cm}^3$ ], Essence of 1 g should fit. Therefore, in a cubic centimeter [ $\text{cm}^3$ ]  $\mathbf{X}$  grams of the Essence should fit. As a result,  $\mathbf{X} = 1/6,67 \cdot 10^{-8} = 10^8/6,67 = 1,49 \cdot 10^7$  g, i.e. in a cubic centimeter of the space, the Essence of the order of  $10^7$  grams fits. The resulting value of the supposed Essence's density is the seemingly unusually

high, but it is considerably lower, practically negligible, compared to the density of the substance, from which everything material is built, including ourselves, which is of the order of  $10^{12} - 10^{14} \text{ g/cm}^3$ . In other words, the substance is from 100000 to 10 000 000 (one hundred thousand to ten million) times more dense than the Essence, from which it originates and where it is "immersed", distributed, dispersed, everywhere in the universal space, or concentrated in galaxies, suns, planets, molecules, atoms, elementary particles.

At so specified value of the Essence density, it follows that every point and area of it experiences and performs pressure at the same time from and on the adjacent points and zones and through them on the whole Essence. This results in compensated and approximately balanced pressure at any point of the universal space. The whole universal space is filled homogeneously (tightly), isomorphic (no separate points) and isotropic (no separate directions) by the Essence, with defined value of the the density and temperature, probably close to absolute zero, i.e. around  $3^0 \text{ K}$ . In the field theory this state is defined as a scalar field, scalar or tensor of rank zero, without preferential points and directions [2]. This state precisely forms and in a much higher degree physically meets the definition of a continuum, adopted artificially for etc. space-time continuum, composed of two very different non-physical categories.

Anthropic principle, widely used in science, provides evidence that the Essence state and condition is not stationary, and its parameters should be changed in time. Probably, the reaching a limit value of the Essence density (and possibly of the temperature) leads to a state at which spontaneously (cumulatively, explosively) a synthesis occurs or separation from the Essence of condensed entities of higher density, compared to the initial one in the Essence environment. Much more likely, it is a process of generation and formation from the Essence of the primary entities in the entire universal space, in the entire the Universe or in its separate areas, but not the alleged "big bang" with its vaguely attributed parameters and singularity. Hypothesis presented here also implies and suggests that in the Essence evolution there was an event of the characteristics of the "Big Bang", because science objectively dates the age of its consequences, but not explosion of that supposedly "fireball" with those fantastic parameters - temperature of  $1,5^{12} \text{ K}$ , density of  $10^{94} \text{ g/cm}^3$  and duration of  $10^{-43} \text{ s}$ , but a "burst" or perhaps a continuous process of condensation of the known material formations from the objectively existing Essence, without any

singularities, but with precise values of its parameters [3]. These formed primary formations were substantially of greater density than that of the Essence. Their form is surely spherical because of the same pressure in all directions, maintained by the Essence. The availability of these formations creates anomalies, distorts the homogeneity of the scalar field and the symmetry of the Essence pressure around them. This results in occurrence of an area of "shadow" around each formation, leading to shielding of the pressure of the surrounding Essence and as a consequence its imbalance in these areas. There is a prerequisite for a different pressure than the average pressure of the Essence primary scalar field and its gradient, i.e. the pressure of the Essence towards the formation acquires a value higher than the fixed one and also direction. Mathematically this can be expressed by the pressure vectors or tensors of the first rank. The value of the pressure's vector in any point of the formation shielding area, at any moment of time should be directly proportional to its mass (M) as a product of its density ( $\rho$ ) and its volume (V), which physically sets its "shadow" or shield potential (real analogue of the hypothetical gravitational potential) and inversely proportional to the distance (r) to it  $P = M/r$ . The direction of the pressure vector is to the center of the formation. Symbolically, thus described physical model and its mathematical equivalent in vector form can be represented by the expression:

$$(1) \quad \mathbf{P}(\mathbf{r}, t) = \frac{M}{r^2} \cdot \mathbf{r}$$

where:

- $\mathbf{P}(\mathbf{r}, t)$  - the Essence pressure vector at a point of radius vector  $\mathbf{r}$  in Descartes coordinate system with beginning at the center of the formation, at time  $t$  ;
- $\mathbf{r}$ -vector having a direction toward the center of the formation and the absolute value of  $r$ , which is equal to the distance to the formation

The vector values are presented by means of bold symbols. Respectively,  $r$  is in the second degree in the denominator of (1). For ease of presentation, the factor  $4\pi$  is not entered in the denominator.

If a formation "B" is located in the "shadow" potential of the "A" formation, due to the pressure gradient, the formation "B" will be pushed

to the formation “A” and acquire an acceleration. Naturally, the formation "B" also has shielding potential and causes vectors of pressure, so the formation “A” and formation “B” will be pushed towards each other without ever being attracted by some mysterious force, defined as gravity. The force  $F$ , by which the two material bodies are driven by the pressure of the Essence to each other should be equal to the scalar product of the vectors of the pressure to the two bodies, or:

$$(2) \quad F = P_1 \cdot P_2 \cdot \cos \varphi, \text{ where } \varphi \text{ is the angle between } P_1 \text{ and } P_2.$$

The development of (2) through  $P_1$  and  $P_2$  according to (1), leads unambiguously to known classical formula of Newton about the force of attraction of two material bodies in the Universal space.

In the general case, if there are more than two formations, and due to the overlap of their screening zone, a resultant force is formed as a result of the Essence pressure. The total pressure vector of the Essence must be equal to the sum of the vectors of the Essence pressure to the available formations.

$$(3) \quad \mathbf{P}(\mathbf{r}, t) = \sum_{i=1}^n \mathbf{P}_i(\mathbf{r}, t)$$

For the marginal case of universal space with the presence of multiple physical formations, it can be formulated the following summary: the Essence pressure at any point of the universal space forms a vector, which is equal to the sum of the vectors of all formations available in the space.

As a result of the action of shady potentials and formed Essence pressure vectors, the movement of each formation is of a direction and a trajectory, determined by all other physical bodies in the universe. The influence of the nearest physical bodies is most expressed, as a result of an inverse proportionality dependence of the pressure vector magnitude from the distance. Since all physical objects in the universe are in constant motion and at regular periodicity to each other, the Essence pressure summary vector at any point and any time is fixed. As a result, each formation has an exactly defined direction, a trajectory and periodicity of the movement. Only the Essence is stationary.

## **Cosmological model of the universe without gravity**

Initial condition of the universe (or its separate areas) should be a scalar field with defined above parameters - density, internal pressure and temperature without any formations. Reaching a limit „critical” value of the density (and possibly the temperature) leads to spontaneous (explosive) synthesizing of formations by compacting large amount of Essence in defined volumes, resulting in a reduced average density of the Essence and hence, its internal pressure drop.

These formations of density, significantly higher than the Essence average density, represent the lowest levels of the substance structuring, that build all other known entities of the matter. That should be the "bright matter" of the Universe, and the primary Essence from which it originates should be the "dark" matter. The substance entities are submerged in the Essence and are closely covered by it. Two questions arise. The first question: in the process of "condensation" what part of the Essence is compacted and converted into substance. Contemporary science assumes that a small fraction of Essence has become a substance, from 4% to 10%, and the average density of the substance in the Universe is from  $10^{-29}$  to  $10^{-31}$  g/cm<sup>3</sup>, and the value of  $10^{-28}$  is determined as “critical” density. Second question: at what spatial scales the action took place, i.e. the size of the primary formations - the range of particles' size of  $10^{-13}$  -  $10^{-14}$  cm, or the range of quark of  $10^{-17}$  cm, Planck length, or J. A. Wheeler's geon of  $10^{-33}$  cm, Compton's length of  $10^{-54}$  cm, or lower level. Let us disregard the sizes of the primary formations and assume, that they are around an average-statistical value. Any arising formation creates around itself "shady" or shielding areas for the pressure, because of the considerably higher density than that of the Essence, covering them. The impaired wholeness of the Essence continuum, results in asymmetry of the pressure on the formations, the consequence of which is the movement of formations in the Essence environment. The movement of any entity is a function of the complex influence of three factors: the Essence pressure asymmetry, the dispersion of the formation sizes and screen zones overlapping. According to the mechanics, two main types of movement are known - rotation and translation. Logically, the rotational movement should cause electrification of the formations as a result of the constant friction with the Essence. This may be the genesis of the one of the three main types of interactions - electromagnetic

The second type of movement - translation, according to this hypothesis,

is not due to gravity, but because of the pushing of the formations to one another. There are two consequences:

- quantitative accumulation and formation of structures and configurations of increasingly higher level - from elementary particles, atoms, molecules and chain structures of atoms and molecules, organic compounds, planets, suns, galaxies;
- well-defined orbits and trajectories of the formations movement, due to their complex mutual influence through shield areas and modulated pressure of the Essence.

The presented above concepts regarding the levels of structuring and movement of physical formations give grounds of acceptance the universal pressure of the Essence as a major factor, instead of attraction of bodies or gravity.

This hypothesis of the Universe model allows logically to explain all observed physical and astronomical phenomena and processes. There are two fundamental questions to answer. The first one - are the processes in the Universe single without repeat or cyclical? The second one – do they cover all Universal space simultaneously or its separate zones shifted in time. Their clarification is under investigation

## **References**

1. Relativitätstheorie – Aktuell. Ein Beitrag zur Einheit der Physik von Prof. Dr.rer. nat.habil. Ernst Schmutzer. Friedrich-Schiller-Universität Jena. BSB B G.Teubner. Verlagsgesellschaft. 1979.
2. G y a r m a t i, I. Non-equilibrium thermodynamics. Field Theory and Variational Principles. 1970.
3. W e i n b e r g, S. The First Three Minutes. A Modern View on the Origin of the Universe. Basic Books, Inc., Publishers. New York. 1977.

## **ХИПОТЕЗА ЗА КОСМОЛОГИЧЕН МОДЕЛ НА ВСЕМИРА БЕЗ ГРАВИТАЦИЯ**

***В. Велков***

### **Резюме**

Статията представя хипотеза за космологичен модел на Всемира в отсъствието на гравитация като причина за притеглянето на материалните тела. Поставени са пет фундаментални въпроса,



свързани с гравитацията, на които съвременната наука не предлага удовлетворителни отговори и на тази база е потърсена причина или фактор, играещ ролята на гравитация. За такъв е определен факторът налягане, създаван от основополагаща физическа същност, изпълваща всемирното пространство и формираща скаларно поле или тензор от нулев ранг. За първи път са определени някои от основните физически свойства и параметри на тази същност, в частност плътността, чията стойност, изчислена на базата на гравитационната постоянна на Нютон –  $G$ , е получена от порядъка на  $1,5 \cdot 10^7 \text{ g/cm}^3$ . Хипотезата допуска, че от тази същност чрез кондензация се формират материалните образувания, елементарните частици с плътност от порядъка на  $10^{12} - 10^{14} \text{ g/cm}^3$ , които нарушават хомогенността на скаларното поле на същността, създавайки зони на сянка около себе си и съответно асиметрия в налягането на същността. Нарушената асиметрия в налягането е определена като причина за изтласкването на телата едно към друго, а не предполагаемото гравитационно взаимодействие, нямащо физическа предпоставка и основа. На базата на хипотезата е предложен космологичен модел на Всемира без гравитация. Предложените хипотеза и модел не противоречат на предшестващи теории и математически описания на наблюдаваните процеси и взаимодействия във Всемира. Напротив потвърждават ги, изключвайки всякакви сингулярности и неопределености в тях и ги допълват с физически обосновани доводи за образуването, движението и наелектризирането на материалните образувания и формираните на тяхна база тела.

## VARIATIONS OF SUBSTORMS CONNECTED WITH DIFFERENT SOLAR WIND CONDITIONS

*Veneta Guineva<sup>1</sup>, Irina Despirak<sup>2</sup>, Boris Kozelov<sup>2</sup>*

<sup>1</sup>*Space Research and Technology Institute – Bulgarian Academy of Sciences*

<sup>2</sup>*Polar Geophysical Institute, Apatity, Russia*

*e-mail: v\_guineva@yahoo.com; despirak@pgia.ru; boris.kozelov@gmail.com*

### **Abstract**

*All-sky cameras data at Kola Peninsula from 2012/2013 winter season have been used to study the variation of substorm development in different conditions of interplanetary medium. Solar wind and interplanetary magnetic field parameters were taken from CDAWeb ([http://cdaweb.gsfc.nasa.gov/cdaweb/istp\\_public/](http://cdaweb.gsfc.nasa.gov/cdaweb/istp_public/)). Using WIND satellite data for the examined periods, the different solar wind streams were revealed: recurrent streams from coronal magnetic holes (RS) and magnetic clouds (MC) connected with non-stationary processes at the Sun. It is known that these solar wind structures are the sources of geomagnetic storms. Furthermore, the storms originating from these sources differ in intensity, recovery phase duration, etc. We investigated substorm development during storms caused by different sources in the solar wind. Substorm onset time and further development were verified by ground-based data of IMAGE magnetometers network and by data of all-sky cameras at Apatity and Lovozero. The particularities in behaviour of substorms observed during storms connected with solar wind recurrent streams and with magnetic clouds are discussed.*

### **Introduction**

Substorms are a specific phenomenon, related to a number of processes in the magnetosphere and ionosphere, generalized by Akasofu [1]. It was established that the substorm development goes on in the following way: the substorm expansion phase begins with the flash of one arc, usually the most equatorial one between the existing already discrete auroral arcs. After this the auroral bulge - an area occupied by bright, short-lived arcs, forms. It is expanding in all directions, mainly toward the pole, to the West

and to the East [2, 3]. At the time of maximal stage of substorm development the auroral bulge reaches its greatest width and occupies a maximum area. Further, during the recovery phase, the auroral bulge begins to shrink, its polar edge moves to the equator and, the South one – to the pole, the bright discrete arcs degenerate into irregular strips and fade [4, 5].

It is known, that the substorm generation and development depends on the conditions in the solar wind [e.g., 6, 7, 8]. The solar wind conditions include the solar wind parameters values, as well as the presence of different solar wind streams and their structure [9]. The solar wind streams can be recurrent streams (RS) originating from coronal magnetic holes, characterized by a 27-day recurrence, which predominate during solar minimum [10], and magnetic clouds (MC) originating from coronal mass ejections (CME) giving rise to sporadic flows, generated more often during a solar maximum [11, 12]. These solar wind structures are usually the source of geomagnetic storms that differ by their main characteristics depending on the generating structure. Therefore the substorms arising during different solar wind flows or under quiet conditions will differ by substorm onset location latitude, substorm polar edge latitude, auroral bulge extent etc.

Apatity is settled at auroral latitudes. Its geographic coordinates are: 67.58°N, 33.31°E, and the corrected geomagnetic ones – 63.86°N, 112.9°E. This location is expedient to examine the variety of substorms.

The goal of this work is to study substorm development as seen from Apatity under different interplanetary and geomagnetic conditions.

### **Instrumentation and data used**

All-sky cameras data at Kola Peninsula from the 2012/2013 winter season have been used. The all-sky cameras observational system has being built in Apatity since 2008. It comprises 5 all-sky cameras with different fields of view providing simultaneous observations from spatially separated points. The cameras characteristics, their mutual situation and the measurement process are described in detail by Kozelov et al. [13, 14].

Solar wind and interplanetary magnetic field parameters were taken from CDAWeb ([http://sdaweb.gsfc.nasa.gov/cdaweb/istp\\_public/](http://sdaweb.gsfc.nasa.gov/cdaweb/istp_public/)). WIND satellite data revealed different solar wind streams: recurrent streams from coronal magnetic holes (RS) and magnetic clouds (MC) connected with non-stationary processes at the Sun or quiet conditions for the examined periods.

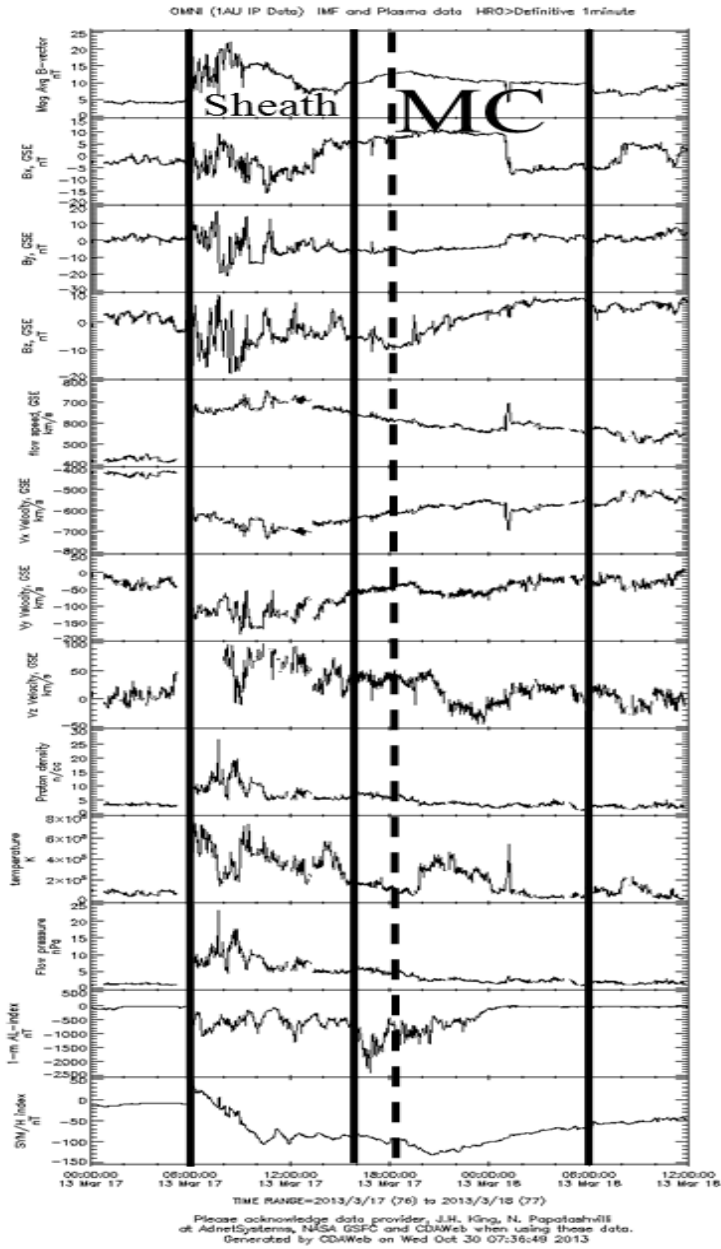
Substorm onset time and further development were verified by ground-based data of IMAGE magnetometers network (using meridional chains), Lovozero and Loparskaya magnetometers and by data of Apatity all-sky cameras.

The measurements during 2012/2013 season were examined together with the interplanetary conditions during the measuring periods. The recurrent streams and magnetic clouds were detected. The substorms developed over Apatity were identified and the solar wind conditions during these substorms times were verified. Three typical cases were chosen presenting the variety of substorm developments over Apatity: during a magnetic cloud under highly disturbed conditions, during a recurrent stream under disturbed conditions and in non-storm time, under quiet conditions.

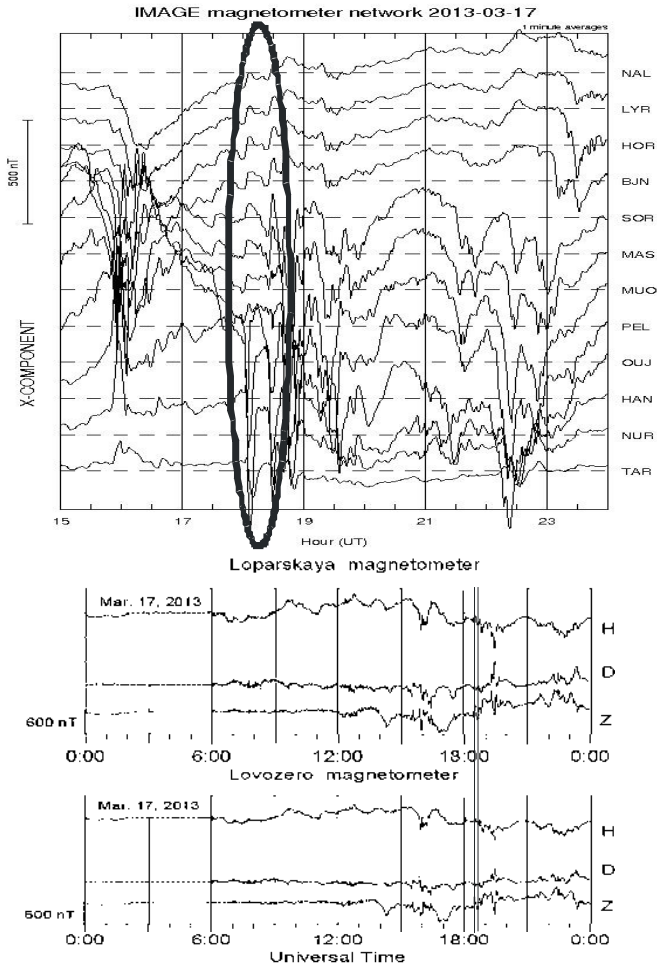
## **Results**

Case 1: 17.03.2013.

On 17.03.2013 a magnetic cloud passed by the Earth. Some solar wind and interplanetary magnetic field (IMF) characteristics by WIND are presented in fig.1. The straight vertical lines mark the boundaries of Sheath (06-15 UT on 17 March 2013) and MC (15 UT, 17 March – 6 UT, 18 March 2013) on 17-18 March 2013. A geomagnetic storm developed during this time. The Dst index reached -140. Under these highly disturbed conditions, during the main phase of the storm, two consecutive substorms were generated in 18:28 UT and 18:39 UT, 17 March 2013. The time of the substorms is marked by the dotted line in fig.1. The substorms generation and further development can be traced out through the magnetic field X-component records of the stations of the longitudinal chain TAR-NAL presented in the upper panel of fig.2. In the lower panel of fig.2 the progress of the magnetic field components registered in 2 stations close to Apatity, Loparskaya and Lovozero, are presented. The substorms developed during one of the most disturbed periods of the day. They were observed from Apatity. The all-sky camera registered the substorm onset and further development. In fig.3, chosen images of the substorm development are shown. The substorm beginning as seen from the station, the polar edge movement to the North, reaching the station zenith (18:32 UT) and surpassing it, the second intensification in 18:39:40 UT and its travel to North, the bulge expanding in the whole field of view are seen. The world directions are marked in the first image. The universal time is written above each image.



*Fig. 1. IMF components, solar wind velocity and some other parameters, characterizing the geomagnetic conditions on 17-18 March 2013. The straight vertical lines point out the boundaries of Sheath and MC. The dotted line mark the time of the substorms development*

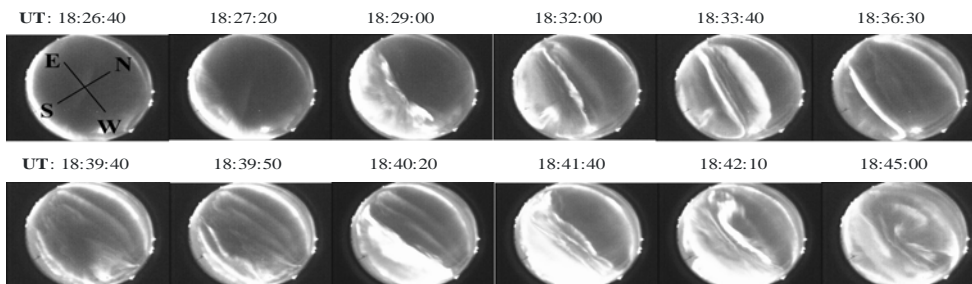


*Fig. 2. X-component of the magnetic field by the stations of the TAR-NAL longitudinal chain on 17 March 2013 (up). The studied substorms are pointed out by an ellipse. And: magnetic field components by Loparskaya and Lovozero stations (down). The straight lines mark the beginning of the consecutive substorms in question*

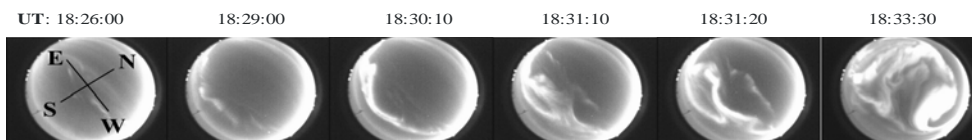
Case 2: 29-30 March 2013.

During 29-31 March 2013, a recurrent stream (RS) in the solar wind was observed. The CIR region lasted from 3 to 18 UT on 29 March, and the recurrent stream – from 18 UT on 29 March to 14 UT on 31 March 2013.

The recurrent stream caused a geomagnetic storm with minimal  $D_{st}=-65$  nT. The conditions can be considered as disturbed. Three substorms developed during RS: two substorms during the main phase of the storm (in 18:28 UT and 23:08 UT, 29.03.2013,  $D_{st}=-45\div-50$  nT) and one – during the recovery phase (in 19:08 UT, 30.03.2013,  $D_{st}=-40$  nT). In fig.4 some images from the first substorm development during the main phase of the geomagnetic storm are presented. The auroral oval emissions were lying over Apatity latitudes. Just before the substorm onset in 18:28 UT the arcs were moving to the South. During the bulge formation its polar edge moved in S-N direction, reaching zenith in 18:31:10 UT. In 18:31:20 UT the polar edge surpassed zenith location and after 18:32:40 UT the whole field of view was occupied by the auroral bulge forms. The second substorm followed the same behavior.



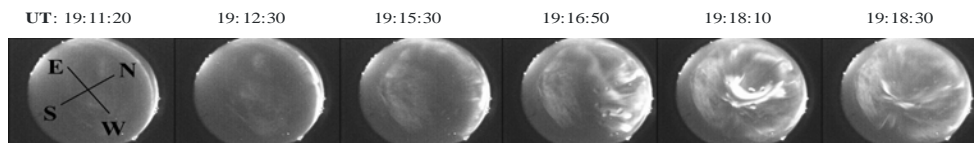
*Fig. 3. Chosen all-sky camera images presenting the substorm beginning and development as seen from Apatity on 17 March 2013, during the main phase of a geomagnetic storm generated by MC. Substorm beginning, polar edge movement to the North, surpassing station zenith, the second intensification in 18:39:40 UT and its motion to North, the bulge expanding in the whole field of view are seen*



*Fig. 4. Selected images of the substorm onset and development during the main phase of a geomagnetic storm caused by RS on 29 March 2013. The substorm onset to the South of the station, the bulge formation, the polar edge of the bulge motion in S-N direction and the bulge expansion over the whole field of view are observed*

The picture of the third substorm development looked different (fig.5). Chosen images of the substorm development in 19:11:20 UT on

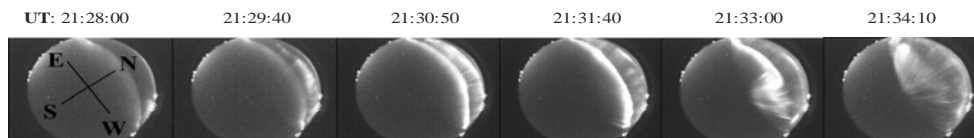
30.03.2013 during the recovery phase of the geomagnetic storm associated with RS are shown in fig.5. The substorm onset was to the North of Apatity and the expansion of the South part of the substorm bulge is observed from the station.



*Fig. 5. Some images of the substorm development from 19:11:20 UT on 30.03.2013 during the recovery phase of the geomagnetic storm associated with RS. The substorm onset is to the North of Apatity and the motion of the South edge of the substorm bulge in N-S direction is observed from the station*

Case 3: 10.04.2013.

On 10 April 2013 a substorm occurred in non-storm, quiet conditions. The auroral oval lied at higher latitudes, auroral activity was seen in the Northern part of the field of view. The substorm onset was in 21:28 UT at the South border of the auroral oval, to the North from Apatity. The South edge of the auroral bulge was seen to travel to the South reaching Apatity zenith about 21:33:00 UT. This substorm development was presented by chosen images in fig. 6.



*Fig. 6. Images of a substorm development on 10.04.2013, under quiet conditions. The substorm onset was to the North of Apatity and the South edge of the bulge was seen to move in N-S direction in the field of view*

## Discussion

We studied three cases of substorm generation and development under different conditions. In the first case, the geomagnetic conditions were highly disturbed. A magnetic cloud passing by the Earth caused a strong geomagnetic storm, with minimal value of  $D_{st}$  index -140 nT. The auroral oval was located at lower latitudes, to the South of Apatity. Both examined substorms occurred consecutively during the main phase of the storm. Their



onset locations were as well to the South of Apatity. Thus, the polar edge of the auroral bulge was observed to move fast towards North, to reach and surpass the zenith. After the second intensification, the substorm bulge spread over the whole field of view, the station staying inside the bulge.

In the second case, the geomagnetic conditions were also disturbed. There was a recurrent stream in the solar wind. A geomagnetic storm was generated, with minimal  $Dst = -65$  nT. Three substorms were examined. Two of them developed during the main phase of the storm. The substorm onset was to the South of Apatity and during the auroral bulge evolution the polar edge of the bulge moved in S-N direction over the station. The third substorm developed during the recovery phase the storm arising from RS. The auroral activity was to the North from the station and the movement of the equatorial edge of the substorm bulge could be seen in N-S direction before the spread of the bulge all over the field of view.

Case 3 represents a substorm generated in quiet conditions. In this case the auroral oval was at higher latitudes, to the North of Apatity. The substorm onset was to the North of the station, and during the bulge development, the motion of the equatorial edge of the bulge was seen in the field of view.

Therefore our results confirm that in disturbed geomagnetic conditions, when storms are generated, the auroral oval lies at lower latitudes. Thus the substorm onset location is to the South of Apatity and the motion of the polar edge of the substorm bulge can be seen moving in S-N direction over the station. And vice versa, under quiet conditions or during the recovery phase of a geomagnetic storm, the auroral oval is located at higher latitudes, to the North of Apatity. The substorm arise to the North and during the bulge expansion the movement of the its equatorial edge in N-S direction can be observed.

## **Conclusions**

We investigated substorm development during storms caused by different sources in solar wind and during quiet conditions using observations of auroras in Apatity during 2012/2013 winter season.

It is shown that 2 types of substorm development occur over Apatity.

First type: substorm onset is to the South of Apatity, and the “usual” development of the substorm bulge is seen – from South to North; the polar edge of the bulge is observed to pass over zenith.

Second type: the auroral oval is situated at higher latitudes, substorm generates to the North from Apatity, and the movement of the auroral bulge to the South is seen from Apatity, i.e. the equatorial edge of the auroral bulge is observed.

It is shown that the first type of substorm development over Apatity happens during geomagnetic storms, associated with both magnetic clouds and high speed recurrent streams of the solar wind.

The second type of substorm development is observed during quiet (non-storm) conditions or during the storm recovery phase.

## References

1. A k a s o f u, S. - I. Several 'controversial' issues on substorms. *Space Sci. Rev.* 113, pp.1-40, 2004.
2. A k a s o f u, S. - I. The development of the auroral substorm. *Planet. Space Sci.* 12, pp.273-282, 1964.
3. A k a s o f u, S. - I. Dynamic morphology of auroras. *Space Sci. Rev.* 4, pp.498-540. 1965.
4. S t a r k o v, G. V., Y a. I. F e l d s h t e i n. Substorms in the polar auroras. *Geomagnetism and aeronomy* 11, pp.560-562, 1971.
5. I s a e v, S. I., M. I. P u d o v k i n. Polar aurora and processes in Earth magnetosphere (Ed. O.L. A.I., Moscow: Nauka), 1972.
6. S e r g e e v, V. A., A. G. Y a k h n i n, N. P. D m i t r i e v a. Substorm in the polar cap – the effect of high-velocity streams of the solar wind. *Geomagn. Aeron.* 19, pp.1121-1122, 1979.
7. Y a h n i n, A. G., I. V. D e s p i r a k, A. A. L y u b c h i c h and B. V. K o z e l o v. Solar wind control of the auroral bulge expansion. In *Proceedings of the 7<sup>th</sup> International Conference on Substorms*, Levi, Finland, 2004, Ganushkina N. and T. Pulkkinen (Ed.), (Helsinki: Finnish Meteorological Institute), pp.31-34, 2004.
8. D e s p i r a k, I. V., A. A. L u b c h i c h, H. K. B i e r n a t, A. G. Y a h n i n. Poleward expansion of the westward electrojet depending on the solar wind and IMF parameters. *Geomagn. Aeron.* 48 (3), pp.284-292, 2008.
9. D e s p i r a k, I. V., A. A. L u b c h i c h, A. G. Y a h n i n, B. V. K o z e l o v, H. K. B i e r n a t. Development of substorm bulges during different solar wind structures. *Ann. Geophys.* 27, pp.1951-1960, 2009.
10. P u d o v k i n, M. I. Solar wind, *Soros Educational Journal*, 12, pp.87-94, 1996.
11. W a n g, Y. - M., N. R. S h e e l e y, J. r. Global evolution of interplanetary sector structure, coronal holes, and solar wind streams during 1976-1993: Stackplot displays based on solar magnetic observations, *J. Geophys. Res.*, 99, pp.6597-6612, 1994.
12. B u r l a g a, L. F., L. K l e i n, N. R. S h e e l e y, J. r. M i c h e l s, D. J. H o w a r d, R. A. K o o m e n, M. J. S c h w e n n, and H. R o s e n b a u e r. A magnetic cloud and a coronal mass ejection, *Geophys. Res. Lett.*, 9, pp.1317-1320, 1982.

13. Kozelov, B. V., S. V. Pilgaev, L. P. Borovkov, V. E. Yurov. Multi-scale auroral observations in Apatity: winter 2010-2011, "Physics of auroral phenomena", Proc. XXXIV Annual Seminar, Apatity, pp.129-132, 2011.
14. Kozelov, B. V., S. V. Pilgaev, L. P. Borovkov, V. E. Yurov. Multi-scale auroral observations in Apatity: winter 2010-2011, Geosci. Instrum. Method. Data Syst., 1, pp.1-6, 2012.

## **ИЗМЕНЕНИЯ ПРИ СУББУРИ, СВЪРЗАНИ С РАЗЛИЧНИ УСЛОВИЯ В СЛЪНЧЕВИЯ ВЯТЪР**

*В. Гинева, И. Деспирак, Б. Козелов*

### **Резюме**

За изследване на измененията в развитието на суббурите при различни условия в междупланетното пространство са използвани данните от all-sky камерите в Колския полуостров през зимния сезон 2012/2013 гг. Параметрите на слънчевия вятър и междупланетното магнитно поле са взети от CDAWeb ([http://cdaweb.gsfc.nasa.gov/cdaweb/istp\\_public/](http://cdaweb.gsfc.nasa.gov/cdaweb/istp_public/)). Използвайки спътникови данни от WIND за разглежданите периоди, са намерени случаина различни потоци в слънчевия вятър: рекурентни потоци от коронални магнитни дупки (RS) и магнитни облаци (MC), свързани с нестационарни слънчеви процеси. Нещо повече, магнитните бури, възникнали от тези източници, се различават по интензивност, по продължителност на фазата на възстановяване и т.н. Разгледано е развитието на суббури по време на бури, породени от различни източници в слънчевия вятър. Времето на възникването и понататъшното развитие на суббурите са потвърдени по наземни данни от мрежата от магнитометри IMAGE по данни от all-sky камерите в Апатити и Ловозеро. Дискутирани са особеностите в поведението на суббурите, наблюдавани по време на магнитни бури, свързани с рекурентни потоци и магнитни облаци.

## **CROP MONITORING USING SPOT-VGT NDVI<sub>s</sub> S10 TIME-SERIES PRODUCT FOR NORTHEAST BULGARIA**

***Vassil Vassilev, Eugenia Roumenina***

*Space Research and Technology Institute – Bulgarian Academy of Sciences  
e-mail: vassilev\_vas@space.bas.bg*

### ***Abstract***

*The objects of this investigation are the major crops in the Northeast region of Bulgaria, namely winter wheat, winter barley, oilseed rape, sunflower and maize. The article covers the subject of crop monitoring at regional scale with low-resolution and high revisit time Earth Observation (EO) product. The study is focusing on processing and interpretation of Normalized Difference Vegetation Index (NDVI) time-series for crop monitoring, with three different objectives: crop identification, crop phenology estimation, and crop anomaly events detection. The crop identification process was assessed using similarity value analysis between the NDVI crop values from SPOT-VGT NDVI<sub>s</sub> S10 product and the high-resolution satellite images for a test site in the region of interest. Knowledge of crop phenology was used for vegetation growth parameters extraction from the temporal profiles. To detect the crop anomaly events, correlation between the average yield for the major cultivated crops and the highest reached NDVI values of the identified crops was done with confidence level of 95%, the relevant  $r$  values are  $\geq 0.75$  and  $\leq -0.75$  for five variables. The results show high correlation ( $r$ ) for winter barley at  $r + 0.99$ , sunflower and oilseed rape cultivars have equally high values at  $r + 0.84$ . Winter wheat has a good correlation with  $r + 0.65$ , while maize cultivars have positive correlation at  $r + 0.37$ . The presented investigation shows the significant potential of using low spatial resolution satellite data for crop monitoring at regional scale in conjunction with agro-phenological information derived from the National Institute of Meteorology and Hydrology (Bulgarian Academy of Sciences), high-resolution images for accuracy assessment and yield statistics. This research contributes for a successful application and elaboration of the existing JRC MARS methodology. The continuity of time-series vegetation monitoring is assured by the launch of PROBA-V mission in 2013 as a successor of SPOT-Vegetation.*

## 1. Introduction<sup>1</sup>

Satellite Remote Sensing (RS) provides synoptic, objective and relatively homogeneous data which can be geographically and temporally registered. Therefore, RS is an efficient tool for providing standard, high quality information on agriculture, evenly over broad-scale territories. The Monitoring Agriculture with Remote Sensing (MARS) project of the European Union was established in order to define and demonstrate how RS can be used operationally to supplement, interpret, and standardize agricultural statistical data provided by conventional techniques [1,2]. Satellite RS techniques have been proven to be effective and useful in broad-scale agricultural surveys such as: Large Area Crop Inventory Experiment (LACIE) project in the USA and MARS project in Europe [3,4]. These projects such as LACIE and Crop Identification Technology Assessment for Remote Sensing (CITARS) demonstrate the capabilities of RS for crop inventory and forecasting [5,6]. Currently, the Group of Earth Observation (GEO) is integrating a Global Crop Monitoring initiative called GEOGLAM [7].

Crop identification during the growing season is a major challenge for forecasting crop production as well as for controlling area-based subsidies in the European Union member states [6]. The basis for separation one crop from another is the supposition that each crop species has a unique visual appearance and spectral signature on the image. However, separating these species may be difficult because of variations in soil properties, fertilization, pest condition, irrigation practices, planting dates, as well as intercropping, and tillage practices [8]. Vegetation types can be characterized using their seasonal variations in the Normalized Difference Vegetation Index (NDVI) time-series, which include a series of images, acquired each 10-days and showing the crop development dynamics. For example, the winter wheat phenophases like tillering and flowering as well as harvest, can be successfully identified using sensors with different spatial resolution in various band combinations and severe ground surveys,

---

<sup>1</sup> Abbreviations used:

NIMH-BAS – National Institute of Meteorology and Hydrology-Bulgarian Academy of Sciences

MARS - Monitoring Agriculture with Remote Sensing

LACIE - Large Area Crop Inventory Experiment

CITARS - Crop Identification Technology Assessment for Remote Sensing

including collecting information for defining training samples for the supervised classification [9,10]. A number of different methods have been developed during the last two decades to discriminate crop types using data from NDVI and from the Advanced Very High-Resolution Radiometer (AVHRR). These methods employ a variety of different approaches including temporal profiles of crop phenology manifested in the NDVI [11,12], and classification of multi-temporal data [13,14], which can be applied on variously managed crop areas worldwide.

The purpose of this case study comprises of crop monitoring at a regional scale (Northeast Bulgaria), and it includes the following tasks:

(1) Identification of the major crops (winter wheat, winter barley, sunflower and maize) using cluster analysis method upon a 10-day SPOT-VGT NDVI S10 time-series product with low spatial resolution of 1000 m by extracting summarized agro-phenological information and NDVI values derived from high-resolution satellite images.

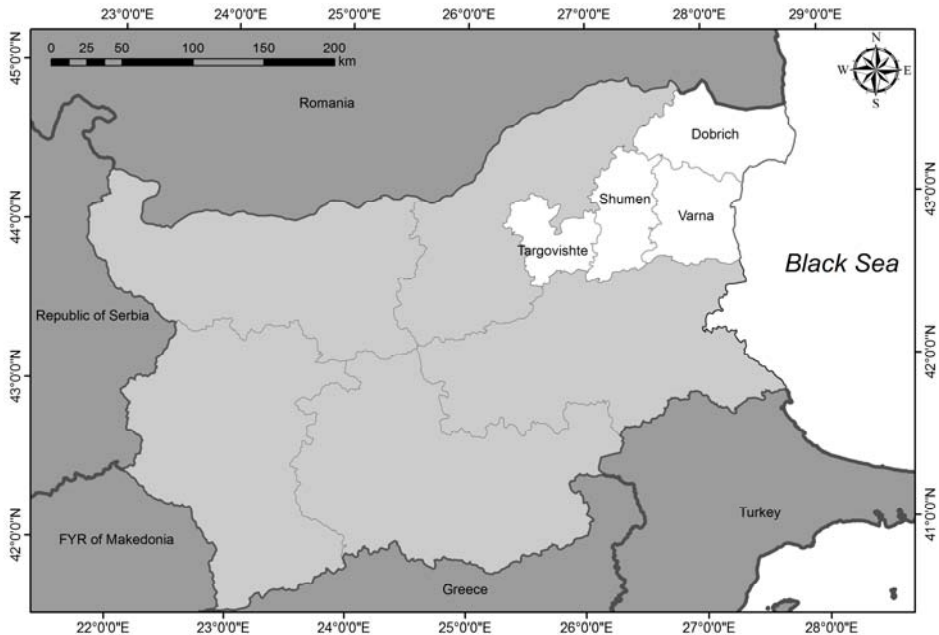
(2) Onset recognition of the crop growing period, length of the reproductive growth period and the entire crop growing season for the winter and summer crops for each studied year. Knowledge of crop phenology was used for vegetation growth parameters extraction from the temporal profiles.

(3) Crop anomaly events detection using yearly NDVI time-series cluster analysis and quantitative data.

## **2. Materials, methods and data used**

The study area is the North-East Bulgaria region, which includes the following regions: Targovishte, Shumen, Varna and Dobrich. The area represents intensively cultivated area sowed mostly with cereals and sunflower. This territory is one of the main agricultural regions of the country. The geology is presented mainly by Miocene limestone, clay and marl covered subsequently by loess. The area is part of the European-continental climatic province of the temperate climatic belt. Climate is moderately warm with no distinctive dry season. Mean annual air temperature is 10.2°C. The maximum precipitation is in June and the minimum – in February, with overall annual precipitation of around 540 mm. Due to the carbonate bedrock, i.e limestone, marl; the hydrographic network is represented by intermittent streams. The main soil types are chernozems from the zonal ones and fluvisols from the azonal ones. Figure

## 1. Study area



*Fig. 1. Study area*

The major crops winter wheat, winter barley, sunflower and maize on the arable territory of the Northeast region of Bulgaria are investigated in the present case study.

The satellite data used herein was provided by the Agri4cast Action at the Monitoring Agricultural Resources Unit (Joint Research Centre, Ispra, Italy). The data set includes five time-series (2007-2011) with 36 stacked 10-day NDVI maximum value composites for each year from 01 January until 31 December. The NDVIs S10 smoothed actual product was registered by the low spatial resolution (1000 m) of SPOT-VGT sensor. Thus, totally 180 low resolution satellite images were used for the present case study. Then, agro-phenological ground data was collected from the monthly open access bulletins (available at [www.meteo.bg](http://www.meteo.bg)) by National Institute of Meteorology and Hydrology at the Bulgarian Academy of Sciences (NIMH-BAS).

High-resolution satellite images are used to complement the crop identification process. The satellite images chosen for that purpose are: SPOT-4 HRVIR sensor, with 4 multispectral bands with 20 m spatial

resolution and 1 panchromatic band with 10 m spatial resolution. The spectral portions are the following: green band - 0.50 – 0.59  $\mu\text{m}$ ; red band - 0.61 – 0.68  $\mu\text{m}$ ; near infrared band - 0.78 – 0.89  $\mu\text{m}$ ; shortwave infrared band - 1.58 – 1.75  $\mu\text{m}$  and the panchromatic band - 0.48 – 0.71  $\mu\text{m}$ . The temporal resolution of the SPOT-4 satellite is 26 days and has 60 km scene width. Additionally, three LANDSAT-5 TM satellite images were used as well. The spatial resolution of each image is 30 m. in the visible and infrared bands and 120 m. in the thermal bands. The spectral portions of the bands are the following: blue band - 0.45 – 0.52  $\mu\text{m}$ ; green band - 0.52 – 0.60  $\mu\text{m}$ ; red band - 0.63 – 0.69  $\mu\text{m}$ ; near infrared band - 0.76 – 0.90  $\mu\text{m}$ ; shortwave infrared and middle infrared bands - 1.55 – 1.75  $\mu\text{m}$ ; 2.08 – 2.35  $\mu\text{m}$  and thermal band - 10.40 – 12.50  $\mu\text{m}$ . The temporal resolution of the LANDSAT-5 TM satellite is 16 days and the scene width is 185 km. All of the chosen high-resolution satellite images are situated in a test site part of the Northeast region of Bulgaria, where ground data was collected and are selected to correspond to a major phenological stage of crop development for the agricultural year 2011.

The most commonly used RS vegetation index for agricultural applications is the NDVI, expressed by the following formula:  $NDVI = (NIR - VIS) / (NIR + VIS)$ , where *VIS* and *NIR* stands for the spectral reflectance measurements acquired in the visible red and near-infrared regions, respectively [15]. NDVI is a commonly used space-observed measure of the chlorophyll activity. It ranges typically from 0.15 (bare soils) to 0.80 (dense vegetation).

An arable mask was applied, which was aggregated to the spatial resolution of the SPOT-VGT NDVIs S10 product using information from CORINE 2000 database [16]. The Northeast region of Bulgaria was cropped and images were stacked on yearly basis (2007-2011) (one file compiles 36 bands, representing the 36 decades of the year).

The *k*-mean and Iterative Self-Organizing Data Analysis (ISODATA) clustering algorithms are the most frequently used ones in RS. The ISODATA algorithm was selected in this study because it allows different number of clusters, while the *k*-mean algorithm assumes that the number of clusters is known a priori [17,18,19]. Unsupervised ISODATA classification with five classes was used on the individual yearly stacked images in ERDAS Imagine software, based on the temporal syntheses generated in the previous stage. The arable territory of the Northeast region of Bulgaria was divided into five clusters based on the time-profile



differences of their NDVI values using this approach. As a result of the above classification five clusters were defined and the analysis was conducted by extracting the mean NDVI values for each decade for every cluster separately. As a result yearly NDVI time-series profiles were created.

The developing stages used in the present investigation for winter crops are: (1) sowing; (2) emergence; (3) tillering; (4) heading; (5) flowering; (6) grain filling periods (milk and dough development); (7) ripening; and (8) harvest. On the other hand, the developing stages for spring crops include: (1) sowing; (2) vegetative; (3) flowering; (4) grain filling; (5) ripening; (6) maturity; and (7) harvest.

The crop identification process was accomplished using the time-series cluster analysis, summarized agro-phenological information derived from the monthly bulletins that include the most important information such as: phenological stage and the agro-technical treatments throughout each decade of the growing season for the major cultivated crops. Additionally, high resolution satellite images were utilized in order to identify the major crops. Thus, the maximum NDVI values for the major phenological stages for winter and spring crops were extracted both from the low-resolution product and high-resolution satellite images. The high-resolution satellite images are acquired in the agricultural year 2011, which is labeled as normal in a test site where ground data was collected. This will help identify the major cultivated crops on the low-resolution SPOT-VGT NDVI S10 product for the whole 5 years.

Knowledge of crop phenology was used for vegetation growth parameters extraction from the temporal profiles. An approach partly based on Reed et al. (1994) was applied to identify the moment when the NDVI exhibits a sudden increase that can signal the onset of significant photosynthetic activity. The seasonal duration of the entire crop growing season, measured in decades, was derived by subtracting the time of onset of greenness from the time of the end of season. After that, the smoothed data were used to identify the maximum NDVI value for the growing season for each crop. Finally, the onset of the crop growing period, length of the reproductive growth period and the entire crop growing season for the winter and spring crops for each studied year were identified using the time-series cluster analysis profiles as reference and measured in decades of the year.

Crop anomaly events detection was performed in order to investigate the capabilities of the low resolution satellite product for detecting the ground observed anomaly events using yearly NDVI time-series data. Additionally, the quality of the anomaly was assessed using quantitative data. Since, the anomaly events have their serious impact on the NDVI values and consequently on the yield figures a correlation analysis was conducted. Correlation between the average yield figures of the major cultivated crops (winter wheat, winter barley, sunflower, maize and oilseed rape) for the region derived from official statistics and the maximum NDVI values reached for each crop for the five year period was extracted.

### **3. Results and discussions**

#### ***3.1. Identification of the major crops using SPOT-VGT NDVIs S10 satellite product***

A consideration amongst the five year period studied using the ground data show some anomaly events such as: (1) bad overall agro-phenological conditions with low yield figures (2007); (2) most favourable conditions in agro-phenological aspect with highest yield in 20 years (2008); and (3) meteorological conditions delayed the harvest effecting both the NDVI values and yield figures (2010); These considerations now will be assessed applying the remote sensing data.

The following crops: (1) mixed crops; (2) winter wheat; (3) winter barley; (4) sunflower; and (5) maize; were identified to be predominantly cultivated for each of the classes (1-5) using as reference the time-series cluster analysis, summarized agro-phenological information for the chosen years (2007-2011) was prepared, but for formatting issues only the information between may and october is presented in (Table 1) and maximum NDVI values for the identified crops derived from high-resolution satellite images.

Time-series cluster analysis profiles for each of the identified crops for the five year period were created, in order to evaluate similarity between the profiles (Figure 2). The class that makes exception is the class mixed crop, which shows no consistency and agreement between the five yearly profiles and clearly presents a mixture of cultivars, which in consequens has large vegetative period spreading from 8<sup>th</sup> decade to the 30<sup>th</sup> decade (Figure 2). Therefore, the class was assigned to be a mixed crop class, rather than identifying a single crop. Although, for the crop anomaly event detection section, where quantitative data will be introduced, oilseed rape yield

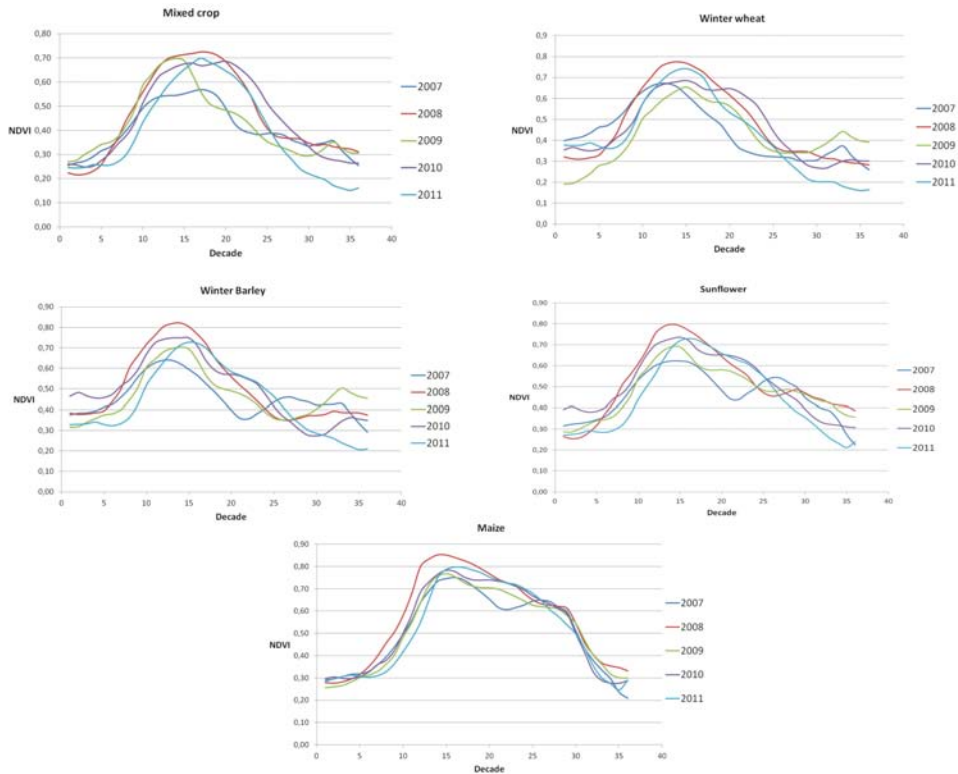
figures will be assigned to this class. For the other crop classes identified namely winter wheat, winter barley, sunflower and maize a similarity between the time-series cluster analysis profiles was observed for the studied years (Figure 2). The variety amongst the other crop profiles is due to agrometeorological conditions experienced in each individual year.

*Table 1. Agro-phenological summary data from the monthly NIMH-BAS bulletins*

Month Year	May	June	July	August	Sept.	Oct.
2007	High temp. Low soil moisture content. WW and WB shortening of phases - flowering. M. vegetative, 3-9 leaf. S. vegetative, 2-4 leaf.	2: M. - vegetative S. - flowering 1: WB. harvest 2-3: WW. harvest; Fruit trees - pick	Drought conditions, 2-3: M. grain filling (milk dough)	1: intensive rainfall 2-3: M. grain filling (dough dev.)- 3: late hybrids grain filling (milk dough dev.) Low yield figures.	Intensive rainfall 2: M. late hybrids end their dev. 1: late harvest due to rainfall 3: WB.WW Sowing. 2-3: grape vintage	Good soil moisture content. WW - emergence (1-2 leaf), third leaf Late sowing of winter crops
	<b>May</b>	<b>June</b>	<b>July</b>	<b>August</b>	<b>Sept.</b>	<b>Oct.</b>
2008	Late sowing of spring crops. 1- emergence (3-5 leaf), S - vegetative, 2-4 leaf. 2- M vegetative - flowering 3- WW, WB- grain filling (milk dev.) 3- S - flowering	> biomass of spring crops. 1- WB grain filling (dough dev.) 2- WW and WB - ripening., R. - flowering. 2- S -flowering 3- stress. 3-M flowering 2- WB. harvest 3- WW. harvest	2- shortening of phases spring crops. M. - grain filling 2- Early hyb.grain filling (milk dough). 3 - S. and M. grain filling (dough dev.) 3- S. ripening. 3- 100% WB. harvest and 95% WW.	Hot and dry 1- fast dev. M. grain filling (dough dev.) 2- S - beginning of ripening 3- S. harvest.	1- Drought 2- rainfall 1-2- average late hyb.M. ripening - maturity 1-2- S. harvest 100%, M. early hyb.	1-rainfall Late sowing 2-3- increase emergence, 1-3 leaf. 3- emergence 2-3 increase sowing rate, 80% -WW, 50% -WB
	<b>May</b>	<b>June</b>	<b>July</b>	<b>August</b>	<b>Sept.</b>	<b>Oct.</b>
2009	Low soil water content	3- rainfall. 1 - WW milk dev., WB - dough dev. 2- 3 - WW WB. Rip. and	1-good water content 2-3- drought 3- S. -	2-3- drought 2- M- maturity. 2- late M. - grain filling, ripening 3	1-3 late M. maturity 1- S. end of harvest 2-3- M. harvest	Good water cont. .2- rainfall - late sowing 3-

	1-yellow.2-3- (shortening) Flowering and grain filling 3-end of sowing late hyb. M.	maturity. 3- M.S. veg., flowering phase. 2- harvest WB, 2-3 –WW	flowering, grain filling 3-late M – flowering, early - grain filling, ripening	– S. harvest		emergence 3-Sowing 75-80% of W crops
	<b>May</b>	<b>June</b>	<b>July</b>	<b>August</b>	<b>Sept.</b>	<b>Oct.</b>
<b>2010</b>	1-2- M. – vegetative (3–5–7 leaf), S. vegetative 2–4 leaf.1-flowering 2- mass flowering 3WW, WB. Flowering, grain filling.3-WB. Mass grain filling (milk dough) 3-S. M.> biomass 3-S. flowering.	1-2 WW. From milk to dough dev. 3-M. and S. max biomass flowering and grain filling 3-early hyb. Grain filling  3- WB. harvest  Rainfall - low grain quality	1-slow dev. M.S.flowering to grain filling S. grain filling (dough dev)  3-WW. harvest	Drought 1-S. ripening. Late hyb. M. grain filling (milk to dough dev.) 3 – S. mass low arable land maturity 2-harvest WW. 3-S. harvest and early hyb. M. 3- deep soil plowing	2- average late hyb. M. ripening and late hyb. Dough dev. 2- S. maturity 3-rainfall delay harvest of spring crops. Emergence of early rapeseed, WW and WB.3 - sowing mass	2, 3- emergence. 2-rainfall delay sowing of winter crops.
	<b>May</b>	<b>June</b>	<b>July</b>	<b>August</b>	<b>Sept.</b>	<b>Oct.</b>
<b>2011</b>	1- WW.WB. heading and beg. Flowering. 1- M. vegetative 3-5-7 leaf. S. vegetative 2-leaf. 3- WW. WB flowering and beginning grain filling. 1- late sowing of spring crops.	1-WW, WB., milk dev. 1 – WB. Ripening maturity.1-R. - ripening. 1-high biomass spring crops. 2-WW. Dough dev. 2-S. (south) beg. Flowering 2-3-WB. harvest	1-WW. dough dev. 1-M. early hyb. Flowering, aver. Early hyb. And late hyb. Vegetative. 3- aver.early M. grain filling and early dough dev. 3- S. beg. Ripening. End WB. Harvest and 85% WW.	1-2- late hyb. Beg. Milk dev. 2-S. mass ripening and maturity.3- aver. Late hyb. Dough dev. And late hyb. Milk dev. 3- S. end of dev.	Dry month. 2- 1- aver. Late hyb. M. dough dev. Ripening 2- end S. harvest 2- harvest of early and average hyb. M. 3- sowing WW, WB. At places.	3- sowing winter crops 3- emerg. 3- R. mass emergence 2- rainfall obstruct from sowing of WW and WB. 3- increase cereals area.

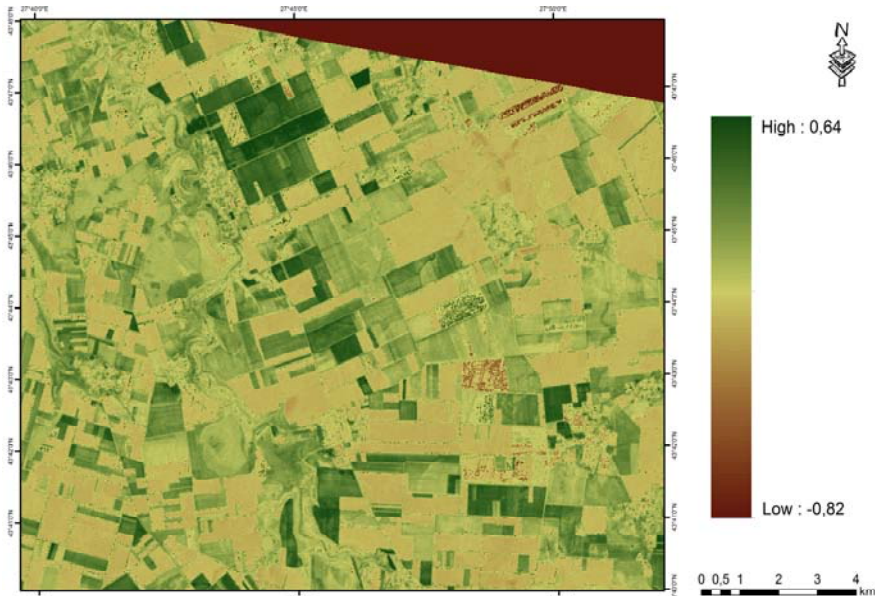
List of abbreviations used in Table 1. 1, first decade; 2, second decade; 3, third decade; WB, winter barley; WW, winter wheat; R, rapeseed; S, sunflower; M, maize



*Fig. 2. NDVI time-series cluster analysis profiles for the identified crops (2007-2011)*

Supervised classification with the maximum likelihood classifier algorithm was applied on the high-resolution images using as reference the field data to identify the training samples for each crop on the selected images and assess the crop identification process on the SPOT-VGT data. Thus, after the crop identification process, accuracy assessment was applied on the three crop identification classifications to evaluate the accuracy. Overall classification accuracy for the SPOT-4 HRVIR image was 87.62%; and for the LANDSAT-5 TM images in the range 82-94% overall accuracy. Afterwards, the maximum NDVI values were derived from these images for the major identified crops in order to compare them with the values derived from the representative decades of the SPOT-VGT NDVIs time-series data. The SPOT-4 HRVIR image is acquired on 24.03.2011, when winter crops are at heading phenophase, while spring crops are either at beginning of vegetative phase, still bare soil or not sown. The highest NDVI value for the

SPOT-4 image is 0.50 for winter wheat, while for SPOT-VGT NDVI S10 is 0.47 (Figure 3).



*Fig. 3. NDVI image derived from SPOT-4 HRVIR sensor, acquired on 24.03.2011*

The first LANDSAT-5 TM satellite image is acquired on 29.05.2011, when the winter crops are at flowering and grain filling phenophases, while spring crops are at vegetative phase of their development. The maximum NDVI from the LANDSAT-5 TM is 0.74, while from the SPOT-VGT product it is 0.72 (Figure 4.).

The second LANDSAT-5 TM satellite image was acquired on 21.06.2011, when winter crops are at ripening and dough development stage, while spring crops are at flowering phenophase. At this stage of the agricultural year there is big similarity observed, because the values for winter wheat are 0.64 from LANDSAT image and 0.63 from SPOT-VGT product. The sunflower class is with 0.67 NDVI from the high-resolution image and 0.70 from SPOT-VGT product. The identified maize class show close values with 0.76 NDVI from LANDSAT image, while from SPOT-VGT product at 0.79 (Figure 5.). Additionally, the third LANDSAT-5 TM satellite image acquired on 08.08.2011 was introduces, where winter crops are already harvested, but spring crops are at ripening and maturity phenophases. The sunflower values are at 0.57 from LANDSAT and 0.50

from SPOT-VGT, while for maize cultivars at 0.61 and 0.65, respectively (Figure 6.).

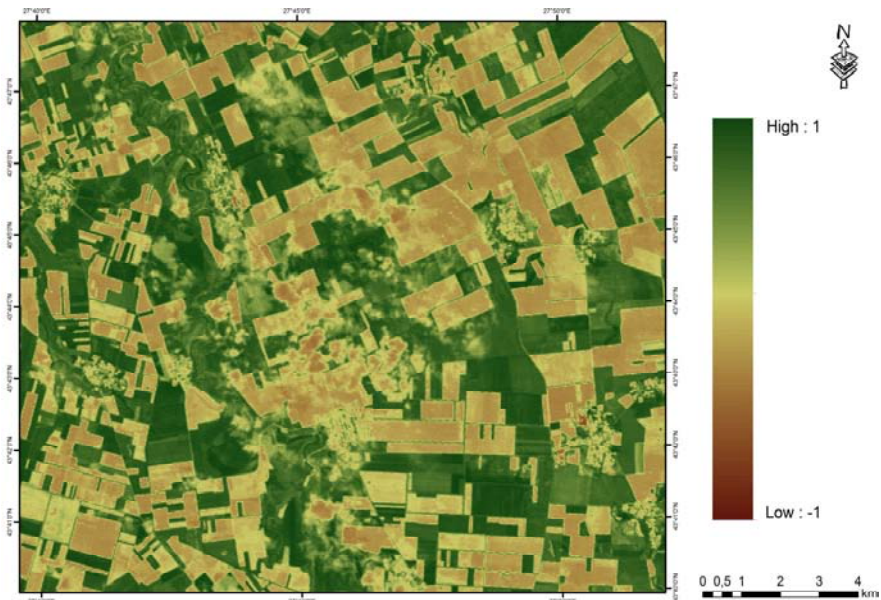


Fig. 4. NDVI image derived from LANDSAT-5 TM sensor, acquired on 29.05.2011

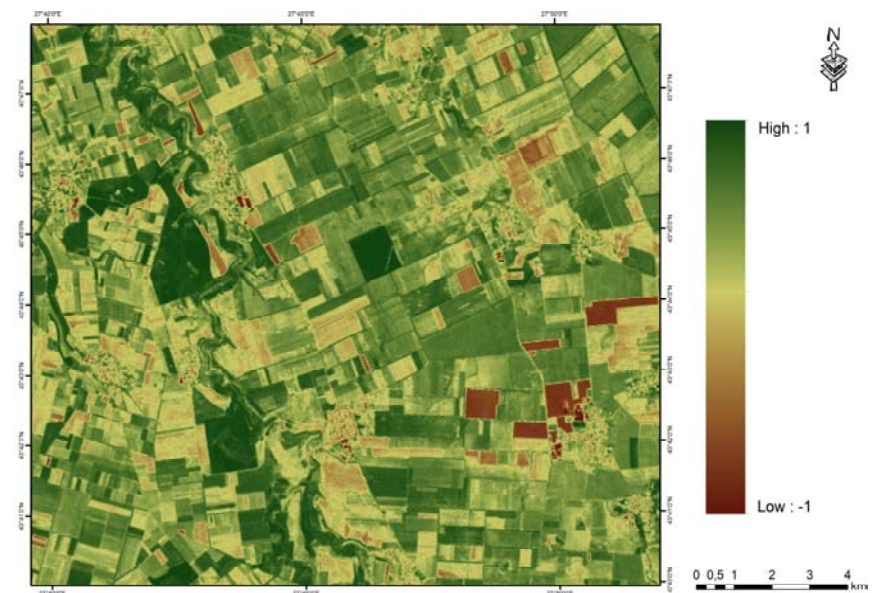


Fig. 5. NDVI image derived from LANDSAT-5 TM sensor, acquired on 21.06.2011

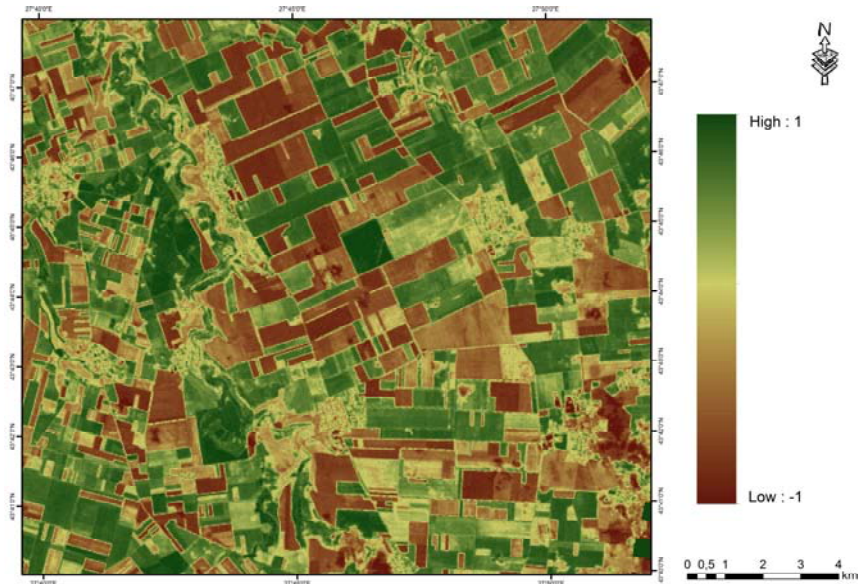


Fig. 6. NDVI image derived from LANDSAT-5 TM sensor, acquired on 08.08.2011

### ***3.2. Identifying the onset of the growing period, length of the reproductive growth period and the entire growing season for the crops***

The results obtained in this section are partly based on the Reed et al. (1994) approach. Additionally, knowledge of crop phenology was used for vegetation growth parameters extraction from the temporal profiles. The onset of the crop growing period, maximum NDVI values reached, length of the reproductive growth period and entire crop growing season are extracted using the NDVI time-series cluster analysis profiles for the identified crops (2007-2011) presented in Figure 2 for comparison.

The mixed class identified has onset of the crop growing period ranging from the 1<sup>th</sup> decade of 2007 till the 7<sup>th</sup> decade of 2011. The maximum NDVI values are from 0.56 to 0.72 between 14 and 20 decade for the five years period. The length of the reproductive growth period for the mixed class is between 5-7 decades. The entire crop growing season ranges from 25 to 35 decades in the five year period. Hence, the above data indicate that the class represents a mixed crop cluster.

The winter wheat class shows onset of the crop growing period for the 5-year period which starts from the 1<sup>th</sup> decade of 2007 to 7<sup>th</sup> of 2011. The maximum NDVI for the class winter wheat is in the range 0.70 - 0.80 within 14<sup>th</sup> and 15<sup>th</sup> decades. The length of the reproductive growth period is



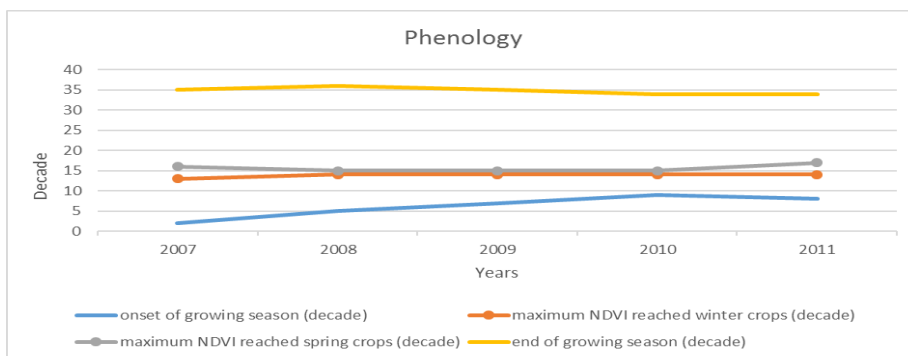
between 6 and 9 decades and the entire crop growing season ranges between 20 and 25 decades.

The winter barley class reveals onset of the crop growing period from the 3<sup>th</sup> decade of 2007 to 7<sup>th</sup> decade of 2011. The maximum NDVI is in the range 0.63 - 0.82 between 13<sup>th</sup> -16<sup>th</sup> decades. The length of the reproductive growth period is between 7 and 9 decades while, the entire crop growing season is between 21 and 25 decades.

The sunflower class shows onset of the crop growing period from the 3<sup>th</sup> decade of 2008 to 7<sup>th</sup> decade of 2011. The maximum NDVI values reached for the five year period is between 0.62-0.80 in the range of 14<sup>th</sup> - 17<sup>th</sup> decades. The length of the reproductive growth period is between 8 and 10 decades and the entire crop growing season for the sunflower cultivars is 22 and 27 decades.

The maize class reveals onset of the growing period from the 5<sup>th</sup> decade of 2008 to 7<sup>th</sup> decade of 2011. The maximum NDVI reached is between 0.78 and 0.85 in the 14<sup>th</sup> decade for 2008 and 16<sup>th</sup> decade for 2007. The length of the reproductive growth period is between 8 and 10 decades while, the entire crop growing season is between 25 and 28 decades.

In addition, the start of the growing season, end of growing season, maximum NDVI values reached for winter crops and maximum NDVI values reached for spring crops was prepared in a figure based on ground data and farmers inquires for the year 2011 (Figure 7).



*Fig. 7. Crop phenology parameters extraction*

Hence, the above data reveals that overall there is similarity in the length of the reproductive growth period and the entire crop growing season between the winter crops (wheat and barley) and spring crops (sunflower

and maize) depending on experienced anomalies. The crop phenology results show good relation between the parameters derived from ground and remote sensing data.

### ***3.3. Crop anomaly events detection using yearly cluster NDVI time-series image analysis and quantitative data***

The agro-phenological information together with the agro activities done for each 10-day period are extracted from the monthly bulletins and implemented in the crop anomaly events detection using yearly NDVI time-series cluster analysis derived from the SPOT-Vegetation NDVI product. The quality of the crop anomaly events detection was assessed using quantitative data. Yield figures for the major crops for the five year period derived from official statistics from the Bulgarian Ministry of Agriculture and Foods and making correlations with the maximum NDVI values reached for the growing season. The time-series cluster analysis is given below.

#### ***3.3.1. Analysis of 2007***

The year was characterized as anomalous. The winter crops at the beginning of the year were ahead of their development by 45 days. The crops were at tillering in February and in heading phenophase in March. Shortening of the phenophase periods were observed due to bad agrometeorological conditions in May. As a result the yield from both winter and spring crops were low. The harvest of the late maize cultivars was delayed because of intensive rainfall in the beginning of September.

The identified winter wheat and barley classes exhibited NDVI values above 0.38 for the first decade (Figure 8a). Such values are a clear indication of winter crops. The cultivars of winter wheat and barley reached their maximum NDVI values of 0.67 and 0.64, respectively, at the end of April (11-12<sup>th</sup> decade) at flowering stage (Figure 8a). Afterwards, in the middle of May the winter crops were in grain filling and ripening development stages. Finally the harvest of the winter barley fields at maturity stage took place in the beginning of June (16<sup>th</sup> decade), while the fields sown with winter wheat were harvested at the end of June (17<sup>th</sup> and 18<sup>th</sup> decade). The maize and sunflower classes identified showed the highest NDVI values in June (16-17<sup>th</sup> decade), which corresponds to flowering development stage with NDVI values at 0.75 for maize and 0.62 for sunflower. The harvest of the late maize hybrids was delayed due to

intensive rainfall. As a result of that high NDVI values up to 0.61 (Figure 8a) were observed until mid September (25-26<sup>th</sup> decade).

The winter wheat class occupies large areas in the Northeast part of the region, while the spring crop classes are mostly situated in west and south parts of the studied region (Figure 8b).

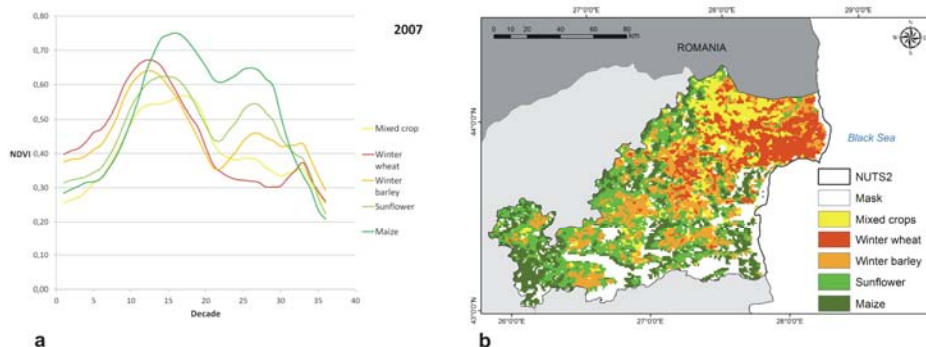


Fig. 8. a) NDVI cluster time-series cluster analysis profiles for 2007  
b) Cluster map of actual NDVI values for 2007

### 3.3.2. Analysis of 2008

The year was characterized as favorable in terms of the agrometeorological conditions and the applied agrotechnical measures. Thus, the average crop yield figures were the highest for the past 20 years.

The identified winter crop classes reflected very accurately the occurred late onset of tillering and heading phenophases in the beginning of March due to the late snow melt (Figure 9a). Then winter crop classes reached their peak of vegetative biomass at flowering stage in the end of April and beginning of May. Exceptionally high NDVI values were reached - 0.82 for winter barley and 0.77 for winter wheat because of the extraordinary good agrometeorological conditions observed. Winter wheat cultivars were at dough development, while winter barley were at maturity stage in mid June (17<sup>th</sup> decade), which accommodated better crop identification. The harvest was conducted at the end of June for winter barley, while for winter wheat it took place in the beginning of July. The spring crops were at their highest biomass accumulation at the beginning of June with NDVI values at 0.79 for sunflower and 0.85 for maize. The maize cultivars kept high NDVI values until September, due to the development of late maize hybrid.

Winter crop classes occupy northeast part of the region, while the spring crops are distributed in the west and south parts of the region (Figure 9b.)

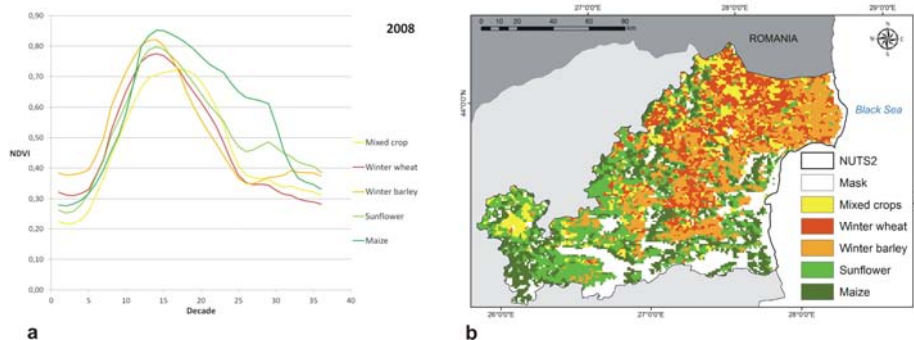


Fig. 9. a) NDVI cluster time-series cluster analysis profiles for 2008  
 b) Cluster map of actual NDVI values for 2008

### 3.3.3. Analysis of 2009

The year was described as normal considering the agrometeorological conditions. The identified winter crop cultivars were at tillering and heading phenophases in their majority in March. Then in the end of April and beginning of May (14-15<sup>th</sup> decade) the winter crops were at flowering stage. At that point the maximum accumulated green biomass was reached with NDVI values for winter barley - 0.70 (14<sup>th</sup> decade) and for winter wheat - 0.65 (15<sup>th</sup> decade). The harvest of the winter barley occurred in the middle of June (17<sup>th</sup> decade), while in the 18<sup>th</sup> decade was the harvest of the winter wheat. This information accommodates better crop identification process. The spring crops reached their maximum of accumulated green biomass in June (15<sup>th</sup> -16<sup>th</sup> decade) at flowering phenophase. The NDVI values were 0.69 for sunflower and 0.77 for maize. In September the late maize hybrids still kept high NDVI values - 0.61. Winter crops that were already sown at that point started their development from 0.30 NDVI in September and by the end of the year in tillering phenophase were at 0.50 NDVI values (Figure 10a).

The winter crops and mixed crop clusters occupy Northeast part of the region, while the sunflower class is mainly in the rest of the region covering the central and southwest part of the area studied (Figure 10b).

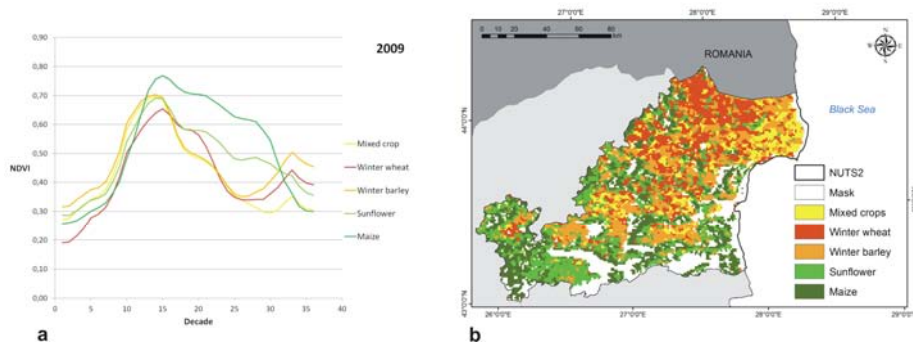


Fig. 10. a) NDVI cluster time-series cluster analysis profiles for 2009  
 b) Cluster map of actual NDVI values for 2009

### 3.3.4. Analysis of 2010

The year was considered unfavourable because of bad agrometeorological conditions which delayed the harvest and as a consequence affected the grain quality and yield values.

The identified classess experienced a slight increase of NDVI values due to relatively high temperatures, which kept the vegetative state of the winter crops in the beginning of year. Afterwards, in the middle of the month the temperatures decreased rapidly, which returned the crops to dormancy. Nevertheless, this anomalies were clearly identified using the NDVIs S10 time-series cluster analysis profiles (Figure 11a). Until the beginning of March, when the vegetative state of the winter crops was renewed, low NDVI values were experienced. At that point the NDVI values of winter crops were at 0.35-0.43 and in tillering and heading phenophases. The highest green biomass accumulated at the beginning of May at flowering phenophase with values 0.69 for winter wheat and 0.75 for winter barley. Winter barley cultivars were at grain filling (dough development) stage, while winter wheat cultivars were at milk development in the end of May (15<sup>th</sup> decade). Winter crops experienced high NDVI values up until the end of July (21<sup>th</sup> decade) because of intensive rainfall delayed harvest was observed. On the other hand the spring crops reached their maximum green biomass accumulation at the end of May and the beginning of June at flowering phenophase, with NDVI values for sunflower at 0.74 and maize at 0.78. The bad agrometeorological conditions delayed harvest of spring crops as well. Finally, sunflower cultivars were

harvested in September, while the late maize hybrids in October (Figure 11a).

The winter crops are distributed in the Northeast part of region, while the rest of the region was occupied by a combination of mixed crop class, sunflower and maize (Figure 11b).

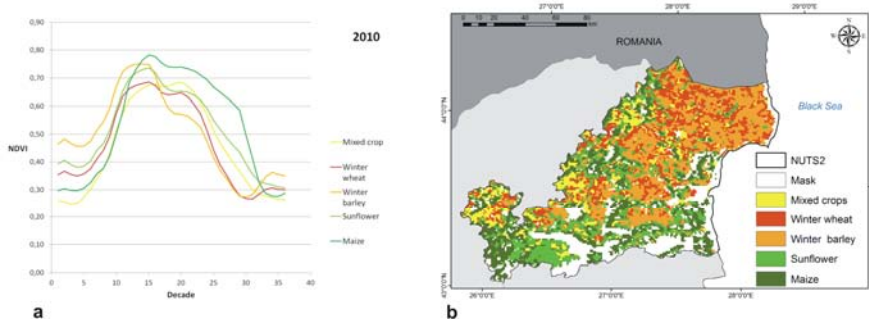


Fig. 11. a) NDVI cluster time-series cluster analysis profiles for 2010  
b) Cluster map of actual NDVI values for 2010

### 3.3.5. Analysis of 2011

The year was characterized as normal for all cultivated crops. The winter crops started the year with NDVI values in the range 0.33-0.38. Winter crops were at heading phenophase in the beginning of April. Winter crop classes reached their maximum accumulated green biomass in May (14<sup>th</sup> decade) with NDVI values at 0.74 for winter wheat and 0.73 for winter barley (Figure 12a). Winter crops were harvested in the end of June and beginning of July. The sunflower class reached its maximum NDVI values in mid June (17<sup>th</sup> decade) with NDVI values at 0.72. The maize class reached NDVI values of 0.80 at the end of June (18<sup>th</sup> decade). The class maintained high values of up to 0.72 (Figure 12a) until the 23<sup>th</sup> decade of the year.

The winter wheat and mixed crop classess occupy North and Northeast parts of the region. Sunflower cultivars were present in the central parts of the region, while maize cultivars were sown in the south part (Figure 12b) where highest altitudes of the region can be observed.

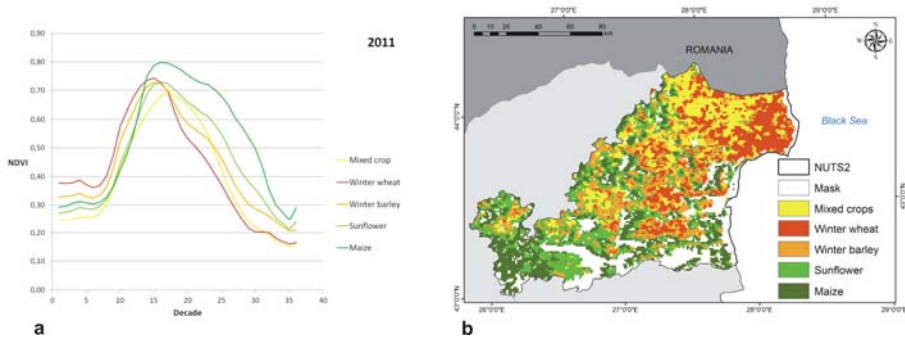


Fig. 12. a) NDVI cluster time-series cluster analysis profiles for 2011  
 b) Cluster map of actual NDVI values for 2011

Additionally, for quality assessment a correlation process was prepared. Correlation between the average yield figures for the region derived from official statistics for the major cultivated crops (winter wheat, winter barley, sunflower and maize) and the maximum reached NDVI values from the time-series analysis for the five year period with confidence level of 95%, the relevant  $r$  values are  $\geq 0.75$  and  $\leq -0.75$  for five variables was accomplished. For the mixed crop class the yield figure that was taken from official statistic was the one from oilseed rape, since presumably that cultivar have some big parts in that class (Table 2). The correlation results show that, there is high correlation ( $r$ ) between the yield and highest NDVI values for winter barley at  $r + 0.99$ , sunflower and oilseed rape have equally high values at  $r + 0.84$ . Winter wheat has a good correlation with  $r + 0.65$ , while maize cultivars have positive correlation at  $r + 0.37$  (Table 3.).

Table 2. Statistics for derived average yield and maximum NDVI values

<b>Average Yield (kg/dca)</b>	<b>2007</b>	<b>2008</b>	<b>2009</b>	<b>2010</b>	<b>2011</b>
Winter wheat	253.5	472.5	344.9	411.6	362
Winter barley	283.4	421.8	345.7	374.2	340
Maize	101.2	406.6	415.3	598.6	626
Sunflower	95.7	198.8	185.6	209.3	210
Rapeseed	182.7	276.1	221.8	277.8	257
<b>Maximum NDVI reached</b>	<b>2007</b>	<b>2008</b>	<b>2009</b>	<b>2010</b>	<b>2011</b>
Rapeseed	0.56	0.72	0.69	0.68	0.69
Winter wheat	0.68	0.78	0.65	0.68	0.73
Winter barley	0.64	0.82	0.71	0.75	0.72
Sunflower	0.62	0.79	0.69	0.74	0.72
Maize	0.75	0.85	0.76	0.78	0.80

Table 3. Correlation analysis for the major cultivated crops

Correlation	Winter wheat	Winter barley	Maize	Sunflower	Oilseed rape
$R^2$	0.65	0.99	0.37	0.84	0.84

#### 4. Conclusions

Identifying the possibility of crop monitoring at regional scale using time-series of SPOT-VGT NDVIs S10 vegetation product in an intensively cropped area in Northeast Bulgaria was investigated in this case study. The study applying SPOT-VGT NDVIs S10 satellite product for crop monitoring including the following tasks: crop identification, crop phenology estimation and crop anomaly events detection covering intensively cropped area (Northeast Bulgaria). The crop identification process was assessed using similarity value analysis between the maximum NDVI values derived from the low-resolution SPOT-VGT NDVIs S10 product and the high-resolution satellite images for a test site in the region of interest. The article shows similarity in the length of the reproductive growth period and the entire crop growing season between the winter crops (wheat and barley) and spring crops (sunflower and maize) depending on experienced anomalies. The crop phenology results show good relation between the parameters derived from ground and remote sensing data. The crop anomaly events detection was quantified using correlation between the average yield for the major cultivated crops and the highest reached NDVI values of the identified crops show high correlation for winter barley at  $r^2$  0.99, sunflower and oilseed rape have equally high values at  $r^2$  + 0.84. Winter wheat has a good correlation with  $r^2$  + 0.65, while maize cultivars have positive correlation at  $r^2$  + 0.37. The applied methodology proves that the low resolution satellite images with high-revisit period are an ideal solution for crop monitoring on large arable territories. However low resolution satellite vegetation products must always be supported and used in combination with agro-phenological ground data, quantitative data and some high-resolution satellite images for better crop monitoring results. Although, the SPOT-VGT sensor successfully retired on 01.06.2014 the continuity of such low resolution data for time-series vegetation monitoring is assured by the launch of PROBA-V mission in 2013.



## Acknowledgments

The present study is a part of the PhD thesis of V. Vassilev. He would like to express his gratitude to the MARS Unit, Agri4cast action at the Joint Research Center of the European Commission for the satellite data obtained from SPOT-VGT NDVIs S10 product.

## References

1. Meyer-Roux, J., P. Vossen. The first phase of the MARS project, 1988–1993: overview, methods and results. In: Official Publications of the E.U., Luxembourg (Ed.), Report EUR 15599 EN. Conference on the MARS project: Overview and prospectives, Belgirate, 1994, 33-79.
2. DeWinné, P. 2004. Les Besoins de la Direction Generale VI: Agriculture. In: Office for official publications of the E.U., Luxembourg (Ed.), Report EUR 15599 EN, 2004. Conference on the MARS project: Overview and prospectives, Villa Carlotta, Belgirate, Lake Maggiore, Italy, 17-22 (in French).
3. Pitts, D. E., G. Badhwar. 1980. Field size, length, and width distributions based on LACIE ground truth data. *Remote Sensing of Environment*, Volume 10, Issue 3, 201-213.
4. Cohen, Y., M. Shoshany. 2002. A national knowledge-based crop recognition in Mediterranean environment *International Journal of Applied Earth Observation and Geoinformation*, 4, 75- 87.
5. MacDonald, R. 1984. *IEEE Transaction on Geoscience & Remote Sensing*, GE-22, 473-481.
6. Blaes, 2005. Efficiency of crop identification based on optical and SAR image time series. *Remote Sensing of Environment*, 96 352 – 365.
7. GEO 2013. Progress on GEOGLAM Implementation First steps towards implementation 2013-2014 Phase I and II. 28th Executive Committee – 16-17 July 2013.
8. Ryerson, R. A., P. J. Curran, P. R. Stephens. 1997. Agriculture. In: Philipson W.R. (Ed.) *Manual of Photographic Interpretation*. 2nd ed. American Society for Photogrammetry and Remote Sensing, Bethesda, MD, 365-397.
9. Townshend, J., Justice C., Li W., Gurney C., McManus J. 1991. Global land cover classification by remote sensing: present capabilities and future possibilities. *Remote Sens Environ*, 35, 243-255.
10. Vassilev, V. 2013. Crop Identification Using Satellite Images and Vegetation Products. PhD thesis work. Prof. Marin Drinov Academic Publishing House. pp. 154 ISBN 978-954-322-633-7. (In Bulgarian).
11. DeFries, R., M. Hansen, J. Townshend. 1995. Global discrimination of land cover types from metrics derived from AVHRR pathfinder data. *Remote Sens Environ*, 64 (3), 209-222.

12. Reed, B. C., J. F. Brown, Vander Zee D., Loveland T. R., J. W. Merchant, D. O. Ohlen. 1994. Measuring phenological variability from satellite imagery. *Journal of Vegetation Science*, 5, 703-714.
13. Brown, J. F., T. R. Loveland, J. W. Merchant, B. C. Reed, D.O. Ohlen. 1993. Using multisource data in global land-cover characterization: Concepts, requirements, and methods. *Photogramm Eng Remote Sens*, 59(6), 977-987.
14. Loveland, T. R., J. W. Merchant, J. F. Brown, D.O. Ohlen, B.C. Reed, P. Olson, J. Hutchinson. 1995. Seasonal land-cover regions of the United States. *Annals of the Association of American Geographers*, 85, 339-355.
15. Rouse, J., R. Haas, J. Schell, D. Deering. 1973. Monitoring vegetation systems in the Great Plains with ERTS. In: *Third ERTS Symposium, 1973, NASA SP-351 I*, 309-317.
16. Bossard, M., J. Feranec and J. Othel 2000. CORINE land cover technical guide – Addendum 2000. Technical report No 40. European Environmental Agency EEA Copenhagen.
17. Groom, B. G., Fuller R. M., Jones A. R. 1996. Contextual correction: techniques for improving land-cover from remotely sensed images. *Int J Remote Sens*, 17, 69-89.
18. Garcia-Consuegra, J., G. Cisneros. 1999. Establishing spatially continuous in a non-supervised way. In: *Proceedings of the IEEE International Geoscience and Remote Sensing Symposium (IGARSS'99)*, 1999, Hamburg, Germany.
19. Yuan, H., S. Khorram, , Dai X. L. 1999. Applications of simulated annealing minimization technique to unsupervised classification of remotely sensed data. In: *Proceedings of the IEEE International Geoscience and Remote Sensing Symposium (IGARSS'99)*, 1999, Hamburg, Germany.

## **МОНИТОРИНГ НА ЗЕМЕДЕЛСКИТЕ КУЛТУРИ ЧРЕЗ ВРЕМЕВИ СЕРИИ ОТ SPOT-VGT NDVIs S10 ПРОДУКТ ЗА СЕВЕРОИЗТОЧНА БЪЛГАРИЯ**

***В. Василев, Е. Руменина***

### **Резюме**

Обект на настоящето изследване са основните отглеждани земеделски култури в североизточния район на България и по конкретно: зимна пшеница, зимен ечемик, рапица, слънчоглед и царевица. Целта на статията е мониторинг на земеделските култури на регионално ниво с дистанционни данни със ниска пространствена разделителна способност (ПРС) и висока времева разделителна способност (ВРС). Изследването е концентрирано върху обработка и интерпретация на времеви серии от Нормиран Разликов Вегетационен

Индекс с цел мониторинг на земеделски култури с три различни под-етапи на работа: разпознаване на земеделски култури, определяне на фенологични параметри и разпознаване на аномалните земеделски събития. Разпознаването на земеделските култури е оценена посредством сходство на стойностите на Нормирания Разликов Вегетационен продукт с ниска ПРС и тези извлечени от спътникови изображения с висока ПРС върху тестови участък разположен в района на изследване. Познания за фенологията на земеделските култури е използвано при определяне на фенологични параметри от времевите профили от данни. Разпознаване на аномалните земеделски събития е извършено с помощта корелация между средните стойности на добивите за основните култури и достигнатите през земеделската година максимални стойности на Нормираният Разликов Вегетационен Индекс за разпознатите култури за период от пет години (2007-2011) с праг на достоверност от 95% и значими стойности от  $\geq 0.75$  и  $\leq -0.75$  за пет променливи. Резултатите показват висока корелация ( $r$ ) за зимен ечемик  $r + 0.99$ , посевите на слънчогледа и зимна рапица са с еднакви стойности от  $r + 0.84$ . Зимната пшеница има добра корелация със стойности  $r + 0.65$ , докато посевите на царевица имат позитивна корелация от  $r + 0.37$ . Представената методика доказва значителния потенциал при използването на спътниковите изображения с ниска ПРС за целите на мониторинг на земеделски култури на регионално ниво в допълнение с агро-фенологична информация извлечена от месечните бюлетини на Националния Институт по Метеорология и Хидрология към Българската Академия на Науките, спътникови изображения с висока ПРС и статистика за средните добиви за основните земеделски култури. Това изследване допринася за успешното приложение и внедряване на съществуващата методология на MARS отдела към Европейската Комисия и допълването и със агро-фенологична, изображения с висока ПРС и статистически данни за добивите. Продължаващото използване на данни с ниска ПРС с цел мониторинг на земеделските култури на регионално ниво е подсигурано с успешното изтрелване на микро спътника PROBA-V през 2013 г., продължение на мисията на SPOT-Vegetation.

## **CROP AREA ESTIMATES BASED ON PER-PIXEL SUPERVISED CLASSIFICATION ON EO-1 ALI IMAGE FOR A TEST SITE IN NORTHEAST BULGARIA**

*Vassil Vassilev*

*Space Research and Technology Institute – Bulgarian Academy of Sciences  
e-mail: vassilev\_vas@space.bas.bg*

### **Abstract**

*The purpose of this article is to investigate the crop area estimates based on per-pixel classification for Zhiten test site situated in Northeast Bulgaria. The chosen satellite image is acquired from multispectral EO-1 ALI sensor on 09.07.2011. The methodology of this article includes the following working stages: 1) applying arable mask from CORINE 2006 land-cover database; 2) conducting per-pixel supervised classification using the maximum likelihood classifier (MLC) algorithm for crop identification; 3) applying accuracy assessment tool in ERDAS Imagine and deriving accuracy totals and kappa statistics; 4) calculating crop area estimated based on pixel-counting technique. The overall classification accuracy for the EO-1 ALI image is 96.24% and overall kappa statistics is 0.9397. The high overall accuracy can be accomplished after carefully choosing representative training samples. The beginning of July can be a perfect time to separate spring crops (sunflower and maize cultivars) and assess crop area estimated for all cultivated crops based on per-pixel classification with overall accuracy above 95%. The down side of this study is that at the time of image acquisition the winter crops are difficult to separate, since they are already with very low reflectance values.*

### **1. Introduction<sup>1</sup>**

Currently a major challenge in agricultural applications is forecasting crop production using low and coarse resolution satellite images,

---

<sup>1</sup> Abbreviations used:

MARS – Monitoring Agriculture with Remote Sensing

LACIE – Large Area Crop Inventory Experiment

CITARS – Crop Identification Technology Assessment for Remote Sensing

NDVI – Normalized Difference Vegetation Index

while for high resolution (HR) satellite images one of the hottest topics is controlling area-based subsidies and applying precision agriculture practices amongst others. Satellite Remote Sensing (RS) provides synoptic, objective and relatively homogeneous data which can be geographically and temporally registered. Therefore, RS is an efficient tool for providing standard, high quality information on agriculture, evenly over broad-scale territories. The Monitoring Agriculture with Remote Sensing (MARS) project of the European Union was established in order to define and demonstrate how RS can be used operationally to supplement, interpret, and standardize agricultural statistical data provided by conventional techniques [1,2]. Satellite RS techniques have been proven to be effective and useful in broad-scale agricultural surveys such as: Large Area Crop Inventory Experiment (LACIE) project in the USA and MARS project in Europe [3]. Additionally, experiments from LACIE and Crop Identification Technology Assessment for Remote Sensing (CITARS) projects have also been conducted to demonstrate the capabilities of RS for crop inventory and forecasting [4,5].

Vegetation types can be characterized using their seasonal variations in the Normalized Difference Vegetation Index (NDVI) time-series, which include a series of images, acquired on weekly or decadal basis and showing the crop development dynamics. For example, the winter wheat phenophases like tillering and flowering as well as harvest, can be successfully identified using sensors with different spatial resolution in various band combinations and severe ground surveys, including collecting information for defining training samples for the supervised classification [6]. A number of different methods have been developed during the last two decades to discriminate crop types using data from NDVI and from the Advanced Very High-Resolution Radiometer (AVHRR). These methods employ a variety of different approaches including temporal profiles of crop phenology manifested in the NDVI [7,8], and classification of multi-temporal data [9,10], which can be applied on variously managed crop areas worldwide.

Crop identification during the growing season is a major challenge for forecasting crop production as well as for controlling area-based subsidies in the European Union member states [5]. The basis for separation one crop from another is the supposition that each crop species has a unique visual appearance and spectral signature on the image. However, separating these species may be difficult because of variations in soil properties,

fertilization, pest conditions, irrigation practices, planting dates, as well as intercropping, and tillage practices [11], all of which can be adopted in precision farming using high quality satellite images. Thus, high-resolution satellite images are the key to the above mentioned difficulties.

The purpose of this case study is to investigate crop area estimates based on per-pixel classification for Zhiten test site situated in Northeast Bulgaria, and it includes the following tasks:

- (1) Applying arable mask from CORINE 2006 land-cover database;
- (2) Conducting per-pixel supervised classification using the maximum likelihood classifier (MLC) algorithm for crop identification;
- (3) Applying accuracy assessment tool in ERDAS Imagine and deriving accuracy totals and kappa statistics;
- (4) Calculating crop area estimated based on pixel-counting technique.

## **2. Materials, methods and data used**

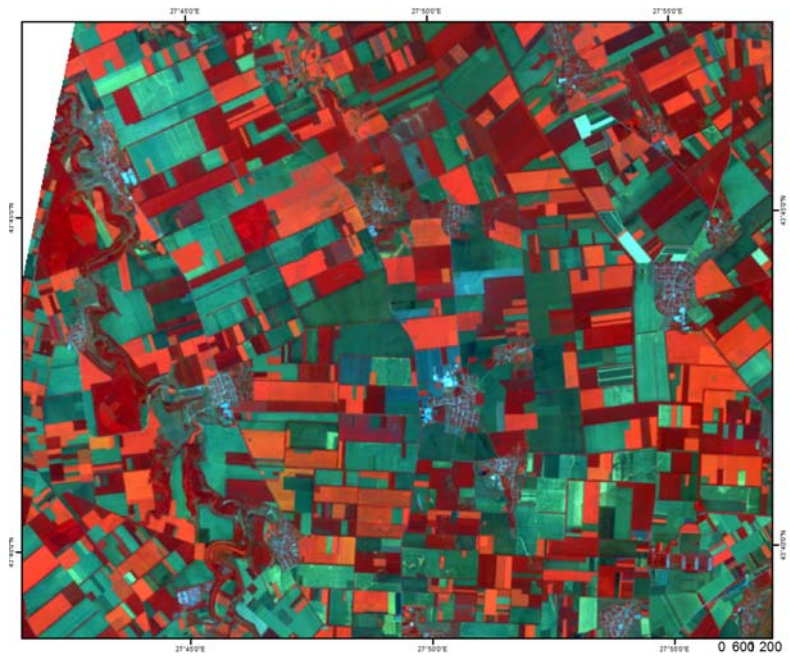
The study area – part of Zhiten test site is situated in North-East Bulgaria. The area represents intensively cultivated area sowed mostly with cereals and sunflower. This territory is one of the main agricultural regions of the country. The area is part of the European-continental climatic province of the temperate climatic belt. Climate is moderately warm with no distinctive dry season. Mean annual air temperature is 10.2°C. The main soil types are chernozems from the zonal ones and fluvisols from the azonal types.

The major cultivated winter crops (wheat and oilseed rape) and spring crops (sunflower and maize) were investigated in the present case study.

During the 2010-2011 agricultural season and in particular in the period between March–July 2011 four exhaustive field surveys were carried out and ground data was collected and organized in a GIS geodatabase. Field data was collected in the framework of a project financed by the Belgian Federal Science Policy Office (BELSPO) under the PROBA-V Preparatory Programme, with acronym – PROAGROBURO [12]. The ground-truth data consists of descriptions of the LU/LC types, phenological stages and vegetation cover of crops, GPS measurements, and photos. The collected ground data will contribute to selecting appropriate training samples for the supervised classification on the chosen satellite images. A multispectral EO-1 ALI image acquired on 09.07.2011 was used for the present investigation (Fig.1 and Fig. 2).



*Fig. 1. Raw EO-1 ALI image True color composite*



*Fig. 2. Raw EO-1 ALI False color infrared composite*

The spatial resolution of the image is 10m in the panchromatic band and 30m for the 9 multispectral bands: blue bands (0.43 – 0.45  $\mu\text{m}$ ; 0.45 – 0.51  $\mu\text{m}$ ); green band (0.52 – 0.60  $\mu\text{m}$ ), red band (0.63 – 0.69  $\mu\text{m}$ ), NIR bands (0.77 – 0.80  $\mu\text{m}$ ; 0.845 – 0.895  $\mu\text{m}$ ) and SWIR bands (1.20 – 1.30  $\mu\text{m}$ ; 1.550 – 1.750  $\mu\text{m}$ ; 2.080 – 2.350  $\mu\text{m}$ ). The temporal resolution of the satellite is 16 days, which makes it appropriate for monitoring agricultural applications.

An arable land mask using CORINE data was applied on the EO-1 ALI image in order to classify only the arable land and reduce the occurrence of mixed pixels with other non arable classes.

The *k*-mean and Iterative Self-Organizing Data Analysis (ISODATA) clustering algorithms are the most frequently used ones in RS. The ISODATA algorithm was selected in this study because it allows different number of clusters, while the *k*-mean algorithm assumes that the number of clusters is known a priori [13,14,15]. Unsupervised ISODATA cluster classification with four classes was applied to spectrally discriminate the crops and to collect the necessary information in order to delineate the training samples for the supervised per-pixel classification.

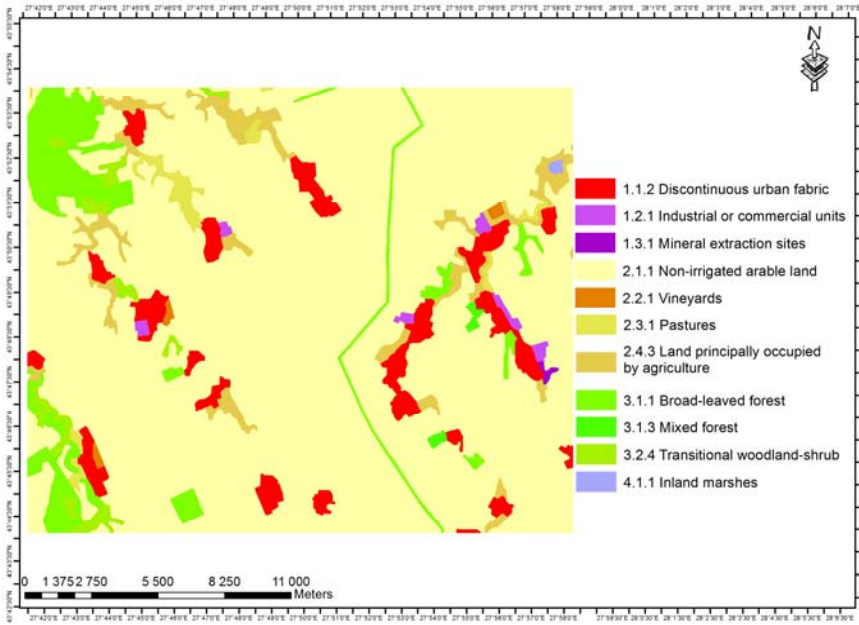
Per-pixel supervised classification using the Maximum Likelihood Classifier (MLC) algorithm was applied on the arable territories of the test site for crop identification purposes. In the MLC procedure, at least 10–15 independent training cases per class were used, so that its mean and variance can be estimated. Around 160-170 randomly distributed points were used for accuracy assessment for the classified image. The process continued with crop area estimates based on pixel counting technique. This step can be accomplished only if the pixel-based crop identification overall accuracy is higher than 95%.

### **3. Results and discussions**

#### ***3.1. Applying arable mask from CORINE 2006 land-cover database***

An arable land mask using CORINE 2006 land-cover data was applied on the EO-1 ALI image in order to classify only the arable land and reduce the occurrence of mixed pixels. In Fig.3 all the land cover classes present in the test area are shown and 2.1.1. Non-irrigated arable land class was used to build the mask layer.



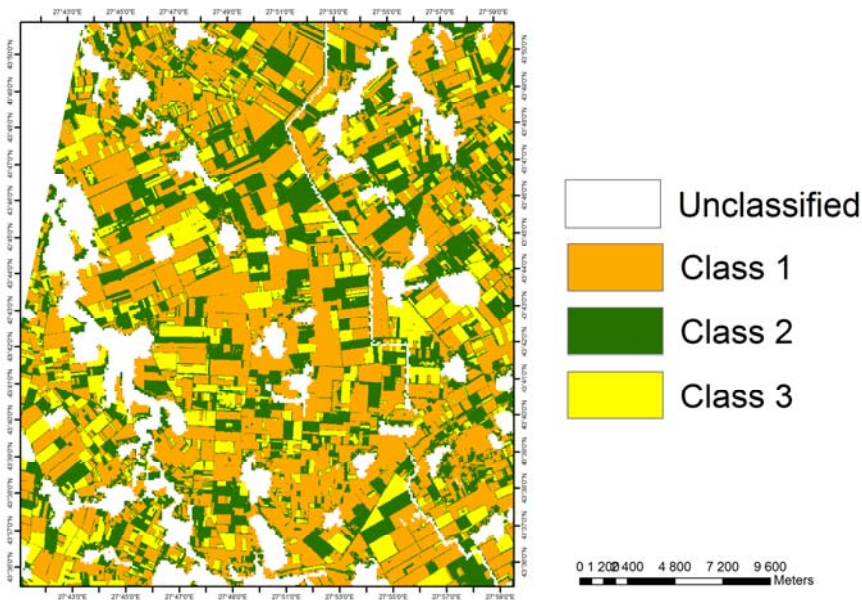


*Fig. 3. CORINE land cover classes*

### ***3.2. Conducting per-pixel supervised classification using the maximum likelihood classifier algorithm for crop identification***

The crop identification process was accomplished firstly by conducting unsupervised classification (using ISODATA algorithm) with 4-5 classes for the multispectral EO-1 ALI image (Fig.4.).

This spectral information was used together with the ground data as an indicator where to draw training samples for the supervised classification. The unsupervised classification is traditionally the first step and is accommodating the interpretation of the images. Supervised classification using the Maximum Likelihood Classifier (MLC) algorithm was applied to the arable land images. In the MLC procedure, a key concern is to collect a training set comprising of at least 10–30 independent training cases per class per discriminatory variable (e.g. band) to allow the formation of a representative description of the class, so that its mean and variance can be reasonably estimated [16].



*Fig. 4. Unsupervised classification on EO-1 ALI satellite image acquired on 09.07.2011*

For example, the spectral response of an agricultural crop class in an image might vary as a function of variables such as: the crops growth stage, topographic position, density of vegetation cover, health, impact of management activities, substrate conditions and instrument view angle [17].

The gathered training set from the field data was good enough to make representative training samples for the arable land classes. The unsupervised classification in combination with the ground information helped to choose and delineate appropriate training samples for the supervised classification of the EO-1 ALI image. The investigated phenological stages based on the image acquisition date are: dough development for winter wheat and flowering phase for early sown hybrids and vegetative phase for late sown hybrids of maize cultivars. The identified classes and their distribution in percentage for the EO-1 ALI satellite image are: winter crops - 35.37 %; sunflower – 17.19%; maize – 20.39%; stubble fields – 0.17%; and class unclassified which includes the no data part and the applied mask of the image – 26.33% (Fig.5),

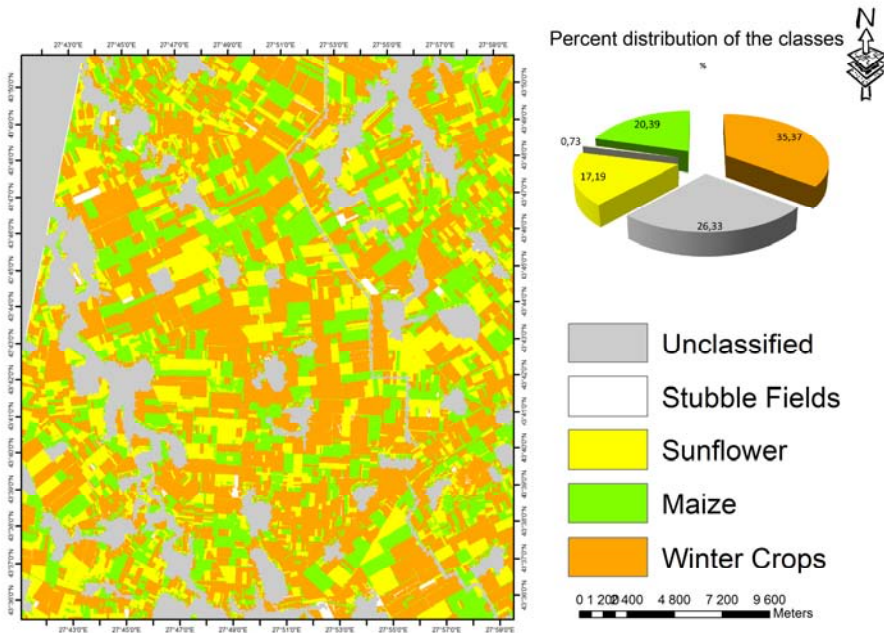


Fig. 5. Per-pixel supervised classification of EO-1 ALI satellite image acquired on 09.07.2011

### 3.3. Applying accuracy assessment tool in ERDAS Imagine and deriving accuracy totals and kappa statistics

Accuracy assessment tool in ERDAS Imagine software was utilized for assessing the accuracy of the per-pixel classified images of EO-1 ALI. Around 180-190 randomly distributed points were assessed for the classified image. Accuracy assessment was applied on the EO-1 ALI classified image for crop identification using its spectral resolution by applying visual interpretation on the panchromatic and both on the unsupervised and supervised classifications in combination with the ground data.

The achieved results on the overall classification accuracy for the EO-1 ALI image is 96.24% and overall kappa statistics is 0.9397 (Table 1).

The EO-1 ALI accuracy assessment shows that the class stubble fields can not be assessed because of the small part of the image occupied. The sunflower class has Producer's accuracy of 89.47%, which is the only accuracy that is below 90%, since all the other classes have accuracies well above 90%. Considering the achieved result based on the per-pixel classification which is above 95%, this gives a possibility to apply pixel-

counting method to calculate the area estimates, as it would not introduce much bias in the calculation.

*Table 1. Accuracy totals for EO-1 ALI satellite image*

<b>Class Name</b>	<b>Reference Totals</b>	<b>Classified Totals</b>	<b>Number Correct</b>	<b>Producers Accuracy (%)</b>	<b>User Accuracy (%)</b>
Stubble fields	2	0	0	-	-
Sunflower	38	34	34	89.47	100.00
Maize	55	57	54	98.18	94.74
Winter wheat	92	96	92	100.00	95.83
<b>Totals</b>	<b>187</b>	<b>187</b>	<b>180</b>		

Overall accuracy 96.24% and overall kappa statistics is 0.9397

### ***3.4. Calculating crop area estimated based on pixel-counting technique***

The crop area estimates were calculated for the EO-1 ALI satellite image using the per-pixel supervised classifications. The crop area estimates are calculated using the followed formula: number of pixels for each class of the classified image multiplied by the area represented by each pixel in the chosen image based on [18]. This method was selected because the overall classification accuracy was high enough (above 95% overall accuracy) to apply that method and in the same time not to introduce bid bias. The whole territory occupies 234.5 km<sup>2</sup>. The crop area estimated for the EO-1 ALI image classes show the following estimates: winter crops - 83 km<sup>2</sup>; sunflower – 40.3 km<sup>2</sup>, maize – 47.8 km<sup>2</sup> and stubble fields class occupies 1.7 km<sup>2</sup>. The rest of the image is occupied with the class unclassified, which includes both the no data part of the image and the applied mask with 61.8 km<sup>2</sup>.

## **4. Conclusions**

The presented methodology provides opportunity to calculate crop area estimates based on per-pixel supervised classification with higher than 95% overall accuracy. The results are encouraging and show that EO-1 ALI satellite image with both good spatial and spectral resolution and acquired in

July are beneficial for conducting crop area estimates on a highly cultivated crop area. The high overall accuracy can be accomplished after carefully choosing representative training samples. The beginning of July can be a perfect time to separate spring crops (sunflower and maize cultivars) and assess crop area estimated for all cultivated crops based on per-pixel classification with overall accuracy above 95%. The down side of this study is that at the time of image acquisition the winter crops are difficult to separate, since they are already with very low reflectance values.

## References

1. Meyer-Roux, J., P. Vossen. 1994. The first phase of the MARS project, 1988–1993: overview, methods and results. In: Official Publications of the E.U., Luxembourg (Ed.), Report EUR 15599 EN. Conference on the MARS project: Overview and prospectives, Belgirate, 1994, 33-79.
2. DeWinné P. (2004). Les Besoins de la Direction Generale VI: Agriculture. In: Office for official publications of the E.U., Luxembourg (Ed.), Report EUR 15599 EN, 2004. Conference on the MARS project: Overview and prospectives, Villa Carlotta, Belgirate, Lake Maggiore, Italy, 17-22 (in French).
3. Cohen, Y., M. Shoshany. 2002. A national knowledge-based crop recognition in Mediterranean environment International Journal of Applied Earth Observation and Geoinformation, 4, 75- 87.
4. MacDonald R. 1984.. IEEE Transaction on Geoscience & Remote Sensing, GE-22, 473-481.
5. Blaes, 2005. Efficiency of crop identification based on optical and SAR image time series. Remote Sensing of Environment, 96 352 – 365.
6. Townshend, J., C. Justice, W., Li, C. Gurney, J. McManus. 1991. Global land cover classification by remote sensing: present capabilities and future possibilities. Remote Sens Environ, 35, 243-255.
7. DeFries, R., M. Hansen, J. Townshend. (1995). Global discrimination of land cover types from metrics derived from AVHRR pathfinder data. Remote Sens Environ, 64 (3), 209-222.
8. Reed, B. C., J. F. Brown, D. VanderZee, T. R. Loveland, J. W. Merchant, D. O. Ohlen. 1994. Measuring phenological variability from satellite imagery. Journal of Vegetation Science, 5, 703-714.
9. Brown, J. F., T. R. Loveland, J. W. Merchant, B. C. Reed, D. O. Ohlen. 1993. Using multisource data in global land-cover characterization: Concepts, requirements, and methods. Photogramm Eng Remote Sens, 59(6), 977-987.
10. Loveland, T. R., J.W. Merchant, J. F. Brown, D. O. Ohlen, B. C. Reed, P. Olson, Hutchinson J. 1995. Seasonal land-cover regions of the United States. Annals of the Association of American Geographers, 85, 339-355.

11. Ryerson, R. A., P. J. Curran, P.R. Stephens. 1997. Agriculture. In: Philipson W.R. (Ed.) Manual of Photographic Interpretation. 2<sup>nd</sup> ed. Americal Society for Photogrammetry and Remote Sensing, Bethesda, MD, 365-397.
12. Roumenina, E., V. Kazandjiev, P. Dimitrov, L. Filchev, V. Vassilev, G. Jelev, V. Georgieva, H. Lukarski. 2013. Validation of LAI and assessment of winter wheat status using spectral data and vegetation indices from SPOT VEGETATION and simulated PROBA-V images. Int J Remote Sens, 34(8), 2888-2904.
13. Groom, B.G., R. M. Fuller, A. R. Jones. 1996. Contextual correction: techniques for improving land-cover from remotely sensed images. Int J Remote Sens, 17, 69-89.
14. Garcia-Consuegra, J., G. Cisneros. 1999. Establishing spatially continuous in a non-supervised way. In: Proceedings of the IEEE International Geoscience and Remote Sensing Symposium (IGARSS'99), 1999, Hamburg, Germany.
15. Yang, H., S. Khorrani, X. L. Dai. 1999. Applications of simulated annealing minimization technique to unsupervised classification of remotely sensed data. In: Proceedings of the IEEE International Geoscience and Remote Sensing Symposium (IGARSS'99), 1999, Hamburg, Germany.
16. Piper, J. (1992). Variability and bias in experimentally measured classifier error rates. Pattern Recognition Letters, 13, 685-692
17. Fody, G. M., 2002. Status of land cover classification accuracy assessment. Remote Sens. Environ. 80, 185-201.
18. Gallego (2004): Remote sensing and land cover area estimation, International Journal of Remote Sensing, 25:15, 3019-3047.

**ОЦЕНКА НА ЗЕМЕДЕЛСКИТЕ ПЛОЩИ ЧРЕЗ  
ПИКСЕЛНО-ОРИЕНТИРАНА КОНТРОЛИРАНА  
КЛАСИФИКАЦИЯ ВЪРХУ ИЗОБРАЖЕНИЕ НА EO-1 ALI  
ЗА ТЕСТОВИ УЧАСТЪК ЖИТЕН, РАЗПОЛОЖЕН  
В СЕВЕРОИЗТОЧНА БЪЛГАРИЯ**

***В. Василев***

***Резюме***

Целта на настоящият доклад е да се определят засетите площи със земеделски култури на основата на пикселно - ориентирана класификация върху тестови участък Житен, разположен в Североизточна България. Избрано е спътниково изображение заснето от спътника Earth Observation-1 със сензор ALI на 09.07.2011. Методологията в настоящето изследване включва следните етапи на работа: 1) прилагане на маска, включваща само обработваемите земи на територията за

изследване от базата данни на CORINE 2006 земно покритие; 2) провеждане на пикселно-ориентирана класификация по алгоритъма на максималното подобие с цел разпознаване на земеделските култури върху изображението; 3) прилагане на инструмента „оценка на точността“ в програмния продукт ERDAS Imagine и извличане на показателите обща точност и капа статистика от класифицираното изображение; 4) изчисляване на заетите площи по принципа на броя пиксели. Достигната обща точност на класификацията е 96.24 % и капа статистика от 0.9397. Високата обща точност е постигната чрез прецизен подбор на обучаващите множества включени в алгоритъма. Началото на месец юли може да се определи като идеален избор за разпознаване видовете пролетни култури (слънчоглед и царевица) и освен това за определяне на заетите площи за всички разпознати култури на основата на пикселно-ориентирана класификация с обща точност от над 95 %. Ограничението при проведеното изследване е, че по-времето на провеждането му (началото на месец юли) е трудно да се отделят по спектрални отражателни характеристики посевите на зимните култури.

## **SATELLITE HYPERSPECTRAL EARTH OBSERVATION MISSIONS - A REVIEW**

***Lachezar Filchev***

*Space Research and Technology Institute – Bulgarian Academy of Sciences  
e-mail: lachezarhf@space.bas.bg*

### ***Abstract***

*During the past 20 years the satellite hyperspectral earth observation missions proved their capability to provide critical information in numerous application areas as of military as of civilian origin. With the advancement of technologies for data acquisition, data storage, computation, and telemetry, it was made possible to decrease the cost of development of such systems and also to make them more readily available not only for scientific applications.*

*The article presents an overview of the past, present, and planned future hyperspectral remote sensing missions used for earth observation. The review revealed that the interest in developing such systems is growing continuously but is outpaced by the development of their airborne analogues. This is attributed to the fact that spatial and temporal resolution of the space systems is not competitive to the more readily deployed airborne (airplane or drone) hyperspectral systems.*

### **1. Introduction**

The ever growing demand for specific information for the remotest and inaccessible places on Earth, has driven the development of the satellite hyperspectral sensors. They come as successors of the multispectral sensors which were in development and operational use since the onset of the civilian space era with the launch of Earth Resources Technology Satellite-1 (ERTS-1, also known as Landsat 1 after renaming the program to *Landsat* in 1975) in 1972 (Landsat 1 History, 2014). Although the hyperspectral remote sensing systems provide markedly different capabilities for image acquisition they also introduce a whole new range of issues to be solved.



At present, there are many definitions of *hyperspectral imaging* or *imaging spectroscopy* (both terms are used interchangeably) but all of them could be narrowed down to the following two definitions.

The *imaging spectrometry* (or imaging spectroscopy) is defined as: ‘the simultaneous acquisition of spatially co-registered images in many spectrally contiguous bands’. *Hyperspectral (spectral) imaging* is defined also as imaging narrow contiguous spectral bands over a continuous spectral range, which produces the spectra of all pixels in the scene. In this sense a sensor with only 20 spectral bands each 10 nm wide can also be a hyperspectral when it covers the spectral range from 500 to 700 nm. The second definition for the hyperspectral imaging states is that a system is a hyperspectral if it acquires 40 or more narrow spectral bands (10÷20 nm) simultaneously (Van Der Meer and De Jong, 2006). However, the second definition with the threshold of 40 bands is only detailing the first one. Furthermore, the number of bands could not be a decisive for a system to be a hyperspectral since they can be few and scattered in farther parts of the spectrum where the absorption features of interest are located. The hyperspectral satellite systems can also be grouped according to the imager type, the acquisition type and other characteristics of the satellite itself into different groups which is not an objective of present study.

The hyperspectral satellite remote sensing systems for Earth observation are used primarily, but not limited to, to the following civilian applications: geology (mineralogy and mining activities), agriculture (crops identification, vegetation status, and stress), forestry (species identification and stress detection), and environmental monitoring (oceanic and land monitoring, coastal monitoring, and vegetation monitoring), security. However, the still developing hyperspectral technologies and the limited capabilities of the hardware and telemetry as well as the high volume of the hyperspectral sensors’ data, prevent their widespread and operational use.

The purpose of present study is not to provide a detailed classification of all the satellite hyperspectral imagers that have been flown in space but a review which later on can be built upon, debated, complemented, objected or even used as a basis for a more detailed investigation on the topic. The study does also aim specifically at Earth remote sensing satellite imagers since there are numerous examples used in studying the planets of the Solar system.

The main objective of the review is to study the developments of hyperspectral satellite missions for Earth remote sensing in the past decades until present and to study the future perspectives.

### *1.1. Early days*

The onset of satellite hyperspectral remote sensing era comparing to the explosive developments of their multispectral counterparts was slow. This may be explained with the fact that the technology for the first was slowly developing. The main reason for that could be chiefly attributed to the huge volume of spectral imaging data being stored onboard and the broadband telemetry which was not available at that time to downlink the data to Earth. Therefore the beginning of the hyperspectral satellite remote sensing era was hampered and started first with testing of non-imaging hyperspectral systems followed by the development of prototypes of airborne hyperspectral imagers. The airborne hyperspectral systems were the necessary step due to the limiting factor of limited data storage and telemetry capacity. About the time of first airborne systems the first software systems, such as *Spectral Analysis Manager (SPAM)* by Jet Propulsion Laboratory (JPL), for handling the big amounts of data were developed based on pioneering algorithms for information extraction.

One of the first non-imaging examples of hyperspectral remote sensing systems is the Bulgarian spectrometric system *SMP-32* launched onboard of Meteor-Priroda "Bulgaria-1300-II" satellite from Plesetsk on 7 August 1981. The instrument has 32 spectral bands ( $\lambda=457\div 888$  nm; 14 nm spectral resolution, 280 m) Ground Sampling Distance (GSD) (Serafimov, 1984; Ivanova, 2011). The gathered data is stored on two tape recorders, each with a capacity of 60 megabit. The main transmitter radiates 10 W in the 130 MHz band. The spectrometric system was developed at Space Research and Technology Institute at the Bulgarian Academy of Sciences (SRTI-BAS) (formerly the Space Research Institute at the BAS) and as its predecessors, i.e. *Spektar-15* which has 15 spectral bands flown on Salut-6 space station, is a non-imaging spectrometer (Serafimov, 1984). The principle of acquisition is of a whisk broom nadir-looking detector but without a scanning mechanism to reconstruct an image. The "INTERCOSMOS 22" satellite, which is carrying the instrument onboard, is still in orbit and is classified by NORAD under an ID 12645, Int'l Code NSSDC/COSPAR: 1981-075A (INTERCOSMOS 22, 2014). During the 80s of 20<sup>th</sup> century, based on the experience gained from the development of

*SMP-32*, the *Spektar-256* spectrometer was developed by SRTI-BAS and the Institute of Technical Cybernetics and Robotics at the BAS. The spectrometer was collecting the spectra in two modes: 1) 128 bands and 2) 256 bands, in the spectral range ( $\lambda=480\div810$  nm). It was actively used onboard of MIR space station for over 12 years (Getsov, 1999). The experiments onboard of MIR were carried out using jointly a topographic photo camera KATE-140 with the *Spektar-256* spectrometer. The camera frames were used to locate the GSD of the spectrometer in order to identify the land-cover type. For that purpose the pointing-mode instrument was affixed so that the GSD was positioned precisely at the center of the frame acquired by the KATE-140 camera. Some of the scientific experiments carried out with the instrument from Bulgarian scientists were: *Stara planina*, *Ocean*, *Contrast and Pollution*, *Colour and Colour Perception* with a principal investigator (PI): Acad. D. Mishev; *Trakia*, *Mizia* with a PI: Prof. H. Spiridonov (Mishev, 1986; Mishev and Dobrev, 1987; Getsov, 1999; Ivanova, 2011).

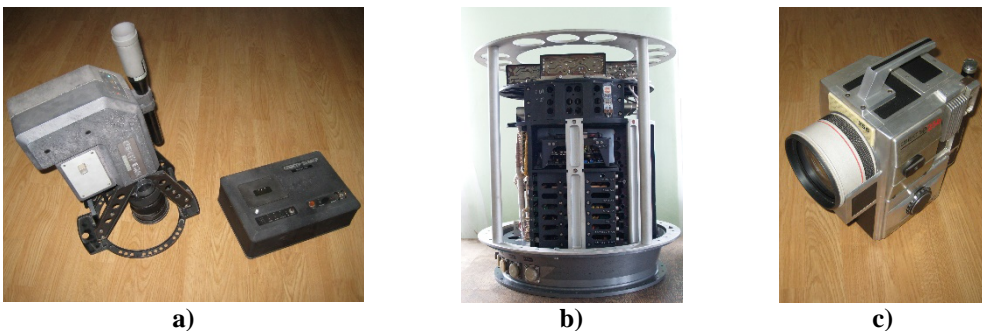


Fig. 1. a) *Spektar-15*; b) *SMP-32*, and b) *Spektar-256*  
(Photos courtesy: Prof. DSc G. Mardirossian)

### 1.2. Hyperspectral imagers

Before the beginning of the satellite era for the hyperspectral imagers there were at least 20 years of development of their aircraft equivalents. In the beginning of 1980s at the Jet Propulsion Laboratory (JPL) (Pasadena, CA) was developed the *Airborne Imaging Spectrometer (AIS)* (128 spectral bands,  $\lambda=1.2\div2.4$   $\mu\text{m}$ , 10 nm spectral resolution, 8 m SR). Later on, based on its legacy, NASA and JPL developed the *Airborne Visible/InfraRed Imaging Spectrometer (AVIRIS)* imaging spectrometer (224 spectral bands,  $\lambda=0.4\div2.45$   $\mu\text{m}$ , 10 nm spectral resolution, 11 m SR for

an 11 km × 11 km scene). The instrument was tested in 1987 and began operations in 1989 (Baret and Curtis, 1997; Campbell, 1996).

In the beginning of 90s of the 20<sup>th</sup> century NASA and TRW corporation co-developed a spectrometric system *HyperSpectral Imager (HSI)* for the mission *LEWIS*, which was designed to shoot in 128 bands in the spectral range  $\lambda=0.4\div 1\ \mu\text{m}$  and another 256 bands in  $\lambda=0.9\div 2.5\ \mu\text{m}$ , or in total 384 bands, Figure 2a (Van Der Meer and De Jong, 2006). The spectral resolution in both spectral ranges were respectively 5 nm and 6.5 nm, which comparing to the present-day satellite hyperspectral systems is still unravelled. Three days after the launch on 23 August 1997 the control of the satellite was lost and subsequently entered the Earth atmosphere in September 1997 (Lewis (SSTI 1), 2014).

Another imaging spectrometer developed by the U.S. Air Force Research Laboratory at that time was *Fourier Transform Hyperspectral Imager (FTHSI)* of *MightySat II* (Sindri P99-1) satellite, Figure 2b. The instrument was designed with 256 bands operating in the range  $\lambda=0.35\div 1.05\ \mu\text{m}$ . The satellite was launched on 19 July 2000 from VAFB, CA and re-entered the Earth atmosphere on 12 November 2002 with 100% mission success for FTHSI (Mightysat, 2014).



**a)** (image credit: NASA)

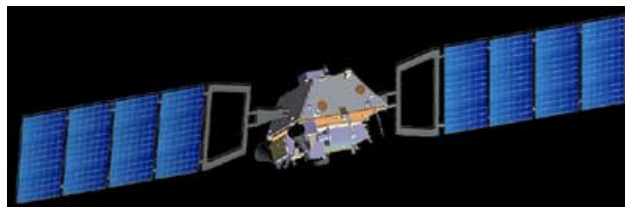


**b)** (image credit: General Dynamics)

*Fig. 2. a) An artist rendition of LEWIS in space and b) MightySat-II spacecraft without FTHSI instrument*

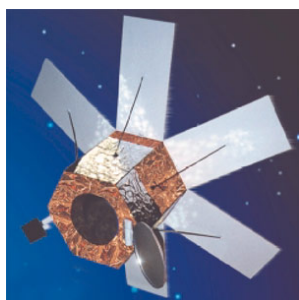
Another hyperspectral earth observation mission, which also was unsuccessful and developed by U.S. Air Force, was *Naval Earth Map Observer (NEMO)*, Figure 3. Unlike the existing hyperspectral satellite sensors, such as *EO-1/Hyperion* and *CHRIS/PROBA*, *NEMO* has a dual purpose of military and civil emergency. It was designed to carry on-board *Coastal Ocean Imaging Spectroradiometer (COIS)* instrument which was

designed to acquire images in the spectral range  $\lambda=400\div2\,500$  nm with a spectral resolution of 10 nm. The designed width of the scene was 30 km, with a pixel size of  $60\text{ m}\times 30\text{ m}$  SR. It featured also an improved Signal-to-Noise ratio (S/N ratio) compared to the previous similar systems such as *High Resolution Imaging Spectrometer (HIRIS)*. *NEMO* was planned for launch in 2000, but the program has been put on hold and subsequently cancelled (NRL to Develop Navy Earth Map Observer (NEMO), 1997; NEMO, 2014).

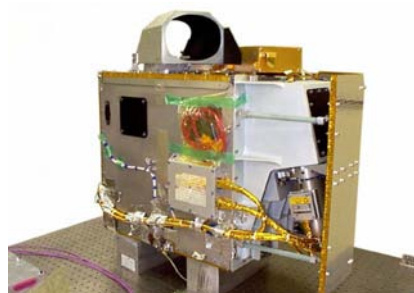


*Fig. 3. An artist rendition of NEMO in space*

The satellite *OrbView-4*, a.k.a. *Warfighter*, developed by Orbimage, was scheduled to have one panchromatic band with 1 m GSD, a multiband system with 4 m GSD and 200 bands in the spectral range  $\lambda=0.4\div2.5$   $\mu\text{m}$ , with 8 m GSD but for civil and scientific purposes the data was planned to be provided only as a resampled product with 24 m GSD, Figure 4a. *OrbView-4* had the ability to shoot at different angles - with a tolerance of  $\pm 45^\circ$  from nadir look angle. The *OrbView-4* was lost during a launch failure on September 2001 when the Taurus-2110 carrier rocket suffered a loss of control which was recovered but the orbit was not achieved (Boucher, 2001; *OrbView-4*, 2013).



**a)** (image credit: OSC)



**b)** (image credit: NASA)

*Fig. 4. a) An artist rendition of OrbView-4 in space, b) EO-1/Hyperion hyperspectral imager*

Only after the emergence of the new satellite platforms developed under the *New Millennium Program (NMP)* by National Aeronautics and Space Administration (NASA), such as Earth Observer-1 (NMP/EO-1), with the spectrometer *Hyperion* on board, and *PROject for OnBoard Authonomy (PROBA)*, with the hyperspectral instrument *Compact High Resolution Imaging Spectrometer (CHRIS)*, developed by the European Space Agency (ESA), launched in 1999 and 2001 respectively, the satellite imaging spectrometry for civil and scientific applications became possible (Van der Meer, de Jong, 2006).

The NMP/EO-1 mission carries on-board three radiometers: 1) the *Advanced Land Imager (ALI)* – a multispectral pushbroom radiometer with 1 panchromatic and 9 multispectral bands; 2) the *Hyperion* – an imaging spectroradiometer, Figure 4b; and 3) the *Linear Etalon Imaging Spectrometer Array (LEISA) - Atmospheric Corrector (LAC)*. The *EO-1/Hyperion* is a grating imaging spectrometer with a 30 m Ground Sampling Distance (GSD) and 7.7 km swath width. It provides 10 nm (sampling interval) contiguous bands of the solar reflected spectrum  $\lambda=400\div 2\ 500$  nm. The *LAC* is an imaging spectrometer operating in the spectral range  $\lambda=900\div 1\ 600$  nm, which was suited for the EO-1 Science Validation Team to monitor the atmospheric water absorption lines for correction of atmospheric effects in multispectral imagers during the first year of the mission (Beck, 2003; EO-1, 2013; Earth Observing 1 (EO-1) Sensors, 2014).

The *CHRIS/Proba* imaging spectrometer objective is the collection of Bidirectional Reflectance Distribution Function (BRDF) data for a better understanding of spectral reflectance, Figure 5 (PROBA instruments, 2014). The *PROBA* mission carries onboard also a panchromatic camera HRC, a miniaturized telescope of Cassegrain type with an aperture size of 115 mm and a focal length of 2 296 mm, which can acquire images with an area of 25 km<sup>2</sup> with a 5/8 m GSD. The *CHRIS* was flown onboard of the PROBA-1 satellite, in 2001 (Figure 3). The *CHRIS* instrument provides 18 spectral bands in Mode 2, 3, and 4 and 37 spectral bands in Mode 5 in the VNIR range ( $\lambda=415\div 1\ 050$  nm) at a GSD of 17 m. CHRIS can be reconfigured to provide 63 spectral bands (the instrument is fully programmable to up to 150 bands) at a GSD of about 34 m in Mode 1 (PROBA-1/CHRIS, 2014). Each nominal image forms a square sized scene (13 km × 13 km) at perigee. Each scan is executed at different view angles (-55°, -36°, 0°, 36°, and 55°), 5 consecutive pushbroom scans by the single-line array detectors, to the

target within a  $55^\circ$  cone centred at the target zenith (PROBA Instruments, 2014). The mission is in now in extended mode and offers only to registered users, Category-1 Proposals using Third Party Mission (TPM) data, tasking and archived images from ESA's image archive.

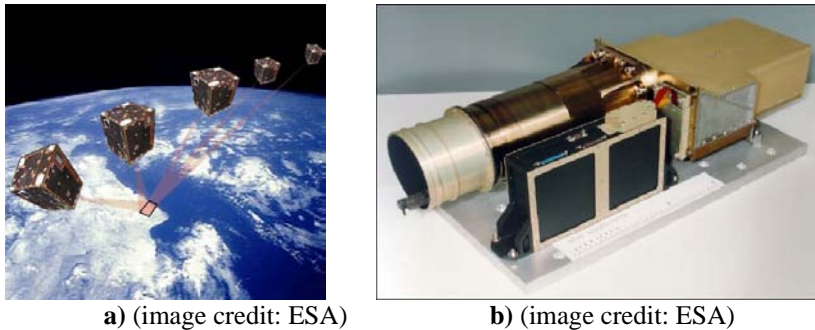


Fig. 5. a) Artist rendition of CHRIS/PROBA multi-angle acquisitions and b) CHRIS/PROBA instrument

In the late 80s and early 90s of 20<sup>th</sup> century within the *Earth Observing System (EOS)* Programme of NASA were planned two hyperspectral instruments, *High Resolution Imaging Spectrometer (HIRIS)* and *Moderate Resolution Imaging Spectrometer-Nadir (MODIS-N)*. The *High Resolution Imaging Spectrometer (HIRIS)* was designed to capture 192 bands with a spectral resolution of  $\lambda=9.4\div 11.7$  nm (nominal 10 nm) in different areas of the electromagnetic spectrum in the range  $\lambda=0.4\div 2.5$   $\mu\text{m}$  (Dozier, 1988). The swath width was 30 km with 30 m SR and a viewing area of 25 off track and  $+60/-30$  in track (Barrett and Curtis, 1997). If we compare *HIRIS* with the successful *EO-1/Hyperion* mission it can be easily seen that *EO-1/Hyperion* bears some of this instrument characteristics.

Within the EOS program, which provides for developing of several satellites EOS designed for 15 years of work, the *MODIS* instrument was launched on board of EOS-AM1 satellite, Figure 6a. It began operation on February 2000. The *MODIS* covers a swath width of 2 300 km, with almost daily acquisition, running in 36 bands in the spectral range  $\lambda=0.4\div 14.4$   $\mu\text{m}$ . Two bands have a SR of 250 m (VNIR), five bands 500 m SR, and the remaining feature 1 000 m SR (Kramer, 2002).

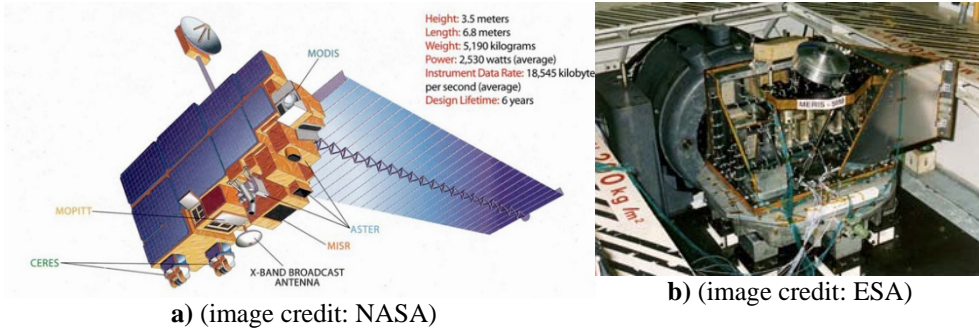


Fig. 6. a) An artist rendition of EOS-AM 1 (Terra) with the instruments on-board and b) MERIS in the testing facilities of ESA

Another example of a hyperspectral imaging system is the 14-band *Advanced Spaceborne Thermal Emission and Reflection Radiometer (ASTER)*, working on the same satellite as MODIS, Figure 6a. It was developed jointly by a US-Japanese group and is with less revisit capabilities (60 km), but features a better SR. Three bands in the VIS range have a SR of 15 m (spectral resolution of 6-10 nm), 6 bands in the NIR are with 30 m SR and 5 bands in the TIR - with 90 m SR (ASTER, 2014).

The European analogue of MODIS, but primarily oriented towards ocean studies, was *MEDium Resolution Imaging Spectrometer (MERIS)* onboard of ENVISAT, Figure 6b. MERIS provided regular acquisitions until the ENVISAT stopped transmitting data in 2012. The imager consisted of 15 band system, operating in the VIS and the NIR ranges ( $\lambda=390\div1040\ \mu\text{m}$ ) with  $300\div1200\ \text{m}$  SR. The 7-band AATSR system, also onboard of ENVISAT, acquired with a 1 km SR in the VS, NIR, and TIR spectra, which allowed solving the problem of monitoring the concentration of phytoplankton biomass of vegetation, surface temperature of the water and the land (MERIS, 2014).

The planned *Australian Resource Information and Environment Satellite (ARIES)* was designed to cover the visible (VIS) and near IR spectral (NIR) range (or VNIR)  $\lambda=400\div1\ 050\ \text{nm}$ , spectral sampling 20 nm, and subsequent continuation in Short Wave InfraRed (SWIR-2) spectral range  $\lambda=2000\div2\ 500\ \text{nm}$  with a minimum distance of 16 nm between bands, for a total of 105 bands at 30 m SR for a swath of 15 km (Roberts et al. 1997; Merton, Huntington, 1999; Van der Meer, de Jong, 2006; ARIES, 2009). The instrument was also envisaged to acquire scenes between  $\pm 30^\circ$  which give it a multi-angle acquisition capability similarly to the German's



EnMap satellite. Even though the concept of the mission was of a good standing it was cancelled.

The *Hyperspectral Imager for the Coastal Ocean (HICO)* camera on board of International Space Station (ISS) is part of the *HICO* and RAIDS Experiment (HREP-HICO). This instrument is currently flown onboard of the ISS since 2009, to study the composition of water and land along the coasts. Each scene covers an area of about 48 km × 200 km, which captures features like river outflow plumes or algae blooms, and lets scientists do environmental characterization of coastal regions (HREP-HICO, 2014). Only in 2009 the instrument acquired more than 1700 images with 95m<sup>2</sup> GSD.

### 1.3. Future missions

Within the *Environmental Mapping and Analysis Program (EnMap)*, a mission of DLR, is prepared the *HyperSpectral Imager (HSI)* instrument, Figure 7. Designed to record bio-physical, bio-chemical and geo-chemical variables on a global basis and thus, to increase the understanding of biosphere/geosphere processes and to ensure the sustainability of our resources (EnMap, 2013). It is also a new generation of hyperspectral imager which offers a multi-angle acquisitions in ±30° off nadir, see Table 1 for mission characteristics.

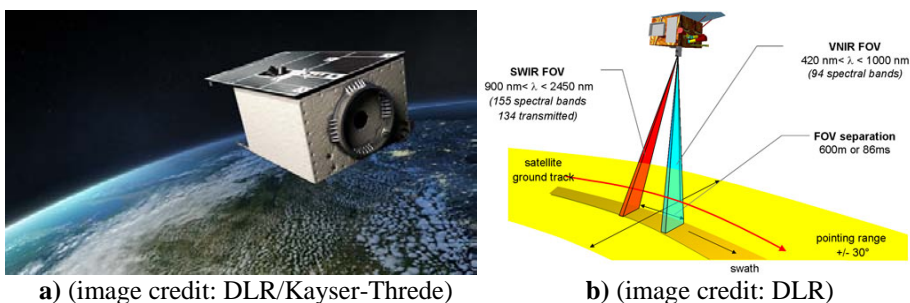
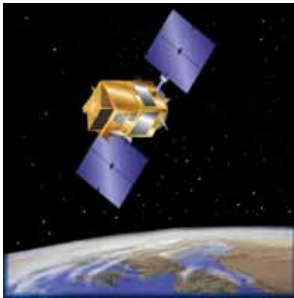


Fig. 7. a) An artist rendition of EnMap in space, and b) EnMap satellite ground track with acquisition modes

The mission of *Hyperspectral Infrared Imager (HyspIRI)* satellite, see Figure 8b, will be to be used to study the world's ecosystems and provide critical information on natural disasters such as volcanoes, wildfires, and drought, i.e. similarly to what the *EO-1/Hyperion* is used for in its Extended Mission. The imaging spectrometer will be acquiring its

images in the spectra range from the VIS to SWIR ( $\lambda=380\div 2\ 500$  nm) in 10 nm narrow contiguous bands along with a multispectral imager acquiring from 3 to 12  $\mu\text{m}$  in the mid and thermal infrared (TIR) (HyspIRI, 2013).



a) (image credit: IOCCG)



b) (image credit: JPL-CalTech)

Fig. 8. Artist renditions of a) ARIES and b) HyspIRI in space

The *Infrared Atmospheric Sounding Interferometer (IASI)*, is a Michelson Interferometer, and according its very narrow bands of acquisitions it belongs to the ultraspectral imagers. It measures the spectral distribution of the atmospheric radiation, is a key payload element of the MeTop series of European meteorological polar-orbit satellites. Developed jointly by Centre National D'Études Spatiales (CNES) and EUMETSAT it was flown onboard of the meteorological satellite MeTop-A in 2006 and MeTop-B in 2012 (IASI – the project main steps, 2014). The last one of series is to be launched on MeTop-C in 2015-2016, see Table 1. Its main purpose of the instrument is to temperature, moisture and trace gases across the atmospheric column (Bioucas-Dias et al 2013).

The most recent *PRISMA (PREcursor IperSpettrale of the application mission)* mission, developed by the Italian Space Agency (ASI), is scheduled for launch by the end of 2015, see Table 1.

The Canadian Aerospace Agency (CAA) is also developing its own hyperspectral satellite mission *Hyperspectral Environment and Resource Observer (HERO)*, which is designed to be used on an operational basis, see Table 1 (Jolly et al 2002; Buckingham et al 2002).

The *VEN $\mu$ S (Vegetation and Environment monitoring on a New Micro-Satellite)* mission is jointly developed by CNES and Israeli Space Agency (ISA) and is expected to be launched and operational in 2016. The VEN $\mu$ S scientific objective is the provision of data for scientific studies

dealing with the monitoring, analysis, and modelling of land surface functioning under the influences of environmental factors as well as human activities (Vegetation and Environment monitoring on a New Micro-Satellite, 2014).

Last but not least, it is important to note the emergence of some commercial mixed-type multi- and hyperspectral systems such as WorldView-2 and WorldView-3, which bear some of the characteristics of hyperspectral systems, such as narrow bands dedicated to specific application studies, such as ocean colour and vegetation stress (WorldView-2, 2014; WorldView-3, 2014).

## **2. Future prospects**

The review of the development of the past, contemporary, and planned future hyperspectral satellite systems for Earth observation revealed that the interest in developing such systems is growing steadily. However at present the developments of space systems are outpaced by the development of their airborne analogues. This is attributed due to the fact that the spatial scale of the area covered as well as the temporal resolution of the space systems is not competitive to the more readily deployed airborne (airplane or drone) systems. The relatively higher costs, necessary human capital, and facilities to develop and deploy into orbit and to maintain a hyperspectral satellite remote sensing system are still decisive factors for the observed phenomenon. Nevertheless, there are some signs that some leading space agencies, such as CAA and ASI, are taking steps to use the hyperspectral satellite systems on an operational basis.

## **3. Acknowledgements**

The author is deeply appreciated to all that helped him to carry out this study. Special thanks to Prof. DSc G. Mardirossian for providing photos of the *Spektrar-15*, *SMP-32*, and *Spektar-256* spectrometers. All the used photos, figures, and renditions of satellites in space are copyright of the respective owners.

Table 1. A comparative table for the main sensor and satellite characteristics of some past, present, and planned future satellite hyperspectral remote sensing missions for Earth observation (Sources: Kramer, 2002; Ward, 2012 with modifications)

Main characteristics	EO-1/Hyperion (NASA) <sup>*</sup>	HL-1/HIS (CAST) <sup>*</sup>	PROBA/CHRIS (ESA) <sup>*</sup>	Sambandhasat ZASat/ISI (S. Africa Sun Space) <sup>*</sup>	ARTEMIS (US Air Force) <sup>**</sup>	METOP-SG/LAST <sup>†</sup> (CNES/EUMETSAT)	Enlapp (DLR/OHB Systems) <sup>**</sup>	PRISMA/HYC (ASI) <sup>**</sup>	HypRI (NASA) <sup>**</sup>	ARIES (CSIRO) <sup>**</sup>	Venus <sup>**</sup> (CNES & Ben Gurion State University)	HERO (CASI) <sup>**</sup>
Spectral range (°)	VIS, NIR & SWIR 0.4-2.5 µm (123 bands)	VIS & NIR 0.4-2.5 µm (123 bands)	VIS & NIR 0.415-1.05 µm (5-12 nm) 1,200 SN	VIS, NIR & SWIR 0.44-2.35 µm (-10 nm)	VIS, NIR & SWIR 0.4-2.5 µm (64 bands) (0.5 cm <sup>-1</sup> )	VIS & NIR 0.42-1.03 µm (5-10 nm) NIR & SWIR 0.9-2.5 µm (10-20 nm)	VIS & NIR 0.4-0.9 µm (0.4-1 µm) NIR & SWIR 0.9-2.5 µm (10-20 nm)	VIS, NIR & SWIR 0.38-2.5 µm 7.5-12 µm (4-12 µm)	VIS, NIR & SWIR 0.4-2.5 µm (4-12 µm)	VIS, NIR & SWIR 0.4-2.5 µm (4-12 µm)	VIS & NIR 0.415-0.91 µm	VIS, NIR & SWIR 0.4-2.5 µm (10 nm)
Panchromatic band	-	-	1	-	-	-	-	-	-	1	-	-
VIS bands (380-700 nm)	35	3	15	-	-	89 (0.42-1 µm)	30	-	-	0.4-1.0 µm	8	-
NIR bands (750-1400 nm)	35	2	4	-	-	89 (0.42-1 µm)	30	-	-	1.0-2.0 µm	4	-
SWIR bands (1.4-3 µm)	172	1	0	-	-	155 (0.9-2.5 µm)	160	-	-	2.0-2.5 µm	-	-
MIR bands (3-8 µm)	0	1	0	-	-	0	0	-	-	-	-	-
LWIR bands (8-15 µm)	30	10; 140 (30); 140	1837/63 (150)	15	5	-	0	0	-	-	-	-
Spatial resolution (m)	7.5	360; 720 / 30	14	-	-	V: 1.2 km H: 15 km	30	30	60	10 (µm) 30 (hyper) 15 (ar radar)	5.1 (radar)	30
Swath (km)	705	649	556	564	-	817	653	614/720	626	500	27.5	~700
Altitude (km)	cont. 16 bit 220; (242)	136	19-63	200	400	8461 (1621)	discrete	discrete	discrete	discrete	discrete	discrete
Radiometric resolution	1	2	1	1	1	213	1	1	1	105	12	2-200
No of bands	200	31	2 (mid bandwide)	-	-	27 (VZA5°) 4 (VZA50°)	29	29	519	7	2 (±30° view mode)	3
Temporal resolution (days)	2111/2000	5/09/2008	22/10/2001	17/09/2009	-	2020-2021	-	end of 2015	-	-	2016	-
Launch date	1 <sup>†</sup>	≥3	2	≥3	-	5 (METOP) 8.5 (METOP-SG)	5	-	-	-	3.5	5
Lifetime (Years)	98.21 <sup>*</sup>	97.55 <sup>*</sup>	97.9 <sup>*</sup>	98 <sup>*</sup>	-	98.704 <sup>*</sup>	97.56 <sup>*</sup>	98.15 <sup>*</sup>	-	-	98.27 <sup>*</sup>	-
Orbit Inclination	-	-	-	-	-	-	-	-	-	-	-	-

<sup>†</sup> Calibrated bands  
<sup>‡</sup> An Extended Mission  
<sup>\*</sup> ongoing mission  
<sup>\*\*</sup> planned mission

## References

1. ARIES, 2009. URL: <http://www.ioccg.org/sensors/aries.html> (date accessed: 10 June 2014)
2. ASTER, 2014. URL: <http://asterweb.jpl.nasa.gov/> (date accessed: 10 June 2014)
3. Barrett, E. C. and L. F. Curtis, 1997. Introduction to Environmental Remote Sensing. 3<sup>rd</sup> ed., Singapore, Chapman & Hall.
4. Bioucas-Dias, J. M., A. Plaza, G. Camps-Valls, P. Scheunders, N. M. Nasrabadi, and J. Chanussot, 2013. Hyperspectral Remote Sensing Data Analysis and Future Challenges. *Geoscience and Remote Sensing Magazine, IEEE*, 1(2), pp. 6–36. ISSN: 2168-6831. DOI: <http://dx.doi.org/10.1109/MGRS.2013.2244672> (date accessed: 10 June 2014)
5. Beck, R. 2003. EO-1 User Guide, University of Cincinnati: 74 p.
6. Bucher, T., 2001. Taurus Launch ends in Failure, URL: <http://www.spaceref.com/news/viewnews.html?id=389> (date accessed: 10 June 2014)
7. Buckingham, R., Staenz, K., Hollinger, A., 2002. Review of Canadian Airborne and Space Activities in Hyperspectral Remote Sensing. *Canadian Aeronautics and Space Journal*, 48(1), pp. 115–121.
8. Campbell, J. B., 1996. Introduction to Remote Sensing, 2<sup>nd</sup> ed., Taylor & Francis, London.
9. Dzier, J. HIRIS - The High Resolution Imaging Spectrometer. In: *Proceedings SPIE 0924, Recent Advances in Sensors, Radiometry, and Data Processing for Remote Sensing*, 23 (October 12, 1988); doi:10.1117/12.945667
10. EO-1, Enhanced Formation Flying (EFF), 2013. URL: <http://eo1.gsfc.nasa.gov/new/Technology/FormFly.html> (date accessed: 10 June 2014)
11. Earth Observing 1 (EO-1) Sensors, 2014. URL: <http://eo1.usgs.gov/sensors> (date accessed: 10 June 2014).
12. EnMap, 2013. <http://www.enmap.org/> (date accessed: 24 June 2014).
13. EnMap (Environmental Monitoring and Analysis Program), 2013. URL: <https://directory.eoportal.org/web/eoportal/-/enmap> (date accessed: 10 June 2014).
14. Getsov, P., 1999. Scientific-Technical Programme of the Second Bulgarian-Russian Space Flight, the SHIPKA Project: major objectives, tasks, and results, In: 10 Years Space Project “Shipka”, SRI-BAS. (in Bulgarian)
15. HICO and RAIDS Experiment Payload - Hyperspectral Imager for the Coastal Ocean (HREP-HICO), 2014. URL: [http://www.nasa.gov/mission\\_pages/station/research/experiments/689.html](http://www.nasa.gov/mission_pages/station/research/experiments/689.html) (date accessed: 10 June 2014).
16. HypSIRI Homepage, 2013. HypSIRI Mission Study, URL: <http://hypsiri.jpl.nasa.gov/> (date accessed: 10 June 2014).
17. Infrared Atmospheric Sounding Interferometer (IASI), 2014. URL: <http://smsc.cnes.fr/IASI/> (date accessed: 10 June 2014).
18. INTERCOSMOS 22, 2014. URL: <http://www.n2yo.com/?s=12645> (date accessed: 10 June 2014).
19. Ivanova, T. 30 Years "BULGARIA-1300" Satellites, In: *Proceedings of Seventh Conference with International Participation Space, Ecology, Safety (SES) 2011*, 29 November – 1 December 2011, Sofia, Bulgaria, pp. 9–16.
20. Jolly, G. W., Rowlands, N., Staenz, K., Hollinger, A., 2002. A Canadian Spaceborne Hyperspectral Mission. In: *Proceedings of International Geoscience and Remote Sensing Symposium*, Toronto, Ontario, Canada, pp. 967–969.
21. Kramer, H., 2002. *Observation of the Earth and its Environment*, 4th ed. 2002, pp. 1514. Springer Verlag, ISBN: 3-540-42388-5

22. Landsat 1 History, URL: [http://landsat.usgs.gov/about\\_landsat1.php](http://landsat.usgs.gov/about_landsat1.php) (date accessed: 10 June 2014).
23. Lewis (SSTI 1), 2014. URL: [http://space.skyrocket.de/doc\\_sdat/lewis.htm](http://space.skyrocket.de/doc_sdat/lewis.htm) (date accessed: 10 June 2014).
24. MERIS, 2014. URL: <https://earth.esa.int/web/guest/missions/esa-operational-eo-missions/envisat/instruments/meris> (date accessed: 10 June 2014).
25. M i s h e v, D. N. and T. B. D o b r e v, 1987. Remote Sensing Methods in Geophysics and Geology – Aerospace Methods for Studying the Earth. Sofia, Technica. (in Bulgarian)
26. M i s h e v, D. Spectral Characteristics of Natural Objects, Publishing House Bulgarian Academy of Sciences, Sofia, 1986, 150 p.
27. Mightysat, 2014. URL: <https://directory.eoportal.org/web/eoportal/satellite-missions/m/mightysat> (date accessed: 10 June 2014).
28. M e r t o n, R. and H u n t i n g t o n, J., 1999. Early simulation results of the ARIES-1 satellite sensor for multi-temporal vegetation research derived from AVIRIS. In: Proceedings of the 8<sup>th</sup> Annual JPL Airborne Earth Science Workshop, pp. 8–14: NASA, JPL Pasadena, CA.
29. NEMO, 2013. [http://space.skyrocket.de/doc\\_sdat/nemo.htm](http://space.skyrocket.de/doc_sdat/nemo.htm) (date accessed: 10 June 2014).
30. NRL to Develop Navy Earth Map Observer (NEMO), 1997. URL: <http://www.nrl.navy.mil/media/news-releases/1997/nrl-to-develop-navy-earth-map-observer-nemo> (date accessed: 10 June 2014).
31. P e a r l m a n, J., C. S e g a l, L. B. L i a o, S. L. C a r m a n, M. A. F o l k m a n, W. B r o w n e, L. O n g, S. G. U n g a r. Development and Operations of the EO-1 Hyperion Imaging Spectrometer. SPIE 4135, Earth Observing Systems V, 243, 2000, 11.
32. PROBA, Instruments, 2014. URL: <https://earth.esa.int/web/guest/missions/esa-operational-eo-missions/proba/instruments> (date accessed: 10 June 2013).
33. PROBA-1/CHRIS, 2014. URL: <https://earth.esa.int/web/guest/-/proba-chris-level-1a-1488> (date accessed: 24 August 2014).
34. R o b e r t s, E., B o l d i n g, G., B u n d y, D., D o u g a n, S., F r a n z e n, R., H a r k n e s s, L., P e t k o v i c, M., P f i t z n e r, L., and R u t t e n, D. The Australian Resource Information and Environment Satellite (ARIES), Phase A Space Segment Study. In: National Space Engineering Symposium (11th: 1997: Sydney, N.S.W.). 11<sup>th</sup> National Space Engineering Symposium: Proceedings, The. Barton, ACT: Institution of Engineers, Australia, 1997: 13-19. National conference publication (Institution of Engineers, Australia); no. 97/01. (URL: <http://search.informit.com.au/documentSummary;dn=211105285378437;res=IELENG> ISBN: 0858256681).
35. Orbview-4, 2013. [http://space.skyrocket.de/doc\\_sdat/orbview-4.htm](http://space.skyrocket.de/doc_sdat/orbview-4.htm) (date accessed: 24 August 2014).
36. S e r a f i m o v, K. B. Bulgarian space activity. Advances in Space Research, 3(10–12), 1984, 1–6. DOI: [http://dx.doi.org/10.1016/0273-1177\(84\)90052-8](http://dx.doi.org/10.1016/0273-1177(84)90052-8)
37. SumbandilaSat - formerly ZASat-002 (South African Satellite), 2014. URL: <https://directory.eoportal.org/web/eoportal/satellite-missions/s/sumbandilasat#foot17%29> (date accessed: 24 August 2014)
38. Vegetation and Environment Monitoring on a New Micro-Satellite, 2014. URL: <http://smc.cnes.fr/VENUS/> (date accessed: 24 August 2014).
39. V a n D e r M e e r, F. and S. M. d e J o n g, 2006. Imaging Spectrometry: Basic Principles and Prospective Applications, Springer, 403 p.
40. W a r d, S., 2012. CEOS, The Earth Observation Handbook, ESA, SP-1325. ISBN 978-92-9221-423-4

41. WorldView-2, 2014. URL: <https://eoportal.org/web/eoportal/satellite-missions/v-w-x-y-z/worldview-2> (date accessed: 24 August 2014)
42. WorldView-3, 2014. URL: <https://eoportal.org/web/eoportal/satellite-missions/v-w-x-y-z/worldview-3> (date accessed: 24 August 2014)

## **РАЗВИТИЕ НА СПЪТНИКОВИТЕ СПЕКТРОМЕТРИЧНИ ДИСТАНЦИОННИ ИЗСЛЕДВАНИЯ – ОБЗОР**

*Л. Филчев*

### **Резюме**

В настоящата статия е направен обзор на миналите, настоящи и някои планирани бъдещи спектрометрични спътникови системи за дистанционно наблюдение на Земята. През последните 20 години системите за спектрометричните спътникови системи за наблюдение на Земята се установиха, като надежден източник на информация в множество приложни области, както с военно, така и гражданско предназначение. С напредването на технологиите за събиране, пренос и съхраняване на данни, стана възможно да се намалят разходите за развитие на спектрометричните спътникови системи, а също и да станат по-достъпни извън техните строго научни приложения. Направена е сравнителна характеристика на съществуващите спектрометричните спътникови системи и са дискутирани тенденциите в развитието им.

## **DEVELOPMENT OF THE EXPERIMENTAL MULTIROTOR UNMANNED AERIAL VEHICLE HELICOPTER MODELS OF THE XZ-SERIES**

*Svetoslav Zabunov, Peter Getsov, Garo Mardirossian*

*Space Research and Technology Institute – Bulgarian Academy of Sciences  
e-mail: s14@ialms.net*

### ***Abstract***

*In a large number of cases, depending on the aims and tasks of the remote Earth sensing experiment, the usage of airplane and helicopter flying laboratories is economically well-founded. On the other hand, surveys of dangerous areas are often needed (wildfires, radiation accidents, explosion hazard facilities, etc). In all those cases it is expedient to use unmanned aerial vehicles (UAVs). During the last few years, the radio controlled UAVs have gained large prominence, specifically the multirotor helicopters have established themselves as the standard surveying and research flying platforms. They are predominantly used for the purpose of remote sensing studies.*

*In the current article, authors have presented the benefits of the unmanned multirotor helicopters, designed for remote sensing applications of specific areas of the Earth surface. The idea and realization of three new models of multirotor helicopters from the XZ-series are disclosed. The major technical and operational capabilities are analyzed and diagrams of the avionics of the discussed models are shown. Special attention is devoted to the airframes. The implementation of the XZ-series helicopters in projects developed in Space Research and Technology Institute at the Bulgarian Academy of Sciences is discussed. Mainly, attention is drawn to the National Aerospace System for remote sensing of the Earth in the context of its usage for monitoring and protection from natural disasters.*

### **Introduction**

In some cases, for the purpose of remote sensing over test areas and firing grounds, it is necessary to obtain photographs from low altitude (10–



100 m) and scale in the order of 1:500 or 1:700. The area covered by such photographs may be in the order of several hundred to several tens of square meters. The utilization of aircraft and helicopter laboratories in such cases is economically feasible. In other cases, remote sensing surveys over dangerous in radiation or other sense areas, large fire zones, explosive hazardous depots and so on are required. In all those cases it is recommended that unmanned aerial vehicles (UAVs) are being used, also called remote controlled or radio controlled flying models. It is possible to engage specifically designed for the above purposes UAVs or general purpose models.

During the last few years, the radio controlled UAV multirotor helicopters become more and more topical as research and mainly as remote sensing platforms. These helicopters are distinguished with lowered complexity low price and small dimensions. Particularly appreciable benefits in comparison to the classic small helicopters are the absence of cyclic and collective pitch control of the rotor blades. This fact extremely simplifies the design and thus lowers the initial cost of the system and at the same time reduces the maintenance costs of such a multirotor helicopter, while the probability for a catastrophic crash is lowered. Another benefit is the lower rotors diameter of the multirotor helicopters in comparison to the classic small helicopters with only one rotor. Thus, the kinetic energy in any of the rotors of the multirotor helicopter is considerably lower than the energy in the single rotor of the classic small helicopter. The latter feature increases safety during operation of the multirotor helicopters. Furthermore, some small multirotor helicopters have frames around their propellers in order to increase even more the safety of operation.

Different designs and configurations have been developed: with two propellers, with three propellers and so on. Most common are the four-rotor helicopters, because this number of rotors is the minimal number that ensures full control without the need of additional control surfaces or rotor tilt mechanisms.

Table 1 discloses representative models of UAV helicopters with one or several rotors.

*Table 1*

Name	Country of manufacture	Rotor number	Propulsion	Optimum payload, kg	Total weight, kg	Service ceiling, km
Black Hornet Nano	Norway	1	Electrical	0.005	0.016	0.030
XZ-1	Bulgaria	4	Electrical	0.2	0.8	4.0
XZ-2	Bulgaria	8	Electrical	0.4	1.6	5.0
ARF MikroKopter	Germany	8	Electrical	1.4	5.0	4.0
Skeldar V-150	Sweden	1	I.C.E.	55	150	3.5
Parrot AR.Drone	France	4	Electrical	0.5	2.3	2.4
INFOTRON IT180 UAV	France	2	I.C.E.	5.0	19.0	3.0
БИЛИА ZALA 421-22	Russia	8	Electrical	2.0	8.0	1.0
Honeywell RQ-16 T-Hawk	USA	1	I.C.E.	2.0	8.4	3.2

### **Unmanned helicopters of the XZ-series**

The XZ-series occupies a competitive place among the modern UAV helicopters. The models in the series encompass a number of innovations in the avionics features and components as well as in the design of the airframe. The first member of the series is XZ-1. This is a four-rotor helicopter, meant as a test bed during the development of the MotorA motor controller series from version 1.0 to version 5.0 and the Z-Pilot v1.0 autopilot. XZ-1 is a proof of concept of certain innovations such as the patented technology battery unit BatA. The general appearance of XZ-1 is shown on Fig. 1.



*Fig. 1. General view of XZ-1*

Fig. 2 presents the airframe plan of XZ-1, which is in the well-known “H”-configuration. The benefits of this configuration exceed its drawbacks and for this reason the given design was used in the first model of the series. The benefits of the “H”-design toward the classic “X”-design follow:

1. The inevitable torsion and bending of the airframe is beneficiary, because it happens mainly during yaw orientation change. This torsion accelerates the yaw motion in the desired direction and increase the efficiency of the yaw orientation change process.

2. “H”-airframe offers a fuselage where on lots of modules may be easily installed.

3. First person view video camera (FPV) is attached to one end of the fuselage and is not “shadowed” by the propellers.

4. The moment of inertia along the pitch axis is increased thus making the helicopter more stable.

5. “H”-airframe guarantees counter rotation for each tandem of rotors, mounted at the ends of any of the two rotor beams. The opposite direction of rotation causes the gyroscopic effects of the two rotors on one beam to cancel out in contrast to “X”-airframe where both propellers on each beam are rotating in one and the same direction causing strong unwanted gyroscopic effects.

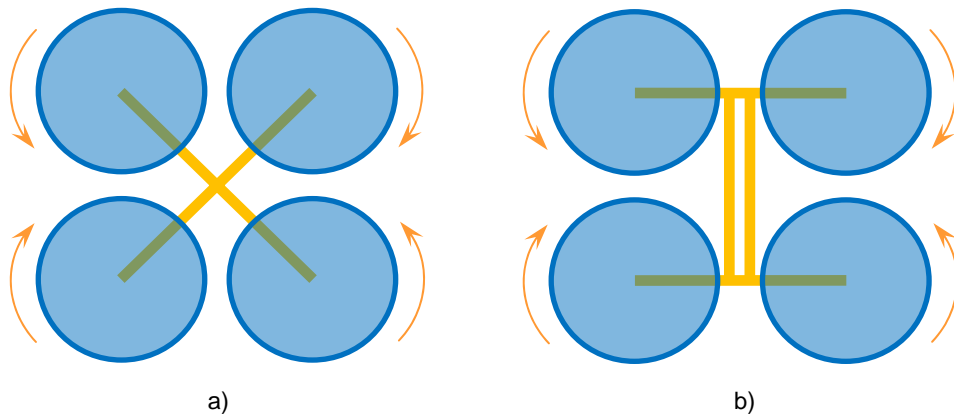


Fig. 2. a) Classic four-rotor helicopter in “X”-configuration also called “cross” or „star”; b) XZ-1 is based on the “H”-configuration also called “fuselage”

Drawbacks of the “H”-airframe toward the “X”-airframe:

1. “H”-airframe is heavier with about 10% compared to “X”-airframe with the same rigidity due to the presence of fuselage and the larger distance between the propellers.
2. “X”-airframe is simpler to manufacture.

### Technical characteristics of XZ-1

The main characteristics of XZ-1 are demonstrated in table 2.

*Table 2*

Type	Experimental
Number of rotors	4
Propulsion	Electrical
Energy source	Electric battery
Total mass	0.8 kg
Payload	0.2 kg
Service ceiling	4 km
Autopilot system	<ol style="list-style-type: none"> <li>1. Z-Pilot v1.0</li> <li>2. Autopilot sensor unit SensorA v1.0 Includes: <ul style="list-style-type: none"> <li>• Gyroscope</li> <li>• Accelerometer</li> <li>• Magnetometer</li> <li>• Barometer</li> <li>• Thermometer</li> </ul> </li> <li>3. GPS unit</li> </ol>
Payload	<p>Additional sensor unit SensorB v1.0 Includes:</p> <ul style="list-style-type: none"> <li>• Thermometer</li> <li>• Moisture meter</li> <li>• Ionizing radiation meter (beta and gamma)</li> <li>• Non-ionizing radiation meter</li> <li>• Gas sensors (CH<sub>4</sub>, SO<sub>2</sub>, CO<sub>2</sub>, H<sub>2</sub>S, O<sub>2</sub>, NH<sub>3</sub>, etc)</li> </ul>
Motor controllers	MotorA v5.0
Patented innovations	Battery block BatA v1.0

Diagram of the helicopter avionics is presented in Fig. 3. Special attention is drawn to the motor controllers. One motor controller drives two motors, placed at the ends of a beam in the helicopter airframe. Two

controllers are used. The latter are connected to the autopilot using digital interface. The communication protocol allows starting, stopping and power control based on a rich set of parameters. Autopilot receives information from the motor controllers about the rotations per minute, the used power, etc. The helicopter orientation is calculated through sensors, placed in the main autopilot sensor board SensorA. Unit DistanceA serves to calculate the distance to ground and near objects. To the autopilot are attached several other modules: light signal unit, GPS, radio transceiver and payload. The payload of XZ-1 is 200 gr and consists of additional sensor unit SensorB. The payload of XZ-1 is 200 gr and consists of additional sensor unit SensorB.

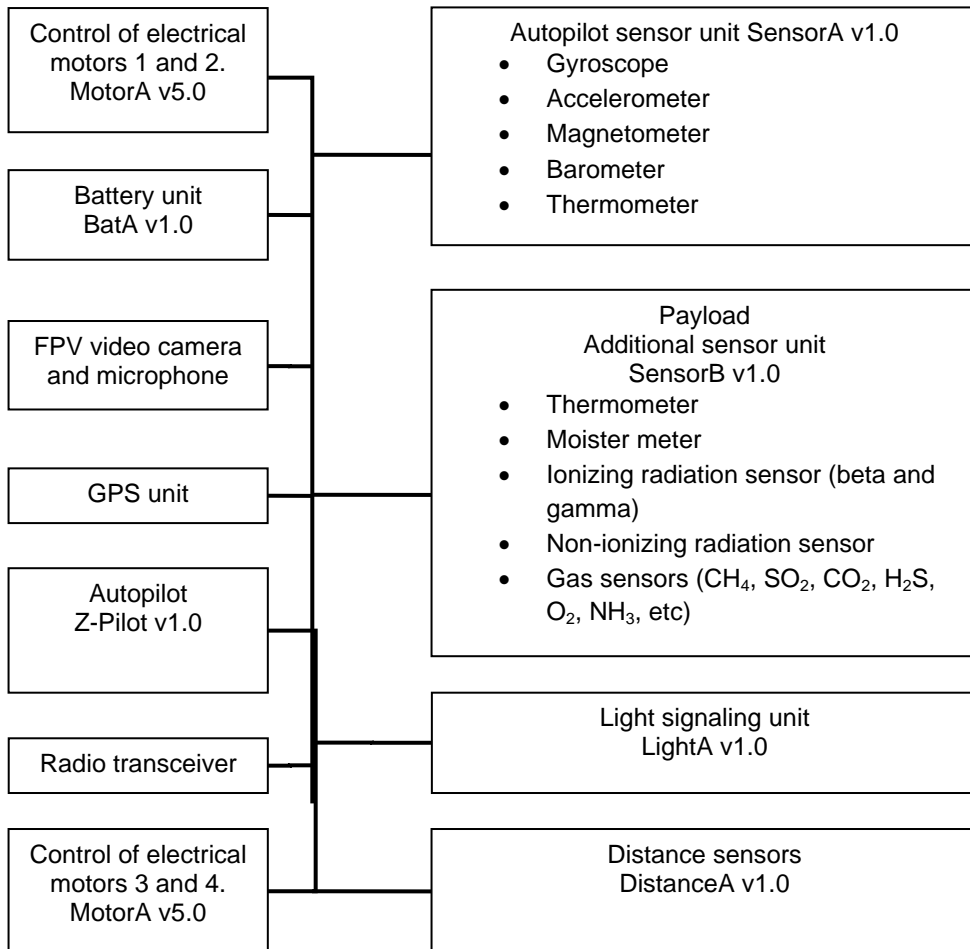
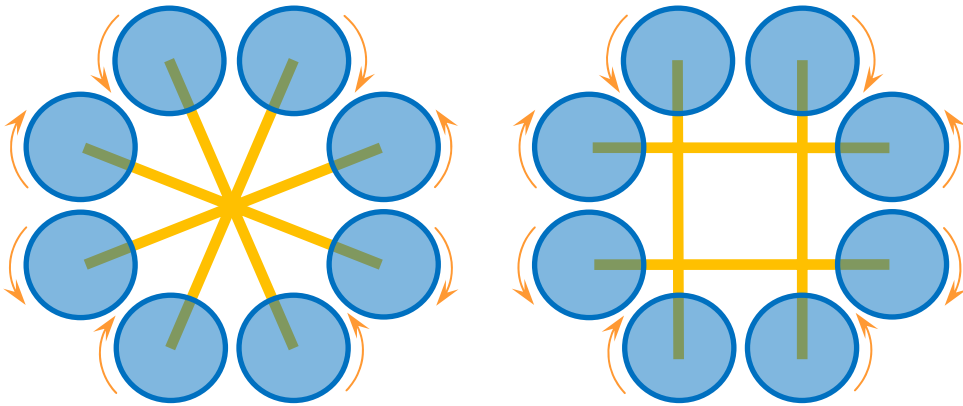


Fig. 3. Diagram of XZ-1 avionics

## XZ-series helicopters with 8 rotors

In order to increase the reliability of the helicopters and their payload capabilities, without increasing the rotor diameter, helicopters with greater number of rotors are used. XZ-series helicopters XZ-2 and XZ-3 have eight rotors each and can carry two times more weight in respect to XZ-1. Fig. 4 shows a classic airframe of an 8-rotor helicopter. The airframe is a “star”-type one. This type of airframes is widespread, but has serious drawbacks seen with “naked” eye. The rotor distribution in space requires a large sized airframe with extreme distances between the propellers. Such an airframe becomes heavy and cannot easily go through narrow openings on buildings. The rigidity of this airframe against torsion is extremely insignificant due to beams mounting in a single point.

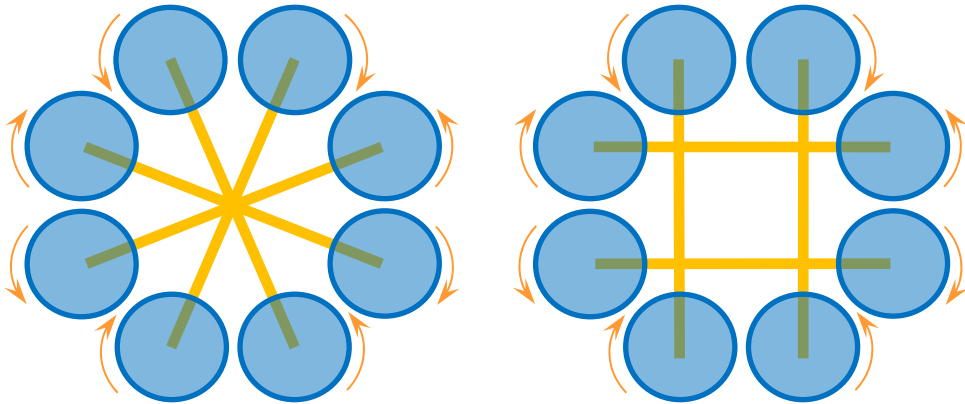


*Fig. 4. Classic 8-rotor helicopter in “star”-configuration*

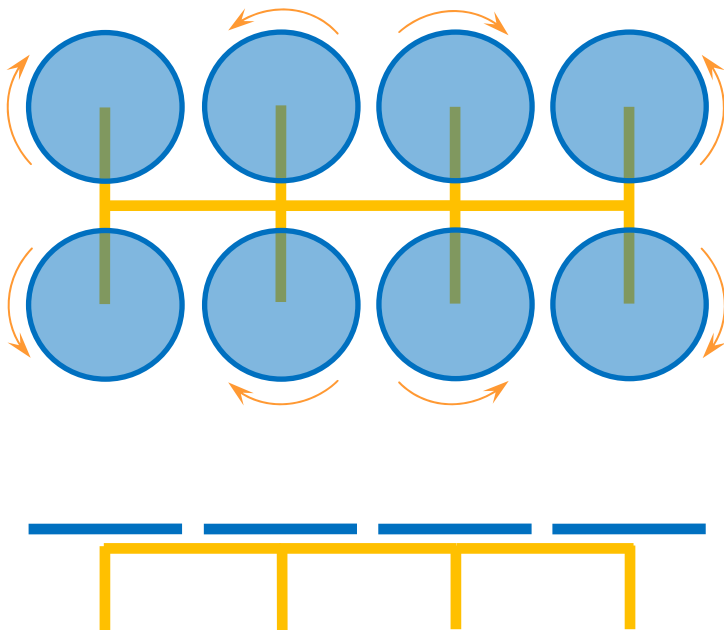
A similar airframe is the “square”-construction airframe. It is shown on Fig. 5. The “square”-airframe has all the drawbacks of the “star”-airframe except that it is more resistant to torsion. This resistance is not significant.

To address these drawbacks the XZ-series offer models XZ-2 and XZ-3. XZ-2 is presented on fig. 6. It is based on the “H”-airframe of XZ-1. Thus XZ-2 offers a fuselage with all the accompanying benefits resulting from this construction. On the other hand, the propellers of XZ-2 are placed close to each other thus ensuring the helicopter can pass through narrower openings. The beams connecting the rotors are short and rigid, and hence the construction is lighter and more stable than the classic airframe constructions. Placement of units of the avionics and the payload is

comfortable and the video camera is not jeopardized from visual interference from the propellers. The shorter overall length of the airframe beams of XZ-2 leads to lower aerodynamic drag in comparison to the “star”-airframe and the “square”-airframe.



*Fig. 5. Helicopter with 8 rotors in “square” configurations*



*Fig. 6. XZ-2 uses „fuselage”-design, which is derived from the “H”-airframe of the XZ-1 four-rotor helicopter*

## Technical characteristics of XZ-2

The main characteristics of XZ-2 are presented in table 3.

Table 3

Type	Experimental
Number of rotors	8
Propulsion	Electrical
Energy source	Electric battery
Total weight	1.6 kg
Payload	4 kg
Service ceiling	5 kg
Autopilot system	<ol style="list-style-type: none"><li>1. Z-Pilot v2.0</li><li>2. Autopilot sensor unit SensorA v2.0 Includes:<ul style="list-style-type: none"><li>• Gyroscope</li><li>• Accelerometer</li><li>• Magnetometer</li><li>• Barometer</li><li>• Thermometer</li></ul></li><li>3. GPS unit</li></ol>
Payload	Video camera with gyroscopically stabilized platform.

XZ-2 avionics diagram is shown on Fig. 7. The new motor controller MotorA v6.0 drives only one motor. This fact allows the motor controller to be placed closer to the motor in order to decrease the electromagnetic interference. Autopilot Z-Pilot v2.0 uses a larger number of sensors spread along the airframe in a unique configuration aiming at increasing the signal to noise ratio.

Another model of the XZ-series is XZ-3 helicopter. The difference between XZ-2 and XZ-3 is found in the airframe design. Similar to the first two models of the series, XZ-3 owns planar airframe, nevertheless its airframe has properties of a volumetric airframe, namely the XZ-3 airframe is superiorly resistant to torsion and bending in comparison to all so far mentioned 8-rotor helicopter airframes (fig. 8). This fact is due to the crossed structure of the airframe that exhibits features of a three-dimensional airframe structure, for example geodetic structure, monocoque structure, etc. At the same time the XZ-3 airframe is planar. Any axis of torsion meets resistance, cause by bending of one of the airframe beams.



This capability of XZ-3 is not present in the other 8-rotor helicopters. Also, XZ-3 has smaller dimensions compared to the classic models such as “star”-airframe and “square”-airframe thus becoming light and maneuverable.

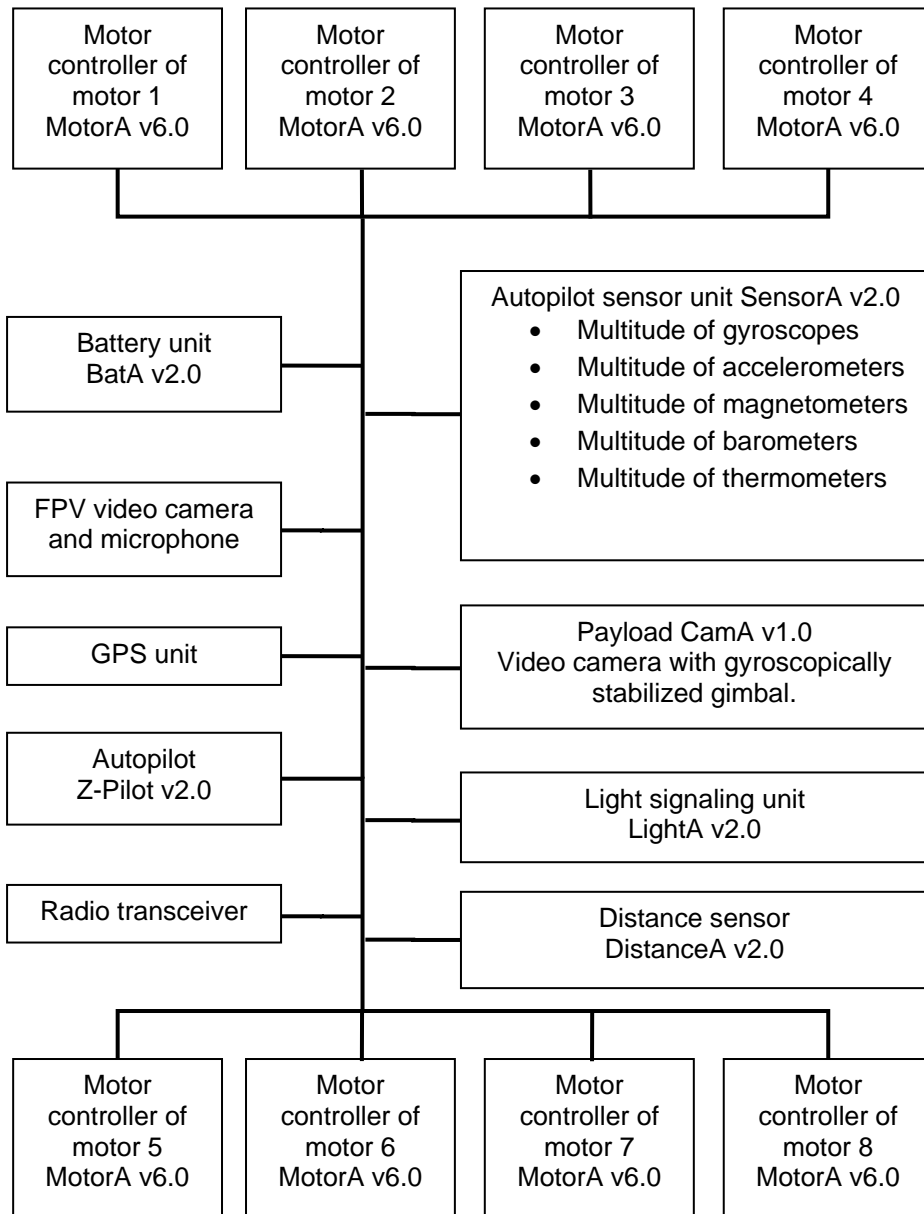
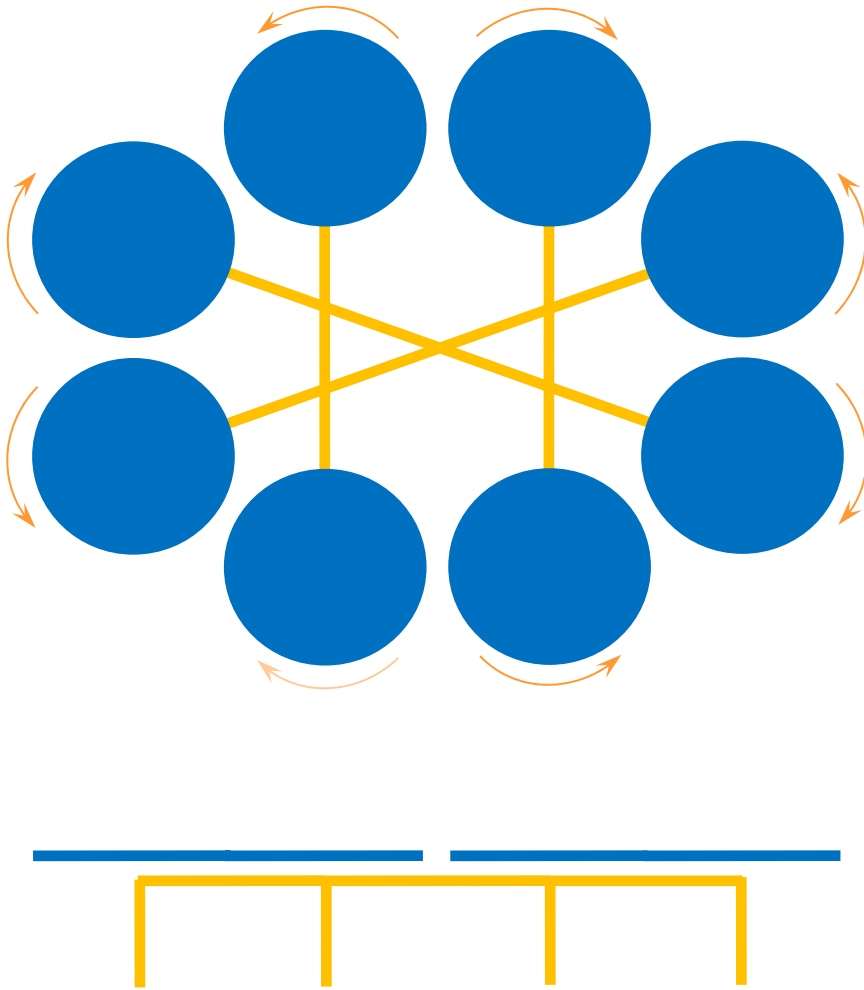


Fig. 7. Diagram of the XZ-2 avionics



*Fig. 8. XZ-3 with its unique configuration*

## **Conclusion**

The developed models of the XZ-series offer the opportunity to demonstrate innovations in the unmanned multirotor helicopter design and serves as a well suited test bed for experimentation and improvements. In the future the XZ-series helicopters will be implemented in different projects. Example candidates are pollution monitoring, disaster management, remote sensing, geophysical surveying, rescue missions, etc.

## References

1. P o u n d s, P., R. M a h o n y, P. C o r k e, (December 2006). "Modelling and Control of a Quad-Rotor Robot". In the Proceedings of the Australasian Conference on Robotics and Automation. Auckland, New Zealand.
2. H o f f m a n, G., H. H u a n g, S. L. W a s l a n d e r, C. J. T o m l i n, (20–23 August 2007). "Quadrotor Helicopter Flight Dynamics and Control: Theory and Experiment". In the Conference of the American Institute of Aeronautics and Astronautics. Hilton Head, South Carolina.
3. З а б у н о в, С., П. Г е ц о в, Г. М а р д и р о с я н. Управление на трифазен безколекторен електродвигател". Патентно ведомство на Република България 111720 / 12.03.2014
4. Г е ц о в, П. Национална аерокосмическа система за дистанционни изследвания на Земята и приложението ѝ за мониторинг и защита от природни екокатастрофи. Докторска дисертация, ИКИТ-БАН, София, 2012, 259 с.
5. Г е ц о в, П. Национална аерокосмическа система за мониторинг и защита от природни екокатастрофи. Акад. издат. "Проф. Марин Дринов", София, 2014, 240 с.
6. М а р д и р о с я н, Г. Въведение в космонавтиката. Акад. издат. "Проф. Марин Дринов", София, 2012, 260 р.
7. М а р д и р о с я н, Г. Основи на дистанционните изследвания. ИКИТ-БАН, София, 2014.
8. Авиация: Энциклопедия (Гл. ред. Г. П. Свищёв). Большая Российская энциклопедия, Москва, 1994, 736 с.

## ЕКСПЕРИМЕНТАЛНИ МОДЕЛИ МУЛТИРОТОРНИ БЕЗПИЛОТНИ ХЕЛИКОПТЕРИ ОТ СЕРИЯТА XZ

*С. Забунов, П. Гецов, Г. Мардиросян*

### Резюме

В редица случаи в зависимост от целите и задачите на експеримента за дистанционно изследване на Земята използването на самолетни и вертолетни лаборатории е икономически необосновано. От друга страна често се налагат изследвания в опасни райони (горски пожари, радиационни аварии, взривоопасни обекти и др.). Във всички тези случаи е целесъобразно използването на безпилотни летателни апарати (БЛА). През последните години все по-актуални стават радиоуправляемите безпилотни мултироторни хеликоптери като платформи за реализация на изследователска дейност, и преди всичко за дистанционни изследвания.

В статията са представени предимствата на безпилотни мулти-роторни хеликоптери предназначени за дистанционни изследвания на специфични райони от земната повърхност. Разкрита е идеята и реализацията на три нови модела мултироторни хеликоптери от серията XZ. Анализирани са основните технико-експлоатационни параметри и блоковата схема на авиониката. Особено внимание е отделено на планерите. Дискутирано е внедряването на хеликоптерите XZ в разработваната в Space Research and Technology Institute at the Bulgarian Academy of Sciences национална аерокосмическа система за дистанционно изследване на Земята, в контекста на използването ѝ за мониторинг и защита от природни екокатастрофи.

## SOME AEROSPACE APPLICATIONS OF OPTICAL POLYMERS

*Ivan Nikolov<sup>1</sup>, Stefka Kasarova<sup>2</sup>, Nina Sultanova<sup>2</sup>*

*<sup>1</sup>Sofia University, Faculty of Physics, Dept. of Optics and Spectroscopy*

*<sup>2</sup>University "Assen Zlatarov" – Bourgas, Dept. of Mathematics and Physics  
e-mail: kasarova\_st@yahoo.com*

### ***Abstract***

*Optical polymers (OPs) are widely used in optoelectronic stations intended for remote imaging diagnostics of Earth's surface. A number of new applications in aerospace technology of polymer materials such as hybrid and nanocomposite structures are pointed out. A multi-spectral camera for remote analysis of forest and agriculture areas is presented. Remote sensing spectrometer setups with a 3D hyper-spectral cube of the Earth's pictures are discussed. Image quality of optical elements is guaranteed on base of calculated geometrical and wave aberrations. An analysis for thermo-optical aberrations is fulfilled. An optimized video-spectrometer mirror-lens system intended for a SITE CCD sensor is explained.*

*Biomedical applications of OPs are included. It is pointed out that doctors control constantly the medical characteristics of eye vision and digestive tract of pilots before every flight. Polymer helmet and binocular displays, used by spacemen and aviators, are analyzed. A swallowable disposable capsule camera, made of OPs, and intended for remote biomedical examinations of the aviation staff is pictured.*

### **1. Introduction**

Imaging spectrometer systems present a new generation of equipment tools, intended for remote sensing (RS), of various natural objects located on the surface of the Earth and planets [1-14]. The essence of RS consists in obtaining the necessary information about the observed object by measuring its distance, as well as in processing of received remote data on energy and polarization characteristics of heat radiation emitted, reflected or scattered by Earth land- or ocean-surface and atmosphere in different regions of the electromagnetic spectrum. These radiance

measurements are used for environmental and defense applications, weather prediction, and global change studies. RS methods enable determination of objects' location and describe temporal dynamics of the major natural forms and phenomena of Earth resources [2, 15]. Some optical systems intended for remote research are examined in [3].

RS instruments and systems are widely used in the last decades for high-quality spectral radiation measurements from satellite-, aircraft-, and ground-based laboratories. [1, 2, 4, 6-14, 16]. Basic peculiarity of RS optical devices is their high information capacity for the transfer and processing of optical images. Data obtained from different ground swaths is detected by two-dimensional (2D) CCD matrices and recorded in the spectrometer. The created 2D optical image is scanned sequentially and registered in lines in different bands of the spectrum [6]. The video spectrophotometric information is downloaded in the memory of the optical device and forms the so called *Hyperspectral Cube*. The method involves acquisition of image data of the 2D photo in many contiguous spectral bands and monochromatic images from 310 to 900 are recorded. Information volume of a hyperspectral cube is about  $10^9$  bits for one pixel on the Earth surface. For one revolution around the Earth, the remote system can accumulate about 50-100 thousands of photos, and the volume of the optical memory exceeds  $10^{12}$  bytes [3, 4, 6-14]. The objective of the video spectrometer Vega 2, which has been used for photographing and investigation of Halley's comet, is based on the optical scheme of Cassegrain [3, 17].

In Bulgarian Academy of Science, under the guidance of academician D. Mishev, multichannel spectrometric systems Spectrum-15 [2, 3] and Spectrum-256 [4] were constructed which have been used by the aircraft of Mir space station. The contemporary hybrid devices, widely applied in aerospace experiments, provide imaging of remote objects in all parts of the electromagnetic spectrum, including UV, VIS and NIR spectral bands, and accomplish spectral-zonal photometry of Earth surface [1-4, 6-8]. The recorded images are then subjected to optical and digital processing to obtain the maximum information about the investigated remote objects [3, 4]. However, wavelengths at which absorption of light by Earth atmosphere occurs are eliminated. This is a restriction for the applied optical instruments. It is important to emphasize that directly measured characteristics of the radiation field as brightness or intensity are functions of two types of independent variables [2]: 1) wavelength, field of view, zenith and azimuth angle of Sun, etc.; 2) parameters that depend on the

distribution of the basic physical characteristics of the atmosphere (air temperature, concentration of gas components, aerosols, and the like.). The obtained spectral images are particularly suitable for the study of characteristics and the dynamic status of plant sites, and also to create methods for determining the influence of different vegetation and stress factors.

Multi-spectral imaging in orbital stations of satellites Landsat and Spot is carried out within three to seven clear spectral regions. NASA satellites are the first spectrometers having high resolution for operation in space which take photographs of the Earth surface in 384 narrow bands for the spectral region from 400 to 2500 nm [6].

Unique properties of OPs as reduced weight and cost, high impact and shatter resistance, and ability to integrate proper mechanical and optical features make them preferred materials in the design of aerospace optic instruments and devices [18]. Most popular for this purpose are the acrylic based polymers, polycarbonates, cyclo olefin polymers and copolymers, polystyrenes, alicyclic methacrylate copolymers [5]. Obviously, unique priority of polymers for biomedical applications is safety. Some measured optical and material characteristics of OPs are reported. In this paper we also present the design of a remote imaging mirror-lens polymer system, based on the classical Cassegrain optical scheme, which is widely used in astronomy and space research. It is composed of a concave primary mirror and a convex central mirror, and the foci of both mirrors coincide [17]. Popular objectives consist of two spherical mirrors and aberration compensators [3].

## **2. Analysis of Video Spectrometers Optical Schemes**

Principal optical scheme of an imaging spectrometer with a pushbroom approach to image acquisition is illustrated in Fig. 1a and for a linear scanning system - in Fig. 1b. Video spectrometer examines a photographed ground swath located perpendicular to the satellite motion. The spectral cube contains 384 color images with a detailed data about spectral signatures of objects in each pixel (Fig. 2: water, soil, grass). Remote sensing of Earth has a history: each of the agricultures and its vegetation is observed from space station using satellites and video spectrometers [1, 2, 4, 6]. Moreover, with the help of video spectroscopy it is possible to control the early detection of diseases in wheat and trees, the

location of minerals, fish migration and a number of similar processes at the Earth surface. Spectral image is a collection of images of one and the same

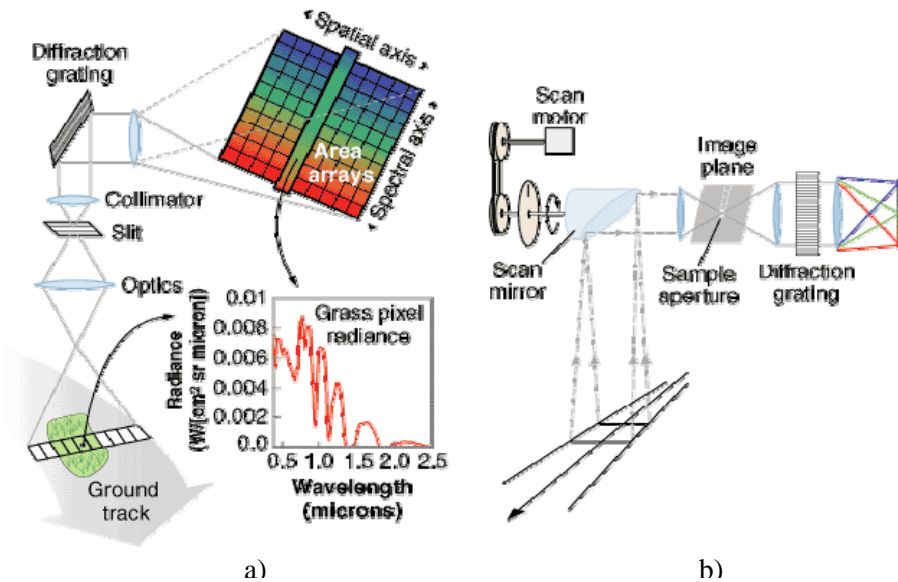


Fig. 1. Imaging Spectrometer Optical Setups: (a) a push-broom design; (b) a line-scanner device for reflection spectra

object in different parts of the spectrum (Fig. 2). The usual picture is two-dimensional with XY axes, but spectral images have a third dimension, i.e. spectral axis Z. This creates a spectral cube of each frame, where each copy of the image along the vertical axis Z is a set of images seen in colors at fixed wavelengths. Classical spectrometers collect measurement data in a single spectral curve and provide this information through a series of numbers or in graphical form. Video spectrometers generate full details for the whole investigated surface of the Earth object [4, 5-14]. Video spectrometer, type "Pushbroom", works mainly as a manual copier in space: the optical instrument rotates around the Earth and "is sweeping" information from all object points in its field of view (Fig. 1a). The technique "Whiskbroom" scans the area in the field of view of the device by scanning mirrors or specialized optics similarly in the way a TV set scans quickly the light beam on the screen (Fig. 1b).



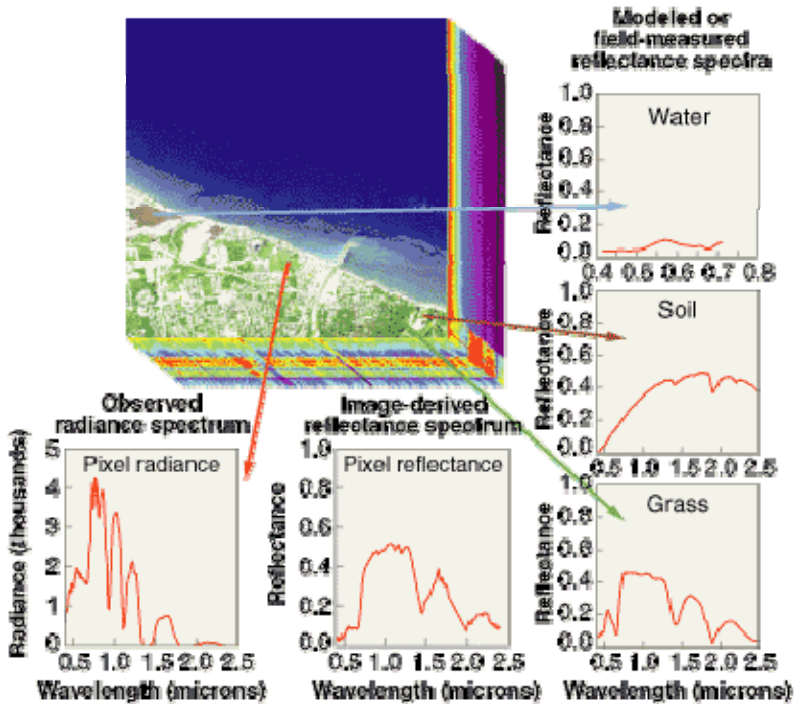


Fig. 2. Decoding of images of objects recorded by the video spectrometer in the hyperspectral cube: water, soil and grass

Video spectrometers are divided into the following major groups: multispectral (a number of groups), hyperspectral (several hundreds of groups) and ultraspectral (several thousands of groups). Each group provides progressively more information in the form of a dense aggregations of one image. Multispectral video spectrometers generally use the method of whiskbroom. Hyperspectral system applies pushbroom and whiskbroom setups in order to gain as much information as possible. Ultraspectral video spectrometers combine several instruments and both methods to gather the most detailed information [6-11]. Data processing of spectral luminance is used for a wide range of purposes such as: identification of minerals in rocks and soil, measured organic content, pollution of oceans and groundwater, etc. [15].

Remote imaging technologies provide registration of the absorption properties of geographic elements such as plant areas, rocks or urban areas. Multi-spectral imaging devices operate in 3 or 7 spectral bands (Fig. 3).

Hyper-spectral imaging devices photograph the surface of the Earth with high resolution in 384 narrow spectral bands in the range from 400 to 2500 nm [6, 7, 11]. The spectrometer for visible and near IR spectrum covers 400-1000 nm range with a band width of the channels of 5 nm. Optical instruments for short-wave IR range covers 900-2500 nm spectrum with a band width of the channels of 6.4 nm. Hyper-spectrometric data are recorded, compressed and subsequently processed by means of optical and digital tools. Calibration is performed before and after each spectrometric measurement to correct the data.



*Fig. 3. Remote UltraCam device for a multi-channel video spectrometer*

Different components, fabricated from optical polymers, are applied in the remote systems such as colour filters, scanning mirrors, protective windows, aspherical lenses for the imaging objectives, diffraction grating replicas, et al. Video data of the Earth surface is produced by the use of cameras for spectral photometry or hyperspectral systems [3-6]. For example, the unit Telops Hyper-Cam is the first spectral imaging camera [12]. It is a compact portable device with high resolution spectral imaging of Earth surface and atmosphere in land-, air-, and ecological applications. The

system may record images of cloud, luminance surfaces, geological and mineral formations, forest fires, pollution of water basins, volcano eruptions, military objects, etc.

The innovative optical instruments for hyperspectral remote measurements work in a broad spectral range from 400 nm to 14  $\mu\text{m}$  and register images of distant objects. For satellite imaging cameras with 14-bit CCD detectors and format of 14000 x 9000 pixels are used. For example, the hyperspectral UltraCam device has 13 CCD detectors, among them 9 photo arrays create a wide panchromatic focal plane and the rest 4 matrixes ensure the red, green, blue and infrared channels (Fig. 3).

An optical aberration is a departure of the performance of an optical system from the predictions of paraxial optics [3, 17, 19]. Aberrations of optical systems are monochromatic and chromatic. Monochromatic aberrations are: spherical aberration, coma, astigmatism, field curvature and distortion. Spherical aberration is the only form of monochromatic axial aberration produced by rotationally symmetrical surfaces centered and orthogonal in regard to the optical axis. Spherical aberration will appear whenever the homocentricity of the incident optical beam is altered [17]. If all rays originating from the object, inclined by angle  $w$  in respect to the optical axis, are collected at one point in the plane of Gauss and this point does not coincide with the position of the image, this aberration is called distortion. Distortion is not affected by the relative aperture of the telescope objective but the radial displacement is proportional to the cube of the point field angle. In many of the astrophysical problems distortion does not influence the image quality. If for an infinitely distant object point, the optical system is free of distortion, it is called to be orthoscopic [3, 17].

Manufacturers of video spectrometers install and align the equipment according most stringent technical requirements, taking into account the field conditions of the environment. To achieve high optical performance with minimal weight of the imaging objective reflective schemes are used. In spectrophotometers concave holographic diffraction gratings are applied for aberration correction. The optical modulus is designed with an increased relative aperture at high image quality, aberrations are corrected and distortion of the objective is reduced in remote sensing systems [20, 21]

Refractometry of OPs ensures reliable determination of refractive and dispersive characteristics of polymer materials necessary for the spherochromatic correction in the design of optical systems [18, 22].

### 3. Characteristics of Optical Polymers

Application of OPs in the design of optical elements and systems is defined by their optical as well as mechanical and thermal characteristics. In aerospace instruments principal polymers as polycarbonate (PC), polymethyl methacrylate (PMMA), polystyrene (PS), methyl methacrylate styrene copolymer (NAS), as well as newer materials such as cyclic olefin copolymer (COC) and amorphous polyolefin (Zeonex) are used [5].

We have studied refraction, dispersion and transmission of over sixteen OPs, among them principal, as well as different trade-marks of polymer companies. Important optical parameters as refractive indices at the d-line (587.6 nm)  $n_d$  for VIS spectrum, as well as at s- (852.1 nm)  $n_s$  and t- (1013.9 nm) line  $n_t$  for the NIR band, Abbe numbers  $v_d$  and  $v_{879}$ , spectral transmission range  $SR$  have been measured or calculated [5, 18, 22]. Results of some of the studied OPs are presented in Table 1.

OPs are more sensitive to temperature environment conditions than optical glasses [18]. Contemporary optical devices with polymer components are designed in a large service temperature range from  $-40\text{ }^\circ\text{C}$  to  $+60\text{ }^\circ\text{C}$ . Among all OPs the PC material is with highest service temperature up to  $+130\text{ }^\circ\text{C}$  and broadest operating temperature band  $-137^\circ\text{C}\div 130^\circ\text{C}$  [18]. The Bayer polymer in Table 1 is a polycarbonate material too. Cyclic olefin copolymer, with a similar  $n_d$  as acrylic materials, provides a higher-temperature alternative. Its highest service temperature of  $123^\circ\text{C}$  is about  $30^\circ\text{C}$  higher than PMMA. Designers of polymer optics should be aware that environmental conditions should not exceed prescribed temperature requirements of the polymer producing companies. Another important parameter is the thermal expansion coefficient  $\alpha_T$  of polymers which is with one order of magnitude greater than glasses. Refraction of OPs is also influenced by temperature and thermo-optical aberrations of polymer optical systems arise. Variations of refractive index of OPs with temperature  $\Delta n/\Delta T$  are referred in literature as thermo-optic coefficients [22]. On base of our measurements in the temperature interval from  $10\text{ }^\circ\text{C}$  to  $50\text{ }^\circ\text{C}$ , the values of the thermo-optic coefficients have been calculated. Obtained results for  $\Delta n_d/\Delta T$  and  $\alpha_T$  from literature data [18] are included in Table 1. High-performance lens systems that require large temperature band operating conditions are more suited for hybrid glass-plastic design.

Mechanical properties of OPs are very important for their aerospace applications, too. High impact-resistance  $I$  is required (Table 1). The PC material with its extremely high  $I$  value is the most suitable polymer for

safety glasses, helmets and systems with long service durability. Another parameter for mechanical strength of OPs is their Young's tensile modulus  $E$ . Dynamic coefficients, obtained by means of our ultrasound measurements, are included in Table 1 and allow comparison with glass catalogue data [18]. Polymers have considerably lower density  $\rho$  which is from 2 to 4 times smaller in comparison to glasses. This is a great advantage of plastics which guarantees reduction of weight of the end optical systems. A ultra-lightweight, space-based telescope in geosynchronous orbit with a 20 m diameter, using polymer membrane optics and developed by Ball Aerospace & Technologies Corp has been reported recently [23]. This technology reduces the mass of large aperture telescopes by nearly an order of magnitude compared to those with conventional optics.

Table 1. Characteristics of optical polymers

	PC	PMMA	PS	Zeonex E48R	Optorez 1330	Bayer
$n_d$	1.5849	1.4914	1.5917	1.5309	1.5094	1.5857
$n_s$	1.5690	1.4837	1.5762	1.5228	1.5022	1.5705
$n_t$	1.5654	1.4819	1.5726	1.5209	1.4992	1.5669
$v_d$	29.1	59.2	30.5	56.5	52.0	30.0
$v_{879}$	54.6	96.7	56.4	100.5	71.7	54.3
$\Delta n_d/\Delta T, \times 10^{-4},$ $K^{-1}$	-1.00	-1.30	-1.31	-1.26	-1.20	-1.20
$SR, nm$	380÷1600	360÷1600	380÷1600	360÷1200	410÷?	380÷1600
$\alpha_T \times 10^{-5}/^{\circ}C$	6.6÷7	5÷9	6÷8	6	7	6.5
$I, J/m$	600÷850	16÷32	19÷24	21	-	850
$E, GPa$	2.78÷3.37	4.17÷5.57	3.69	3.66	6.10	2.98÷3.53
$\rho \times 10^3, kg/m^3$	1.195	1.187	1.040	1.007	1.202	1.204

#### 4. Analysis of the Thermo-optical Aberrations of Polymer Optical Systems

Calculation of geometric and wave aberrations is demanded to ensure image quality of optical elements. Residual monochromatic aberrations and chromatism distort processed information of analyzed objects. Influence of air temperature, humidity, pressure, etc. on image quality should be also regarded. Among common criteria of optoelectronic devices is determination of their point spread function and modulation transfer function. Transformation of light brightness at each point of the object surface into spatial frequency distribution of intensity in the image or

photonic sensor (CCD, etc.) plane is realized by a Fourier transform. Software programs on optical design calculate geometric and wave aberrations as well as point spread and modulation transfer functions if the material and design parameters are introduced as input data. However, the influence of environmental conditions is not considered. The aim of the optical design of systems with polymer or glass components is to ensure transfer of the object image to the detector with possible highest contrast and negligible distortion.

Temperature variations induce thermo-optical aberrations of polymer objectives which degrade image quality. The variety of available optical grade polymers is limited compared to that of glass and therefore possible combinations of OPs to create achromatic systems are restricted. The basic lens equation for its optical power  $\Phi_\lambda$  is:

$$(1) \quad \Phi_\lambda = 1/f'_\lambda = (n_\lambda - 1) (\rho_1 - \rho_2) + \rho_1 \rho_2 (n_\lambda - 1)^2 d/n_\lambda,$$

where  $n_\lambda$  is the index of refraction of the optical material at the d- standard wavelength  $\lambda_d$  or  $\lambda_e$  (546.1 nm),  $f'_\lambda$  – lens back focal length,  $\rho_1 = 1/r_1$  and  $\rho_2 = 1/r_2$  – curvatures and  $r_1$  и  $r_2$  – radii of curvature of spherical lens surfaces,  $d$  – lens thickness along the optical axis. Longitudinal chromatic aberration  $\Delta s'_{FC}$  (axial separation between the red/blue F/C image distances) is:

$$(2) \quad \Delta s'_{FC} = -f'_d / v_d,$$

where  $v_d$  is the Abbe number at the d-line and F- and C- are the Fraunhofer lines with wavelengths  $\lambda_F = 486.1$  nm and  $\lambda_C = 656.3$  nm, respectively.

Differentiating of Eq. (1) with respect to  $n_d$ , we can determine the chromatic change of optical power  $\Delta\Phi_d$  of a lens with thickness  $d$  as follows:

$$(3) \quad \Delta\Phi_d = [(\rho_1 - \rho_2 + \rho_1 \rho_2 d (1 - 1/n_d^2))] \Delta n_{FC},$$

where  $\Delta n_{FC} = n_F - n_C$  is the principal dispersion of the polymer material. When service temperature is changed the refractometric parameters as  $n_d$ ,  $v_d$  and  $\Delta n_{FC}$  are altered.

At a given  $n_d$  of the polymer material optimal lens design parameters  $r_1$ ,  $r_2$  and  $d$  are calculated to achromatize the position of its focal plane and achieve an achromatic lens. The chromatic change of focal length  $\Delta f'_d$  is then calculated by means of Eq. (3):

$$(4) \quad \Delta\Phi_d = F (\Delta n_{FC}) = \Delta f'_d / f_d'^2 \quad \text{or} \quad \Delta f'_d = f_d'^2 \Delta\Phi_d.$$

Achromatization of a single lens is difficult and therefore doublets and triplets are calculated to achieve minimal residual spherochromatism. When focal lengths at different wavelengths are equal  $f'_F = f'_C$  and  $\Delta\Phi_d = 0$  but  $f'_d \neq f'_F$ , residual chromatism exists and the spherochromatism is determined by the difference of spherical aberrations  $\Delta S'_F - \Delta S'_C \neq 0$ .

The refractive index  $n_T$  of optical material at a given temperature  $T$  in °C is determined by the expression:

$$(5) \quad n_T = n_\lambda + \beta_{T,\lambda} (T - 20^\circ),$$

where  $n_\lambda$  is the catalogue refractive index at a given wavelength  $\lambda$ , measured at temperature of 20 or 22 °C according to the European or USA standard and  $\beta_{T,\lambda} = \Delta n_\lambda / \Delta T$  is the thermo-optic coefficient at a certain wavelength  $\lambda$ .

Denoting the thermo-optic constant  $V_{T,\lambda} = [\beta_{T,\lambda} / (n_\lambda - 1)] - \alpha_m$ , we get:

$$(6) \quad n_T = n_\lambda + [(n_\lambda - 1) (V_{T,\lambda} - \alpha_T)] T / n_\lambda,$$

where  $\alpha_T$  is the thermal expansion coefficient of the material or the relative elongation of the polymer sample at measured temperature  $T$  and  $\alpha_m$  is the mean coefficient in the temperature interval from -60 °C to +20 °C or from +20 °C to +120 °C [17, 18].

For optical materials the thermo-optic constant  $V_{T,\lambda}$  characterizes the change in refractive index and dispersion of the refractive element with temperature. The values of  $\beta_{T,\lambda}$  and  $V_{T,\lambda}$  are standardized and are presented in optical database for glasses, plastics, ceramics, nano-composites, etc.

Temperature change of refractive index  $\Delta n_T$  in respect to  $n_\lambda$  at standard temperatures:

$$(7) \quad \Delta n_T = n_T - n_\lambda,$$

can be used to analyse the thermo-optical aberrations in the design of optical systems [18]. For principal OPs, on base of our measurements,  $\Delta n_T \times 10^{-4}$  °C for the d-line is: 9.0 (PMMA), 13.0 (PS) and 5.0 (PC) in the temperature interval between 10 and 20 °C; and 39 (PMMA), 39.3 (PS) and 30 (PC) in the range (20 ÷ 50) °C.

In case of an achromatic system (Fig. 4a) with two PC mirrors, mirrored surfaces undergo thermal linear expansion but  $\Delta n_T$  of the PC material doesn't change their optical power. The mirror focal length  $f'_m$  is determined only by its radius of surface curvature  $r_m$  as follows [3, 17]:

$$(8) \quad f'_m = r_m / 2 \quad \text{и} \quad \Delta f'_T = 0.5 r_m T \alpha_T,$$

where  $\Delta f'_T$  is the temperature change (the thermo-optical aberration) of focal length which is calculated by means of Eqs. (1) and (4).

A spherical mirror has about eight times smaller spherical aberration in comparison to an analogous plano-convex lens and [3]:

$$(9) \quad \Delta S'_m = -0,25 \rho_m h^2,$$

where  $h$  is the height of the incident ray ( $h_{max} = D/2$ ),  $D$  is the mirror diameter and  $\rho_m = 1/r_m$  is the curvature of the mirrored optical surface.

The optical power  $\Phi_m$  of the two-component mirror system (Fig. 4a) is calculated according the expression:

$$(10) \quad \Phi_m = 1/f'_m = -(\Phi_1 + \Phi_2 + \Phi_1 \Phi_2 d),$$

where  $d$  is the separation distance between the components along the optic axis,  $f'_m$  is the focal length of the mirror system,  $\Phi_1$  and  $\Phi_2$  represent the optical power of the two spherical mirrors. Temperature alternation of the optical power  $\Delta\Phi_T$  is determined by differentiating of Eq. (10) taking into account variations of mirror focal lengths  $\Delta f'_{m_1}$  and  $\Delta f'_{m_2}$  caused by thermal changes of the mirror radii  $\Delta r_{1T}$  and  $\Delta r_{2T}$ :

$$(11) \quad \Delta\Phi_T = \Delta f'_T / f_m^2 = -(\Delta\Phi_{1T} + \Delta\Phi_{2T} + \Phi_1 \Phi_2 \Delta d_T),$$

where  $\Delta\Phi_{1T}$  and  $\Delta\Phi_{2T}$  are variations of the optical power of components. Small values of second order are neglected but for the temperature interval  $\Delta T = 40^\circ$  (from  $-10^\circ\text{C}$  to  $+30^\circ\text{C}$ ) the  $\Delta\Phi_T$  value is significant.

The optical power of a plano-convex lens is calculated as follows [3]:

$$(12) \quad \Phi = 1/f' = (n_d - 1) / r \quad \text{or} \quad r = (n_d - 1) f',$$

where  $r$  is radius of the convex surface curvature and  $f'$  is the lens focal length.

Differentiation of Eq. (12) in respect to temperature change of the lens back focal length  $f'$  gives:

$$(13) \quad \Delta f'_T = (\Delta r_T - f' \Delta n_T) / (n_d - 1),$$

where  $\Delta r_T$  is calculated by the relation  $\Delta r_T = r T \alpha_T$  for the temperature interval from  $-10^\circ\text{C}$  to  $+30^\circ\text{C}$ . Spherical aberration of the plano-convex lens is determined by [3]:

$$(14) \quad \Delta S' = -0,5 (n_d h^2) / (n_d - 1) r,$$

where  $h = D/2$  is the lens aperture diameter.



The size of the image  $Y'$  at the back focal plane of the imaging objective is determined by the relation [3, 17]:

$$(15) \quad Y' = f' \operatorname{tg} \omega,$$

where  $\omega$  is the objective field of view. Temperature change of the image size is calculated by:

$$(16) \quad \Delta Y'_T = \Delta f'_T \operatorname{tg} \omega,$$

where  $\Delta f'_T$  is determined by Eq. (13).

For an achromatic objective the temperature optical power change of first order is calculated by the relation:

$$(17) \quad \Phi_1 / v_1 + \Phi_2 / v_2 = 0; \quad \Delta \Phi_{1,T} = - (v_1 / v_2) \Delta \Phi_{2,T},$$

where  $\Phi_1$  and  $\Phi_2$  represent optical power of the positive and negative lens and  $v_1$  and  $v_2$  – Abbe numbers of OPs at the standard wavelength  $\lambda_d$ . Alterations  $\Delta \Phi_{1,T}$  and  $\Delta \Phi_{2,T}$  are calculated by consecutively differentiating of Eq. (1) in respect to  $\Delta n_T$ ,  $\Delta r_T$  and  $\Delta d_T$  for each of the lenses. On the base of the partial dispersion formula [18] the temperature change of first order of the Abbe number is determined as:

$$(18) \quad \Delta v_{d,T} = (v_d \Delta n_{d,T}) / (n_d - 1),$$

where  $n_d$  and  $v_d$  is the refractive index and Abbe number of the applied polymer, respectively and  $\Delta n_{d,T}$  is calculated by means of Eq. (7). Lateral chromatism is obtained on base of Eq. (15) as:

$$(19) \quad \Delta Y'_{FC} = Y'_F - Y'_C,$$

where  $Y'_F$  and  $Y'_C$  are the image sizes created by the positive system (lens, achromat or triplet) at standard wavelengths  $\lambda_F$  and  $\lambda_C$ . The chromatic image error  $\Delta Y'_{FC}$  depends on principal dispersion of OPs  $\Delta n_{FC} = n_F - n_C = (n_d - 1) / v_d$ .

## 5. Lens Design for a Remote Sensing Device

Spectrometric systems Spectrum-15 and Spectrum-256, intended for RS of Earth, were used during the flights of the Bulgarian astronauts G. Ivanov and A. Aleksandrov. Presented design of the aberration compensators for the objective, used in the video spectrometers, is based on the theory of optical systems [3, 17]. Objectives with excellent optical characteristics and aberration correction in the full field of view are required

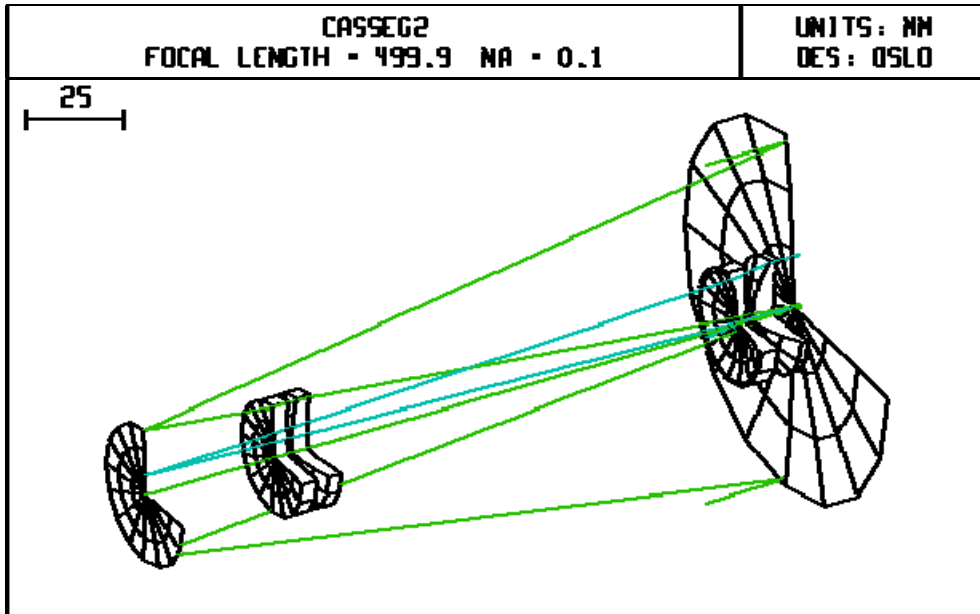
for remote sensing spectrometers. Decrease of distortion is necessary for the optical schemes of cameras with CCD arrays [20, 21]. Coma, which is the second odd aberration, is difficult to be eliminated in case of systems with a limited number of components. OSLO optics software has been used for the study of properties of the synthesized objective with two aberration compensators. Analysis of the wave aberrations as well as of the point spread function is required to determine the energy distribution in the Airy's diffraction pattern [21].

The modular approach for the synthesis of complex optical systems is very flexible and convenient for objectives used in various applications of instrument engineering and optoelectronic devices [3, 17]. Odd aberrations as meridional coma and distortion are difficult to be eliminated in the full field of view of the objectives. The influence of the meridional coma is analysed by relating comatic circles' radii with all of the design parameters of the afocal double lens compensator [3]. The modular approach consists in attaching of two lens compensators to the Cassegrain objective, which is comprised of two basic mirrors, in order to achieve a separate correction of the meridional coma and distortion (Fig. 4b).

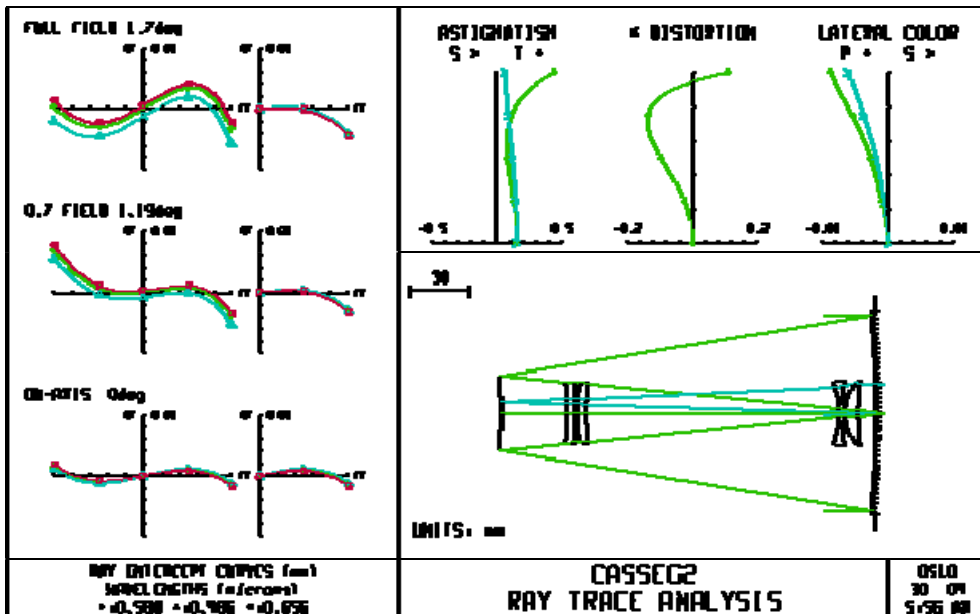
A method for aberration correction of the considered mirror-lens objective is proposed. If the design parameters of the optical system are assumed as back focal length  $f' = 500$  mm, relative aperture  $D/f' = 1:5$  and field of view  $2\omega = 3.4^\circ$ , and it consists of two permanent polycarbonate spherical mirrors and two varying quartz aberration compensators located close to the mirrors, the aberration compensation is realized by: a) the first afocal compensator for correction of spherical aberration and meridional coma (Fig. 4a); b) second compensator, located next to the primary mirror, to reduce field aberrations as astigmatism and distortion (Fig. 4b); c) relative motion of the first compensator away from the convex mirror to reduce vignetting of obliquely incident rays (Fig. 5); d) relative motion of the second compensator away from the concave mirror to improve aberration correction but reduces field of view (Fig. 5); e) diffraction at entrance pupil of the objective doesn't restrict its resolution ability (RA) and the meridional coma is the most significant residual aberration (Fig. 4b and d).

The image quality of the proposed optical system is verified on base of calculated modulation transfer function (Fig. 4c) and point spread function (Fig. 4d). Two modifications of the mirror-lens objective are

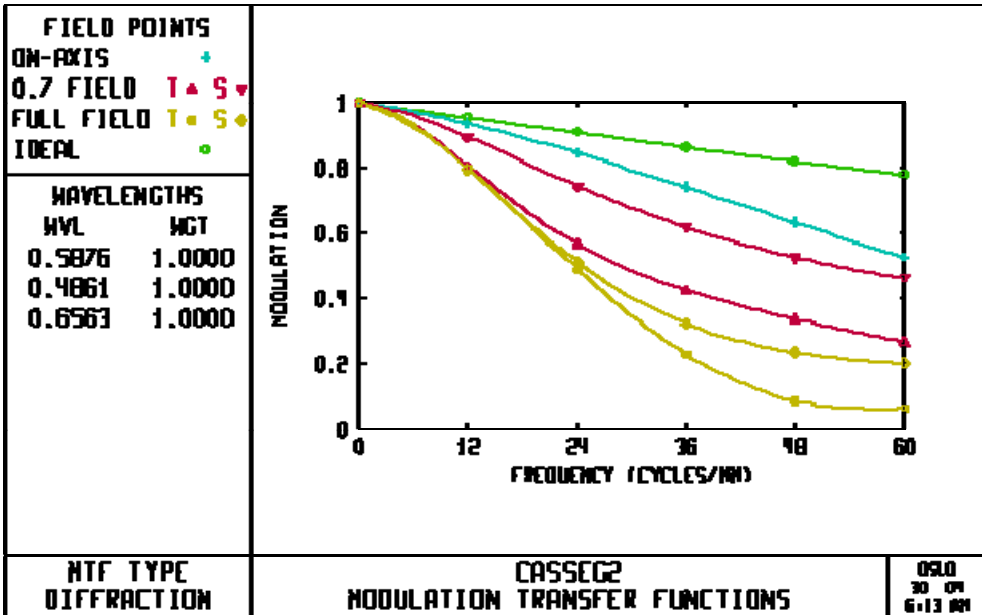
investigated: 50 % vignetting of the obliquely incident rays and without ray vignetting at the end of the field of view [21].



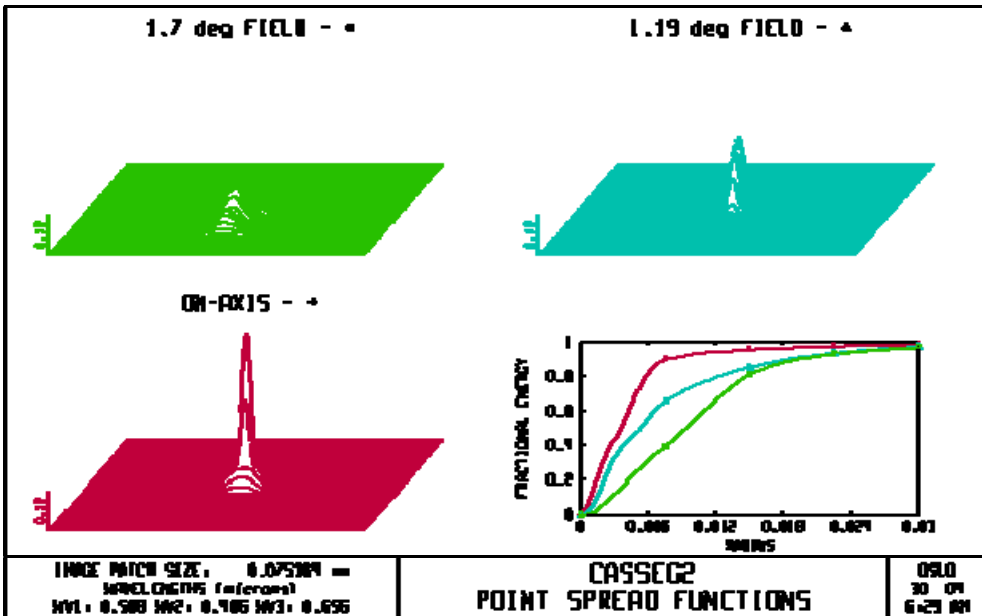
a)



b)



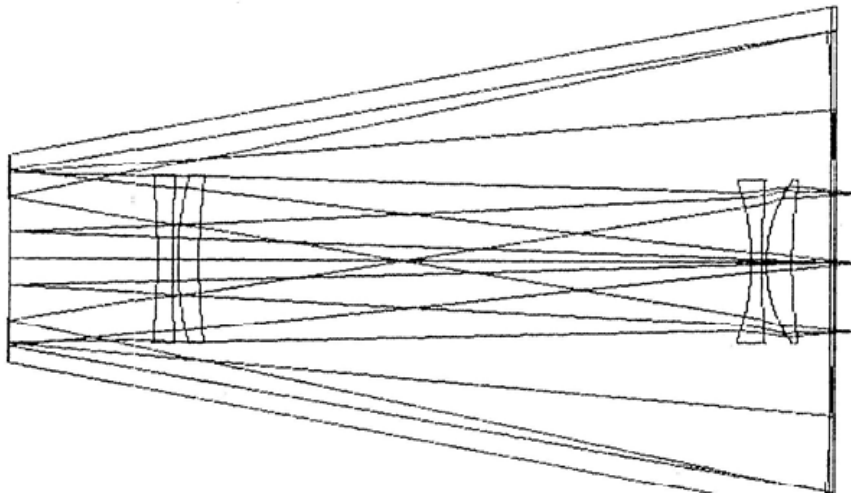
c)



d)

Fig. 4. Remote imaging mirror-lens system with two aberration compensators:  
 (a) a 3D design of the objective; (b) geometric aberrations and ray trace analysis;  
 (c) modulation transfer function; (d) point spread functions

The design of the final hybrid objective with on-axis and oblique ray tracing is presented in Fig. 5. Mirrors are made of polycarbonate shells mirrored with aluminum coatings and protected with anti-abrasive layers to minimize the size and weight of the objective in the remote sensing spectrometer. Field aberrations are reduced to a spot size below 0.013 mm. The achieved aberration point spread spot is significantly smaller than the CCD pixel (0.016 x 0.016 mm or 0.024 x 0.024 mm). The modulation transfer function of the obtained objective reaches spatial frequencies of 40 lin/mm (Fig. 4c) and meets the requirements of the video-spectrometric modulus [3, 20, 21].

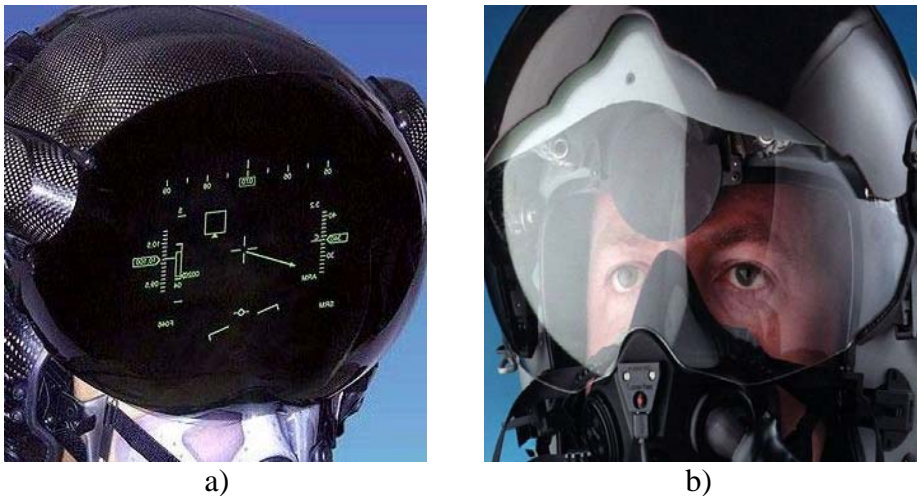


*Fig. 5. Final design of remote imaging mirror-lens objective with on-axis and oblique ray tracing*

## **6. Applications of Optical Polymers in Remote Imaging Systems**

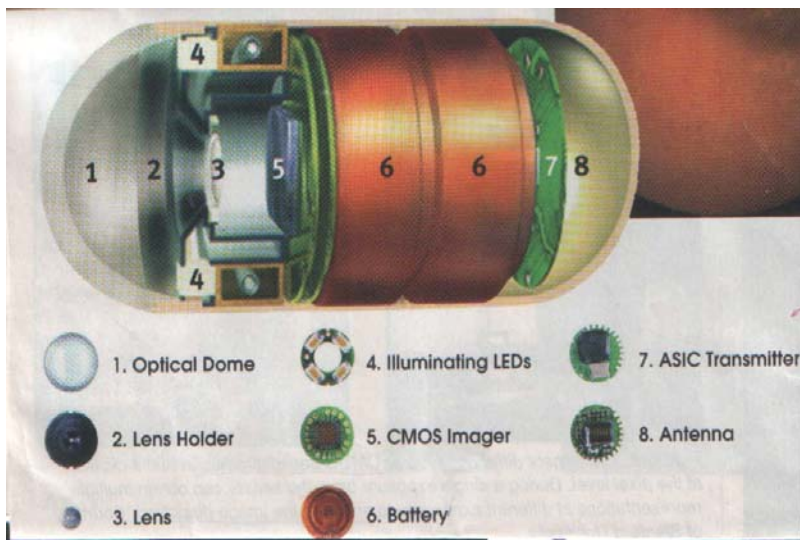
Vision plays a crucial role in life and labor activity of people [3, 4, 24]. Up to 86-90% of the information about the world is perceived by eyes and then transferred to the brain. Optical methods facilitate physicians in the diagnosis of vision and establishment of the state of health of people applying for various professional positions (drivers, pilots, police officers, etc.). Information abilities of vision reach  $10^{12}$  bits (bio-computer) at about 14 Hz clock frequency of brain during stereoscopic observation of coloured objects, which is comparable to the volume of known terabyte optical memories [4, 25, 28]. The eyes function in a huge dynamic range from  $10^{-7}$

cd/m<sup>2</sup> to 10<sup>5</sup> cd/m<sup>2</sup> during light/dark adaptation as RA and visual contrast sensitivity constantly change. Cinema / TV transmissions are performed at a frequency of 24/25 fps at information volume of the images around 10<sup>6</sup> bits. The human eye has a momentum approximately 0.1s perception of light images in which the critical frequency of vision is 16-25 Hz for watching cinema / TV movies [24, 29]. The spaceman vision reality is given in [4]. The eye's contrast sensitivity is evaluated as 1 – 2%. The speed of the visual reactions of pilots reaches 0.05 - 0.025s and they operate at critical frequencies up to 50-60 Hz. High visual facilities of astronauts, pilots, and operators of high-speed machines are certified by measuring methods of ophthalmology. For aerospace staff the visual requirements demand stereoscopic RA to 3-5", linear RA of at least 0.05 mm at the plane of the measuring scale, and sustainable observation of the control panels of the monitoring devices of about 3 to 5 min. In Fig. 6 aerospace helmet displays for remote connection with the pilots in flight are presented. Frontal transparent helmet modules for stereoscopic display are made of PC polymer material, which has the highest impact strength (Table 1). Binocular display is assembled with different optical polymer systems: magnifiers, VIS or NIR goggles, viewfinders, measuring screens, etc. Work surfaces of the PC front module displays of helmets are covered with anti-reflective, hydrophobic anti-abrasive optical layers.



*Fig. 6. Helmet displays for remote aerospace systems: a) Binocular Display improves pilots' eyesight options for target designation; b) Helmet Display system increases the accuracy of pilots's measurements*

“One picture is worth a thousand words”: physicians recognize the tissues of living organs using qualitative color medical images. A swallowable capsule camera made from optical polymers can transmit up to 50 000 color pictures for the digestive tract of the pilot [26, 27]. A remote medical control can be fulfilled when the patient swallows the camera with a size of a drug capsule, which moves smoothly and painlessly through the esophagus tract by means of peristalsis (Fig. 7). Traveling in the living body, the capsule transmits video signals received by an antenna located outside the body of the respondent. Photos are saved in a wireless device installed in the belt of the pilot. Through Internet line doctors supply recorded medical data in a computer station that is equipped with software for processing of optical images. A short video movie with information about the pilot’s digestive tract during the remote examination is obtained. The capsule camera, shown in Fig. 7, represents a remote imaging tool: the patient with it is far away from the medical command center (in flight, at work, on a business trip, on the road, etc.). The polymer video capsule is removed from the body in the natural way, i.e. it is a disposable optical device. The respondent doctor at the diagnostic center receives the recorded images of the esophageal tract and remotely connects and consults the patient by means of telecommunication equipment (video mobile phones, optical Internet networks, etc.).



*Fig. 7. A polymer swallowable capsule camera for remote diagnostics of aircraft’s digestive tract (Tufts University School of Medicine, Boston, MA)*

The optical dome (1) in Fig. 7 and the cylindrical body of the disposable capsule are produced from a bio-inert full-polymerized PMMA material. The endoscopic objective (3) is assembled from PMMA and PS lenses designed for a good spherical and chromatic correction over the image field [5, 18]. The frontal surface of the optical dome (1) is sputtered with anti-reflexive and anti-acid coatings.

OPs have a broad range of applications: single lenses and lens arrays, assembled components, aspheric polymer layers deposited on glass lenses, metal-ceramic mirrors with protective polymer coatings, mirror optical systems, integrated optoelectronic modules, etc. [5, 18]. In recent years polymer optoelectronics is introduced: nanocomposite materials with a negative refractive index, polymer pads with arranged metal atoms, surface diffraction films and plasmon structures, one-dimensional arrays of micro-lenses for coupling of micro-lasers with vertical cavity for fiber optic communication modules, two-dimensional nano-focusing arrays for recording and reading data from terabyte memories, OP matrices with arranged magnetic dipoles, nano-and micro-magnets, magnetic heads, etc.. [18, 25].

## **7. Summary and Conclusions**

Polymer materials are widely applied in science and technology, optoelectronics, aerospace, defense industry, etc. Optical, mechanical and thermal characteristics of OPs are pointed out. The design and aberration analysis of a mirror-lens objective based on the Cassegrain optical scheme, used in video spectrometers for remote sensing, is proposed. Formulae for thermo-optical aberrations of polymer optics are derived. Geometrical and physical optics form the theoretical bases of the hyperspectral measurements which are intended for colour imaging and monitoring of global surfaces. A SITe 1100 x 330 Scientific-Grade CCD sensor with imaging area of 26.4 x 7.92 mm and pixel size 0.024 x 0.024 mm with high quantum efficiency from the UV to NIR spectral region (280 ÷ 1100 nm) has been proposed. The optical module of the imaging spectrometer works at 200 mm aperture diameter and focal length of 500 mm with good aberration correction of the objective. The optimized scheme is compact and the objective is with small longitudinal dimensions and limited central vignetting for location of the image behind the principal mirror (Fig. 5). The linear dimension of the imaging field is 30.7 mm and the maximal diameter of the aberration spot is



0.013 mm in the VIS spectrum which is twice smaller than the given pixel size of the CCD imaging array (Fig. 4).

The new applications of OPs are designs of hybrid and nano-composite devices used in aircraft and communication networks. The innovative robotic and adaptive stations are under research and development, intended for generation and remote transmission of million colour and spectral-zonal images of the Earth surface. The new OPs are applied in nano-photonics for the design and fabrication of nano-scale components, information systems for image processing, micro- and helmet-displays, nano-computers, etc. The doctors are responsible to examine the parameters of eyesight and digestive tract of pilots before every flight. The binocular and helmet displays secure a remote vision control of aviators in flight using transmitting/receiving images from/to the aerospace center. A swallowable polymer camera is presented for remote biomedical testing of the spaceman stomach with intestines. Our research is directed to the analysis and synthesis of nanocomposite OPs applied for the realization of hybrid optoelectronic devices that can be used in remote stations for recording of ecological catastrophes and hyper-spectral pictures.

## References

1. Космическая оптика.- Пер. с англ., изд. „Мир”, Москва, 1985.
2. М и ш е в, Д. Дистанционни изследвания на Земята от Космоса. изд. на БАН, София, 1981, 206 с.
3. Н и к о л о в, И. Оптични методи и системи (за запис и обработка на информация). Унив. изд. „Св. Климент Охридски”, София, 1993, 272 с.
4. М а р д и р о с я н, Г. Природни екокатастрофи и тяхното дистанционно аерокосмическо изучаване. Акад. изд. „Проф. Марин Дринов“, София, 2000, 387 с.
5. N i k o l o v, I., N. S u l t a n o v a, S. K a s a r o v a, Polymer materials for NIR and laser applications, SES 2013, 9<sup>th</sup> Sc. Conf. with Int. Part. “Space, ecology, safety”, 20-22 Nov 2013, Sofia, Bulgaria: (to be published).
6. M a r m o, J. Hyperspectral imager will view many colors of Earth. Laser Focus World, August 1996, pp. 85-91.
7. S c h o t t, J. Spectral data adds a new dimension to remote imaging of Earth. Laser Focus World, August 2004, pp. 76-84.
8. C o s i m o, J. C., C. L. P a r k i n s o n. Satellite-Observed Changes in the Arctic. Physics Today, August 2004, pp. 38-44.
9. J o n e s - B a y, H. A. Hyperspectral imagers shed light on pharmaceutical processing methods. Laser Focus World, December 2004, pp. 95-98.

10. F l a n d e r s, D. R., A. H. M e n g e l, B. S. T e r r y. Remote Sensing Applications in Regional Emergency Management. PHOTONICS SPECTRA, March 2006, pp. 70-76.
11. Н о г а н, Н. Satellite Imagery Comes Down to Earth. PHOTONICS SPECTRA, August 2006, pp. 48-54.
12. www.telops.com (Telops Inc., Quebec, Canada).
13. В а н н о н, D., R. Т h о м а s. Harsh environments dictate design of imaging spectrometer. LaserFocus World, August 2005, pp. 93-97.
14. W e t h e r i l l, G., A. A l r e e, K. B u r k e (Editors). Annual Review of Earth and Planetary Sciences.1991, pp. 351-382.
15. М и с h e v, D. Spectral Characteristics of Natural Formations. BAS Publishers, Sofia, 1986.
16. М и х е л ь с о н, Н.Н. Оптические телескопы (теория и конструкция).- Наука, Москва, 1976.
17. Р у с и н о в, М.М. Техническая оптика.- Машиностроение, Ленинград, 1979, 488 с.
18. С у л т а н о в а, Н., С. К а с ь р о в а, И. Н и к о л о в. Рефрактометрия на оптични полимери (под об. ред. на проф. И. Николов), Унив. Издат. „Проф. д-р Асен Златаров“, Бургас, 2013, 176 с.
19. S m i t h, W. J. Modern Lens Design.- “McGraw Hill”, New York, 1992.
20. N i k o l o v, I., Z. Z a h a r i e v a. Mirror-lens Optical System for Image Spectroscopy Device. Proc. of SPIE, Vol. 3573, 1998, pp. 413-416.
21. N i k o l o v, I., A. К р у м о в, Z. Z a h a r i e v a. Optical Lens Assembly for Image Spectrometry. “Physics Letters”, № 11, 2000 (BPU-4, 22-25 August 2000, Veliko Turnovo).
22. N. G. S u l t a n o v a, S. N. К а с а р о в а, I. D. N i k o l o v, Characterization of optical properties of optical polymers, Optical and Quantum Electronics, Vol. 45, no. 3, 2013, pp. 221- 232.
23. www.photonics.com, Membrane Optics Telescope Demo'd for DARPA, Dec. 9, 2013.
24. M a r r, D. Vision. W. H. Freeman and Company, New York, 1982, 400 p.
25. N i k o l o v, I., K. K u r i h a r a, K. G o t o. Nanofocusing Probe Optimization in a Near-Field Head for an Ultra-High Density Optical Memory. Chapter 2 in Focus on Nanotechnology Research, Ed. Eugene V. Dirote, Nova Science Publishers, Inc., New York, 2004, pp. 19-49.
26. P o w e l l, P. M. Maximizing Output with Miniature Cameras. Photonics Spectra, July 2002, pp. 46 – 52.
27. Н и н д у s, L. A. Medical Imaging Patients Find Easy to Swallow (Swallowable Endoscopy Capsules). ADVANCED IMAGING EUROPE, October 2002, pp. 18-21.
28. К а л и м а н о в а, И., И. Н и к о л о в. Светлинни измервания. Глава 12 в Метрология и измервателна техника под об. ред. на проф. Х. Радев, Софттрейд, София, том 3, стр. 351 - 482.
29. Б а р а б а н щ и к о в, В. А. Динамика зрительного восприятия. Наука, Москва, 1990, 239 с.

## НЯКОИ АЕРОКОСМИЧЕСКИ ПРИЛОЖЕНИЯ НА ОПТИЧНИТЕ ПОЛИМЕРИ

*И. Николов, С. Касърова, Н. Султанова*

### Резюме

Оптичните полимери (ОП) намират широко приложение в оптоелектронните уреди и системи, предназначени за дистанционна образна диагностика на земната повърхност. Дадени са експериментални резултати за някои оптични, механични и топлинни характеристики на основни ОП. Предложен е дизайн на огледално-лещов обектив по схемата на Касегрен, включващ две базови поликарбонатни огледала и два променящи се кварцови аберационни компенсатора. Изчислени са геометричните и вълнови аберации. Обективът е подходящ за работа на видео-спектрометрите за дистанционни изследвания. Представен е анализ на индуцираните термо-оптични аберации на полимерни оптични системи. Илюстрирано е използването на полимерните материали за дистанционно диагностициране на зрението и общото здравословно състояние на авиационния състав посредством поглъщаема капсулна камера за еднократна употреба, фронтални модули на биноккулярни шлемови дисплеи и други съвременни приложения на ОП.

## MICRO- AND NANO-FOCUSING OPTICS INTENDED FOR REMOTE IMAGING SYSTEMS

*Vasil Kavardzhikov<sup>1</sup>, Dessislava Pashkouleva<sup>1</sup>, Ivan Nikolov<sup>2</sup>*

*<sup>1</sup>Institute of Mechanics – Bulgarian Academy of Sciences*

*<sup>2</sup>Sofia University, Faculty of Physics, Dept. of Optics and Spectroscopy  
e-mail: kavarj@imbm.bas.bg*

### **Abstract**

*Some possible remote and aerospace applications of nano-focusing optics are discussed. Optical systems for micro-focusing built by aberration corrected lens modules are presented. Components for nano-focusing in the read/write CD/DVD heads are given also. Diffraction limited spots having diameters from 400 nm to 200 nm are analyzed. Near-field optical technologies for the concentration of laser energy in spots from 200 nm to 100 nm are used in the designed nano-focusing modules intended for the tera-byte drives. Techniques for conversion various laser beams of light through hybrid lenses in which an aspherical refractive surface corrects the longitudinal spherical aberrations are reported. The diffractive surface introduces a negative dispersion and removes the chromatic aberrations in the image plane. Examples of wave-optics nano-focusing numerical modelling fulfilled by Finite Difference Time Domain method are presented. Video-spectrometers and remote imaging systems are analysed as platforms for tera-byte memories.*

### **1. Introduction**

Remote imaging systems are applied for spectral analysis of the Earth's surface [1 - 4]. The optical devices "Spectrum-15" and "Spectrum-256" have been used by Bulgarian spacemen G. Ivanov and A. Alexandrov. These aerospace instruments are intended for remote spectrometry of the Earth and realized at the Bulgarian Academy of Sciences under the supervision of acad. Dimitar Mishev [1, 3, 4]. The innovative tera-byte optical memories are potential candidates for the recording of million

pictures generated by video-spectrometers. A great volume of spectrometric data is transmitted from the aerospace crafts to the analyzing centers [1, 4]. Advanced optical devices have the potential to satisfy the ever-increasing storage demands of computer systems, both in terms of high-capacity and massive transfer rates [5 - 7]. Novel technologies are at various stages of development and promise to provide the next generation of optical storage systems. High-density optical disk memories will require accurate characterization and very precise measurement of the dominant error sources in each micro-technology [7 - 9].

Nano-focusing is determined as light collecting into a spot size diameter under 200 *nm*. The conventional micro-lens systems can focus laser beams into spots from 1  $\mu\text{m}$  to 0.4  $\mu\text{m}$ . Nano-focussing research is a part of the field of nano-photonics directed to nanoscale light-matter interaction and nano-fabrication of optics. The production accuracy of the existing optical technology is from 1/10 wavelength to  $\lambda/20$  that is about 60 – 30 *nm* during the precise micro-lens surface diagnostics.

A huge growth of nano-photonics production can be noted during the first decade of new century in four major directions: materials, biomedicine, molecular electronics, and energy (nano-devices: solar & fuel cells). This tendency was kept also during the next ten years. For example: the governments spent more than \$4 billions on NANO-Tech research in 2004; the EU government funding for nanotechnology was about 1.3 billion Euro from 2002 to 2006; in 2009 the world white market of nano-phonic devices showed a growth rate of 85.8% reaching about \$ 9.33 billions.

The micro-lenses are essential elements of the modern optical-electronic devices. They can be found in aerospace industry, optical communications, interconnections, sensors and displays, charge-coupled device (CCD) cameras. Micro-lenses arrays are key components in modern optical disk memory heads also [5 - 7]. The development of a new ultrahigh-density optical disk head system using a vertical cavity surface emitting lasers (VCSEL) array as a parallel optical beam source, to realize a higher memory density and a fast data transfer rate is in a process of completion at the Terra-byte Laboratory of Tokai University, Japan. It will work at near-field optical conditions, in which the gap between the head output surface and the optical disk surface have to be as narrow as 10 *nm*. A GaP micro-lens array, aligned to the VCSEL-s should concentrate the light at 30 *nm* in diameter apertures opened at micro-lens focus spots in an Au

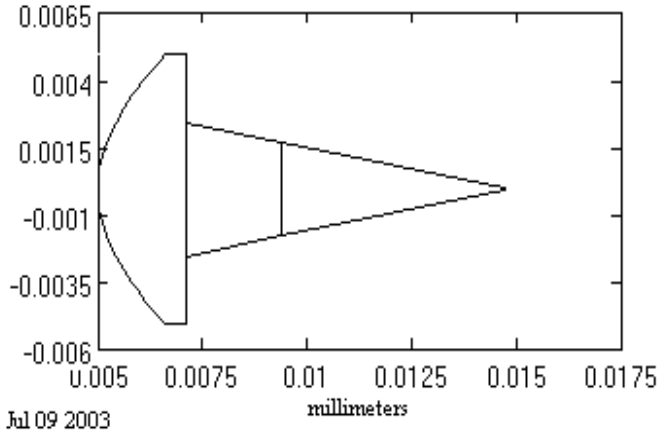
film, deposited on the head output surface with nano-thickness. The modeling, design and fabrication of refractive micro-lens arrays and their integration with VCSEL arrays was accomplished successfully recently. Using the finite difference time domain (FDTD) method a design of a gallium phosphide (GaP) micro-lens array (MLA) optically integrated with a microprobe array has been fulfilled. The measured full width half maximum (FWHM) spot size is only  $520\text{ nm}$  after the fabrication of the GaP MLA [10]. The MLA design and fabrication used in a near-field parallel optical head is also demonstrated.

Some aspects related to the design of a nano-focusing probe intended for a near-field optical head are presented in this report.

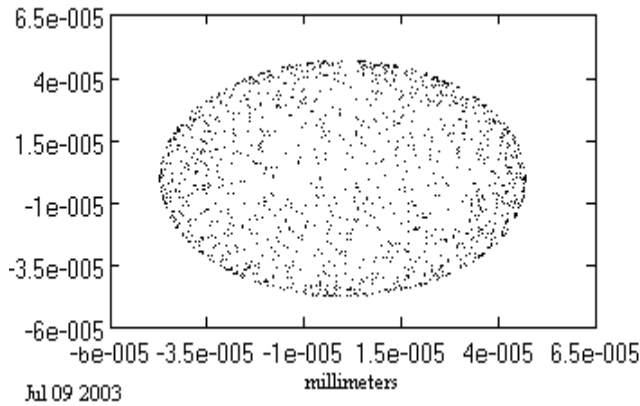
## **2. Design of Micro-lenses for Ultra-high Density Optical Storage**

The main ultra-high density optical storage (UHDOS) requirement is to design free of aberrations nano-focusing recording modules applied in arrayed memory heads and to fabricate nano-photonics integrated structures. We discuss the design characteristics and further methods for amendments the optical performance of the nano-focusing probe realized for a UHDOS system. Some results derived in the development process of nano-focusing probe optimization applying anti-reflection coatings (ARCs) are reported. The balancing of the residual aberrations and technological errors is also evaluated for the developed near-field optical head. This research focuses on the nano-probe configurations with the possible aberration solutions, the recording specifications and theoretical background of the problem, the micro lens (ML) shape and calculation formulae, the ray and wave front analysis, the nano-spots energy distribution and optical power density computing using FDTD numerical method [11].

A preliminary ray-trace analysis of the micrometer-scale lens structure is carried out using the “Interactive Ray Tracing” software [7]. An optical focusing configuration for a spherical surface having a diameter of  $10\ \mu\text{m}$  and focal length of  $10\ \mu\text{m}$  is given in Fig.1a. A computing of 3500 nano-focused rays with the aid of this micro-lens to a spot size under  $85\ \text{nm}$  is shown in Fig. 1b.



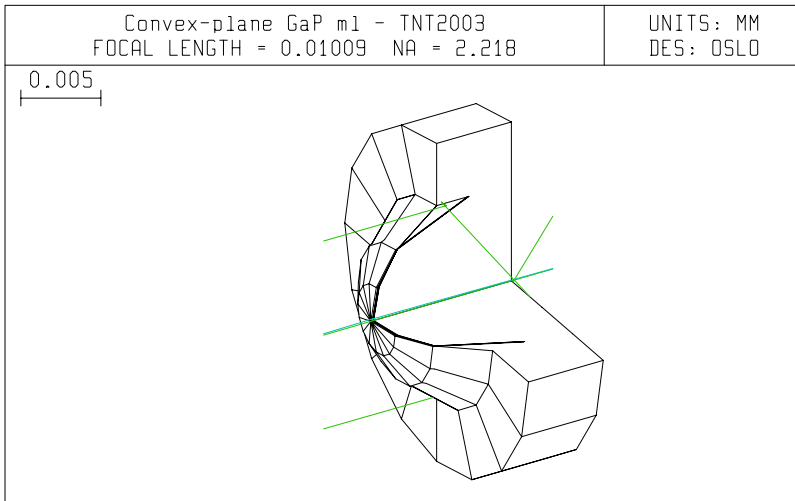
a



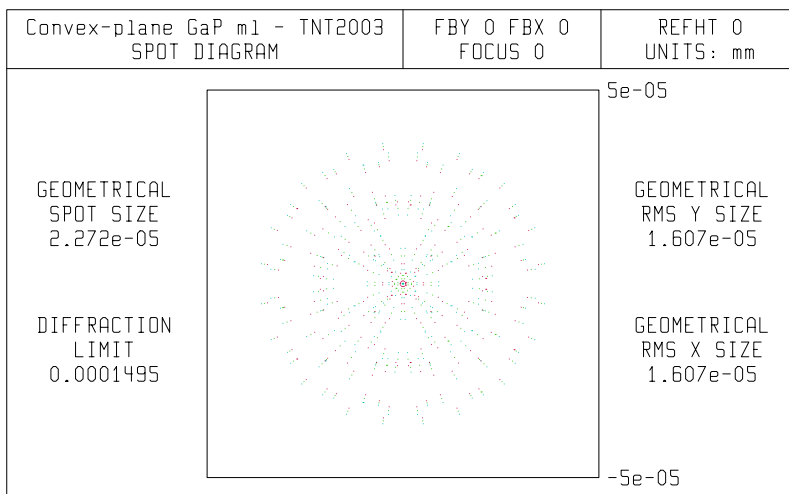
b

Fig. 1. Preliminary ray-trace analysis for a spherical micro-lens

The only ML refractive surface (Fig. 2) focuses a VCSEL beam on the ML rear plane surface. The ML module must be corrected for transversal aberrations on the exit flat GaP surface. The axially symmetric optical surface can be fabricated as spherical or aspherical [7]. The exact ML surface is ellipsoidal for this developed near-field optical head. The nano-aspherization of the ML convex surface is fulfilled using reactive ion etching (RIE) technology during the super-polishing process [7, 12]. The maximal nano-polishing value is about 150 nm on the periphery area of the ML surface having a diameter of 13  $\mu\text{m}$  (Fig. 2a).



a

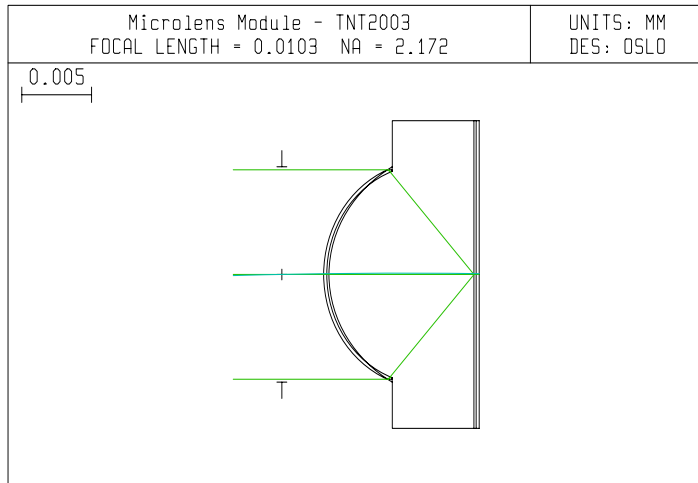


b

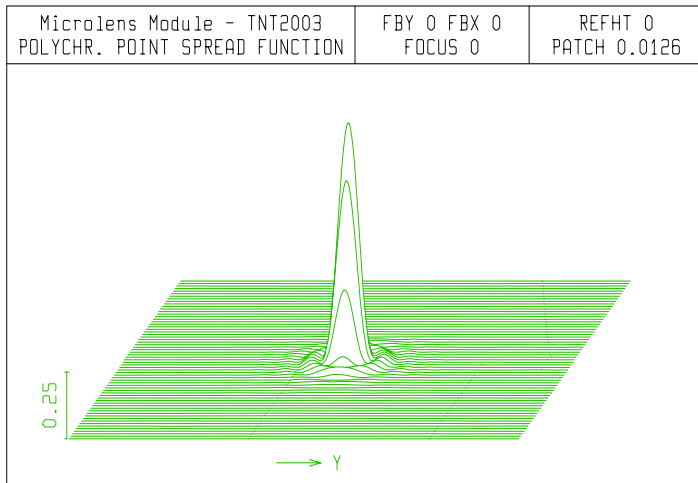
Fig. 2. Micro-lens with aspherical frontal surface

High numerical aperture (NA) convex-plane ML module is designed also using the Optical Software for Layout and Optimization (OSLO). The obtained ML component having NA = 2.17 with anti-reflection coatings (ARCs) is presented in Fig. 3a and the point spread function on the rear ML plane surface with deposited ARCs is given in Fig.3b.





a



b

Fig. 3. High numerical aperture (NA) convex-plane micro-lens (ML) module

### 3. Wave-optics Nanofocusing Numerical Modelling

Finite Difference Time Domain (FDTD) Method [11] is used for 3-D simulation of electromagnetic field (light) propagation of in a non-magnetic environment using. The derivatives in the time are expressed by finite difference approximations. The Maxwell's equations in this case are:

$$(1) \quad \nabla \times E(r,t) = -\mu \frac{\partial H(r,t)}{\partial t}, \quad \nabla \times H(r,t) = \sigma E(r,t) + \varepsilon \frac{\partial E(r,t)}{\partial t},$$

where  $E$  is electric fields,  $H$  is magnetic fields,  $\varepsilon$  is electric susceptibility of the medium,  $\mu$  is magnetic permeability of the medium and  $\sigma$  is media conductivity.

The temporal derivatives in these equations are written using finite difference approximations:

$$(2) \quad E^n = \frac{1 - \frac{\sigma \Delta t}{2\varepsilon}}{1 + \frac{\sigma \Delta t}{2\varepsilon}} E^{n-1} + \frac{\Delta t}{1 + \frac{\sigma \Delta t}{2\varepsilon}} \nabla \times H^{n-\frac{1}{2}},$$

$$(3) \quad H^{n+\frac{1}{2}} = H^{n-\frac{1}{2}} + \frac{\Delta t}{\mu} \nabla \times E^n,$$

where  $\Delta t$  is step in time and  $n$  is index of the respective step.

The spatial derivatives  $\nabla \times E(r,t)$  and  $\nabla \times H(r,t)$  are written by their components and are also presented using central finite difference approximation (Fig. 4).

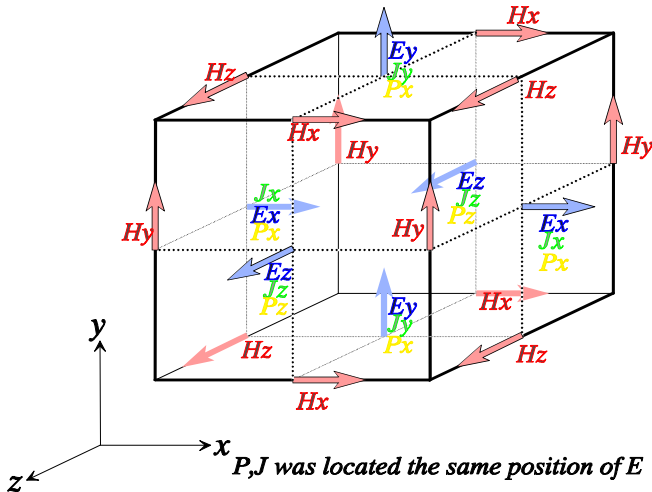
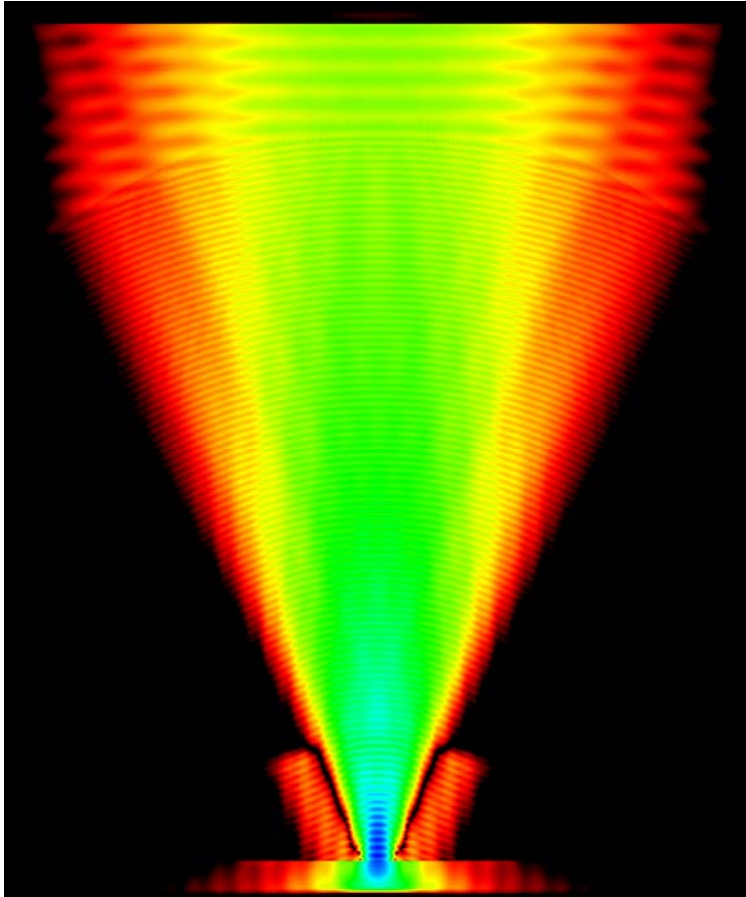


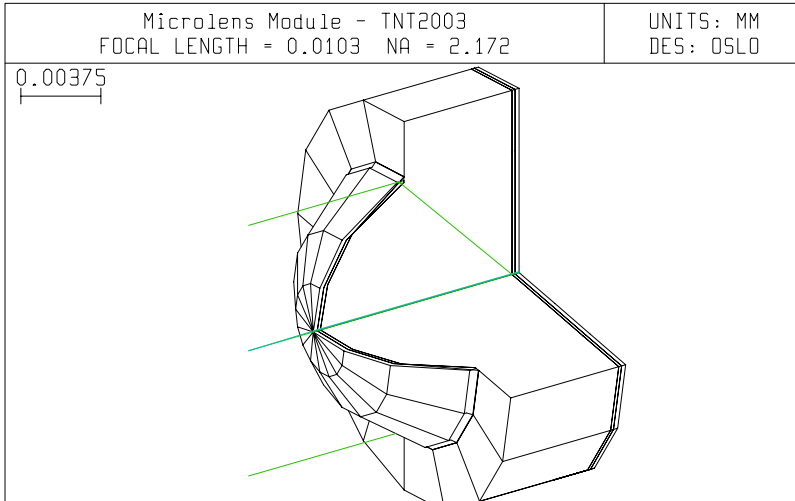
Fig. 4. 3-D spatial coordinates location in the vector cube

A pseudo color 2-D picture of the light propagation at a GaP wafer after a ML, made by the same optical material without surface NANO-focusing optimization, derived numerically by FDTD method is shown in Fig. 5. The focused spot diameter is about  $250\text{ nm}$ .

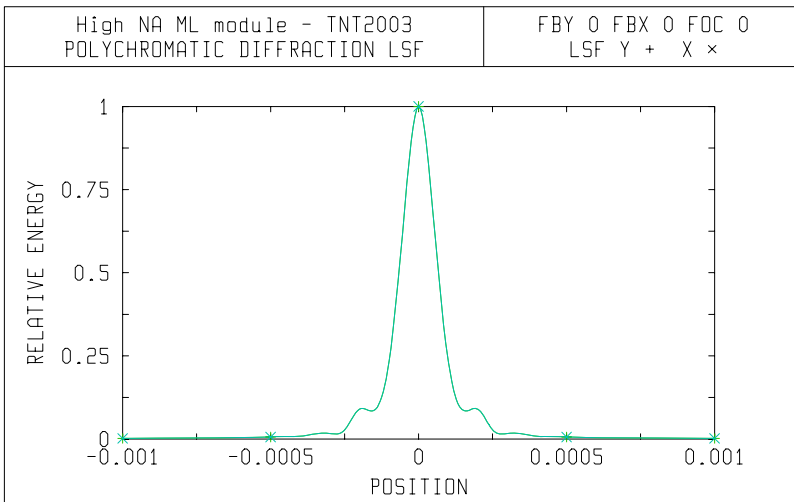


*Fig. 5. 2-D FDTD NANO-spot of about  $250\text{ nm}$*

An optimized 3-D structure of the GaP micro-lens with anti reflection coating, and the lens diffraction knife-edge function with a full width at half maximum (FWHM) size of  $130\text{ nm}$ , obtained by OSLO program, are plotted in Fig. 6.



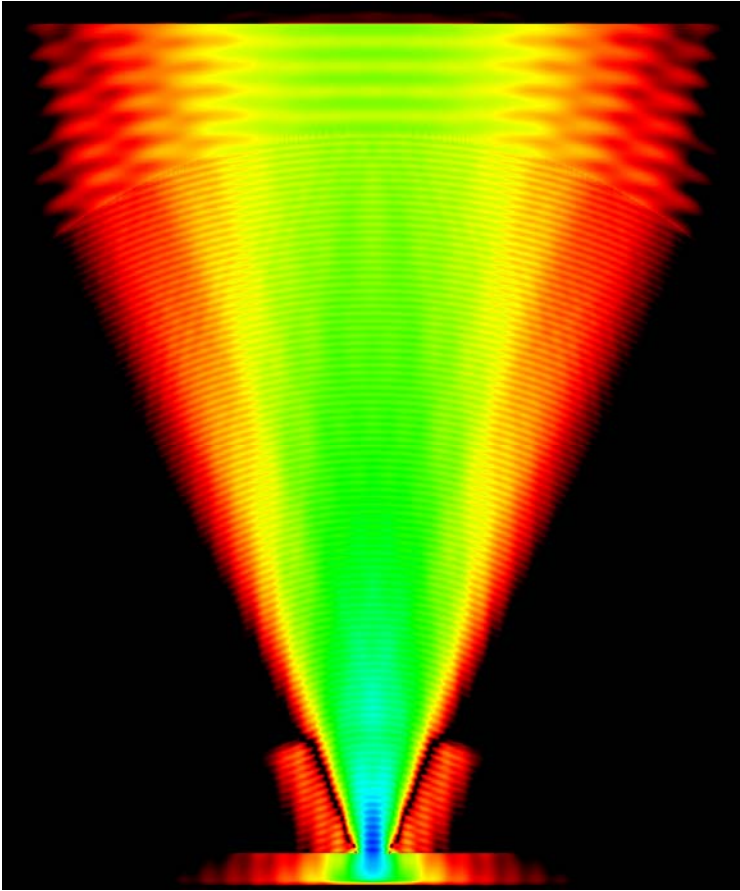
a



b

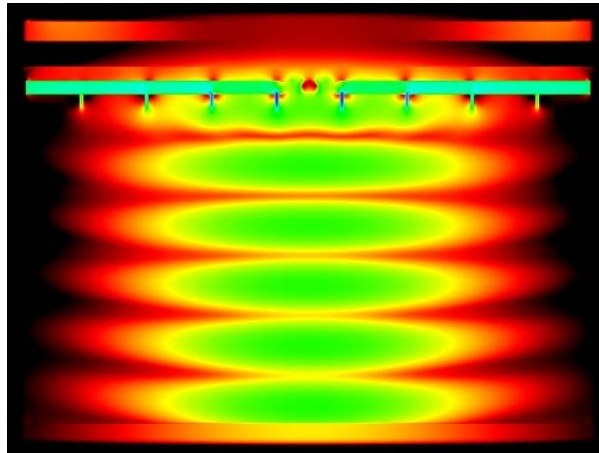
*Fig. 6. Nano-focusing module optical design*

The FDTD method 2-D pseudo color picture of the light propagation of this lens is presented in Fig. 7. Its optical power density is focused to a spot of 200 nm.

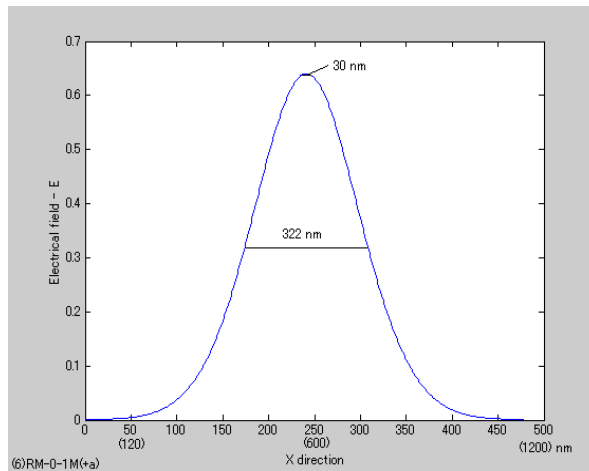


*Fig. 7. 2-D FDTD nano-spot of about 200 nm*

It is seen from the reported results that the optimization of nano-focusing system UHDOS by means of optical design software allows reaching the spot of the focused light energy with a minimum diameter of 200 nm. But in order to achieve recording terra byte densities on a standard optical disk with a diameter of 120 mm, the laser beam spot radius should be about 30 nm. Another physical principle is used in addition to satisfy this requirement. A computational domain structure is defined for FDTD-simulation, according to which a collimated light beam with wavelength  $\lambda = 780 \text{ nm}$ , propagating through a CaP wafer, is directed along a nano structured Au layer, deposited on the wafer surface. An aperture with diameter of 30 nm was made in the central part of this film (Fig. 8a).



a



b

Fig. 8. The 2-D electric field intensity distribution of in recording media plane

During the FDTD simulations the thickness of the gold coating, the distance between the teeth of the grating thickness or height have been varied, keeping fixed the nano-aperture diameter - 30 nm, the thickness of the air layer between the recording medium and Au layer - 20 nm, and the recording medium thickness - 20 nm. Configuration and dimensions of the nano-structure gold coating at which the laser light spot of 30 nm over the recording medium surface was obtained, delivering energy sufficient enough to realize its phase transition (Fig. 8b).

## 4. Conclusion

The ultra-high density near-field optical memories are under research and development (R&D), because a number of computer modules having tera-byte capacities can be fabricated at present [5 - 9, 13, 14]. The fabricated micro-lens is one of the basic elements of such memory. It is covered by ARC system of  $\text{SiO}_2/\text{Si}_3\text{N}_4$  type applied to the fabricated micro-lens as a hard protective structure [8, 9, 13]. After the nano-polishing process the GaP micro-lens array's plane surface is coated with a thin  $\text{Si}_3\text{N}_4$  protective layer. The optical sensitive IR film is sputtered over the  $\text{Si}_3\text{N}_4$  layer for the next nano-recording procedure. The obtained nano-focusing probe has an enlarged NA of 2.153 (Fig. 6). This NA value is about three times larger than the previous published result [5]. The optimized arrayed probe possesses nano-focusing energy efficiency about 43 times higher than the values published in the reports of the previous papers [8]. The computed nano-focused spots diameters are from 20 nm at the geometrical micro-lens limit, up to 130 nm at the diffraction FWHM size applying ARC systems (Fig. 3 and Fig. 6). The realized nano-focusing probe is an aberration-free optical system computed for geometrical spots and optimized for wave-front spread functions and FDTD spot sizes [9, 13].

Using an optimization with two-layer and one-layer anti-reflection coatings (ARC) one can obtain an energy throughput from 4.0 to 4.75 times higher than the output of the micro-lens without ARC [8]. The FDTD calculated spot size is limited to 200 nm for a micro-lens radius of 6  $\mu\text{m}$  (Fig. 7). This spot is near to the diffraction limit of 150 nm computed for the same ARC optimization design of the nano-focusing probe. An additional advantage of the ARC process is that it can fabricate multilayer nano-films having a good quality.

Additional application of gold nano-structured thin coating on the recording probe output surface allows further concentration of the light energy delivered through the optical focusing system in a nano-sized spot necessary to achieve terra-byte optical recording density and energy - quite sufficient for inducing a phase transition of the recording medium through available power of the VCSEL radiation. This option applied in combination with the produced micro-lens focusing system, provides a good potential for optimal design and implementation of a write/read head for the ultra-high density optical storage.

Video frames consist of an average volume about  $10^5$ - $10^6$  bits which reflects the visual speed of 0.1 - 0.05 s for the receiving simultaneous

images. The retina compresses visual information from  $10^{12}$  bits to  $10^6$  bits and the brain detects luminance and geometrical features of the observing objects [3, 4]. The video spectrometer generates hyperspectral cubes having from 300 to 900 monochrome pictures with capacity up to  $10^9$  bits for every one Earth's strip [15, 16]. The remote camera records up to 60-100 thousand color images during one circle over the Earth requiring a tera-byte optical memory with information capacity of  $10^{12}$  bytes. Our research efforts continue with the lab-grade fabrication of experimental near-field parallel nano-focusing heads applied in the high-density disk memories. The innovative aerospace optical systems are under R&D intended for the generation and remote transmission of million color and spectral-zonal images of the Earth's surface. This volumetric remote data can be stored using parallel tera-byte optical memories.

## References

1. Мишев, Д. Дистанционни изследвания на Земята от Космоса. Издат. на БАН, София, 1981
2. Michnev, D. Spectral Characteristics of Natural Formations. BAS Publishers, Sofia, 1986
3. Николов, И. Оптични методи и системи (за запис и обработка на информация). Унив. издат. „Св. Климент Охридски“, София, 1993
4. Мардиросян, Г. Природни екокатастрофи и тяхното дистанционно аерокосмическо изучаване. Акад. издат. „Проф. Марин Дринов“, София, 2000
5. Psaltis, D., M. Neifeld, A. Yamamura, S. Kobayashi. Optical memory disks in optical information processing. Applied Optics, 29, 1990, 2038-2057
6. US patent 6084848 Two-dimensional near-field optical memory head, Goto K. Tokyo, Japan 2000
7. Nikolov, I. D., K. Goto, S. Mitsugi, Y. Kim, V.I. Kavadjиков. Nanofocusing recording probe for an optical disk memory, Nanotechnology, 13, 2002, 471-477
8. Nikolov, I., K. Kurihara, K. Goto. Nanofocusing Probe Optimization in a Near-Field Head for an Ultra-High Density Optical Memory. Chapter 2 in Focus on Nanotechnology Research, Ed. Eugene V. Dirote, pp. 19-49, Nova Science Publishers, Inc., New York, 2004
9. Nikolov, I.D. Nanofocusing probe limitations for an ultra-high density optical memory, Nanotechnology, 15, 2004, 1076 – 1083
10. Kurihara, K., I. Nikolov, S. Mitsugi, K. Nanri, K. Goto. Design and Fabrication of Microlens Array for Near-Field Vertical Cavity Surface Emitting Laser Parallel Optical Head. Optical review, 10, 2003, 89-95.
11. Musa, S. Computational Nanotechnology Using Finite Difference Time Domain, CRC Press, 2013



12. C o b u r n, J. W. Plasma etching and reactive ion etching. American Institute of Physics Publ. 1982
13. N i k o l o v, I.D. Nanofocusing devices development and nano-medicine, Current Nanoscience, 3, 2005, 211 – 224
14. H e r z i g, H. P. Micro-Optics: Elements, Systems and Applications. CRC Press. 1997
15. M a r m o, J. Hyperspectral imager will view many colors of Earth. Laser Focus World, August 1996, 85-91
16. S c h o t t, J. Spectral data adds a new dimension to remote imaging of Earth. Laser Focus World, August 2004, 76-84

## **МИКРО- И НАНО-ФОКУСИРАЩА ОПТИКА, ПРЕДНАЗНАЧЕНА ЗА ДИСТАНЦИОННИ ИЗОБРАЖАВАЩИ СИСТЕМИ**

*В. Кавърджиков, Д. Пашкулева, Ив. Николов*

### **Резюме**

Обсъдени са възможни приложения на нано-фокусираща оптика при авиокосмически дистанционен мониторинг. Представени са оптични системи за микро-фокусиране, съставени от модули, съдържащи лещи с коригирани аберации, както и оптични системи за нано-фокусиране при оптични CD/DVD глави за четене и запис на информация с терабайтова плътност. Анализирани са дифракционно ограничени фокусни петна с диаметри от 400 *nm* до 200 *nm*. За създаване на оптичните запаметяващи устройства с терабайтова плътност на записа са използвани технологии за концентриране на лазерната енергия в петна с размери от 200 *nm* до 30 *nm*, основани на оптиката на близкото поле. Докладвани са техники за преобразуване на различни лазерни снопове светлината чрез хибридни лещи, в които асферична пречупваща повърхност коригира надлъжните сферични аберации. Дифракционната повърхност въвежда отрицателна дисперсия и премахва хроматичните аберации в равнината на изображението. Представени са примери за числено моделиране на нано-фокусиране в пространството на вълновата оптика изпълнен чрез метода на крайните разлики, развит във времето. Визирани са видео-спектрометри и системи за дистанционен мониторинг чрез системи за запис и обработка на изображения като платформи за оптична памет с терабайтова плътност.

## **SATURATED HYDRAULIC CONDUCTIVITY COEFFICIENT MEASUREMENTS OF BALKANINE™ AND TURFACE® SUBSTRATA THROUGH THE CONSTANT HEAD METHOD**

*Konstantin Metodiev*

*Space Research and Technology Institute – Bulgarian Academy of Sciences  
e-mail: komet@mail.space.bas.bg*

### ***Abstract***

*In the paper hereby results obtained after conducting laboratory measurements of saturated hydraulic conductivity coefficient are presented. The utilized method follows the Constant Head approach. The tested soil samples are zeolite substratum Balkanine™ and clay substratum Turface®. These are artificial media mostly used in greenhouses for plant cultivation on-board space stations under microgravity conditions. The laboratory equipment is discussed and the results are put down for different substrata fractions.*

### **Introduction**

The main objective of studying the hydrodynamic properties of plant root artificial media is selecting an optimal fractional composition of the substrate in order to use it on-board a space greenhouse. By way of example, related experiments were carried out on-board Salyut-7 space station back in 1985, [1]. The goal was studying capillary raise of water within a substratum under microgravity conditions.

In the present study, the saturated hydraulic conductivity coefficient is examined regarding two artificial media extensively used in space experiments. A mineral substratum, based on natural zeolite from a Bulgarian deposit, has been developed since 1979, [2]. This substratum is enriched by nutritive substances further and is called Balkanine™. Another substratum used is Turface®, [3]. The results eventually give a correct idea

of time required for water to move through the media under saturated conditions.

There are two main laboratory methods of analysis that are based on Darcy's law: the constant head (steady state) and the falling head (unsteady state), Wit [4]. In the present article the former approach is solely used. The experiment is motivated by lack of data for the artificial media mentioned above.

## Materials and Methods

The method of study makes use of the U-shaped interconnected vessels' property. It implies that the fluid level is preserved in both arms provided no external pressure is applied onto either of them. The scheme of the experimental set-up is shown in Fig. 1. The main elements are: 1) a cylindrical tube filled with substratum being tested, 2) a socket union fitting with a net with large clearance protecting the substrate from falling, 3) a funnel with an overflow weir, and 4) a drain tube mounted on top of the pipe. The excessive pressure was set by the funnel that went up every 10 cm, thus altering the system equilibrium. The exact water level in the funnel was guaranteed by a weir mounted inside. The filtrate was collected from the drain tube mounted on the main tube's upper end. For a given level of the funnel (head), time for collecting 1 liter of filtrate was measured. This time depends on the excessive pressure value (head), the substratum fraction, and the substratum degree of sealing (treading-in). The amount of water expended on the current measurement was being recovered through an external tank. Each substratum sample was poured and left undisturbed in the container. Prior to measurement, initial soaking in water within one day was performed in order to let the air bubbles out of the tube. What is more, due to the Balkanine dual porosity, the soaking procedure is mandatory so that the micro pores have enough time to get filled in with water.

The experimental goal is determining a relation between the flux

$$(1) \quad J = \frac{Q}{At}, \quad \text{cm}^3 \cdot \text{cm}^{-2} \cdot \text{s}^{-1}$$

and the hydraulic gradient

$$(2) \quad i = \frac{\Delta H}{h}, \quad \text{cm} \cdot \text{cm}^{-1}$$

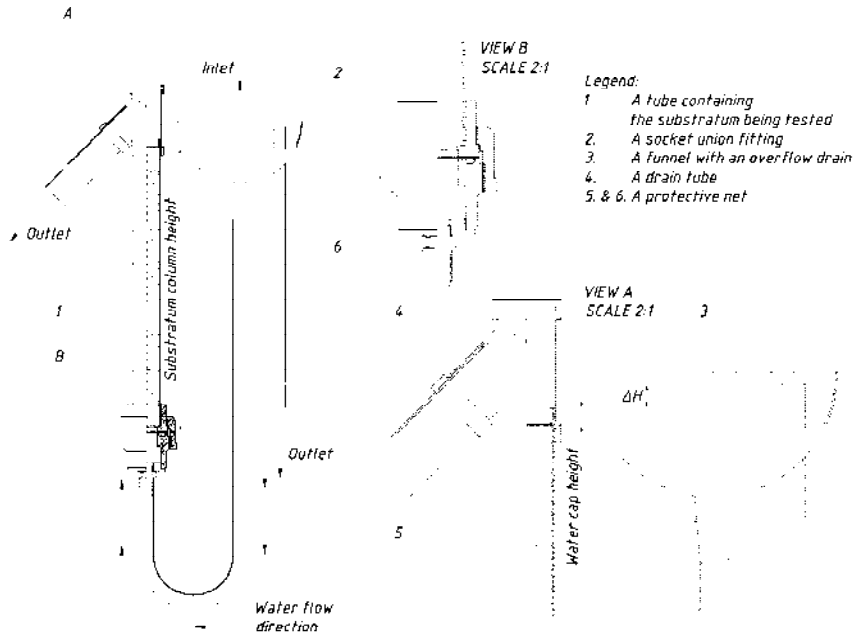


Fig. 1. The experimental stand layout ensuring constant head value  $\Delta H$

In formula (1)  $Q$  is the amount of water, mL, flowing through the cross section  $A$ ,  $\text{cm}^2$ , per unit time  $t$ , s. In formula (2)  $\Delta H$  represents sum of the substratum column, cm, and the top water column, cm  $\text{H}_2\text{O}$ , heights. In addition,  $h$  is the substratum column height, cm, alone. The saturated hydraulic conductivity coefficient  $K_s$ , cm/s, following Darcy, is a constant angular coefficient defining a linear relation between the variables  $J$  and  $i$ . Hence, expressed in terms of finite differences, this coefficient is computed within linear part of the chart according to the formula:

$$(3) \quad K_s = \frac{\Delta J}{\Delta i}, \quad \text{cm.s}^{-1}$$

## Results

Initial data: temperature 20 °C, ambient pressure 101325 Pa, tube internal diameter 4.6 cm. A tap water was used for all experiments with temperature 10 °C.

Substratum Balkanine, fraction 2 ÷ 3 mm, was studied first at different head values, i.e. 10, 20, 30, and 40 cm H<sub>2</sub>O column. The slowest experiment lasted up to 7 min and took place at 10 cm head. The substratum column was 48.5 cm high. The water column above the substratum was 2 cm high. The results are shown in Table 1.

Table 1. Balkanine 2 ÷ 3 mm

Flow Rate, mL/sec		Flow Rate, mL/sec		Flow Rate, mL/sec		Flow Rate, mL/sec	
Head 10 cm	2,848	Head 20 cm	3,878	Head 30 cm	6,280	Head 40 cm	8,630
	2,569		3,789		6,205		8,609
	2,361		3,740		6,218		8,498
	2,192						
	2,085						
Mean	2,411	Mean	3,802	Mean	6,234	Mean	8,579
StdErr	0,122	StdErr	0,033	StdErr	0,019	StdErr	0,033

In accordance with formula (3), the saturated conductivity coefficient  $K_s = 0.6$  cm/s.

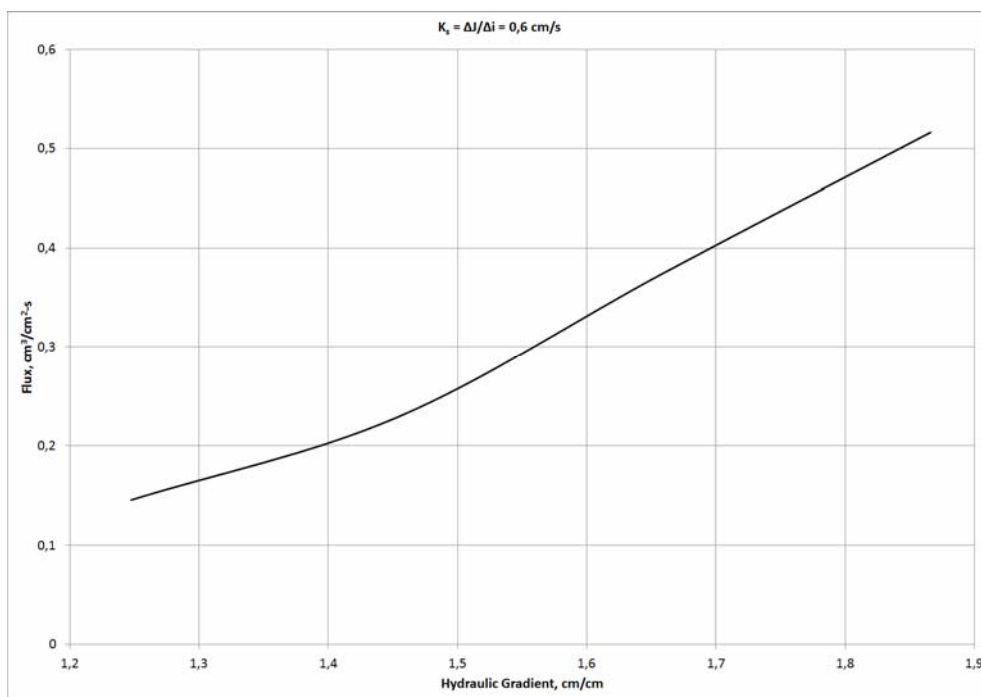


Fig. 2. Balkanine, fraction 2 ÷ 3 mm

The same experiment was carried out with substratum Balkanine, fraction  $1.5 \div 2$  mm. The substratum column was 48.6 cm high. The water column above the substratum was 2 cm high. The results are put down in Table 2.

Table 2. Balkanine  $1.5 \div 2$  mm

Flow Rate, mL/sec		Flow Rate, mL/sec		Flow Rate, mL/sec	
Head 20 cm	1,828	Head 30 cm	2,389	Head 40 cm	4,133
	1,759		2,288		3,647
	1,685		2,311		3,386
					3,259
Mean	1,758	Mean	2,329	Mean	3,606
StdErr	0,034	StdErr	0,0250	StdErr	0,167

The experiment was initiated at 40 cm head in order to let the substratum particles redistribute within the volume thus having the substratum subsided. Head of 10 cm H<sub>2</sub>O column hasn't been considered here because the water flow is too slow. In this case, the saturated conductivity coefficient  $K_s = 0.27$  cm/s.

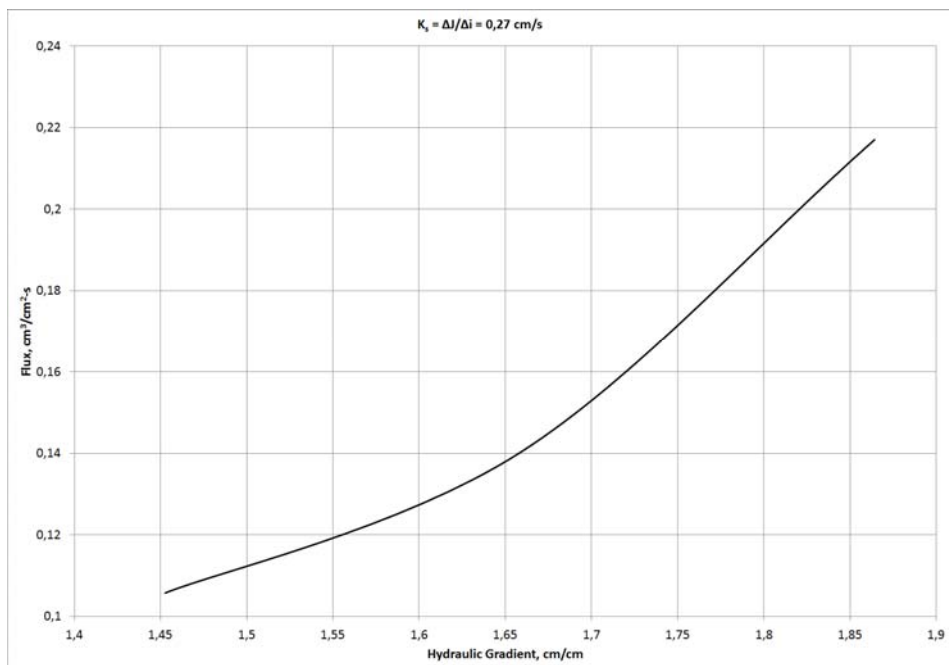


Fig. 3. Balkanine, fraction  $1.5 \div 2$  mm

Next experiment involved substratum Balkanine, fraction 1 ÷ 1.5 mm. The substratum column was 48.9 cm high. The water column above the substratum was 2 cm high. The results are reported in Table 3.

Table 3. Balkanine 1 ÷ 1.5 mm

Flow Rate, mL/sec		Flow Rate, mL/sec		Flow Rate, mL/sec	
Head 20 cm	0,987	Head 30 cm	1,511	Head 40 cm	2,742
	0,989		1,454		2,491
	0,993		1,418		2,314
					2,163
Mean	0,990	Mean	1,461	Mean	2,428
StdErr	0,001	StdErr	0,022	StdErr	0,108

The saturated conductivity coefficient  $K_s = 0.21$  cm/s.

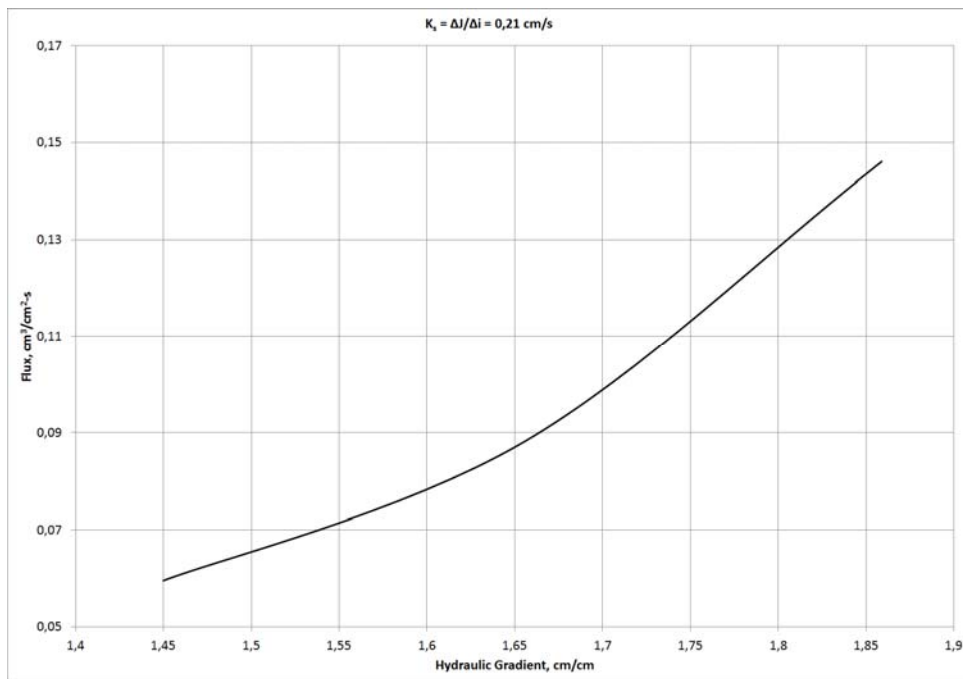


Fig. 4. Balkanine, fraction 1 ÷ 1.5 mm

Results concerning substratum Turface, fraction 1 ÷ 2 mm follow in Table 4. The substratum column was 48.8 cm high. The water column above the substratum was 2 cm high.

Table 4. Turface, fraction 1 ÷ 2 mm

Flow Rate, mL/sec		Flow Rate, mL/sec		Flow Rate, mL/sec	
Head 20 cm	1,110	Head 30 cm	1,696	Head 40 cm	2,480
	1,060		1,647		2,422
			1,577		2,290
Mean	1,085	Mean	1,640	Mean	2,398
StdErr	0,014	StdErr	0,028	StdErr	0,040

In this case, the saturated conductivity coefficient  $K_s = 0.19$  cm/s.

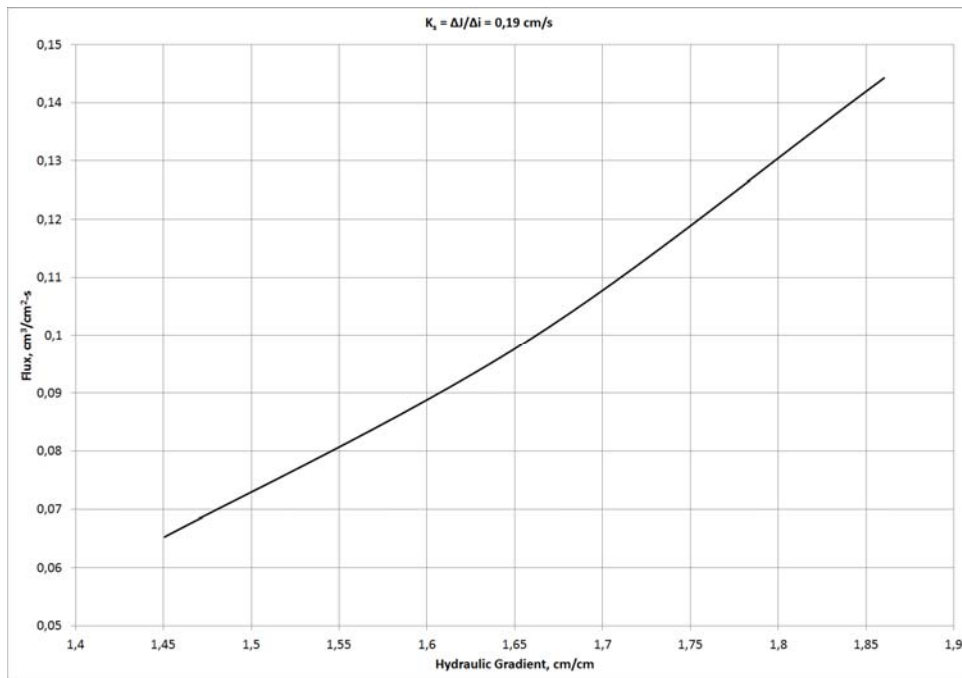


Fig. 5. Turface, fraction 1 ÷ 2 mm



## Conclusion

The proposed experiment has claims on following. The apparatus is simple and affordable enough so that one could carry out measurements with a large variety of soils. Moreover, little has been known so far about the proposed coefficient values of the substrata studied. Hopefully, this article retrieves the missing data.



*Fig. 6. An overview of the tube containing tested substratum*

## References

1. I v a n o v a, T., P. K o s t o v, N. K a n c h e v, S. S l a v c h e v, Studying Substratum Hydrodynamic Properties to Cultivate Plants under Microgravity Conditions, 20<sup>th</sup> Symposium in Space Biology and Medicine, Proceedings vol. II, p. 191, Berlin, DDR, 1987
2. S t o i l o v, G., I. P e t k o v, D. D i m i t r o v, (1979, Bulgarian Patent No 40343), Bulgaria
3. Profile Products LLC, Buffalo Grove, IL, USA
4. W i t, K. E. 1967. Apparatus for measuring hydraulic conductivity of undisturbed soil samples. Technical Bulletin 52. Institute for Land and Water Management Research, Wageningen, 12 p.

## **ИЗМЕРВАНЕ НА КОЕФИЦИЕНТА НА НАСИТЕНА ХИДРАВЛИЧНА ПРОВОДИМОСТ ЗА СУБСТРАТИ БАЛКАНИН И ТУРФЕЙС ПО МЕТОДА НА ПОСТОЯННИЯ ВОДЕН НАПОР**

*К. Методиев*

### **Резюме**

В настоящата работа са представени резултатите от измервания на коефициента на наситена хидравлична проводимост в лабораторни условия. Използван е методът на постоянния воден напор. Изпитваните почвени образци са зеолитен субстрат Балканин и глинен субстрат Турфейс. Това са изкуствени среди, използвани предимно в оранжерии за отглеждане на растения в условията на микрогравитация. Разгледано е лабораторното оборудване. Резултатите са получени за различни фракции на субстратите.

## NEW ANALYTICAL APPROACH FOR COSMIC RAY IONIZATION MODELING IN PLANETARY ENVIRONMENTS BY USING THE IONIZATION YIELD FUNCTIONS

*Peter Velinov*

*Space Research and Technology Institute – Bulgarian Academy of Sciences  
e-mail: pvelinov@bas.bg*

### **Abstract**

*The cosmic rays (CR) influence the ionization and electric parameters in the atmosphere and also the chemical processes (ozone creation and depletion in the stratosphere) in it. CR ionize the whole middle and lower atmosphere, i.e. the stratosphere and troposphere. The cosmic rays are a key factor affecting the atmospheric chemistry and the space weather and space climate in the Earth's environment.*

*Two approaches have been developed to compute the CR ionization, for example:*

- 1) the analytical model CORIMIA - COsmic Ray Ionization Model for Ionosphere and Atmosphere, and*
- 2) the statistical CORSIKA code, including the FLUKA Monte Carlo package, which is based on a Monte Carlo simulation of the atmospheric cascade. Usually the analytical models use the ionizing capability  $C$  function, while the statistical simulations utilize the ionization yield  $Y$  function.*

*In the present work we find connection between the functions  $C$  and  $Y$  and we will proceed to a unified approach to the calculation of atmospheric ionization due to cosmic rays with galactic (GCR), solar (SCR) and interplanetary (anomalous CR, ACR) origin. Formulas for ionizing capability and ionization yield functions are derived for general case, for relativistic approximation (GCR) and for sub-relativistic case (SCR and ACR). The input parameters in the proposed model include the full composition of the CR nuclei groups as follows: protons ( $p$ ,  $Z = 1$ ), alpha particles ( $\alpha$ ,  $Z = 2$ ), and HEZ particles: Light ( $L$ ,  $3 \leq Z \leq 5$ ), Medium ( $M$ ,  $6 \leq Z \leq 9$ ), Heavy ( $H$ ,  $10 \leq Z \leq 19$ ), Very Heavy ( $VH$ ,  $Z \geq 20$ ) and Super Heavy ( $SH$ ,  $Z \geq 30$ ) groups of nuclei.*

*Some practical applications of the obtained results are discussed. The results of the full Monte Carlo simulation which are tabulated in a form of the ionization yield function can be applied much more widely. With the help of the achievements of this work the analytical model CORIMIA can use the results of statistical code CORSIKA that will*

*allow comparison between the two approaches. As is known by CORSIKA is possible to estimate the CR ionization below 20-25 km and by the model CORIMIA - above this altitude. So those two approaches are complementary.*

*The proposed approach can be used at the quantitative consideration and analysis of the solar-terrestrial relationships and the problems of space weather and space climate. It is a theoretical approach and consequently can be applied also for the calculation of ionization effects in the planetary ionospheres and atmospheres.*

## **Introduction**

Presently, there are numerous arguments suggesting that the solar activity variability affects the global climate in different aspects and on different timescales. Several possible mechanisms have been suggested, which can be responsible for the observed relation between the solar variability and the climate: via the changing solar irradiance; by the UV heating of the stratosphere and the consequent circulation variations; or by cosmic rays affecting the cloud formation [1].

Galactic cosmic rays (GCR), solar cosmic rays (SCR) and anomalous cosmic rays (ACR) are responsible for the ionization in the atmosphere and lower ionosphere by electromagnetic and nuclear interactions [2, 3]. Because of their high energy (up to  $10^{21}$  eV) the particles, which originate from the Galaxy can react and produce ionization in the atmosphere until being absorbed in it. The influence of cosmic rays (CR) is important for the electric parameters and the chemical processes - ozone creation and depletion in the stratosphere [2, 4]. Therefore the cosmic rays determine the electric conductivity and influence the global electric circuit of the Earth. There is also combined hypothesis of CR-UV impact on the solar-atmosphere relationships [1].

Effectively the cosmic rays ionize the whole middle and lower atmosphere, i.e. the strato-mesosphere and troposphere. GCR create an independent cosmic ray layer in the lower part (50-80 km) of the ionospheric *D*-region [5, 6, 7, 8]. This cosmic ray layer was called *CR*- or *C*-layer. The contribution (up to several hundred electrons per cubic centimeter) of cosmic rays in the formation of *C*-layer has been confirmed experimentally by the data of rocket flights [9] and absorption measurements by the ionosphere's propagation of long radio waves [7, 8]. Initially the ionization, i.e. the electron production rate  $q$  [ $\text{cm}^{-3}\text{s}^{-1}$ ], of the

galactic cosmic rays in the atmosphere was determined by the empirical formula given in [9]. The electron production rate  $q(h)$  in the ionosphere have been theoretically calculated as a function of height  $h$  firstly in the work [5, 6]. The results obtained have been generalized in [10, 11]. There is used a realistic curved atmosphere to allow computing CR electron production rate profiles. The chemical composition of the atmosphere was taken as  $N_2$ ,  $O_2$  and Ar in the volume fractions of 78.1%, 21% and 0.9%, respectively. The ionosphere's electron density profiles were modeled by four latitudes:  $0^\circ$ ,  $30^\circ$ ,  $41^\circ$  and  $55^\circ$ .

Two approaches have been developed to compute the cosmic ray ionization: analytical and statistical. The mentioned works [10, 11] and the improved model CORIMIA - *COsmic Ray Ionization Model for Ionosphere and Atmosphere* (see the full description in [12]) are created by an analytical approximation of the ionization losses function of Bohr-Bethe-Bloch, while the statistical models are based on a Monte Carlo simulation of the atmospheric cascade [1, 13, 14]. The latter method is an improved Monte Carlo model which is based on an updated version of the CORSIKA code, including the FLUKA Monte Carlo package to simulate the low-energy nuclear interactions, and explicitly the direct ionization by primary CR particles [1, 13, 14].

Usually the analytical models [12] use the ionizing capability  $C$  function [10, 11], while the statistical Monte Carlo simulations utilize the ionization yield  $Y$  function [1, 13, 14]. In the present work we will find connections between the functions  $C$  and  $Y$  and we will proceed to a unified approach to the calculation of atmospheric CR ionization.

In this work also formulas for ionizing capability and ionization yield functions will be derived for relativistic (GCR) approximation, i.e. the particles with relative velocity

$$\beta = v/c \approx 1$$

where  $v$  is velocity of the CR nuclei and  $c$  is the light velocity. Then the sub-relativistic (SCR and ACR) case

$$\beta = v/c < 1$$

will be studied detailed and thus the results will be essentially generalized.

## 1. Model for Electron Production Rate Profiles

During their penetration in the atmosphere the cosmic rays cause ionization of the neutral components. Therefore free electrons are emitted. The ionization production rate  $q$  [ $\text{cm}^{-3}\text{s}^{-1}$ ] at height  $h$  [km] is calculated as a superposition of the effect of different groups of nuclei in the composition of cosmic rays. A three dimensional model for the electron production rate is used [5, 6, 10, 11, 15]:

(1)

$$q(h) = \sum_i q_i(h) = \sum_i \frac{1}{Q} \int_{E_i, \alpha=0}^{\infty} \int_{\theta=1}^{2\pi} \int_{\theta=1}^{\pi/2+\Delta\theta} D_i(E) \left( \frac{dE}{dh} \right)_i \sin(\theta) d\theta d\alpha dE,$$

where  $Q = 35$  eV is energy for formation of one electron-ion pair.  $\alpha$  is the azimuth angle,  $\theta$  is the angle towards the vertical,  $\Delta\theta$  takes into account that at a given height the particles can penetrate from the space angle ( $0^\circ$ ,  $\theta_{\max} = 90^\circ + \Delta\theta$ ), which is greater than the upper hemisphere angle ( $0^\circ$ ,  $90^\circ$ ) for a flat model.  $E_i$  are the corresponding energy cut-offs. The summation of the ionization integral (1) is made on the all groups of nuclei: protons p ( $i = 1$ ), alpha particles  $\alpha$  ( $i = 2$ ) and heavier groups of nuclei - HZE nuclei: light L ( $i = 3$ ), medium M ( $i = 4$ ), heavy H ( $i = 5$ ), very heavy VH ( $i = 6$ ) and super heavy SH ( $i = 7$ ) in the CR composition.

In the expression (1)  $E$  is the full energy (GeV/nuc) of the penetrating particles and the differential spectrum [ $\text{cm}^{-2} \text{s}^{-1} \text{sr}^{-1} \text{GeV}^{-1}$ ] is in the form:

$$(2) \quad D(E) = K E^{-\gamma}$$

$K$  and  $\gamma$  are constants for the galactic cosmic rays;  $(dE/dh)$  are the ionization losses of CR particles according to the formula of Bohr-Bethe-Bloch [9].

Currently, there are mainly three types of models for calculation of the ionization rates in the ionosphere and atmosphere [16]:

- 1) thin target model (for the ionosphere, above 50 km),
- 2) intermediate target model (for the ozonosphere, 30-50 km), and
- 3) full target model (for the troposphere and lower stratosphere, below 25-30 km).

The present paper concerns: 1) the thin target, and 2) the intermediate target models. For the lower and middle atmosphere below 25-30 km, the full target models 3): CORSIKA, GEANT4, etc., are used [16]. These models are not applicable for altitudes above 25-30 km because of the small atmosphere depths there. They require atmospheric depths of at least 3-4 g/cm<sup>2</sup>.

Since the galactic cosmic rays penetrate isotropically from the upper hemisphere from (1) it follows the more simple expression:

$$(3) \quad q(h) = \frac{2\pi}{Q} \int_{E_c}^{\infty} D(E) \left( \frac{dE}{dh} \right) dE$$

as the multiplier  $2\pi$  shows this isotropic influx of the galactic particles;  $E_c$  is the corresponding geomagnetic cutoff energy in GeV/nucl.

The variable of integral (3) can be not only the energy of the CR particles, but also their rigidity  $R$  (GV). In this case the differential spectrum [ $\text{cm}^{-2} \text{s}^{-1} \text{sr}^{-1} \text{GV}^{-1}$ ] will be

$$(4) \quad D(R) = K R^{-\gamma}$$

as the energy cutoff  $E_i$  in (3) must be replaced by the corresponding geomagnetic threshold of rigidity  $R_c$  (GV).

### 1.1. Analytical and Statistical Approaches in Ionization Models and Relationships between them

At the analytical approach the electron production rate  $q(h)$  is closely connected with the cosmic ray ionizing capability. In general the ionizing capability function  $C(h)$  at given altitude  $h$  with atmospheric density  $\rho$  [ $\text{g cm}^{-3}$ ] is determined by the expression [10, 11]:

$$(5) \quad C(h) = q(h) / \rho(h)$$

This function physically represents the number of electron-ion pairs produced in one gram of matter (in this case atmospheric air) per second and characterizes the ionization effectiveness of the radiation factor.

In the statistical approach is calculated initially the ionization yield function  $Y$  [1, 14, 16] which gives the number of ion pairs produced in one

gram of the ambient air at a given atmospheric depth by one nucleon of the primary cosmic ray particle with the given energy per nucleon. Then, the integration by energy is carried out. In this approach all results depend on exact atmospheric density profile. In order to minimize this uncertainty, the CR ionization is computed per gram of the atmospheric matter rather than per  $\text{cm}^3$ . In this case, the uncertainties of the  $q(h)$ , computed using different atmospheric density profiles, do not exceed 1–2% in the low troposphere, which is less than statistical errors of computations.

We want to combine the mentioned two approaches. For this purpose we introduce the function  $Y$  [1, 13, 14, 16] in the expression (3) after which we derive the formula:

$$(6) \quad q(h) = \int_{E_c}^{\infty} D(E)Y(E, h)\rho(h)dE$$

Here  $\rho(h)$  is the density of atmosphere [ $\text{g cm}^{-3}$ ] at height  $h$  and the ionization yield function  $Y$  [electron-ion pairs  $\text{sr cm}^2 \text{g}^{-1}$ ] can be represented as:

$$(7) \quad Y(E, h) = \frac{2\pi}{Q} \left( \frac{1}{\rho} \frac{dE}{dh} \right)$$

Thus, the wanted connection between the functions  $C(h)$  and  $Y(h)$  will be:

$$(8) \quad C(> E_c) = \int_{E_c}^{\infty} D(E)Y(E, h)dE$$

Actually the CR ionizing capability  $C(h)$  depends on the function of ionization losses and ionization potential of the medium  $Q$ , on the type of CR nuclei (or group of nuclei: p, He, L, M, H, VH and SH), on their spectrum and geomagnetic threshold of rigidity.

## 1.2. General Formulas for Ionization Yield Function

Using the relation (7) and the expression for ionization losses [5, 6, 10, 11] we can write the following formula for the ionization yield function:

$$(9) \quad Y(E) = \frac{2\pi}{Q} \frac{0.3 Z^2}{\beta^2} \left( \ln \frac{E}{E_0} \beta + 4.5 - \frac{\beta^2}{2} \right)$$



where  $Z$  is the charge of the penetrating CR particle,

$\beta = v/c$  is the relative velocity, where  $v$  is velocity of the particle and  $c$  is the light velocity;

$E$  and  $E_0$  are the full energy and rest energy of the CR nuclei.

The relationship between  $E$  and  $E_0$  is established using the relativistic equations [11]:

$$(10) \quad E = \frac{E_0}{\sqrt{1-\beta^2}} \quad \text{or} \quad \beta = \frac{\sqrt{E^2 - E_0^2}}{E}$$

$$(11) \quad E = Mc^2 \quad \text{and} \quad E_0 = M_0c^2$$

where  $M$  and  $M_0$  are the mass and rest mass of the particles. If we substitute (10) in (9) we obtain the following expression for the ionization yield function of penetrating CR particles:

$$(12) \quad Y(E) = \frac{2\pi}{Q} 0.3 Z^2 \frac{E^2}{E^2 - E_0^2} \left( \ln \sqrt{E^2 - E_0^2} + 4.5 - \frac{1}{2} \frac{E^2 - E_0^2}{E^2} \right)$$

The rest mass of a proton is  $938 \text{ MeV } c^{-2}$ , i.e.  $E_0 = 0.938 \text{ GeV } c^{-2}$ . If we put

$$(13) \quad E_0^2 = 0.879844 \approx 0.88$$

in (12) we receive the following more concrete presentation:

$$(14) \quad Y(E) = \frac{2\pi}{Q} 0.3 Z^2 \frac{E^2}{E^2 - 0.88} \left( \ln \sqrt{E^2 - 0.88} + 4.5 - \frac{1}{2} \frac{E^2 - 0.88}{E^2} \right)$$

In the development of some problems it is more convenient to use simplified and symmetric equations. That is why sometimes the energy in cosmic ray physics is expressed in units  $E_0 = 0.938 \text{ GeV}$ . In this case, the equation (14) will pass into:

$$(15) \quad Y(E) = \frac{2\pi}{Q} 0.3 Z^2 \frac{E^2}{E^2 - 1} \left( \ln \sqrt{E^2 - 1} + 4.5 - \frac{1}{2} \frac{E^2 - 1}{E^2} \right)$$

This expression will be exploited in the future when examining the variety of cases of cosmic ray influences of the ionization state of the middle atmosphere.

## 2. Relativistic Case – Galactic Cosmic Rays

### 2.1. Relativistic Approximation

Since the galactic cosmic rays are with relativistic energies, then the condition

$$\beta = v/c \approx 1$$

(exactly fulfilled at lower and middle geomagnetic latitudes) is valid. After assuming this ratio from ionization yield function equation (9) follows:

$$(16) \quad Y(E) = \frac{2\pi}{Q} 0.3 Z^2 \left( \ln \frac{E}{E_0} + 4 \right)$$

This means that

$$(17) \quad E \gg E_0 \quad \text{or} \quad E \approx E_k$$

where

$$(18) \quad E_k = E - E_0$$

is the kinetic energy of the particle. If we place  $\ln E_0 = \ln 0.938$  in (16), we will receive the formula:

$$(19) \quad Y(E) = \frac{2\pi}{Q} 0.3 Z^2 (\ln E + 4.064)$$

or

$$(20) \quad Y(E) = \frac{2\pi}{Q} 0.3 Z^2 (\ln E + 4)$$

if the energy is expressed in units  $E_0 = 0.938$  GeV.

## 2.2. Formulas for Ionizing Capability

After substitution the last derived expression (20) in (8) and after the appropriate solution of the integral, we will receive the following formula for the ionizing capability:

$$(21) \quad C(> E_c) = 5.4 \times 10^4 D(> E_c) Z^2 \left( \ln E_c + \frac{1}{\gamma - 1} + 4 \right)$$

where  $D(> E_c)$  is the CR integral spectrum and  $\gamma = 2,5 - 2,6$  is the exponent in differential spectrum [5, 6, 11]. If this exponent  $\gamma$  laid on its average value and if we take into account the relationship  $\ln E_c = 2,3 \lg E_c$ , we will receive the more convenient formula:

$$(22) \quad C(> E_c) = 1.24 \times 10^5 D(> E_c) (\lg E_c + 2)$$

as the energy is expressed everywhere in a natural unit  $E_0 = 0.938$  GeV.

By the formulas (20, 21) can be found another connection between the integrated ionizing capability and the ionization yield function:

$$(23) \quad C(> E_c) = D(> E_c) \left( Y(E_c) + 5.4 \times 10^4 \frac{Z^2}{\gamma - 1} \right)$$

$Y$  function may be represented also through geomagnetic rigidity  $R$  taking into account the ratio [3]:

$$(24) \quad R = (A/Z) E$$

$A$  is the atomic weight and  $Z$  is the charge of the particle. If we use the relationship (24), the following expression in the relativistic case is obtained from (21):

$$(25) \quad C(> R_c) = 5.4 \times 10^4 D(> R_c) Z^2 \left( \ln \frac{Z}{A} R_c + \frac{1}{\gamma - 1} + 4 \right)$$

In this formula may be accounted the different characteristics of cosmic ray particles, for example relations  $A/Z = 1$  for protons and  $A/Z \approx 2$  for heavier nuclei. Thus this formula can be further elaborated.

It should be noted that the particles with the ratio of  $A/Z > 1$  are less deflected by the geomagnetic field, which, in combination with their weaker

heliospheric modulation, makes them very important for the CR ionization [1].

If we take into account the real GCR composition, we can deduce the following a simplified expression:

$$(26) \quad C(> R_C) = 1.56 \times 10^5 D(> R_C) (\ln R_C + 4.15)$$

As the galactic cosmic rays consist of 87% protons (from all nuclei), it is convenient the ionizing capability to be expressed by the integral spectrum of protons:

$$(27) \quad C(> R_C) = 1.8 \times 10^5 D_p(> R_C) (\ln R_C + 4.15)$$

which is suitable for practical calculations.

The following two factors significantly affect ionizing capability  $C$ :

i) latitudinal effect, and ii) 11-years variations of galactic cosmic rays.

i) The latitudinal effect can be shown clearly by expressing the integral spectrum and geomagnetic cut-off rigidity in (26) through the rigidity and then through the geomagnetic latitude  $\lambda_m$ . For this purpose we replace the spectrum (4) in (26), as a result of which we obtain:

$$(28) \quad C(> R_C) = 1.8 \times 10^5 K_p \frac{\ln R_C + 4.15}{(\gamma - 1) R_C^{(\gamma-1)}}$$

Now we will express  $R_C$  by means of the approximation [10, 11]

$$(28) \quad R_C \cong 14.9 \cos^4 \lambda_m$$

in which the geomagnetic field is represented as a dipole. It follows from (28) at

$$\gamma = 2.5$$

that

$$(29) \quad C(> R_C) = 6.3 \times 10^3 K_p \frac{0.576 \ln \cos \lambda_m + 1}{\cos \lambda_m^6}$$

which visibly expresses the latitudinal effect in the distribution of cosmic ray ionizing capability.

ii) The 11-years variations of primary galactic cosmic rays. Their ionizing capability is expressed in the opposite variations of the variations of solar activity levels and the cosmic ray flux. At polar geomagnetic latitudes the integral particle flux increases during the period of the solar minimum twice in relation to the flux in solar maximum, while at equatorial region the variation is small. At middle latitudes the variation is significant.

The galactic cosmic rays initiate a nucleonic-electromagnetic cascade in the atmosphere, affecting its physical-chemical properties and ion balance [1, 13, 14, 16]. This is a dominant source of ionization of the troposphere and stratosphere [1, 11, 17]. Therefore a detailed model of the GCR ionization makes a solid basis for an investigation of the mechanisms of solar-terrestrial physics. The galactic cosmic rays are a key factor affecting the atmospheric chemistry (e.g. the ozone distribution [17, 18]) and the space weather in the extraterrestrial space.

### **3. Sub-relativistic Case – Solar and Anomalous Cosmic Rays**

All types of cosmic rays (GCR, SCR and ACR) influence in a different manner the iono/atmosphere systems of the Earth and planets. The solar cosmic rays produced in solar flares (and in some other high-energy solar processes) are one of most important manifestation of solar activity and one of the main agents in solar-terrestrial relationships. The solar cosmic rays have sufficient energy and intensity to raise radiation levels on Earth's surface. This event is termed a "Ground Level Enhancement" (GLE) [19]. Solar cosmic rays consist of protons, electrons, helium ions, and HZE ions with energy ranging from a few tens of keV to GeV. They are ejected primarily in solar flares and coronal mass ejections (CME). They have a composition similar to that of the Sun, and are produced in the corona by shock acceleration, or when part of the solar magnetic field reconfigures itself.

Moreover the anomalous cosmic rays (ACR) are accelerated in the outer heliosphere from pick-up ions that primarily originate as interstellar neutrals. ACR, among the most energetic particle radiation in the Solar system, are thought to be produced at the termination shock - the boundary at the edge of the Solar system where the solar wind abruptly slows.

Anomalous cosmic rays include large quantities of helium, oxygen, neon, and other elements with high ionization potentials, that is, they require

a great deal of energy to ionize, or form ions [20]. ACR are a tool for studying the movement of energetic particles within the Solar system, for learning the general properties of the heliosphere, and for studying the nature of interstellar material itself. ACR are thought to represent a sample of the very local interstellar medium. They are not thought to have experienced such violent processes as GCR and SCR, and they have a lower speed and energy.

The purpose of the present work is to derive new formulas for ionizing capability  $C$  and ionization yield functions  $Y$  in the case of the solar cosmic rays and anomalous cosmic rays, which requires the obtaining of new convenient sub-relativistic approximations according to their energy.

### 3.1. Formulas for Ionization Losses Function

The ionization losses function of Bohr-Bethe-Bloch is the basis for calculating of electron-ion production rate profiles (1, 3) and ionizing capability at height  $h$  [11]:

$$(30) \quad -\frac{dE}{dh} = 0.3\rho(h)Z^2 \frac{E^2}{E^2 - E_0^2} \left[ \ln \sqrt{E^2 - E_0^2} + 4.5 - \frac{1}{2} \frac{E^2 - E_0^2}{E^2} \right]$$

where  $E_0$  is the rest mass of the particles and  $\rho(h)$  is the density [g cm<sup>-3</sup>] of atmosphere at height  $h$ . The rest mass of the proton is 938 MeV c<sup>-2</sup>, i.e.  $E_0 = 0.938$  GeV c<sup>-2</sup>. If we put

$$E_0^2 = 0.879844 \approx 0.88$$

in (30) we receive the following more concrete presentation:

$$(31) \quad -\frac{dE}{dh} = 0.3\rho(h)Z^2 \frac{E^2}{E^2 - 0.88} \left[ \ln \sqrt{E^2 - 0.88} + 4.5 - \frac{1}{2} \frac{E^2 - 0.88}{E^2} \right]$$

In the development of some problems it is more convenient to use simplified and symmetric equations. That is why sometimes the energy in cosmic ray physics is expressed in units  $E_0 = 0.938$  GeV. In this case, the equation (31) will pass into:

$$(32) \quad -\frac{dE}{dh} = 0.3\rho(h)Z^2 \frac{E^2}{E^2-1} \left[ \ln \sqrt{E^2-1} + 4.5 - \frac{1}{2} \frac{E^2-1}{E^2} \right]$$

We will use this expression most often.

### 3.2. Complementary Expressions for Ionization Yield Function

The ionization yield function  $Y$  [electron-ion pairs sr cm<sup>2</sup> g<sup>-1</sup>] is used usually in the statistical Monte Carlo simulations [1, 3, 13, 14]. It can be represented as (7)

$$Y(E, h) = \frac{2\pi}{Q} \left( \frac{1}{\rho} \frac{dE}{dh} \right)$$

Taking into account formulas (30, 31, 32), we can write from here similar expressions for ionization yield function in different representations (using the full energy  $E$  or kinetic energy  $E_k$ ) according to specific task:

$$(33) \quad Y(E) = 5.4 \times 10^4 Z^2 \frac{E^2}{E^2 - E_0^2} \left( \ln \sqrt{E^2 - E_0^2} + 4.5 - \frac{1}{2} \frac{E^2 - E_0^2}{E^2} \right)$$

(34)

$$Y(E) = 5.4 \times 10^4 Z^2 \frac{(E_0 + E_k)^2}{E_k (2E_0 + E_k)} \left( \ln \sqrt{E_k (2E_0 + E_k)} + 4.5 - \frac{1}{2} \frac{E_k (2E_0 + E_k)}{(E_0 + E_k)^2} \right)$$

(35)

$$Y(E) = 5.4 \times 10^4 Z^2 \frac{(0.938 + E_k)^2}{E_k (1.876 + E_k)} \left( \ln \sqrt{E_k (1.876 + E_k)} + 4.5 - \frac{1}{2} \frac{E_k (1.876 + E_k)}{(0.938 + E_k)^2} \right)$$

Here is used the following relationship between the total energy  $E$ , the rest energy  $E_0$  and the kinetic energy  $E_k$ :

$$(36) \quad E = E_0 + E_k$$

If we express the energy in units  $E_0 = 0.938$  GeV, i.e.  $E = 1 + E_k$  we will receive the frequently used and convenient formula

$$(37) \quad Y(E) = 5.4 \times 10^4 Z^2 \frac{(1 + E_k)^2}{E_k (2 + E_k)} \left( \ln \sqrt{E_k (2 + E_k)} + 4.5 - \frac{1}{2} \frac{E_k (2 + E_k)}{(1 + E_k)^2} \right)$$

### 3.3. Sub-relativistic Approximation

In the previous part 2. was studied the relativistic case

$$(38) \quad \beta = v/c \approx 1$$

This concerns the galactic CR at middle and lower latitudes. However, at higher geomagnetic latitudes the galactic CR penetrate with

$$(39) \quad \beta = v/c < 1$$

In a similar way during geomagnetic storms the geomagnetic threshold of rigidity  $R_c$  decreases and CR particles can penetrate with velocities smaller than the light velocity  $c$ , i.e. they are sub-relativistic. These CR nuclei produce bigger ionization. Therefore, here we will examine the more general case of sub-relativistic ionization. For this purpose we will present the energy  $E$  through rigidity  $R$  using the formula [10, 11]:

$$(40) \quad E = 1 + E_k = \left[ 1 + \left( \frac{Z}{A} R^2 \right)^{1/2} \right]^2$$

in the expression for ionization losses (30, 31, 32). We also use the sub-relativistic presentation for the relative velocity [2, 18]:

$$(41) \quad \beta = \frac{R}{\left[ R^2 + (A/Z)^2 \right]^{1/2}}$$

Here  $Z$  is the charge and  $A$  atomic weight of the penetrating CR particles.

Substituting (40) and (41) in the expression (32) we can obtain the following formula for the ionization losses:



$$(42) \quad -\left(\frac{dR}{dh}\right) = 0.3\rho(h)Z^2 \left[1 + \left(\frac{A}{ZR}\right)^2\right] \left[ \ln \frac{Z}{A} R + 4.5 - 0.5 \frac{1}{1 + (A/ZR)^2} \right]$$

### 3.4. Ionizing Capability of Sub-relativistic Particles

By replacing the last expression (42) and the spectrum (4) in (3), the solution of the integral for  $q(h)$  and taking into account the definition (5):

$$C(h) = q(h) / \rho(h)$$

we will receive the following formula for the ionizing capability:

$$(43) \quad C(h) = 5.4 \times 10^4 \sum_{i=1}^7 D_i(> R_c) Z_i^2 \left( \ln \frac{Z_i}{A_i} R_c + 4.5 \right) \left[ 1 + \frac{\gamma-1}{\gamma+1} \left( \frac{A_i}{Z_i R_c} \right)^2 \right]$$

where  $D(> R_c)$  are the CR integral spectrums of different types of nuclei [9, 11].

The same result is obtained after replacement of the ionization yield function  $Y$  (33-35, 37) in the general expression (3) which in this case will be in the equivalent form (6):

$$q(h) = \int_{E_c}^{\infty} D(E) Y(E, h) \rho(h) dE$$

or

$$(44) \quad q(h) = \int_{R_c}^{\infty} D(R) Y(R, h) \rho(h) dR$$

In the formula (43) we can notice a group of terms corresponding to the relativistic CR particles [11]. If we indicate  $q$  of relativistic CR with  $q(\beta = 1)$  and  $q$  of sub-relativistic ones with  $q(\beta < 1)$ , then from (43) we can write

$$\begin{aligned}
(45) \quad C(\beta < 1) &\approx \sum_{i=1}^7 C_i(\beta=1) \left[ 1 + \frac{\gamma-1}{\gamma+1} \left( \frac{A_i}{Z_i R} \right)^2 \right] \\
&= \left( 1 + \frac{0.43}{R^2} \right) C_p(\beta=1) + \left( 1 + \frac{1.71}{R^2} \right) \sum_{i=2}^7 C_i(\beta=1) \\
&= \left( 1 + \frac{1.35}{R^2} \right) C(\beta=1)
\end{aligned}$$

where  $C_p$  is the ionizing capability of the protons and  $C_i$  - of heavier nuclei: Helium, L, M, H, VH and SH groups of nuclei in the composition of the primary cosmic rays. In equation (45) the capabilities of all particles in the galactic CR composition are summed up. We also took into account that  $Z_i / A_i = 1$  for protons and  $Z_i / A_i \approx 1/2$  for heavier ( $Z_i \geq 2$ ) nuclei. In the expressions (43, 45) must be replaced the real spectrum and chemical composition of the galactic cosmic rays.

It is clear that at  $R < 2$  GV the expressions (42, 43, 45) generalize the results in the part **2. Relativistic Case - GCR** in the present paper. In this way we can write the relationship

$$(46) \quad C(\beta < 1) = C(\beta=1) (1 + p)$$

as the factor  $p$  takes into account the sub-relativistic contribution. At rigidity  $R > 2-3$  GV the two groups of formulas practically coincide.

Analogously of the expression (46) can be derived the following formula for the ionization yield function  $Y$ :

$$(47) \quad Y(\beta < 1) = Y(\beta=1) (1 + p)$$

This formula will be considered and analyzed in detail in a future study.

### 3.5. Spectra and Ionization Yield Functions of Sub-relativistic Particles

The spectra of solar cosmic rays are represented before all in the form of spectrum by kinetic energy [9, 19]:

$$(48) \quad D(E_k) = K E_k^{-n}$$

The experimental data show that the parameter  $n$  has values  $n \sim 3 - 7$  depending on the rigidity of the solar particles and the acceleration mechanisms on the Sun [19]. For example the spectrum of solar CR during the greatest GLE, observed on February 23, 1956 is [10, 21]:

$$(49) \quad D(E_k) = 4 \times 3310^9 E_k^{-5} \text{ proton/cm}^2 \text{ sec ster MeV}$$

This is the extreme case. The shapes and relative slopes of the spectra of different solar energetic particles: protons, alphas and electrons, may vary among cases. There is significant variation from event to event.

We will use the results obtained in the previous parts. Due to the type of the spectrum (48, 49) the ionization yield function may be expressed by means of the kinetic energy  $E_k$ . For this purpose we determine the rigidity  $R$  of the solar particles with charge  $Z$  and atomic weight  $A$  [11]

$$(50) \quad \frac{Z}{A}R = (E^2 - 1)^{\frac{1}{2}} = [E_k(2 + E_k)]^{\frac{1}{2}}$$

which replaced in equation (9) gives the following expression:

$$(51) \quad Y(R) = 5.4 \times 10^{-2} Z^2 \left[ 1 + \frac{1}{E_k(2 + E_k)} \right] \times \\ \times \left[ \ln [E_k(2 + E_k)]^{\frac{1}{2}} + 4.65 - \frac{1}{2} \left( 1 - \frac{1}{(1 + E_k)^2} \right) \right]$$

where  $E$  is the full energy (GeV) of the penetrating particles and  $E_k$  their kinetic energy in GeV.

In their penetration in the ionosphere and atmosphere the particles decrease their energy  $E_k$  which leads to an increase of the ionization yield function. So that the kinetic energy as well as the ionization yield function themselves will depend on the altitude. Now we shall make some considerations concerning the determination of the law of energy decrease  $E_k(h)$ . In order to obtain this law the ionization yield function (5) can be simplified for solar cosmic rays, which are in the majority cases sub-relativistic ( $E_k < 500 - 600$  MeV). Actually for these energies must be taken

into account the absorption of solar particles in the iono/atmosphere. Besides for energies  $E_k < 500 - 600$  MeV the solar cosmic rays have the biggest intensity and ionization yield function  $Y$  and therefore a maximal iono/atmospheric influence.

Using the fact that for the solar CR particles the inequality  $E_k < 2$  GeV is fulfilled, the following simplified formula is derived from the complete expression (51):

$$(52) \quad Y(E_k) = 1.55 \times 10^{-2} Z^2 \frac{\ln E_k + 10}{E_k}$$

If in (52) we ignore the variation of the logarithmic term (it changes much more slowly than the term  $E_k^{-1}$ ), and we solve the equation for ionization path ( $\text{g cm}^{-2}$ ) of the particles [11], we will receive the law that is sought:

$$(53) \quad E_k(h) = \left( E_k^2 - 10^3 \tilde{h} Z^2 \sec \theta \right)^{\frac{1}{2}}$$

Here the energy is expressed in MeV/nucleon;  $\tilde{h}$  is the atmospheric depth ( $\text{g cm}^{-2}$ );  $\theta$  is the penetration angle of solar CR particles in the iono/atmosphere.

### 3.6. Ionizing Capability of Solar and Anomalous Cosmic Rays

$C$  function (5) physically represents the number of electron-ion pairs produced in one gram of matter (in this case atmospheric air) per second and characterizes the ionization effectiveness of the radiation factor [10, 11]. Taking into account the law of energy  $E_k$  decrease (53) and using (51) for the general expression of ionizing capability we can write the following general expression:

$$(54) \quad C(h) = 1.8 \times 10^5 \sum_{i=1}^n \int_{E_{k,\max}}^{\infty} \int_0^{90^\circ} D_i(E_k) 0.3 Z^2 \times \\ \times \frac{\left[ \left( E_k^2 - 10^3 \tilde{h} Z_i^2 \sec \theta \right)^{\frac{1}{2}} + 1 \right]^2}{\left( E_k^2 - 10^3 \tilde{h} Z_i^2 \sec \theta \right) + 2 \left( E_k^2 - 10^3 \tilde{h} Z_i^2 \sec \theta \right)^{\frac{1}{2}}}$$

$$\times \left\{ 0.5 \ln \left( E_k^2 - 10^3 \tilde{h} Z_i^2 \sec \theta \right)^{\frac{1}{2}} \left[ \left( E_k^2 - 10^3 \tilde{h} Z_i^2 \sec \theta \right)^{\frac{1}{2}} + 2 \right] + 4.65 \right. \\ \left. - 0.5 \frac{\left( E_k^2 - 10^3 \tilde{h} Z_i^2 \sec \theta \right)^{\frac{1}{2}} \left[ 2 + \left( E_k^2 - 10^3 \tilde{h} Z_i^2 \sec \theta \right)^{\frac{1}{2}} \right]}{\left[ \left( E_k^2 - 10^3 \tilde{h} Z_i^2 \sec \theta \right)^{\frac{1}{2}} + 1 \right]^2} \right\} \sin \theta d\theta dE_k$$

The summation is carried out by all nuclei in the composition of solar cosmic rays: protons, helium (alphas) etc. The boundary of the integral  $E_{k\max}$  is determined by the following manner:

$$(55) \quad E_{k\max} = \max \left\{ \begin{array}{l} E_{Ri} = 10^3 \left\{ \left[ \left( \frac{Z_i}{A_i} \right)^2 R^2 + 1 \right]^{\frac{1}{2}} - 1 \right\} \\ E_{Ai} = \left( 10^3 \tilde{h} Z^2 \sec \theta + \varepsilon \right)^{\frac{1}{2}} \\ E_{Ei} \end{array} \right.$$

i.e. for each altitude  $E_{k\max}$  is the biggest of the three energies: the energy corresponding to geomagnetic cutoff rigidity  $E_{Ri}$ , to the atmospheric cutoff  $E_{Ai}$ , and to the electric energy cutoff  $E_{Ei}$  outside the geomagnetic field. The energy  $\varepsilon$  is about 0.1 MeV [11].

### 3.7. Lower Energy Approximation

The general formula (54) is complicated because of many not significant terms. If these terms are ignored, as it happened in equation (52), a simplified formula can be derived from (54) for the ionizing capability of solar cosmic rays:

$$(56) \quad C(h) = 5.4 \times 10^4 \sum_{i=1}^n \int_{E_{k \max}}^{\infty} \int_0^{90^\circ} D_i(E_k) 83 Z_i^2 \times \frac{\ln(E_k^2 - 10^3 \tilde{h} Z_i^2 \sec \theta)^{\frac{1}{2}} + 3.2}{(E_k^2 - 10^3 \tilde{h} Z_i^2 \sec \theta)^{\frac{1}{2}}} \sin \theta d\theta dE_k$$

as the integral boundary  $E_{k \max}$  is the same as (55). This formula is much more convenient than the full expression (54), as the difference in the calculations was below 5%. For comparison, the experimental error in the rocket flight measurements is approximately in this range.

### 3.8. Generalisation of the Results for Spherical Iono/Atmosphere

The previous formulas refer to flat model of the iono/atmosphere. However, for the solar particles penetrating at larger angles  $\theta$ , formulas (53 - 56) are not exact. In the case of larger angles  $\theta > 75^\circ$  the sphericity of the iono/atmosphere must be regarded similarly to the case of electromagnetic ionizing radiation, where the Chapman function  $Ch(\theta, h)$  is introduced [10, 11]. In our case of particle ionization the following dependency is valid for solar cosmic rays:

$$(57) \quad dE_k = \frac{5 \times 10^2 \rho(h) Z^2 dl}{E_k}$$

where

$$(58) \quad dl = dh \sec \theta$$

as  $\rho(h)$  is the atmospheric density at the altitude  $h$ . If we integrate the ratio (57) and solve it in comparison with kinetic energy  $E_k$  we receive the law (53). Now the ionizing capability for **monoenergetic particles** will be:

$$(59) \quad C(h) = 15 Z^2 (E_k^2 - 10^3 \tilde{h} Z^2 \sec \theta)^{-\frac{1}{2}}$$

in the case of flat model and

$$(60) \quad C(h) = 15 Z^2 [E_k^2 - 10^3 \tilde{h} Z^2 Ch(\theta, R^*)]^{-\frac{1}{2}}$$

for the case of spherical model.

Equation (57) can be generalized if it is taken into the form:

$$(61) \quad dE_k = \frac{5 \times 10^2 \rho(h) Z^2 dl}{E_k^m}$$

Than (59, 60) appears as a particular case of the common formula at  $m = 1$ . And at  $m = -1$  the dependences of the electromagnetic ionized radiations are obtained [10, 11]. In the monographs [11, 22, 23] calculations were made for the ionization in the ionosphere with parameter  $m = 3/4$ , which improved somewhat the model  $m = 1$ . In the contemporary models CORIMIA - *COsmic Ray Ionization Model for Ionosphere and Atmosphere* [12] and in the model of Dorman [23] at the analytical approximations are used different variable values in the range  $m = -0.1 \div 1$  for the corresponding energy intervals. For the sub-relativistic particles (SCR and ACR) the values  $m$  of the ionization expression (61) are in the range  $m = 1 \div 0.1$ . By increasing of the energy of CR particles decreases the parameter  $m$ . At high energies  $\approx 1$  GeV/nucl the parameter  $m$  falls to 0. For the relativistic energies  $> 3-5$  GeV/nucl (which are characteristic for GCR) begins slowly logarithmic increase of the ionization losses and the parameter  $m$  becomes  $m = -0.1$ .

## Conclusion

In the present work we discovered a connection between the two approaches: the determination of ionizing capability  $C$  (used by the analytical model CORIMIA) and the ionization yield  $Y$  function (used by the statistical code CORSIKA). We found a consistent method for the calculation of atmospheric ionization due to cosmic rays with galactic, solar and interplanetary (anomalous CR) origin.

The results of the full Monte Carlo simulation which are tabulated in a form of the ionization yield function [1] can be applied much more widely. With the help of the achievements of this work the analytical models CORIMIA can use the results of statistical code CORSIKA that will allow comparison between the two approaches. As is known by CORSIKA is possible to estimate the CR ionization below 20-25 km and by the model

CORIMIA - above this altitude. So those two approaches are complementary.

So two useful approaches have been developed to compute the CR ionization, e.g.: a) the model CORIMIA is analytical [2, 4, 9, 12, 15], while b) CORSIKA code, including the FLUKA Monte Carlo package, is based on a Monte Carlo simulation of the atmospheric cascade [1, 3, 13, 14, 16]. Usually the analytical models use the ionizing capability  $C(h)$  function, while the statistical simulations utilize the ionization yield  $Y(h)$  function.

In part 1.1. *Analytical and Statistical Approaches in Ionization Models and Relationships between them* we have found a new relationship between the functions  $C(h)$  and  $Y(h)$  and we have implemented a unified approach to the calculation of iono/atmospheric ionization due to cosmic rays with galactic, solar and interplanetary origin.

Further a theoretical considerations were carried in relation to these issues in the part 2. *Relativistic Case – GCR*, and part 3. *Sub-relativistic Case – SCR and ACR* for the solar and anomalous CR ionization shall be the basis for a quantitative investigation of the mechanisms for solar-terrestrial influences. The GCR, SCR and ACR are a major factor affecting the physical-chemical processes in the iono/atmosphere, including the electrical conductivities, electrical currents and fields [24] and the iono/atmospheric chemistry - i.e. the variations and planetary distribution of the ozone [17, 18]. All this has important applications for the space weather and space climate [25, 26]. These results will stimulate the quantitative study of the physical processes and physical mechanisms in the Earth's environment and in the Sun – Earth system.

## References

1. U s o s k i n, I., G. A. K o v a l t s o v. Cosmic ray induced ionization in the atmosphere: Full modeling and practical applications J. Geophys. Res., 111, 2006, D21206. DOI:10.1029/2006JD007150.
2. V e l i n o v, P. I. Y., S. A s e n o v s k i, K. K u d e l a, J. L a s t o v i c k a, L. M a t e e v, A. M i s h e v, P. T o n e v, Impact of Cosmic Rays and Solar Energetic Particles on the Earth's Environment. J. Space Weather Space Clim. 3, 2013, A14, 1-17.
3. M i s h e v, A., P. I. Y. V e l i n o v. Influence of Hadron and Atmospheric Models on Computation of Cosmic Ray Ionization in the Atmosphere - Extension to Heavy Nuclei. J. Atmos. Solar-Terr. Phys., 120, 2014, 12, 111-120.



DOI: 10.1016/j.jastp.2014.09.007.

4. V e l i n o v, P. I. Y., M a t e e v, L., Analytical approach to cosmic ray ionization by nuclei with charge  $Z$  in the middle atmosphere - Distribution of galactic CR effects, *Adv. Space Res.*, 42, 1586-1592, 2008.
5. V e l i n o v, P. I. Y., 1965. Electromagnetic Field Variations of Long Wave Propagation in the Quiet and Disturbed Ionosphere. MSc Thesis. Geophysical Institute, Bulgarian Academy of Sciences, Technical University, Sofia, 95 p.
6. V e l i n o v, P. I. Y. An Expression for the Ionospheric Electron Production Rate by Cosmic Rays. *C.R. Acad. Bulg. Sci.*, 19, 1966, 2, 10-112.
7. N e s t o r o v, G., *Physics of the Lower Ionosphere*, Publishing House of the Bulgarian Academy of Sciences, Sofia, 1969.
8. S e r a f i m o v, K., *Physics of the Middle Ionosphere*, Publishing House of the Bulgarian Academy of Sciences, Sofia, 1970.
9. V a n A l l e n, J., in: *Physics and Medicine of Upper Atmosphere*, Chapter XIV, Univ. New Mexico Press, Albuquerque, 1952.
10. V e l i n o v, P. I. Y. On Ionization of the Ionospheric D-Region by Galactic and Solar Cosmic Rays. *J. Atmos. Terr. Phys.*, 30, 1968, 11, 1891-1905.
11. V e l i n o v, P. I. Y., G. N e s t o r o v, L. I. D o r m a n. Cosmic Ray Influence on the Ionosphere and on Radiowave Propagation, Publishing House of the Bulgarian Academy of Sciences, Sofia, 1974.
12. V e l i n o v, P. I. Y., S. A s e n o v s k i, L. M a t e e v. Improved COsmic Ray Ionization Model for Ionosphere and Atmosphere (CORIMIA) with Account of 6 Characteristic Intervals. *C.R. Acad. Bulg. Sci.*, 65, 2012, 8, 1137-1144.
13. M i s h e v, A. Short and Medium Term Induced Ionization in the Earth Atmosphere by Galactic and Solar Cosmic Rays. *Intern. J. Atmos. Sci.*, 1 (1), 2013, Article ID 184508, pp. 1-9. <http://dx.doi.org/10.1155/2013/184508>
14. M i s h e v, A., P. I. Y. V e l i n o v. Atmosphere Ionization Due to Cosmic Ray Protons Estimated with CORSIKA Code Simulations. *C.R. Acad. Bulg. Sci.*, 60, 2007, 3, 225-230.
15. V e l i n o v, P. I. Y., S. A s e n o v s k i, L. M a t e e v. Numerical Calculation of Cosmic Ray Ionization Rate Profiles in the Middle Atmosphere and Low Ionosphere with Relation to Characteristic Energy Intervals. *Acta Geophysica*, 61, 2013, 2, 494-509.
16. U s o s k i n, I., L. D e s o r g h e r, P. I. Y. V e l i n o v, M. S t o r i n i, E. F l u c k i g e r, R. B u e t i k o f e r, G. A. K o v a l t s o v. Solar and Galactic Cosmic Rays in the Earth's Atmosphere. *Acta Geophysica*, 57, 2009, 1/March, 88-101.
17. K i l i f a r s k a, N. An Autocatalytic Cycle for Ozone Production in the Lower Stratosphere Initiated by Galactic Cosmic Rays *C.R. Acad. Bulg. Sci.*, 66, 2013, 2, 243-252.
18. T a s e v, Y., N. K i l i f a r s k a, D. T o m o v a. Statistical Analysis of Solar Proton Flux Influence on Thermodynamics of Middle Atmosphere in the North Hemisphere *C.R. Acad. Bulg. Sci.*, 67, 2014, 1, 95-100.
19. M i r o s h n i c h e n k o, L. I. *Solar Cosmic Rays*, Kluwer Academic Publishers, Dordrecht, The Netherlands, 2001.

20. V e l i n o v, P. I. Y., Effect of the Anomalous Cosmic Ray (ACR) Component on the High-Latitude Ionosphere. C.R. Acad. Bulg. Sci., 44, 1991, 2, 33-36.
21. M e y e r, P., E. N. P a r k e r, J. A. S i m p s o n. Solar Cosmic Rays of February, 1956 and their Propagation through Interplanetary Space, Phys. Rev., 104, 1956, 3, 768-783.
22. D o r m a n, L. I., K o z i n, I. D., 1983, Cosmic Radiation in the Upper Atmosphere, Fizmatgiz, Moscow.
23. D o r m a n, L. I., 2004, Cosmic rays in the Earth's atmosphere and underground, Kluwer Academic Publishers, Dordrecht.
24. T o n e v, P. Estimation of Currents in Global Atmospheric Electric Circuit with Account of Transpolar Ionospheric Potential. C.R. Acad. Bulg. Sci., 65, 2012, 11, 1593-1602.
25. P a n c h e v a, D., P. M u k h t a r o v. Semidiurnal Tidal Response to the Sudden Stratospheric Warming in January 2009 and its Effect on the Ionosphere. C.R. Acad. Bulg. Sci., 65, 2012, 8, 1125-1134.
26. M i s h e v, A., J. S t a m e n o v. Present Status and Further Possibilities for Space Weather Studies at BEO Moussala. J. Atmos. Solar-Terr. Phys. 70, (2-4), 2008, 680-685.

**НОВ АНАЛИТИТИЧЕН ПОДХОД ЗА МОДЕЛИРАНЕ  
НА ЙОНИЗАЦИЯТА НА КОСМИЧЕСКИТЕ ЛЪЧИ  
В ОКОЛОПЛАНЕТНИТЕ ПРОСТРАНСТВА  
ПОСРЕСТВОМ ИЗПОЛЗВАНЕТО НА ПОРАЖДАЩИ  
ЙОНИЗАЦИЯТА ФУНКЦИИ**

*П. Велинов*

**Резюме**

Космическите лъчи (CR) въздействат върху йонизацията и електрическите параметри в атмосферата, а също така и върху нейните химически процеси (образуване и разрушаване на озона в стратосферата). CR йонизират цялата средна и ниска атмосфера, т.е. страто-мезосферата и тропосферата. Така че космическите лъчи са ключов фактор, както за атмосферната химия, така и за космическото време и космическия климат в околоземното космическо пространство.

Съществуват основно два подхода за изчисляването на йонизацията на CR, например: 1) аналитичният модел CORIMIA - COsmic Ray Ionization Model for Ionosphere and Atmosphere, и 2) статистическият модел CORSIKA, включващ програмата FLUKA, която се базира на симулацията на атмосферните каскади по метода Монте Карло. Обикновено аналитичните модели използват функцията на йонизиращата

способност  $C$ , докато статистическите симулации използват пораждащата йонизация функция  $Y$ . В настоящата работа е намерена връзка между функциите  $C$  и  $Y$  и е предложен единен подход за изчисляване на атмосферната йонизация вследствие на космическите лъчи с галактичен (GCR), слънчев (SCR) и междупланетен (аномални CR, ACR) произход.

В работата са изведени формули за йонизиращата способност и пораждащата йонизация функция при общия случай, при релятивистична апроксимация (GCR) и при суб-релятивистичен случай (SCR и ACR). Входните параметри на предложения модел включват пълния състав на групите ядра на космическите лъчи, както следва: протони ( $p$ ,  $Z = 1$ ), алфа частици ( $\alpha$ ,  $Z = 2$ ), и HEZ частици: леки (L,  $3 \leq Z \leq 5$ ), средни (M,  $6 \leq Z \leq 9$ ), тежки (H,  $10 \leq Z \leq 19$ ), много тежки (VH,  $Z \geq 20$ ) и свръх тежки (SH,  $Z \geq 30$ ) групи ядра.

В работата са дискутирани някои практически приложения на получените резултати. Така например, резултатите от пълната симулация по Монте Карло, където са табулирани пораждащите йонизация функции в удобна форма, могат да се приложат много по-широко. С помощта на постиженията на настоящата работа аналитичният модел CORIMIA може да използва резултатите от статистическата програма CORSIKA, което ще даде възможност за сравнение между двата подхода. Както е известно, с помощта на CORSIKA може да се оценява йонизацията на космическите лъчи под 20-25 km, докато с модела CORIMIA – над тези височини. Така че тези два подхода се допълват взаимно.

Предложеният подход може да се използва за количествени разглеждания и анализ на слънчево-земните връзки и за проблемите на космическото време и космическия климат. Това е един теоретичен подход и поради това той може да се приложи също така и за изчисляване на йонизационните ефекти в планетните йоносфери и атмосфери.

**INTERESTING BOOK OF THE DAY**



Even today, at the dawn of the new millennium, despite science and technology highly appraised revelations, ecological catastrophes inflict severe material damages and take a heavy toll of human life in a global scale. Combating against these menaces, mankind justifiably entrusts major hopes to the remote aerospace technologies. In this aspect, the newly loomed into sight book “National aerospace system for monitoring and protection from natural disasters”, issued by Academic Publishing House “Prof. Marin Drinov”, is topical and fascinating to a broad circle

of readers audience.

The author professor Petar Getsov is director of the Space Research and Technology Institute at the Bulgarian Academy of Sciences. He is well-known specialist in the field of aerospace research and technologies and specifically in aerospace control systems. Prof. Getsov has originated 7 books and monographs, over 160 scientific publications, more than 60 innovations, patents and licenses. He leads teams working on a number of valuable international and national space projects.

The book defines the major goals and tasks in creating the concept of complex approach in the remote sensing of Earth and in the National system for monitoring of ecological disasters and critical infrastructures. The fundamental elements of this system were examined and analyzed:

aerospace center for information acquisition, satellite and aviation segment.

The research, analyses, concept and conclusions have brightly pronounced practical orientation, while their implementation would allow prevention and actions during crises, avoidance of the consequences from those and realization of short-term and long-term ecological prognoses.

Informative applications, successfully drawn at the end of the book, facilitate reading and comprehension of its contents.

Foreseeing the liveliness of this subject, the book usefulness and the extremely limited number of such publications in world-wide scale, one could assert that the appearance of the book “National aerospace system for monitoring and protection from natural disasters” is an event in the sphere of application remote sensing aerospace technologies benefiting the ecology avenue.

Prof. Garo Mardirossian

---

Гецов, П. Национална аерокосмическа система за мониторинг и защита от природни екокатастрофи. Акад. издат. “Проф. Марин Дринов”, София, 2014, 231 с.